Collegium Sciences et Technologies
École Doctorale SESAMES

# THÈSE

Présentée pour l'obtention du titre de

## Docteur de l'Université de Lorraine

en Physique

par

## Kuan-Ying HSIEH

## Étude multi-échelle des changements structuraux et leur influence sur les propriétés optiques de complexes photoactifs encapsulés dans des matrices mésoporeuses

*Soutenance publique prévue le 28 octobre 2013*

Membres du Jury :

Rapporteurs :

| | |
|---|---|
| R.B. Neder | Professeur, University of Erlangen (Germany) |
| J. Schefer | Leader Neutron Diffraction group, Paul Scherrer Institut (Switzerland) |

Examinateurs:

| | |
|---|---|
| T. Woike | Professeur, University of Dresden (Germany) |
| H. Rinnert | Professeur, IJL, Université de Lorraine |
| E. Elkaïm | Chargé de recherche, CNRS, Synchrotron Soleil |
| E.-E. Bendeif | Maître de Conférences, CRM², Université de Lorraine |
| D. Schaniel | Professeur, CRM², Université de Lorraine |

Invité : S. Pillet    Chargé de recherche CNRS, CRM², Université de Lorraine

*Laboratoire de Cristallographie, Résonance Magnétique et Modélisations CRM2, UMR CNRS 7036*

# Acknowlegments

# Table of Contents

# Chapter 4     Synthesis and multiscale structural analysis of photoswitchable molecular hybrid materials

# Chapter 5     Structural investigation and photoluminescent properties of embedded neodymium complex

List of publications related to this work

# Chapter 1

# Introduction

Tremendous efforts are currently related to the conception and fabrication of functional molecular materials and devices with fine-tuned optical and magnetic behaviour, in which the individual entities and their spatial arrangement are engineered down to the nanometer scale [1–6]. In this context, thermo- and photo-switchable molecules, which can be reversibly switched between different structural configurations with different physical properties, are interesting candidates for optical applications [7,8], e.g. ultrafast holography, magneto-optical storage devices or medical pharmacology. However, the processing of such materials is not a mature technology as molecular crystals very often do not sustain the demanding conditions in applications (heat load, power density, etc.). Consequently, different methods of incorporating the molecular functionality in mesoporous silica matrices have been developed in recent years, leading to hybrid organic-inorganic nanocomposite materials [9–23]. The properties of mesoporous silica inorganic supports, namely a large surface area, a robust framework with easily accessible pore architectures with narrow and tunable entrances giving free ingress and egress to the guest species, tunable pore size, make them suitable to host small molecules and nanoparticles. In addition, the incorporation of specific functionality within the inner surface of the channels to provide anchoring points for the guest species can prevent leaching. In such nanocomposites, the silica matrix provides mechanical and chemical stability, in addition to optical transparency, and can be used at the same time to arrange the spatial distribution of the molecular objects, and to tune their concentration, and separation distance. The design of nanocomposites with optical or photonic properties is a very mature field of research [24–26]. Numerous organic dyes, with photochromic, photorefractive, second-order non-linear optic functionalities have been elaborated and fully characterized. Magnetic nanocomposite materials have also gained increasing interest, mostly for medical applications, the silica matrix providing

non-toxicity, bio-compatibility, and stability in physiological environments. Among others, $Fe_2O_3@SiO_2$, $Fe_3O_4@SiO_2$, and $CoFe_2O_4@SiO_2$ magnetic composites were reported [11,27,28]. Molecular magnetic clusters, such as the heptanuclear [$Cu_6Gd$] high spin magnetic cluster, have also been immobilized in mesoporous silica [29]. Photoluminescent and photocatalytic [Pt(tpy)Cl]Cl complexes were anchored within functionalized mesoporous silica materials [30]. These series of results demonstrate that isolated molecules, clusters, or nanoparticles can be indeed inserted by wet impregnation methods preserving the molecule integrity inside the nanocavities of mesoporous silica matrices, sometimes functionalized to favour a strong anchoring of the guest molecules. The confined growth of size controlled nanoparticles inside the nanocavities of amorphous or mesostructured silica matrices is a very promising strategy to design nanocomposites with a high monodispersity in nanoparticle size. The templating effect of the host silica matrix confines the supramolecular self-assembly process, and consequently restricts the nanocrystal growth. A careful control of the ageing procedure could allow producing the desired silica xerogels with tailored textural properties and adjustable pore size, thus affording the possibility of assembling and isolating nanoscale objects with tunable sizes, ranging from molecules to molecular aggregates and to crystalline nanoparticles. It is noteworthy that a perfect monodispersity is hardly reachable with alternative synthetic approaches used in the literature to elaborate molecular nanoparticles, such as fast precipitation with a counter solvent, or using water/oil microemulsion, organic polymers, or biomolecular templates.

In order to establish the structure-property relationships of these different nanoscale materials one needs at first a reliable structure description. However, there are currently no robust broadly applicable quantitative methods for solving structures at the nanoscale. Accordingly, deriving the structural organisation and dynamics of nanoparticles in nanocomposites is a very delicate and challenging task. There exist imaging tools (scanning probe microscopies, transmission electron microscopies) which do not yield quantitative 3D structures. Owing to the reduced size of the objects, characterized by a loss of long range translational symmetry and possibly severe structural relaxation, standard crystallographic techniques become inappropriate for studying nanoparticles. New approaches and new experimental tools have to be developed for such nano-crystallographic problems.

One very valuable approach is total scattering and the atomic pair distribution function (PDF) analysis of X-ray and neutron scattering data. Especially, high energy (short wavelength) diffraction data yield short and intermediate range structural information [31]. Total scattering refers to the fact that all (structure-relevant) scattering from a sample is collected, including both Bragg and diffuse components, over a wide

range of reciprocal space where coherent scattering exists. The PDF is obtained when the scattering signal is Fourier-transformed to real-space. The data may be modelled quantitatively without any crystallographic assumption to obtain structural information as a function of the length-scale on the nanoscale. Alternatively, the scattering data may be directly fitted using the Debye equation, a sum of the scattering over all pairs of atoms in the particle, allowing the comparison with a structural model. The PDF approach provides more extensive and accurate structural properties compared, for example, to Extended X-ray Absorption Fine Structure spectroscopy (EXAFS). Although EXAFS is a powerful tool for probing local structure, it provides information only about intermediate atomic ordering (near neighbour pairs), while longer-ranged structural features remain hidden and, consequently, the information available about the relative motion of far neighbour pairs is very limited, uncorrelated thermal parameters are not available as well.

The PDF analysis has been used since the early days of X-ray and neutron crystallography to investigate the framework structure of silica. More recently, structural information on nanoparticles, such as manganese ferrite $MnFe_2O_4$, iron hydroxyoxide $FeOOH$, or ammonia borane $NH_3BH_3$, embedded in mesoporous silica have been derived through the atomic PDF analysis of synchrotron X-ray diffraction data [28,32,33]. Variable temperature analysis for ammonia borane demonstrates that the embedded nanophase does not undergo the structural phase transition at 225 K, as it was observed for the neat molecular crystal. Rather, the tetragonal phase is preserved to higher temperature, and starts to lose structural correlation above 240 K.

The CRM2 laboratory has initiated some years ago the investigation of molecular nanoparticles and nanocomposites using the PDF analysis. In this context the recent development of an approach based on the Debye formalism which allows studying the structure of isolated molecules in amorphous hosts is of particular interest [34], as the Debye Function analysis is performed in reciprocal space contrary to the PDF which is performed in real space.

The aim of this thesis work was to contribute to this fundamental crystallographic problem of analysing nanoscale structures by a systematic investigation of mesoporous hosts loaded with functional molecules, thereby addressing the following scientific and methodological questions

- What is the structure of isolated molecules in a porous or nanostructured environment?
- How does the local environment and the particle size influence the functional properties of the embedded molecule/particle?

- Can we use laboratory X-ray diffractometers to obtain the structural informations (in comparison to synchrotron)?
- What are the limits of the total scattering approach and how do the two analysis methods PDF and Debye compare?

The molecular materials used for the study are photoswitchable mononitrosyl compounds and luminescent rare earth complexes embedded in mesoporous hosts such as silica matrices. Due to their photofunctionality – switching of single ligand groups by light, leading to photochromic changes or luminescence – the structure-property relationship can be studied using diffraction (x-ray and neutron) and optical techniques (absorption, infrared and fluorescence spectroscopy). Further experimental methods to be used are adsorption and TEM (determination of pore size and microsctructure), as well as NMR (local structure and dynamics).

The manuscript is organized in 5 chapters. In chapter two the experimental methods for the molecular and nanoscale structural determination are outlined. Chapter three addresses the important details of the different modelling approaches used in this work: PDF, Debye and reverse Monte Carlo. In chapter four the first of the two applications is presented: the structural study of $Na_2[Fe(CN)_5NO].2H_2O$ (Sodium Nitroprusside, SNP) embedded in porous amorphous silica matrices. Thes example is also used for a thorough comparison of the results obtained from synchrotron and laboratory data. In chapter five the results of the structural study on the second example – a luminescent $Nd^{3+}$ complex embedded in silica matrices – is presented. On this example the PDF and Debye analysis will be compared.

# Bibliography

[1]   A. P. Alivisatos, J. Phys. Chem. **100**, 13226 (1996).

[2]   G. Hodes, Adv. Mater. **19**, 639 (2007).

[3]   A. M. Spokoyny, D. Kim, A. Sumrein, and C. A. Mirkin, Chem. Soc. Rev. **38**, 1218 (2009).

[4]   A. Patra, C. G. Chandaluri, and T. P. Radhakrishnan, Nanoscale **4**, 343 (2012).

[5]   W. Lin, W. J. Rieter, and K. M. L. Taylor, Angew. Chem. Int. Ed Engl. **48**, 650 (2009).

[6]   A. Carné, C. Carbonell, I. Imaz, and D. Maspoch, Chem. Soc. Rev. **40**, 291 (2011).

[7]   O. Sato, J. Tao, and Y.-Z. Zhang, Angew. Chem. Int. Ed Engl. **46**, 2152 (2007).

[8]   M. Goulkov, D. Schaniel, and T. Woike, J. Opt. Soc. Am. B **27**, 927 (2010).

[9]   T. Gacoin, S. Besson, and J. P. Boilot, J. Phys. Condens. Matter **18**, S85 (2006).

[10]  A.-H. Lu and F. Schüth, Adv. Mater. **18**, 1793 (2006).

[11]  A. Parma, I. Freris, P. Riello, D. Cristofori, C. de Julián Fernández, V. Amendola, M. Meneghetti, and A. Benedetti, J. Mater. Chem. **22**, 19276 (2012).

[12]  A. Tissot, J.-F. Bardeau, E. Rivière, F. Brisset, and M.-L. Boillot, Dalton Trans. Camb. Engl. 2003 **39**, 7806 (2010).

[13]  S. Titos-Padilla, J. M. Herrera, X.-W. Chen, J. J. Delgado, and E. Colacio, Angew. Chem. Int. Ed. **50**, 3290 (2011).

[14]  C. Faulmann, J. Chahine, I. Malfant, D. de Caro, B. Cormary, and L. Valade, Dalton Trans. **40**, 2480 (2011).

[15]  J. G. Moore, E. J. Lochner, and A. E. Stiegman, Angew. Chem. Int. Ed Engl. **46**, 8653 (2007).

[16]  J. G. Moore, E. J. Lochner, C. Ramsey, N. S. Dalal, and A. E. Stiegman, Angew. Chem. Int. Ed. **42**, 2741 (2003).

[17]  G. Clavel, Y. Guari, J. Larionova, and C. Guérin, New J. Chem. **29**, 275 (2005).

[18]  B. Folch, Y. Guari, J. Larionova, C. Luna, C. Sangregorio, C. Innocenti, A. Caneschi, and C. Guérin, New J. Chem. **32**, 273 (2008).

[19]  G. Fornasieri and A. Bleuzen, Angew. Chem. Int. Ed. **47**, 7750 (2008).

[20]  P. Durand, G. Fornasieri, C. Baumier, P. Beaunier, D. Durand, E. Rivière, and A. Bleuzen, J. Mater. Chem. **20**, 9348 (2010).

[21]  G. Fornasieri, M. Aouadi, P. Durand, P. Beaunier, E. Rivière, and A. Bleuzen, Chem. Commun. **46**, 8061 (2010).

[22]  V. Monnier, N. Sanz, E. Botzung-Appert, M. Bacia, and A. Ibanez, J. Mater. Chem. **16**, 1401 (2006).

[23] N. Sanz, P. Terech, D. Djurado, B. Demé, and A. Ibanez, Langmuir **19**, 3493 (2003).

[24] B. Lebeau and P. Innocenzi, Chem. Soc. Rev. **40**, 886 (2011).

[25] R. Pardo, M. Zayat, and D. Levy, Chem. Soc. Rev. **40**, 672 (2011).

[26] C. Sanchez, B. Lebeau, F. Chaput, and J.-P. Boilot, Adv. Mater. **15**, 1969 (2003).

[27] R. P. Hodgkins, A. Ahniyaz, K. Parekh, L. M. Belova, and L. Bergström, Langmuir **23**, 8838 (2007).

[28] D. Carta, A. Corrias, and G. Navarra, J. Non-Cryst. Solids **357**, 2600 (2011).

[29] I. Kornarakis, G. Sopasis, C. J. Milios, and G. S. Armatas, RSC Adv. **2**, 9809 (2012).

[30] K. Mori, K. Watanabe, Y. Terai, Y. Fujiwara, and H. Yamashita, Chem. – Eur. J. **18**, 11371 (2012).

[31] T. Egami and S. J. L. Billinge, *Underneath the Bragg Peaks: Structural Analysis of Complex Materials*, 2nd ed. (Pergamon, 2012).

[32] H. Kim, A. Karkamkar, T. Autrey, P. Chupas, and T. Proffen, J. Am. Chem. Soc. **131**, 13749 (2009).

[33] G. Ennas, M. F. Casula, S. Marras, G. Navarra, A. Scano, and G. Marongiu, J. Nanomater. **2008**, (2008).

[34] A. Cervellino, J. Schefer, L. Keller, T. Woike, and D. Schaniel, J. Appl. Crystallogr. **43**, 1040 (2010)

# Chapter 2

# Experimental methods for molecular and nanoscale structural determination

# Chapter 2

# Experimental methods for molecular and nanoscale structural determination

Nowadays, functional materials are often built using units structured on the nanoscale. Due to this limitation of the atomic order to the nanoscale [1,2], as found for example in nanoparticles [3], species encapsulated in mesoporous hosts [4], and bulk crystals with defects/dopants or intrinsic nanoscale order [5,6], the structure determination of such materials is quite challenging. However, a quantitative knowledge of the atomic structure within these materials is a prerequisite to understanding their physical properties.

A century ago, the physicist Lawrence Bragg announced an equation that lead to the well-known success-story of X-ray crystallography [7]. It provides a powerful tool for studying long-range ordered crystalline structures, but breaks down for structures that extend only over a few nanometers. For the crystalline material, the diffraction pattern can be calculated if the unit cell size, symmetry, atom types and their fractional coordinates are known using the structure factor $F_{hkl}$. When dealing with scattering from nano-objects or objects with only partial crystallinity, the Bragg peaks do not contain the whole structural information. Diffuse scattering, which is present in every diffraction pattern but which is usually ignored and considered as a "background correction" in a Rietveld refinement [8–10], needs to be taken into account. The measurement of the complete diffraction pattern, including both the Bragg and diffuse components, is referred to as a total scattering measurement [11–13].

There exist several techniques for probing nanostructure materials. Some are inherently local, such as TEM and scanning probe microscopy. Others are bulk average probes that are sensitive to the local structure, e.g., EXAFS or NMR. In general, none of these techniques contains sufficient information to obtain a unique structural resolution. A coherent strategy is then required combining input from multiple experimental methods as well as theory in a self-consistent global optimization scheme: sometimes that we refer to as "complex modelling". [2]

## 2.1 X-ray and Neutron total scattering

Rather than collecting all the Bragg peaks at discrete angles as is done in single-crystal structure determination, in a total scattering measurement the scattered intensity is measured as continuous function of the scattering angle. This is most conveniently expressed in terms of the wavevector Q that is defined, for elastic scattering, as:

$$Q = |\vec{Q}| = \frac{4\pi \sin\theta}{\lambda} \qquad (2.1)$$

Where $\theta$ is the scattering angle and $\lambda$ is the wavelength of radiation used. For elastic scattering, $\vec{Q}$ is the difference between the incident wavevector $\vec{k_i}$ and the scattered wavevector as $\vec{k_f}$ ($\vec{Q} = \vec{k_i} - \vec{k_f}$) (Figure 2.1).
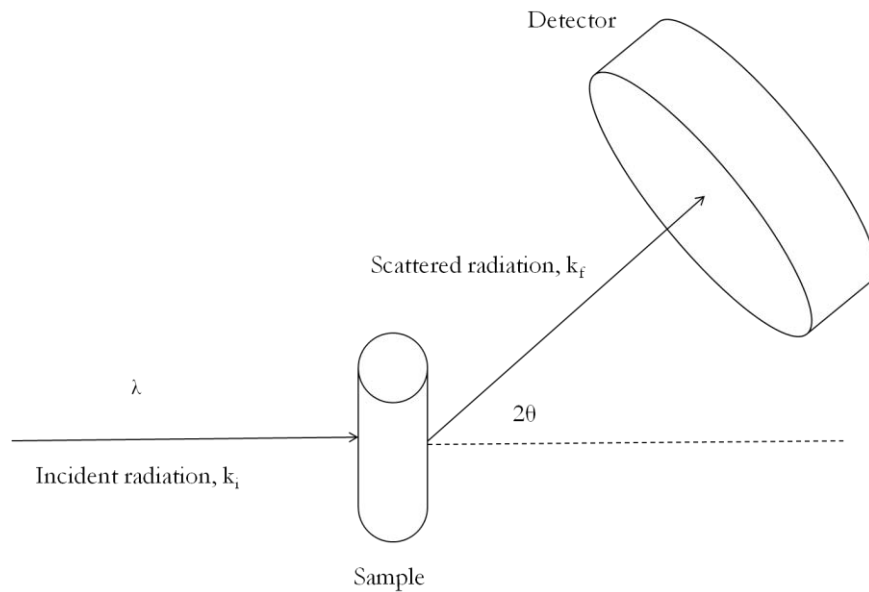


Figure 2.1 Primary layout of x-ray and neutron diffractometer.

## 2.1.1 Coherent Scattering Intensity

X-ray and neutron total scattering measurements have been used for a long time to study the isotropic scattering for a variety of materials from powder, liquid or glass. As usual, in diffraction experiments we measure only the scattered intensity and not the sample scattering amplitude directly. It is important, however, that the measured sample is truly isotropic to avoid texture and preferential powder orientation problems. In this case, the scattered intensity depends only on the amplitude of Q and not on its direction and is described by the standard scattering equation [11].

$$I_{coh}(Q) = \sum_{i=j}^{N} f_i^2 + \sum_{i \neq j}^{N} f_i f_j e^{iQ[r_i - r_j]} \tag{2.2}$$

Where $f$ denotes the Q-dependent atomic form factor for X-ray scattering, and the constant scattering length ($b$) for neutron scattering. Defining $r_{ij} = r_i$-$r_j$ as the length of interatomic vector between the atoms $i$ and $j$, the well-known Debye equation [14] is obtained by performing the powder average:

$$I_{coh}(Q) = \sum_{i=j}^{N} f_i^2 + \sum_{i \neq j}^{N} f_i f_j \frac{sinQr_{ij}}{Qr_{ij}} \tag{2.3}$$

Note that the sum in this equation is divided into two parts, namely terms for which $i=j$, the so-called "self-scattering" terms and terms for which $i \neq j$, the "distinct" or "interference" terms. The self-scattering terms will carry no information on the relative distribution of atoms because it incorporates only the zero distances of an atom whose Q-dependence is due to its form factor $f$.

Figure 2.2 shows $I_{coh}(Q)$ of amorphous $SiO_2$ gel measured by X-ray diffraction and the corresponding "self-scattering" contribution. One can clearly observe that the intensity of the diffracted beam falls off with increasing Q. This is a typical feature for X-ray measurements where the atomic scattering amplitude depends fairly strongly on Q and is usually denoted as f(Q).
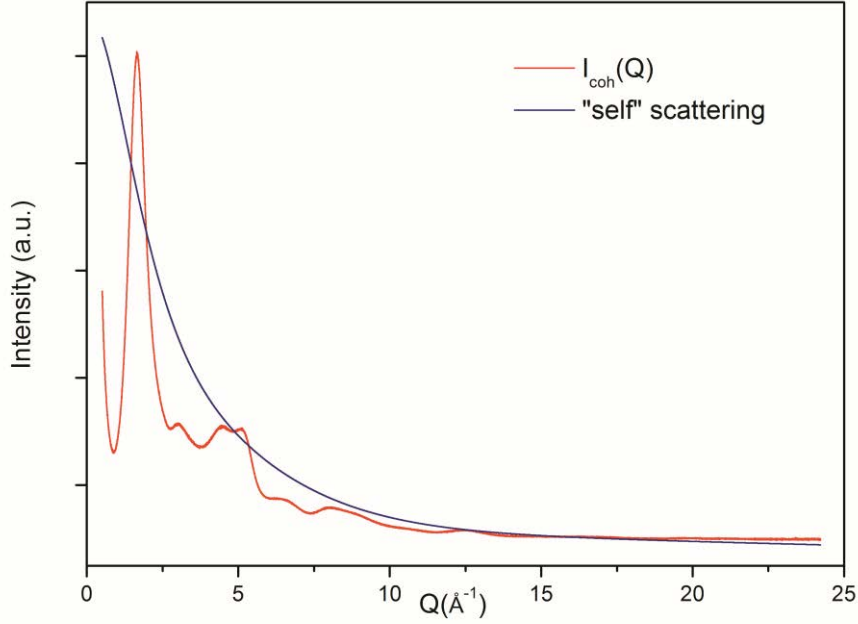
Figure 2.2 Coherent scattering $I_{coh}(Q)$ (blue) and corresponding 'self-scattering" component (red) in the total scattering intensity of amorphous $SiO_2$.

## 2.1.2    The Total Scattering Structure Function

When the measured scattering intensity $I_{coh}(Q)$ is properly normalized by dividing by the total number of scattering centers in the sample, N, and the average scattering factor over all atoms in the sample, $\langle f \rangle^2$, it yields the total scattering structure function S(Q) as described in the following. Equation (2.4) can be easily deduced from equation (2.2):

$$I_{coh}(Q) = N\langle f^2 \rangle + \sum_{i \neq j}^{N} f_i f_j e^{iQ[r_i - r_j]} \tag{2.4}$$

By dividing first by N and then by $\langle f \rangle^2$ we obtain:

$$\frac{I_{coh}(Q)}{N} = \langle f^2 \rangle + \frac{1}{N} \sum_{i \neq j}^{N} f_i f_j e^{iQ[r_i - r_j]} \tag{2.5}$$

$$\frac{I_{coh}(Q)}{N\langle f \rangle^2} = \frac{\langle f^2 \rangle}{\langle f \rangle^2} + \frac{1}{N\langle f \rangle^2} \sum_{i \neq j}^{N} f_i f_j e^{iQ[r_i - r_j]} \tag{2.6}$$

$$\frac{I_{coh}(Q)}{N\langle f \rangle^2} - \frac{\langle f^2 \rangle}{\langle f \rangle^2} = \frac{1}{N\langle f \rangle^2} \sum_{i \neq j}^{N} f_i f_j e^{iQ[r_i - r_j]} \tag{2.7}$$

We define the quantity in Equation (2.7) as S(Q)-1 where S(Q) is the total scattering structure function[*]. Substituting this into Equation (2.7)

$$S(Q) - 1 = \frac{I_{coh}(Q)}{N\langle f \rangle^2} - \frac{\langle f^2 \rangle}{\langle f \rangle^2} \tag{2.8}$$

$$S(Q) = \frac{I_{coh}(Q) - N(\langle f^2 \rangle + \langle f \rangle^2)}{N\langle f \rangle^2} \tag{2.9}$$

Finally, we pull out N by defining $I(Q) = I_{coh}(Q)/N$, so equation (2.9) is simplified to

$$S(Q) = \frac{I(Q) - \langle f^2 \rangle + \langle f \rangle^2}{\langle f \rangle^2} = 1 + \frac{I(Q) - \langle f^2 \rangle}{\langle f \rangle^2} \tag{2.10}$$

The S(Q) includes both Bragg peaks and diffuse scattering and is directly related to the total scattering amplitude of the sample. The Fourier transform of S(Q), is the density-density correlation function that allows for the structure refinement in real space as we discuss in detail later. In general, we assume that scattering from a powder is isotropic, due to the random grain orientation in powders, and it depends on the magnitude of wavevector, not on the direction as we have described above. We will thus

---

[*] Total scattering structure function is defined theoretically in terms of correlation function according to different researchers, frequently leading to confusion in the literature [15]. In this thesis, we use the notation described by Billinge & Egami (1993) [13].

in the following no longer use the vector notation for Q. As an example S(Q) created from the measured I(Q) of $SiO_2$ (Fig. 2.2) is shown in Figure 2.3.
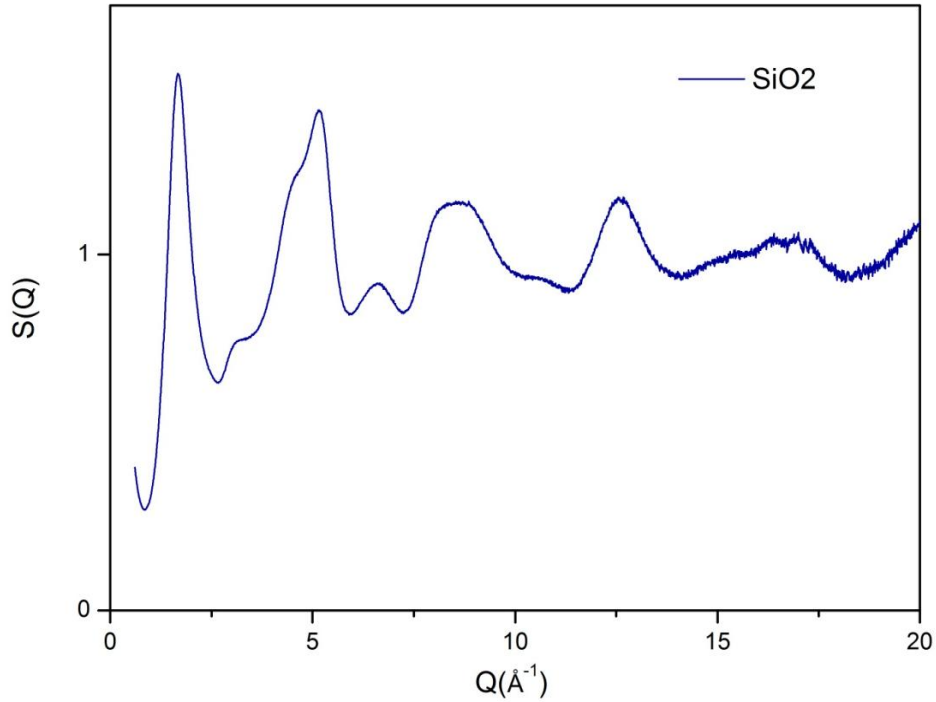


Figure 2.3 Total scattering structure function, S(Q), (the interference part of scattering) created from the $I_{coh}(Q)$ data in Figure 2.2. Note the Bragg scattering at low to medium range Q, and the diffuse scattering is more pronounced at high Q region.

The structure function S(Q) has a few interesting features that we would like to briefly touch on using Figure 2.3 as a reference. First, we note that the function oscillates around the average value $\langle S(Q) \rangle = 1$. We note that the intensity of peaks decreases at higher values of Q. This is due to the atomic thermal motions, which reduce the Bragg scattering intensities. Furthermore, we note that the S(Q) function contains both Bragg intensities, in the form of relatively sharp peaks in the low to middle Q-range, and diffuse scattering intensities much visible in the high Q-range. Usually the measurement of the scattered intensity up to a high value of Q, in general referred to as $Q_{max}$, with good statistics is required for obtaining an accurate quantitative structural analysis. Such high quality data are obtainable by using X-ray synchrotron and/or pulsed spallation neutron

sources that provide high intensity and short-wavelength. The $Q_{max}$ value is a very important parameter in data processing and is not arbitrarily chosen. More details on this parameter are given in the next section. However, we need to be aware of the fact that noise in the data collection has a strong effect on the data quality at high Q because the $\langle f \rangle^2$ (parameter used in the normalization process of the measured $I_{coh}(Q)$) amplifies oscillations in the signal since it approaches 0 at high Q. Therefore, long collection times or high X-ray flux are needed to ensure a good signal-to-noise ratio.

In practice, we use the reduced structure function, $F(Q)=Q[S(Q)-1]$ instead of the total structure function $S(Q)$. The structural information present in $S(Q)$ and $F(Q)$ are the same, but the value of $F(Q)$ is centred around 0 and we observe the diffuse scattering features more clearly than in $S(Q)$ as shown on figure 2.4.
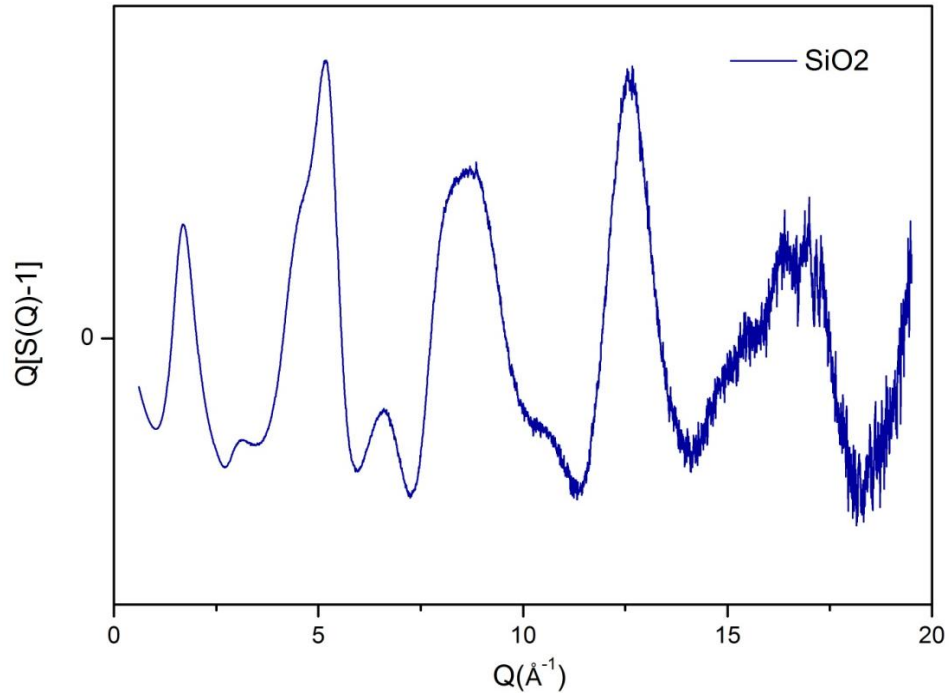


Figure 2.4 Reduced total structure factor $F(Q)=Q[S(Q)-1]$ corresponding to Figure 2.3. Note the $F(Q)$ is centered around 0 and $\langle F(Q) \rangle =0$.

### 2.1.3 Relation with Pair Distribution Function (PDF)

A conceptually simple way to examine the underlying atomic arrangement from the diffraction data is to take the sine Fourier transform of the reduced total structure factor

F(Q) which yields the atomic pair distribution function (PDF) [13]. The mathematical definition of the PDF, G(r), is:

$$G(r) = \frac{2}{\pi} \int_0^\infty Q[S(Q-1)] \sin(Qr)\, dQ$$
$$= 4\pi r[\rho(r) - \rho_0]$$

(2.11)

Where $\varrho(r)$ and $\varrho_0$ are the local number density and average number density, respectively, and r is the radial distance. From Equation 2.11 we see that, as r→0, G(r)→-4π$\varrho_0$. In general, G(r) has a baseline of slope -4π$\varrho_0$ at low r. (Figure 2.5).

G(r) can be considered as a histogram of the atom-atom distances in a material. It gives the probability of finding two atoms separated by the distance r inside the sample. The peaks in the PDF diagram occur thus at values of r that correspond to the average interatomic distances in a material and since ρ(r) oscillates around ρ$_o$ , G(r) should oscillate around zero. The relative intensities of the peaks are related to the number of such interatomic distances in the sample. Thus in principal the PDF contains all the information about the structure of the material. It is noteworthy to mention that the PDF is radially averaged and is a one dimensional function. The PDF is similar to a Patterson map, the difference being that the former takes into account the total scattering (both the Bragg peaks and the diffuse scattering intensities), while the latter only considers the Bragg scattering and so a Patterson map only yields interatomic vectors within a unit cell. While the Bragg scattering yields only the average structure, the PDF method is thus capable of probing both the local and average structure. This combination of local and average structural analysis from the same scattering data represents a clear advantage for a wide range of applications.
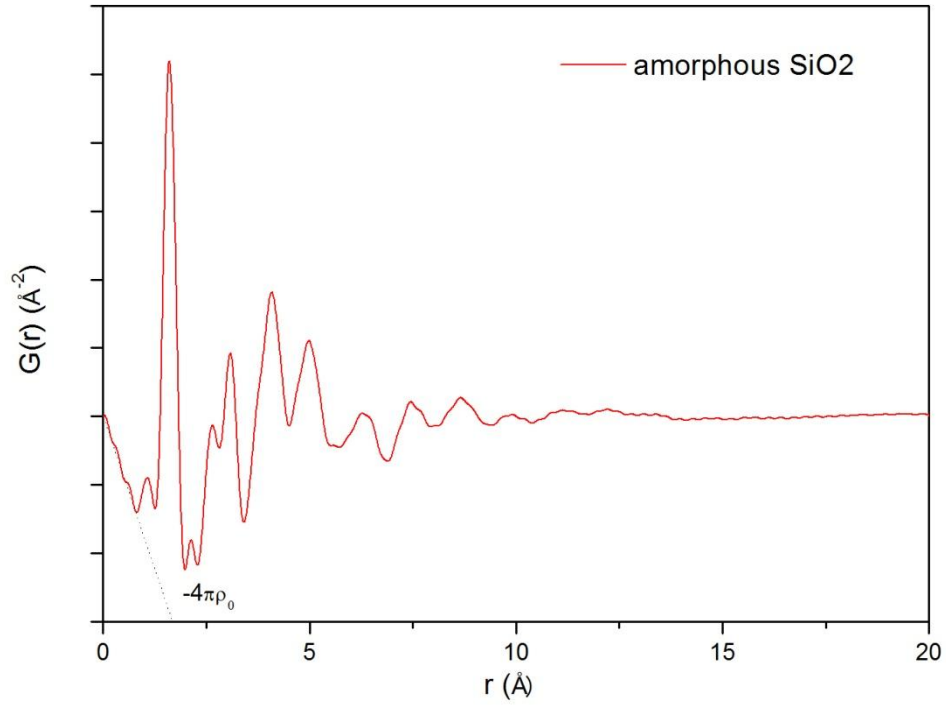
Figure 2.5 Example of a $G(r)$ of amorphous $SiO_2$, Fourier transformed from the $S(Q)$ data in Figure 2.2. The dashed lined represents the baseline of slope $-4\pi\varrho_0$.

The importance of the atomic pair distribution function, $G(r)$, is due to the fact that PDF is related in a simple way to the scattering intensity in X-ray or neutron diffraction experiments and can be directly obtained by Fourier transforming the measured total scattering data. As is clear from equation (2.11) the sine Fourier transform is over all Q space from zero to infinity. Unfortunately, this is not achievable in practice and there will be always a limitation on the accessible $Q_{min}$ and $Q_{max}$ values due to the experimental setup. The termination of the diffraction pattern at a finite value of $Q_{max}$ produces termination ripples, which manifest as false oscillations in the PDF beside the real peaks, increasing therefore the error especially in the low-r region (Figure 2.6). The higher the $Q_{max}$ used in the Fourier transform, the less noticeable the termination ripples. Similarly, the small angle part of the total scattering patterns, delimited by $Q_{min}$, provides information of shapes and size distributions of particles. This information can be lost in

the case of limited low-Q values and leads to biased structural description of the studied materials.
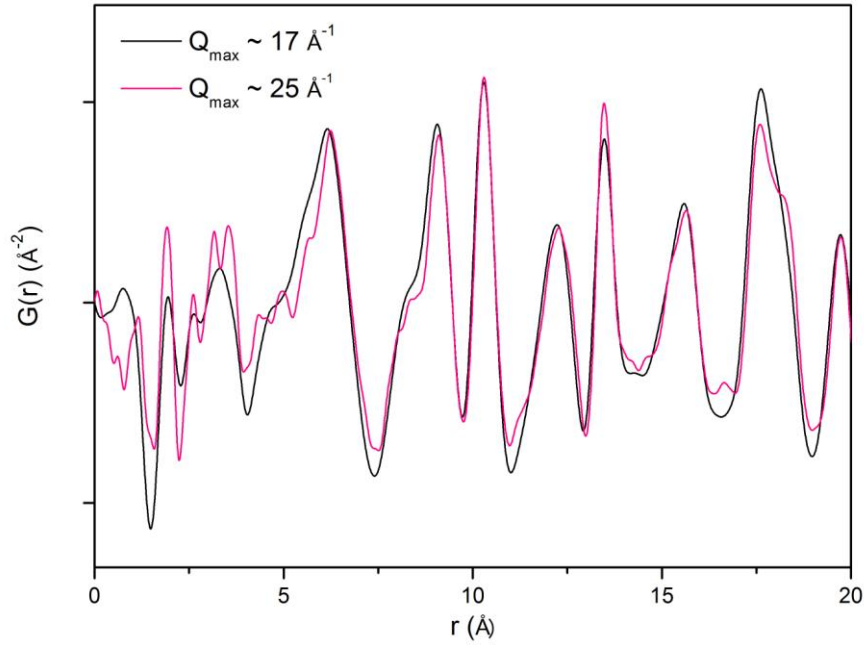


Figure 2.6 Example of experimental PDFs of SNP complex. Black line corresponds to data collected up to $Q_{max} = 25$ Å$^{-1}$ and pink line for the same data terminated at $Q_{max} = 17$ Å$^{-1}$.

Frequently for a laboratory source (long wavelength leading to limited $Q_{max}$) or in the case of measurements of amorphous materials (weak scattering power at high Q), it is common to use a modification function, M(Q), to help reduce the termination ripples that would otherwise occur as a result of the finite Q-range and the limited counting statistics of the scattering data. Alternatively, the step-function describing the experimental Q-range, can be Fourier-transformed to produce the r-space modification function with which theoretical *r*-space functions should be convoluted before comparison or fitting to Fourier-transformed total scattering data [16]. One of the most common functions employed was proposed by Lorch (1969) [17,18]. Equation (2.11) can then be rewritten as:

$$G(r) = \frac{2}{\pi} \int_{Q_{min}}^{Q_{max}} Q[S(Q-1)]M(Q)\sin(Qr)\,dQ$$

$$= 4\pi r \gamma(r)[\rho(r) - \rho_0]$$

(2.12)

Where $Q_{min}$ and $Q_{max}$ represent the finite range in reciprocal space over which the experimental data have been collected. Furthermore, a shape function $\gamma(r)$ can be introduced to handle the missing structural information in the small angle scattering region [18]. An example of the application of a modification function used in the Fourier transformation of the reduced structure factor $F(Q)$ is shown in Figure 2.7.
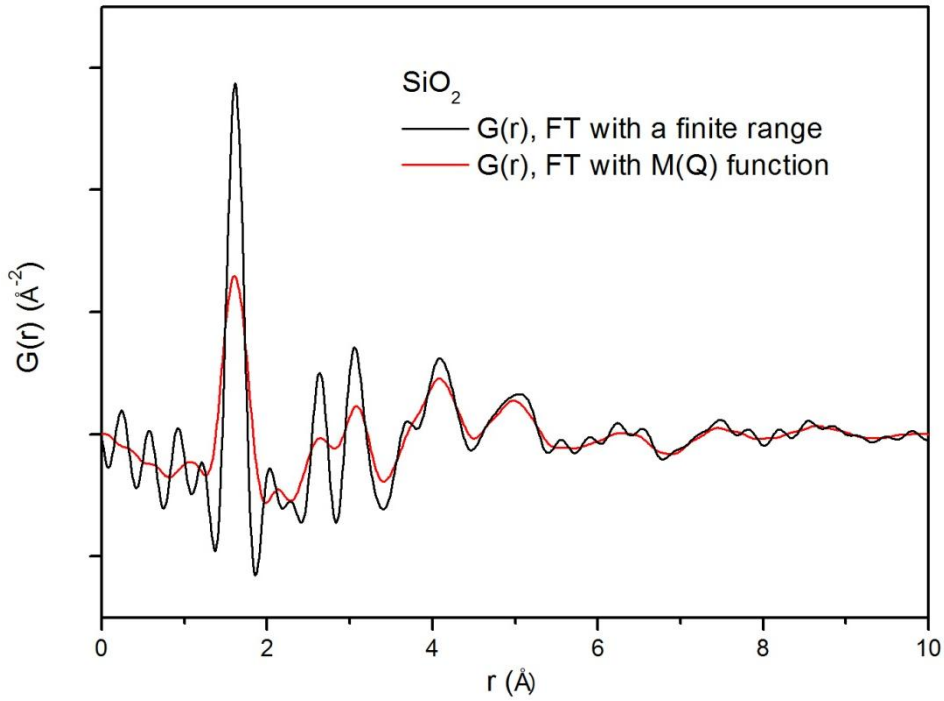


Figure 2.7 Comparison of X-ray $G(r)$ Fourier transformed from a finite Q range ($Q_{max}$ =24 Å$^{-1}$), and $G(r)$ convoluted with a modification function.

## 2. 1.4    Data Collection

The objective of total scattering experiments is to measure extended Q range data with high accuracy. In general these experiments are based on similar data collection strategy as conventional powder diffraction measurement [10,19,20]. However, additional requirements are mandatory for accurate PDF measurements [13,21]. It is noteworthy

that the accuracy in determining Q values and in measuring the intensity is of high importance in a PDF analysis. The accurate Q values defining the Bragg peak positions determine the derived lattice parameters, whereas the determination of the measured intensities gives information about the atomic positions and atomic type within the unit cell. Thus one has to pay attention to the following details.

## 2.1.4.1 Reduce the Experimental Errors

### 2.1.4.1.1 Termination Errors

According to Eq. 2.11, getting high $Q_{max}$ with good statistics is crucial for obtaining accurate PDF with minimized termination ripples and a high r-resolution, which may be approximately given by ($\delta r \sim \pi / Q_{max}$) [13]. For the highest resolution and accurate measurements the use of synchrotron radiation is preferred, however, perfectly acceptable PDFs can be obtained from laboratory measurements as we discuss in chapter 4. For example, using X-ray laboratory sources such as Molybdenum or Silver, scattering data can be collected up to $Q_{max} \sim 17$ Å$^{-1}$ and $\sim 21$ Å$^{-1}$, respectively corresponding to maximum real space resolution $\delta r$ of $\sim 0.18$ Å and $\sim 0.15$ Å respectively. However, the real space resolution is significantly reduced to $\sim 0.39$ Å when the Cu K$_\alpha$ radiation is used as a consequence of a finite $Q_{max}$ of $\sim 8$ Å$^{-1}$. From these examples it can be seen that the $Q_{max}$ termination effects can be significantly reduced by using available in-house sources with shorter wavelength giving access to a higher $Q_{max}$. However, care must be taken since on going from Mo to Ag the diffraction power significantly drops in intensity. A good compromise between the resolution and higher diffracted intensities has therefore to be found for PDF measurements depending on the sample characteristics.

### 2.1.4.1.2 Data statistics and Collection time

The intensity of the diffracted beam falls off with increasing Q. As a result the signal becomes progressively dominated by noise at higher Q-values, which limits the accessible range of data that can be used for the sample characterization. The signal-to-noise ratio can be improved by using appropriate data collection strategy as we will discuss in the following.

### 2.1.4.1.3 Instrumental resolution

Ideally the experimental measurements would involve a diffractometer that can resolve all the details of the scattered intensity $I_{coh}(Q)$. However, real equipments have a limited resolution which, depending on the samples, may have a major effect on the

PDF [21]. The effect of the instrumental resolution is equivalent to multiplying the PDF by a function such as a Gaussian, which causes the PDF to decay at high-r values. For amorphous materials the effect of this damping is negligible, because these materials are dominated by short range order such that their PDF at high r is negligible before the Q-resolution starts to take effect. For crystalline materials, where theoretically the PDF extends to infinity, this issue becomes important, especially when investigating the high-r region. The same applies for the materials that are composed of domain sizes of limited structural coherence. In these cases it becomes crucial to determine if the decay in the PDF is due to the structure (domain size) or due to the instrument resolution. This requires a high resolution PDF experiment from which we can specify the coherent domain sizes for the material under study.

### 2.1.4.2 Diffraction configurations:

The total scattering measurement can be carried out from different powder diffractometer geometries such as a flat-plate symmetric reflection geometry or transmission geometry. The details on these experimental set ups are well documented in the literature [22]. The choice between reflection and transmission configuration depends on the studied sample. In the case of absorbing samples, reflection geometry has the benefit that the absorption and active volume corrections can be derived fairly straightforward for the approximation of a parallel incident beam. However, care must be taken when making the flat plate samples, they should have very uniform thickness and density and the surface should also be as flat and smooth as possible. Another important consideration is that the beam footprint does not extend over the edge of the sample surface area. This will result in an angle dependent drop off in the intensity of the sample especially at low angles which is very difficult to correct. If the studied samples are significantly transparent, then the transmission geometry provides stronger scattering particularly at high angles. This configuration is also more robust than reflection geometry against alignment errors, especially at low angles. For these considerations, the transmission geometry is often used at high energy scattering beamlines.

In PDF measurements it is crucial to collect enough points that the step size is always smaller than the instrument resolution, so all of the Q-space is probed. Adequate collimation before and after the sample is also important to minimize background from air scattering and sample environments. Furthermore, care must be taken to ensure that the focused beam corresponds to the center of the diffractometer and the sample is well aligned.

The total scattering data sets used in this thesis have been collected with Debye-Scherrer transmission set up by using the radiation of a Molybden tube on a laboratory diffractometer (figure 2.8) and synchrotron radiation on the powder station of the Materials Science Beamline at the Swiss Light Source (Figure 2.10). The samples have been prepared in Kapton capillaries of diameter 1 mm. The unwanted signals due to air scattering and the experimental set up (empty capillaries) were measured independently under exactly the same conditions as the sample and are included in the data reduction procedure.

Laboratory X-ray diffraction measurements were performed on a PANalytical X'Pert PRO system equipped with a focusing mirror that acts also as a broad-band monochromator for Mo K$\alpha$ radiation ($\lambda = 0.71073$ Å) (Figure 2.8). Different optical components can be used on the incident and diffracted beam, e.g. the divergence slit of 0.02 mm and additional shielding were applied to the optical path in order to achieve a feature-free background. Data sets have been collected up to an 2$\theta$ angle of 150 degrees corresponding to a maximum scattering vector Q of ~17 Å$^{-1}$.



Figure 2.8 The PANalytical X'Pert PRO powder diffractometer at CRM2.

Using this setup the data collection time is often quite long, typically more than 24 hours per sample. The optimization of the measurements strategy is therefore necessary to improve the data quality especially at high Q values. Variable counting time (VCT) strategies [17,23] can be applied to spend longer counting times at high scattering angles where the intensity of the signal falls-off significantly due to atomic form factor. Figure 2.9 shows an example of the schematic redistribution of measurement times that we have used in our experiments: 1s per step in the region 0-50 degrees, 5 s per step in the region 50-100 degrees and 9 s per step in the region 100-150 degrees.
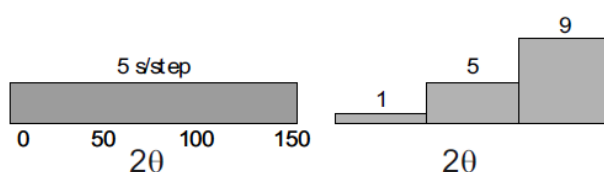


Figure 2.9 Data collection strategy uses constant counting time (left) and variable counting time (right) as a function of 2 theta.

We also used the synchrotron radiation for the PDF studies. The experiments were carried out on the powder diffractometer of the Material Science beamline of the Swiss Light Source (SLS) at the Paul Scherrer Institut (Villigen, Switzerland). Data were collected using a monochromatic beam of wavelength $\lambda$ = 0.4962 Å (E = 24.9866 keV). The second generation microstrip detector Mythen II covering 120° with 0.0037° resolution was mounted on Debye-Scherrer transmission set up as shown in Figure 2.10. The used photon energy enables data to be recorded up to $Q_{max}$~25 Å$^{-1}$ to provide the necessary resolution in real-space for quantitative structural analysis to be attempted.

It is clear that PDF measurements using synchrotron radiation provide improved angular resolution and higher intensities. Furthermore, synchrotron sources produce high flux X-rays with tunable wavelengths, which is very helpful in the case of highly absorbing samples and/or materials with large amount of fluorescence radiation when irradiated with conventional laboratory sources. However, one should be aware that problems may be encountered during synchrotron measurements such as position shifts of the X-ray beam, a sometimes reduced beam stability and harmonic contamination.

Figure 2.10 The Debye-Scherrer transmission set up on MS-beamline (SLS), Paul Scherrer Institut.

## 2.1.5    Data Reduction

In a real experiment, a number of corrections must be applied to the measured intensity in order to obtain the coherent scattering intensity, $I_{coh}(Q)$. In principle, the data corrections are well known and established by number of approximations to obtain a reliable normalized S(Q). If data reduction is not carried out properly nonphysical features may appear in the G(r) function. Frequently, an expert eye is needed to minimize errors in the S(Q) in order to ensure that one studies the physics of the system and not experimental artefacts [24].

The experimental intensity of scattered X-rays or neutrons, $I_T$, is actually composed of several parts [13,25]:

$$I_T(Q) = A \cdot P \cdot I_{coh}(Q) + I_{Inc}(Q) + I_{MS}(Q) + I_{BG}(Q) \qquad (2.13)$$

Where A denotes the absorption correction, P the Polarization of the incident beam, $I_{Inc}$ the incoherent scattering intensity, $I_{MS}$ the multiple-scattering intensity, and $I_{BG}$ the background intensity. The structural information is in the coherent scattering intensity, $I_{coh}(Q)$. Therefore, before we can use experimental data for analysis, we must correct the $I_T(Q)$ by removing unwanted scattering.

The incoherent scattering occurs when there is no phase relationship between the scattered waves, meaning that it does not contain structural information. Multiple scattering occurs when X-rays are re-scattered within the sample [26]. Also, the sample container (i.e. a capillary), can contribute to the multiple scattering. Background scattering can be due to the sample container and the environment.

From equations 2.13, there are five main corrections we consider, these corrections can be divided into two groups. The first group contains the additive corrections, such as incoherent scattering, multiple scattering, and background scattering. The second group comprises the multiplicative corrections such as absorption and polarization. There are other corrections that can be applied, such as fluorescence, detector efficiency, etc., but since the goal of this chapter is to be a survey, not a technical manual, they will not be considered here.

There are several programs for processing the proper coherent scattering from raw data, and Fourier transform to PDF: PDFgetX2 [27], PDFgetX3 [28], RAD [29], and GudrunX [25] for X-rays and PDFgetN [30] for time of flight neutrons.

### 2.1.5.1   Multiplicative corrections

#### 2.1.5.1.1        Absorption

The absorption correction is used to account for the X-rays that are absorbed by the sample. To calculate the absorption correction, one needs to know the geometry of the experiment, the energy of the x-rays, the mass absorption coefficient, $\mu(E)$ [31], of the sample, the chemical composition, and its thickness.

Most of these necessary parameters for the absorption calculation are reasonably easy to obtain. The energy of the X-rays used in an experiment should be known ahead of time. The total mass absorption coefficient of a material is a linear addition of the absorption coefficients of each element weighted by the ratio of the elements in the compound. $\mu(E)$ of most elements has been tabulated as a function of X-ray energy by Hubbell [32]. We usually express the mass absorption coefficient of each element divided by its density, $\mu(E)/\varrho$. Fortunately, the densities of the elements have also been tabulated [22]. We multiply the total mass absorption coefficient by the thickness of the sample, $t$, to obtain the value $\mu t$, which is an important variable in the absorption calculation.

Finally, the geometry of the experiment also has an effect on the absorption [13]. The capillary geometry has a complicated correction dependent on the diameter of the capillary. The final absorption correction is tabulated by software using several complicated equations and then applied to the experimental data [13].

### 2.1.5.1.2    Polarization correction

The Thompson scattering process polarizes the scattered x-ray beam [13,25] such that the electric field vector lies in a direction perpendicular to the scattering plane. This affects the measured intensities as a function of the scattering angle. Unlike the other corrections which rely on complicated functions with tabulated values, the polarization correction to account for this angle dependence can be expressed relatively easily as a function of scattering angle and degree of polarization of the incident beam:

$$P(2\theta) = \frac{1 + A\cos^2 2\theta}{1 + A} \qquad (2.14)$$

Where A is a term that depends on the degree of polarization of the incident beam and $2\theta$ is the scattering angle. A, not to be confused with the absorption correction, can take on values between 0 and 1.0, where A = 0 means that the incident beam is unpolarized, while A = 1.0 means that the incident beam is fully polarized.

Synchrotron radiation is theoretically fully plane polarized perpendicular to the scattering plane, and therefore does not need to be corrected for polarization. However, in reality, the beam is not completely polarized and some small corrections might be necessary. On the other hand, Laboratory sources have an essentially unpolarized beam when no monochromator is installed.

There are two special geometries that are worth mentioning [13]. In the first geometry, a monochromator crystal is placed in the unpolarized incident beam (i.e. placed in the beam before it hits the sample). In this case, $A = \cos^2(2\alpha)$, where $2\alpha$ is the scattering angle of the monochromator, in Equation 2.14. In the other geometry, the monochromator crystal is placed in the diffracted beam (i.e. after the beam hits the sample, this is also known as an analyzer). In this case, we use the equation:

$$P(2\theta) = \frac{1 - \cos^2(2\alpha)\cos^2(2\theta)}{2} \tag{2.15}$$

Instead of Equation 2.14.

### 2.1.5.1.3      Considering to Laboratory Source

Laboratory X-ray sources produce a general background Bremsstrahlung radiation caused by the incident electrons being slowed down in the anode materials. This has a characteristic spectrum whose maximum energy corresponds to electron bombardment energy [25]. Furthermore, it is important to reduce or eliminate the unwanted effects, such as usually place an absorbing foil or a monochromator to stop the $K_\beta$ radiation.

## 2.1.5.2 Additive corrections

### 2.1.5.2.1 Incoherent scattering

Incoherently scattering waves do not interfere when those are diffracted off the sample, meaning that there is no phase relationship between the waves. Since structural information in scattering comes from the interference effects of scattered waves, incoherently scattered waves do not contain any structural information. As incoherent scattering mainly consists of Compton scattering, we devote our discussion exclusively to it. Compton scattering is an inelastic incoherent type of scattering that occurs when an incident X-ray photon collides with an electron in the sample and transfers some of its energy to the electron. Thus the scattered photon has a different energy than the incident one.

We correct for Compton scattering by subtracting Compton intensities from the data. These intensities have been calculated as a function of Q from tabulated data of the Compton scattering cross section [33,34]. A proper correction for Compton scattering is very important in high-energy total scattering analysis because the Compton signal can be larger than the coherent scattering intensity at high Q values. This is due to the fact that the elastic scattering cross section decreases while the Compton scattering cross section increases. This also leads to a problem because, as we see in Figure 2.11, at high Q values ($\sim$ 20 Å$^{-1}$ in this case) subtracting the Compton scattering (green) from the experimental scattering intensities (blue, mean-square atomic scattering factor, $<f>^2$) will result in a negative intensity. We solve this problem by applying a smooth attenuation function to the Compton intensities as suggested by Ruland [35] (red in Figure 2.11) and then subtracting the attenuated intensities from those that were collected experimentally.
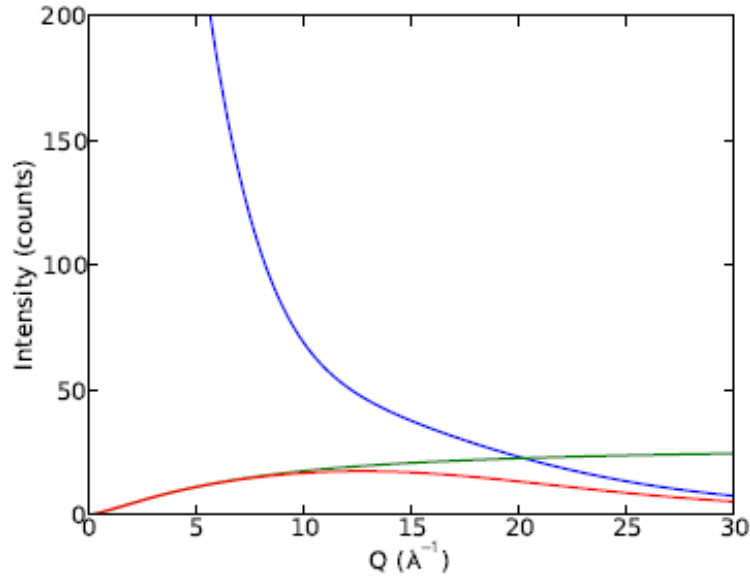
Figure 2.11 Typical Compton correction profile. The blue line is the mean-square scattering factor, $\langle f \rangle^2$, the green line is the tabulated Compton scattering intensity, and the red line is the Compton modified by Ruland attenuation function [13].

### 2.1.5.2.2 Multiple scattering

Multiple scattering occurs when the primary beam is scattered twice or more by the sample and container before reaching the detector. In our analysis, we consider only double scattering because it represents the majority of the contribution of multiple scattering to the data and higher orders are much more difficult to calculate. We also assume that the double differential cross section is isotropic, which is not the case in reality; however the assumption does simplify the math and has been found to work. We further simplify the calculation by separating out the incoherent scattering (i.e. Compton scattering), as done in equation (2.11) so that only completely elastic multiple scattering events need to be considered for this correction. The multiple scattering correction depend on sample thickness, transparency, absorption, experiment geometry, and a complicated function that is dependent on Q, sample absorption, thickness, density, and other parameters. Fortunately, values of this function have been tabulated [36] so that they could be used in computer assisted calculations. Multiple scattering contributions increase with sample thickness and with higher energy X-rays and therefore the

correction is important in PDF experiments where X-ray energies are generally high and the data in the high-Q region contain important information. Finally, multiple scattering is far larger in transmission geometry than reflection geometry.

### 2.1.5.2.3    Background Subtraction

Background scattering intensities is scattering that is not due to the sample. For instance, the sample container (e.g. a capillary) contributes to the background scattering, as does air, and the instrument itself can have a background signal. We want to minimize the contribution of background scattering intensities to the total intensity. This can be done in two ways, first by optimizing the experimental set-up and second by subtracting the background. We optimize the experiment by, for example, using a poorly diffracting sample container (i.e. a Kapton capillary rather than glass) and collecting a dark current on the detector between measurements. To properly subtract the background, we collect three data sets [13]: (1) the sample and container together; (2) an empty container; and (3) the air. The scattering of the container and the air are then subtracted from the total measurement.

## 2.2    Solid state NMR spectroscopy

The main interactions that dominate the NMR lineshape in the solid state include the nuclear dipolar interaction, giving information on the distance between magnetic nuclei, chemical shielding, giving information on the electronic structure, and the quadrupolar interaction, which is determined by the interaction of the nuclear electric quadrupole with the electric field gradient at the nucleus [37].

All experiments were carried out on a high-field Bruker NMR Avance III spectrometer operating at 14T ($^1$H NMR frequency of 600 MHz), installed in CRM2. $^{29}$Si MAS experiments were carried out on a Bruker 4 mm MAS triple-resonance probe. $^{13}$C MAS experiments were carried out on a Bruker 4 mm MAS triple-resonance probe. The MAS spinning speed was set to 12.5 kHz. $^{23}$Na MAS experiments were carried out on a Bruker 2.5 mm MAS double-resonance probe. $^1$H MAS experiments were carried out on a Bruker 2.5 mm MAS double-resonance probe.

## 2.3    UV-vis and Infrared Spectroscopy

UV/Vis and Infrared absorption spectroscopy allow the identification of electronic transitions and molecular vibrations in the studied samples. In the context of this thesis the methods are used as a first quick characterization tool of the hybrid materials and to

verify that the embedded photoswitchable molecules still exhibit their interesting optical properties. UV-Vis absorption spectra were recorded using a Cary 4000 spectrophotometer with a transmission setup.

Infrared spectra have been collected with a Nicolet 5700 FTIR-spectrometer and a resolution of 2 cm$^{-1}$. Fine powder of our samples were mixed with KBr and pressed to pellets. The pellet was fixed on a copper coldfinger with silver conductive paste to provide a uniform cooling of the sample. The cooling down to 80 K was carried out with liquid nitrogen at a pressure of 10$^{-6}$ mbar. KBr windows allowed the measurement in the spectral range of 4000-400 cm$^{-1}$ and the irradiation of the sample with laser light of different wavelengths. The population of the metastable state can be determined by the decrease of the band area of $\upsilon$(NO)-vibration of the GS.

## 2.4    Photoluminescence

Photoluminescence (PL) describes light-emitting phenomenon from a material under optical excitation. When the studied material is excited with light of sufficient energy, photons are absorbed and electronic excitations are created. Eventually, the electrons return to the ground state: if this relaxation is radiative, the emitted light is the photoluminescence signal. The intensity of this signal gives a measure of the relative rates of radiative and non-radiative recombinations. Therefore, the PL spectroscopy is a suitable tool for quantitative characterization of luminescent materials. A noticeable advantage of PL analysis is that it is a simple, versatile, and non-destructive technique and one can derive much information on the emitting material from the analysis of the PL signal.

Since the PL properties are dependent on the concentration of the respective chemical species or on the variation of the physical and chemical properties of the material, we used the PL technique to investigate the size reduction effect on the spectroscopic properties of the neodymium complex, [NdCl$_2$(H$_2$O)$_6$]Cl, embedded in silica matrix with different pores size. Combining the results of such experiments with the derived structural parameters are of high interest for gaining better insight into the structure-property relationship.

The PL measurements were performed in collaboration with the Nanomaterial team of the P2M department (*Institut Jean Lamour, Université de Lorraine*). The PL spectra were obtained using a He–Cd laser ($\lambda$=325 nm) and a photomultiplier operating in the range 800–1500 nm.

## 2.5    Adsorption

Brunauer-Emmett-Teller (BET) measurement aims to explain the physical adsorption of gas molecules on a solid surface and serves as the basis for an important analysis technique for the specific surface of loaded and unloaded $SiO_2$ xerogel matrix. The $N_2$ adsorption isotherms of milled samples were taken on laboratory PhLAM (Université Lille). Specific surfaces were determined using multi-point BET analysis in the $P/P_0$ range of 0.05–0.2. The total pore volume was examined using $P/P_0$ of 0.9 and the micro-pore volume was calculated using $P/P_0$ of 0.2 considering only pores with a radius smaller than 1 nm. Pore size distributions were calculated using the adsorption branch with the Barret–Joyner– Halenda (BJH) theory. Fractal analysis of the adsorption isotherms were applied using the Frenkel–Halsey–Hill (FHH) model [38]. The surface fractal dimension is accessible through a regression of the linear range in a $\ln(N/N_m)$ versus $\ln[\ln(P/P_0)]$ plot, where N is the number of moles of nitrogen adsorbed at a certain $P/P_0$ and $N_m$ is the number of moles of nitrogen in a monolayer Nitrogen adsorption isotherms were obtained.

# Bibliography

[1]   S. J. L. Billinge, Physics **3**, 25 (2010).

[2]   S. J. L. Billinge and I. Levin, Science **316**, 561 (2007).

[3]   R. B. Neder and V. I. Korsunskiy, J. Phys. Condens. Matter **17**, S125 (2005).

[4]   S. J. L. Billinge, J. Solid State Chem. **181**, 1695 (2008).

[5]   C. A. Young and A. L. Goodwin, J. Mater. Chem. **21**, 6464 (2011).

[6]   L. Malavasi, Dalton Trans. **40**, 3777 (2011).

[7]   J. M. Thomas, Nature **491**, 186 (2012).

[8]   T. R. Welberry, *Diffuse X-Ray Scattering and Models of Disorder* (OUP Oxford, 2010).

[9]   C. Giacovazzo, H. L. Monaco, G. Artioli, D. Viterbo, M. Milanesio, G. Gilli, P. Gilli, G. Zanotti, and G. Ferraris, *Fundamentals of Crystallography*, 3rd ed. (Oxford University Press, USA, 2011).

[10]   V. Pecharsky and P. Zavalij, *Fundamentals of Powder Diffraction and Structural Characterization of Materials* (Springer, 2005).

[11]   A. Guinier, *X-Ray Diffraction: In Crystals, Imperfect Crystals, and Amorphous Bodies*, New edition (Dover Publications Inc., 1994).

[12]   B. E. Warren, *X-Ray Diffraction*, New edition (Dover Publications Inc., 1991).

[13]   T. Egami and S. J. L. Billinge, *Underneath the Bragg Peaks: Structural Analysis of Complex Materials*, 2nd ed. (Pergamon, 2012).

[14]   P. Debye, Ann. Phys. **351**, 809 (1915).

[15]   D. A. Keen, J. Appl. Crystallogr. **34**, 172 (2001).

[16]   H. E. Fischer, A. C. Barnes, and P. S. Salmon, Reports Prog. Phys. **69**, 233 (2006).

[17]   E. Lorch, J. Phys. C Solid State Phys. **2**, 229 (1969).

[18]   A. K. Soper and E. R. Barney, J. Appl. Crystallogr. **45**, 1314 (2012).

[19]   P. G. Bruce, *Powder Diffraction: Theory and Practice*, 1st ed. (Royal Society of Chemistry, 2008).

[20]   R. Guinebretière, *Diffraction Des Rayons X Sur Échantillons Polycristallins : Instrumentation et Étude de La Microstructure*, 2e édition revue et augmentée (Hermes Science Publications, 2006).

[21]   X. Qiu, E. S. Božin, P. Juhas, T. Proffen, and S. J. L. Billinge, J. Appl. Crystallogr. **37**, 110 (2004).

[22]  H. P. Klug and L. E. Alexander, *X-ray Diffraction Procedures for Polycrystalline and Amorphous Materials* (Wiley, New York, 1974).

[23]  J. te Nijenhuis, M. Gateshki, and M. J. Fransen, Z. Für Krist. Suppl. **2009**, 163 (2009).

[24]  P. F. Peterson, E. S. Božin, T. Proffen, and S. J. L. Billinge, J. Appl. Crystallogr. **36**, 53 (2003).

[25]  A. K. Soper and E. R. Barney, J. Appl. Crystallogr. **44**, 714 (2011).

[26]  B. E. Warren and R. L. Mozzi, Acta Crystallogr. **21**, 459 (1966).

[27]  X. Qiu, J. W. Thompson, and S. J. L. Billinge, J. Appl. Crystallogr. **37**, 678 (2004).

[28]  P. Juhás, T. Davis, C. L. Farrow, and S. J. L. Billinge, J. Appl. Crystallogr. **46**, 560 (2013).

[29]  V. Petkov, J. Appl. Crystallogr. **22**, 387 (1989).

[30]  P. F. Peterson, M. Gutmann, T. Proffen, and S. J. L. Billinge, J. Appl. Crystallogr. **33**, 1192 (2000).

[31]  C. T. Chantler, J. Phys. Chem. Ref. Data **24**, 71 (1995).

[32]  N. US Department of Commerce, (n.d.).

[33]  D. T. Cromer and J. B. Mann, J. Chem. Phys. **47**, 1892 (1967).

[34]  H. H. M. Balyuzi, Acta Crystallogr. A **31**, 600 (1975).

[35]  W. Ruland, Br. J. Appl. Phys. **15**, 1301 (1964).

[36]  C. W. Dwiggins and D. A. Park, Acta Crystallogr. Sect. **27**, 264 (1971).

[37]  J. A. Ripmeester and C. I. Ratcliffe, in *Mod. Magn. Reson.*, edited by G. A. Webb (Springer Netherlands, 2006), pp. 147–154.

[38]  D. Avnir and M. Jaroniec, Langmuir **5**, 1431 (1989).

# Chapter 3

# Structural Modeling

# Chapter 3

# Structural Modelling

The detailed structural characterization of materials is a prerequisite to the understanding of their physical properties. In chapter 2 we outlined how to obtain the coherent scattering intensity $I_{coh}$ and the corresponding experimental PDF, G(r), from total scattering data. Here we describe the two different approaches that we used to model the total scattering data: (i) the Debye Function Analysis (DFA) which is based on the Debye formula (Eq. 2.3) and is done in reciprocal space by direct modelling of the measured $I_{coh}$, (ii) the analysis of the atomic pair distribution function in real space which models the experimental PDF G(r) that is obtained by the Fourier transform of the total scattering data (Eq. 2.11). Furthermore, a short description of the Reverse Monte Carlo (RMC) approach is given, since it has been applied to obtain a structural model for the $SiO_2$ gel.

## 3.1   Debye Function Analysis (DFA)

A rather robust and intuitive method that allows the calculation of the coherent scattering intensity as a continuous function of Q is based on the Debye equation [1]. It describes the scattered intensity from orientationally isotropic systems (e.g. gas, liquid, or powders):

$$I(Q) = \sum_{j=1}^{N} f_j^2 + \sum_{i \neq j}^{N} f_i f_j \frac{\sin(Qr_{ij})}{Qr_{ij}} \qquad (3.1)$$

Where $f_i$ and $f_j$ are the atomic form factors (or neutron scattering lengths, $b$), $r_{ij}$ the length of the interatomic distances between atoms $i$ and $j$. The scattering power is dependent on Q for X-rays and independent of Q for neutrons, whereas the contribution from thermal vibrations is strongly dependent on Q in both cases.

Since the formula (3.1) takes into account all atoms present in the sample, it quickly becomes very time consuming to calculate the contributions of all atom pairs (the number of terms in the sum in Eq. 3.1 increases with the square of the number of atoms). However, in the past 20 years, the Debye function analysis (DFA) has been reviewed and turned into an efficient tool for characterizing nanocrystalline materials *via* powder diffraction data [2,3]. Several new approaches have been implemented using faster algorithms for the calculation by Hall [4], Cervellino [5], and Proffen & Neder [6]. The DFA has thus become a reliable tool to study larger systems, and was successfully applied to study both the size and shape of nanoparticles [7,8] as well as to identify embedded species within guest-host systems from neutron [9] and X-ray powder total scattering measurements [10,11].

Figure 3.1 illustrates the effect of the different size and shape of SNP nanoparticles on the coherent scattering intensity calculated using the Debye formula:
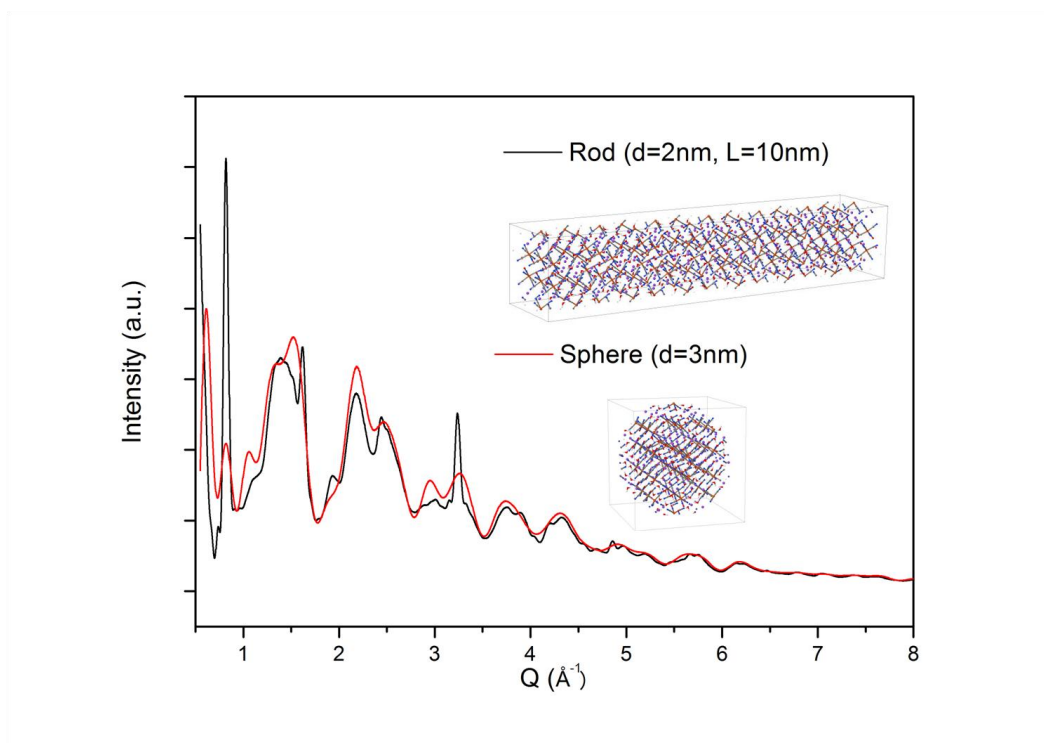
Figure 3.1 Calculations of the Debye equation for different size and shape of SNP nanoparticles.

For judging the quality of fit we used the weighted R-value:

$$R_{wp} = \sqrt{\frac{\sum_j w_j (I_{obs,j} - I_{calc,j})^2}{\sum_j w_j I_{obs,j}^2}} \qquad (3.2)$$

Where $w_j$ is the weighting, $I_{obs,j}$ and $I_{calc,j}$ are observed and calculated intensities, respectively, for each point of j of the diffraction pattern.

A big advantage of the DFA is that it does not rely on high-Q data. In principle it is thus possible to perform a total scattering analysis using a limited Q-range which renders this approach very interesting for laboratory diffractometers or neutron powder diffractometers at thermal or cold sources [5]. However, one has to be aware of this limitation in Q-space resolution and in general one needs to have already a reasonable idea of the structure of the compound one is studying. For the molecular compounds embedded in porous hosts, that we are interested in, a few general considerations have

been proven useful, as explained on the following example. Depending on the average size of the isolated atomic cluster of the embedded substance, an experimental Q-range can be determined. For small clusters of one or two SNP molecules with a diameter of about 10-15 Å (1 -1.5 nm), it is best to choose $Q_{min} \sim 2\pi/D$ and $Q_{max} \sim 2\pi/d$, where D is the cluster diameter and d the nearest-neighbour atomic distance. For SNP, $Q_{min} \sim 0.5$ and $Q_{max} \sim 6$ Å$^{-1}$. However, the range $Q<Q_{min}$ contains also valuable information on the substrate pore size, while it can be convenient to restrict $Q_{max}$ in order to neglect the substrate-guest chemical bonds. So $Q_{min} \sim 0.1$ and $Q_{max} \sim 3$ Å$^{-1}$ is - in this case - a valid choice [9].

## 3.2 Pair Distribution Function

### 3.2.1 Calculating PDF from a model

The PDF diagram contains the weighted bond-length distribution of every pair of atoms within a given material. It can be calculated from a three dimensional structural model by adding up all the weighted atom-atom distances [12] according to:

$$G_{calc}(r) = \frac{1}{r} \sum_{ij} \left[ \frac{f_i f_j}{\langle f \rangle^2} \delta(r - r_{ij}) \right] - 4\pi r \rho_0 \qquad (3.3)$$

Here $f_i$, $f_j$ are the scattering power of atoms i and j respectively, $\langle f \rangle$ is the average scattering power of all atoms in the model, and $\rho_0$ is the average number density. For X-rays the scattering power is the Q-dependent atomic form factor f(Q) and for neutron it is the coherent neutron scattering length b. From equation 3.3 follows that δ functions are generated at every position r corresponding to an interatomic interaction in the structural model. Thus, the PDF, G(r), is directly related to structure of a material. It should be noted that the details and accuracy of the structural information that can be obtained from the PDF analysis depend essentially on the quality of the collected data.

The main difference between the PDF method and conventional average structure analysis of powder diffraction data is how to treat the diffuse scattering intensities in-between and underneath the Bragg peaks. We will discuss in the following, the different relevant parameters that have to be taken into consideration to properly extract the structural information from the PDF analysis.

### 3.2.2 Consider finite Q-range

As we have seen in the previous chapter, the observed PDF is obtained by Fourier transforming the measured coherent diffraction intensity over all Q space. However, the accessible range in Q is in practice limited to a finite value of $Q_{max}$. This truncation of data can be accounted for by multiplication of the structure factor (which extends up to infinity) with a step function cutting off at $Q_{max}$ resulting in the convolution of the PDF with the Fourier transform S(r) of the step function. We calculate thus the model for a finite Q-range by convoluting the $G_{calc}(r)$ function (Equation 3.3) with S(r):

$$S(r) = \frac{\sin (Q_{max} \cdot r)}{r} \tag{3.4}$$

### 3.2.3 Thermal Motion

The experimental PDF peaks have a certain peak width as a result of displacement of atoms from their average position. This peak broadening can be handled by using a method based on the convolution of the function $\delta(r-r_{ij})$ in equation 3.3 with a Gaussian, $T_{ij}(Q)$:

$$T_{ij}(r) = \frac{1}{\sqrt{2\pi}\sigma_{ij}(r)} \exp\left[-\frac{(r - r_{ij})^2}{2\sigma_{ij}^2(r)}\right]\left[1 + (\frac{r - r_{ij}}{r_{ij}})\right] \tag{3.5}$$

The first term in $T_{ij}(r)$ is a simple Gaussian, which is multiplied by a modification function taking into account anisotropic averaging [12]. The width of the function $T_{ij}(r)$ is given by the parameter $\sigma_{ij}(r)$ that represents the deviation of atoms i and j from their average position and thus is correlated to atomic displacement parameters B. Furthermore the $\sigma_{ij}(r)$ shows an r-dependence to account for correlated motion [13,14]. The peaks at small r in experimental PDFs are sharper because of correlated motion of atoms; therefore the r dependence of peak widths is modeled by using equation:

$$\sigma_{ij}(r) = \sqrt{\sigma_{ij}'^2 - \frac{\delta}{r_{ij}^2} - \frac{\gamma}{r_{ij}} + \alpha^2 r_{ij}^2} \qquad (3.6)$$

Here $\sigma_{ij}'$ is the peak width given by the atomic displacement parameters [15], $\delta$ and $\gamma$ determine the sharpening of near neighbor PDF peaks due to correlated motion, in other words the tendency to move in phase [13,14]. It is noteworthy that the term $(\delta/r_{ij}^2)$ is used to describe the low temperature case and the term $(\gamma/r_{ij})$ describes the high temperature behaviour. Note also that these two parameters are highly correlated, therefore in practice only one is refined.

Finally the parameter $\alpha$ (or so called $Q_{broad}$ in the software PDFgui [16]) determines the PDF peak broadening at high distances r due to the instrument resolution. Another method to sharpen the first peaks in the PDF is to define a certain cutoff value in r ($r_{cut}$) and to use a factor ($s_{rat}$) to sharpen the PDF peaks below that defined value. Given that these parameters are used to describe the intramolecular interactions, the values of the ($r_{cut}$) parameter correspond generally to the diameter of the studied molecule.

Fig 3.2 illustrates the simulated PDF of SNP crystalline with different effects which are described above. First, the PDFs were calculated according to Equ. 3.3 thus distribute as a series of sharp $\delta(r)$ functions. Secondly, an experimental finite Q range is considered by convoluting the $\delta(r)$ distribution with a step function, S(r) (Equ 3.4), and results in spurious ripples which come from the Fourier transform. Finally, thermal motions (Equ 3.5) are taken into account and lead to broaden the peak width in PDFs.

The methods described above are standard procedures of simulation from a model. However, when dealing with different systems, e.g. molecular compounds, modeling of displacements from the average position and correlated motion is more complicated [17]. There are a variety of interactions with very different properties and depend on the materials studied. These interactions include, for example, covalent bonds, electrostatic or ionic interactions (e.g. hydrogen bonds), and van der Waals interactions. Further, in the case of nanoparticles, the PDFs will describe the effect of shape and sizes which we will discuss later.
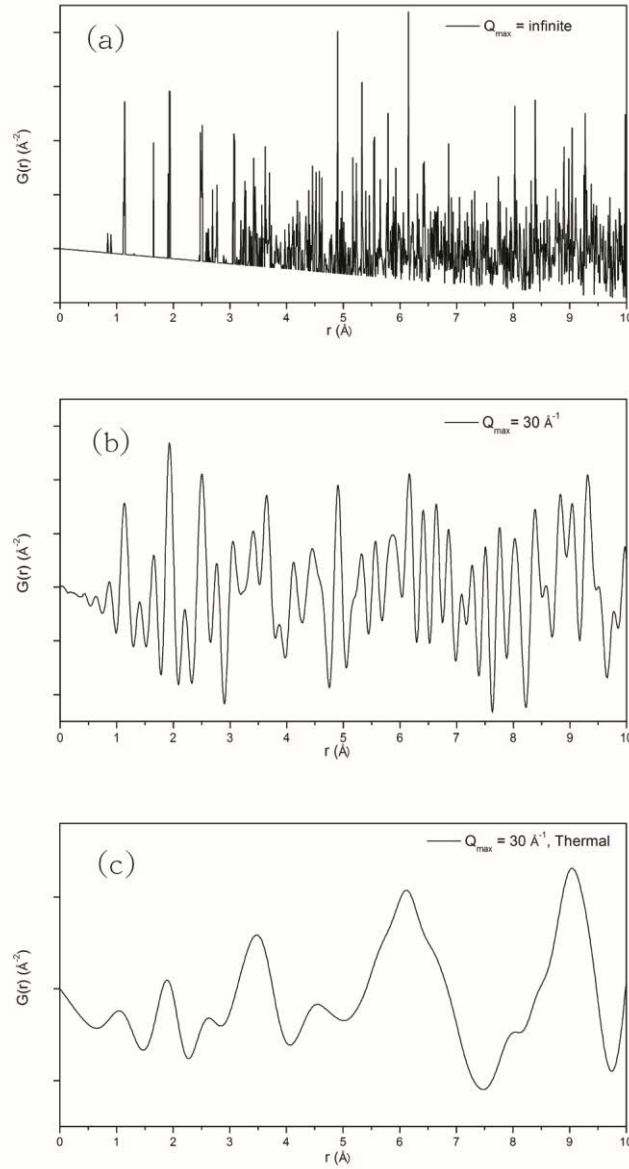
Figure 3.2 Calculating PDF of crystalline SNP according to: (a) equation 3.3 with simple $\delta(r)$ function, (b) Convolute a finite value $Q_{max}=30$ Å$^{-1}$ from equation 3.4, (c) peak broadening caused by thermal motion, convolute $\delta(r)$ by $T_{ij}(r)$ in equation 3.5.

### 3.2.4    Instrumental resolution

The limited resolution of the experiment in Q-space leads to decrease of the amplitude of the PDF peak with increasing r. This can be modeled by a Gaussian damping envelop according to the relation [18] :

$$B(r) = \exp\left[\frac{-\sigma_Q{}^2 r^2}{2}\right] \tag{3.7}$$

Where $\sigma_Q$ is also called $Q_{damp}$ value in pdfGUI software [16]. This parameter is characteristic for every experimental setup and can thus be determined experimentally using a reference substance. As an example, standard Silicon powder (NIST SRM 640d, a = 5.43123 Å) was collected to obtain $\sigma_Q$ in this thesis, as illustrated in Figure 3.3. The value of ~0.017 Å$^{-1}$ was obtained for the transmission setup on the PANalytical powder diffractometer ($Q_{max}$ ~17 Å$^{-1}$), and a value of ~0.0072 Å$^{-1}$ for the setup used at SLS-MS beamline ($Q_{max}$ ~25 Å$^{-1}$).

In general, structural studies on nanocrystalline or amorphous materials do not require experimental set-ups with very high reciprocal space resolution. However, care should be taken if we want to refine crystalline materials.
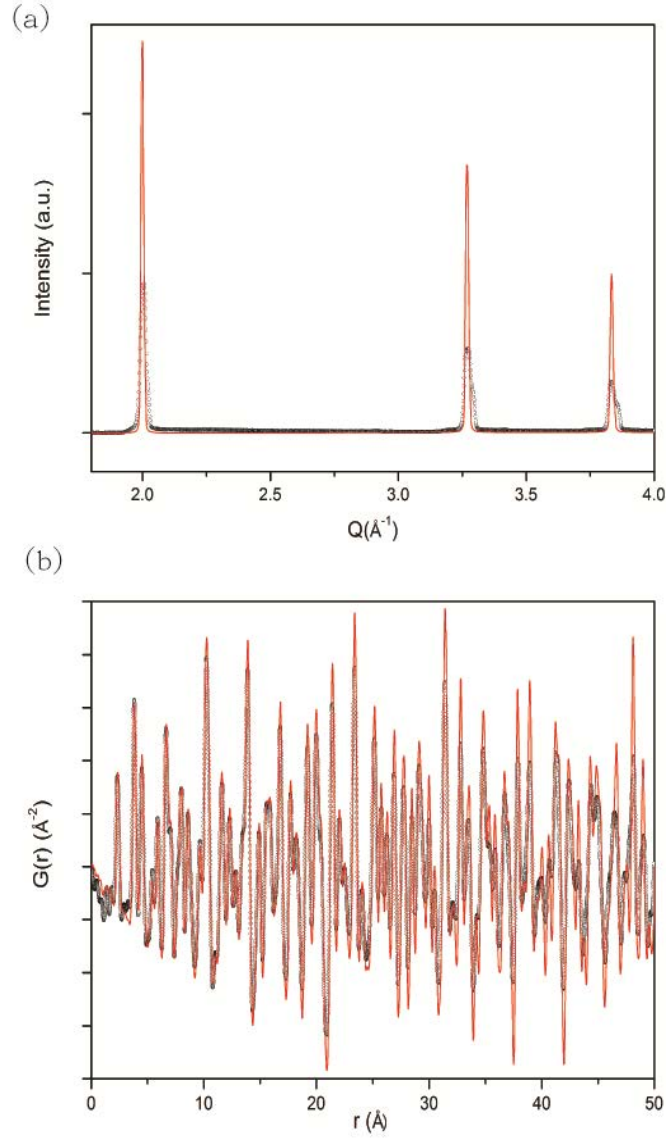
Figure 3.3 (a) Experimental powder patterns for Si standard collected at SLS-MS beamline (solid red line) and in-house PANalytical powder diffractometer at CRM2 (black symbols). The corresponding PDFs are shown in (b), while different Q-space resolution results in differential dampening values in PDFs.

### 3.2.5 PDF of nanoparticles

For a crystal, periodic boundary conditions can be applied to calculate the PDF out to long interatomic distances and the baseline corresponds to a line given by the average number density $-4\pi\varrho_0 r$ as in equation 3.3. However, no interatomic distances exist

beyond the diameter of a finite nanoparticle, and the average number of interatomic distances does not increase linearly with r, but forms a polynominal bell shaped function that is zero beyond the nanoparticle diameter [12]. The exact form of this function depends on the particle shape, as has been shown, e.g. for spheres [19,20], rods and tubes [19], or more complicate core-shell particles [21]. In order to take into account the shape of the nanoparticles, the PDF is multiplied by a shape function, according to equation 3.7:

$$G_{calc}(r,d) = 4\pi r[\rho - \rho_0 f_e(r,d)] \tag{3.8}$$

Where $f_e(r,d)$ is the shape function, and d is the diameter of nanoparticles. Figure 3.4 shows as an example the simulated PDF for spherical 3nm nanoparticles of SNP and its corresponding shape function.
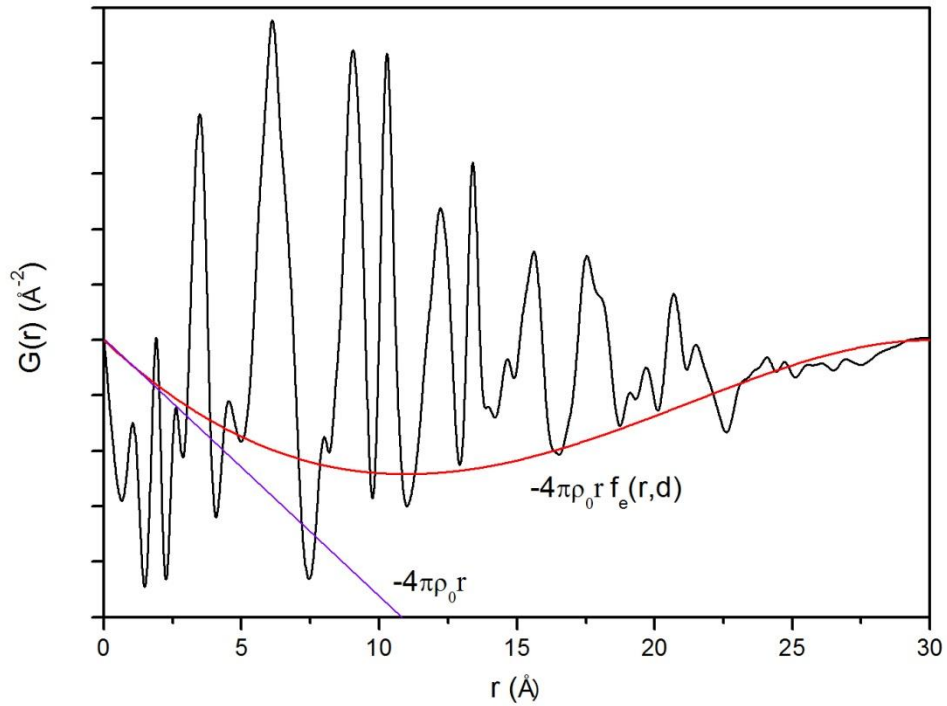


Figure 3.4 Simulated PDF for spherical 3nm nanoparticles of SNP. Two lines are scaled up for comparison: a decreasing line $-4\pi\rho_0 r$ represents the average number of density of SNP, and its corresponding spherical shape function $f_e(r,d)$.

### 3.2.6 Related functions

Finally, we describe the radial distribution function (RDF), R(r) given by:

$$R(r) = 4\pi r^2 \rho(r) \tag{3.9}$$

Which is related to G(r) by:

$$G(r) = \frac{R(r)}{r} - 4\pi r \rho_0 \tag{3.10}$$

The R(r) function is important because it is closely related to the physical structure since R(r)dr gives the number of atoms in a spherical shell of thickness dr at distance r from another atom. For example, the coordination number, Nc, is given by:

$$N_c = \int_{r_1}^{r_2} R(r) dr \tag{3.11}$$

Where $r_1$ and $r_2$ define the beginning and ending positions of the RDF peaks, and dr is corresponding to the coordination shell in the equation.

It should be noted that for a material comprising m atomic species, a single diffraction experiment yields a total G(r), which is the weighted sum of m(m+1)/2 partial PDFs [22]. We can define a partial pair distribution function, $G_{\alpha\beta}(r)$, that is equivalent to G(r) but gives the distribution of atom pairs in the material only coming from atoms of type β around atoms of type α. The total PDF is the weighted sum of all the partial PDFs:

$$G(r) = \sum_{\alpha,\beta} W_{\alpha,\beta} G_{\alpha,\beta}(r) \tag{3.12}$$

The $w_{ij}$ are the weighting factors which depend on the concentration and scattering power of the atomic species.

## 3.3  Reverse Monte Carlo (RMC) method

The Reverse Monte Carlo (RMC) method was first developed by McGreevy and Pusztai (1988) [23] as an approach for building atomic models based on diffraction data rather than interatomic potentials. It was primarily designed for the study of liquids and amorphous materials because of lack of other routes to obtain structural information in such cases. Recently it has become a powerful tool for modelling disorder in crystalline systems as well [24].

In this thesis, the host structure of the $SiO_2$ gel has been simulated by the RMC approach using the EPSR code [25] without applying any empirical potential scheme.

### 3.3.1  Description of the method

In the general approach, a starting configuration of atoms is produced with periodic boundaries, using either a random arrangement of atoms or the crystal structure. This starting configuration must have the correct density and contain the correct ratio of atoms, e.g. 1:2 for $SiO_2$. The RMC simulation then proceeds by moving an atom selected at random within certain constraints. Standard Monte Carlo procedures [26] are used to test whether to accept or reject the move, through calculation of a change in an appropriate "energy" function. In the general approach, the energy function can be associated with the following residuals:

$$\chi^2 = \sum_{i=1}^{n} \frac{[G_{calc}(Q) - G_{obs}(Q)]^2}{\sigma^2} \qquad (3.13)$$

Where the sum is over all n experimental data points, and $\sigma$ is a weight variable that may be taken to be the error of the particular point. If $\chi^2$ following the proposed move is lower than the one determined with the atom in the previous position, $\chi_{new}^2 < \chi_{old}^2$, the move is accepted. Any move that increases $\chi^2$ is by the amount $\Delta\chi^2$ is accepted only with probability $\exp(-\Delta\chi^2/2)$. This sequence is continued until convergence is reached when the atomic configuration is said to describe the data satisfactorily and to be a valid three dimensional representation of the structure (see Figure 3.5).
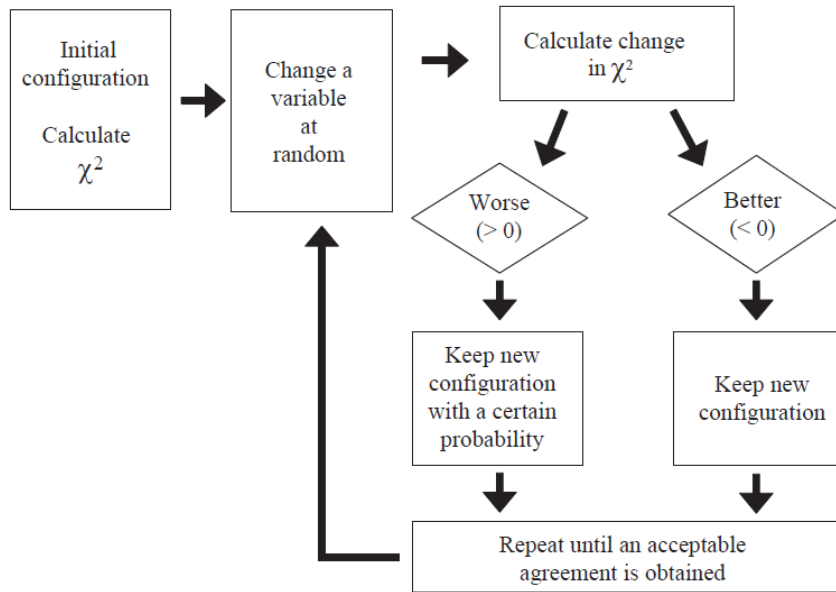
Figure 3.5 Schematic diagram of RMC algorithm [12].

The definition of $\chi^2$ may be generalised to incorporate extra data sets, e.g. joint x-ray and neutron total structure factor, EXAFS measurement, etc. [27] to improve reality of refinement. In this thesis, we generate a three dimensional amorphous silica configuration via this method.

# Bibliography

[1]    P. Debye, Ann. Phys. **351**, 809 (1915).

[2]    N. Pinna, in *Scatt. Methods Prop. Polym. Mater.* (Springer Berlin Heidelberg, 2005), pp. 29–32.

[3]    A. Guagliardi, N. Masciocchi, Associazione italiana di cristallografia, Schweizerische Gesellschaft für Kristallographie, and Paul Scherrer Institut, in (Insurbia University Press, 2010).

[4]    B. D. Hall, J. Appl. Phys. **87**, 1666 (2000).

[5]    A. Cervellino, C. Giannini, A. Guagliardi, and M. Ladisa, Phys. Rev. B **72**, 035412 (2005).

[6]    T. Proffen and R. B. Neder, J. Appl. Crystallogr. **32**, 838 (1999).

[7]    G. Cernuto, N. Masciocchi, A. Cervellino, G. M. Colonna, and A. Guagliardi, J. Am. Chem. Soc. **133**, 3114 (2011).

[8]    F. Niederdraenk, K. Seufert, A. Stahl, R. S. Bhalerao-Panajkar, S. Marathe, S. K. Kulkarni, R. B. Neder, and C. Kumpf, Phys. Chem. Chem. Phys. **13**, 498 (2010).

[9]    A. Cervellino, J. Schefer, L. Keller, T. Woike, and D. Schaniel, J. Appl. Crystallogr. **43**, 1040 (2010).

[10]   D. a. H. Cunningham, W. Vogel, R. M. Torres Sanchez, K. Tanaka, and M. Haruta, J. Catal. **183**, 24 (n.d.).

[11]   W. Vogel, D. a. H. Cunningham, K. Tanaka, and M. Haruta, Catal. Lett. **40**, 175 (1996).

[12]   R. B. Neder and T. Proffen, *Diffuse Scattering and Defect Structure Simulations* (Oxford University Press, 2008).

[13]   I.-K. Jeong, R. H. Heffner, M. J. Graf, and S. J. L. Billinge, Phys. Rev. B **67**, 104301 (2003).

[14]   I.-K. Jeong, T. Proffen, F. Mohiuddin-Jacobs, and S. J. L. Billinge, J. Phys. Chem. A **103**, 921 (1999).

[15]   T. Proffen and S. J. L. Billinge, J. Appl. Crystallogr. **32**, 572 (1999).

[16]   C. L. Farrow, P. Juhas, J. W. Liu, D. Bryndin, E. S. Božin, J. Bloch, T. Proffen, and S. J. L. Billinge, J. Phys. Condens. Matter **19**, 335219 (2007).

[17]   N. Rademacher, L. L. Daemen, E. L. Chronister, and T. Proffen, J. Appl. Crystallogr. **45**, 482 (2012).

[18]   B. H. Toby and T. Egami, Acta Crystallogr. A **48**, 336 (1992).

[19]  R. C. Howell, T. Proffen, and S. D. Conradson, Phys. Rev. B **73**, 094107 (2006).

[20]  K. Kodama, S. Iikubo, T. Taguchi, and S. Shamoto, Acta Crystallogr. A **62**, 444 (2006).

[21]  V. Iorsunskiy, R. B. Neder, A. Hofmann, S. Dembski, C. Graf, and E. Rühl, J. Appl. Crystallogr. **40**, 975 (2007).

[22]  T. E. Faber and J. M. Ziman, Philos. Mag. **11**, 153 (1965).

[23]  R. L. McGreevy and L. Pusztai, Mol. Simul. **1**, 359 (1988).

[24]  M. G. Tucker, M. T. Dove, and D. A. Keen, J. Appl. Crystallogr. **34**, 630 (2001).

[25]  A. K. SOPER, Mol. Phys. **99**, 1503 (2001).

[26]  K. Binder and D. W. Heermann, *Monte Carlo Simulation in Statical Physics: An Introduction* (Springer, Berlin, 2012).

[27]  D. T. Bowron, Mater. Sci. Eng. B **149**, 166 (2008).

# Chapter 4

# Synthesis and multiscale structural analysis of photoswitchable molecular hybrid materials

# Chapter 4

# Synthesis and multiscale structural analysis of photoswitchable molecular hybrid materials

The inclusion of photoswitchable mononitrosyl complexes $[ML_5NO]^x$ (M = metal, L=ligand) into silica matrices is of interest in view of the exploitation of their optical properties for applications such as holography, data storage or medical application [1–4]. In this class of compounds the nitrosyl ligand can undergo photoinduced linkage isomerisation [5,6] resulting in changes of the color and the refractive index of the compounds. Since the linkage isomerism is a molecular property these complexes are suitable candidates for embedding them into host materials such as silica gels [7] and metal-organic frameworks [8] or electrostatic attachment on surfaces [9].

The study of the prototype complex $Na_2[Fe(CN)_5NO]\cdot 2H_2O$ (Sodium Nitroprusside, SNP) embedded in silica matrices showed that the properties of the metastable linkage isomers [10,11] are independent of the particle size [12]. Furthermore this study indicated that at low doping levels the SNP guest might be included as isolated molecules in the mesopores $SiO_2$ host (see paragraph 4.6.3). This finding is in agreement with the results of a neutron diffraction study on a $(CN_3H_6)_2[Fe(CN)_5NO]$ complex

embedded in a silica host [13], which allowed for the identification of the structural fingerprint of isolated molecules in the porous network. In this case however the properties of the linkage isomerisation change insofar as that the achievable population is increased in the gel matrix compared to the crystalline material. In order to be able to derive a structure-functionality relationship and to proceed to a more targeted design of such hybrid complexes, a detailed description of the structural organisation of the guest species and of their immediate surrounding (i.e. silica wall, solvent and counter-ions) is thus absolutely mandatory.

In the following we will present the results of total scattering experiments performed on SNP@SiO$_2$ and discuss in detail the structural information that can be obtained for such molecular hybrid materials from PDF analysis.

# 4.1 Sample Preparation

The synthesis of the molecular hybrid materials is realized by the sol-gel procedure [14]. The advantages of the sol-gel technique are the low temperature processing, which allows an embedding of molecular species, as well as the high variability of compositions.

Two main strategies have been developed herein for the incorporation of the SNP complexes into the silica matrix, namely, *post-doping* and *pre-doping*. The former procedure is the so-called wet impregnation, where a solidified $SiO_2$ monolith is impregnated by immersing it into an aqueous solution of guest species. In the latter procedure the molecular species are added in the form of an aqueous solution to the silica sol before hydrolysis. The mixture then hydrolyses to form a gel and is subsequently dried.

## 4.1.1 Post-doping

### 4.1.1.1 Empty $SiO_2$ host

The empty (Pure) silica xerogel host can be synthesized with any shape and size; herein we prepared $SiO_2$ monoliths which exhibit pore sizes of ca. 1 nm, 5 nm and 11 nm, which are characterized by BET measurement (see Annex. 2). Small pore sizes in the range of 1~3 nm are suited for the inclusion of isolated molecules, while pores with sizes 5 and 11 nm allow *in situ* growing of nano-particles in the matrices.

**(a) Pore sizes of 1~3 nm:**

The $SiO_2$ xerogel of pore sizes ca. 1~3 nm was obtained by the following procedure: 1.5 ml of tetramethoxysilane (TMOS, 98% purity, Fluka), 1.8 ml of methanol (VWR) and 3.6 ml of distilled water were mixed and stirred at room temperature for about 5 minutes which allowed the solution to gel. The mixture was then placed in a glass tube at 50 °C for 3 weeks in an oven to dry and solidify the obtained gel. Finally the dried gels were put in desiccators at $10^{-2}$ mbar in order to remove the residual solvent. Cylindrical transparent rods with a diameter of about 1.0 mm were obtained (see Fig 4.1 (a)) as final product.

**(b) Pore sizes of 5 nm and 11 nm:**

The porous $SiO_2$ matrices with pore sizes of ca. 5 nm and 11 nm were synthesized and provided by the PhLAM laboratory (Universié de Lille 1). These xerogels, having good optical transparency and mechanical strength, were obtained by hydrolysis and polycondensation of TMOS, followed by a drying step and annealing in air at 850°. This

sol–gel process yields a large range of mesoporous xerogels with well controlled pore sizes [15].

### 4.1.1.2    Wet impregnation

The SNP@SiO$_2$ hybrids were prepared by impregnating the empty porous SiO$_2$ monoliths with an aqueous solution of SNP salt (concentration, c = 3.507 mol/L). The SiO$_2$ matrices were slowly immersed into the SNP solution in order to prevent cracking of the monoliths. The monoliths, initially colourless, then became progressively more and more brown-orange indicating the diffusion of the SNP complexes into the silica pore network. After about 24 hours the monoliths displayed homogeneous colouring and were kept at 50 °C for 7 days in an oven. A final drying step was performed at room temperature in desiccators coupled with a primary pump (ca. 10$^{-2}$ mbar) for about 3 days in order to remove the remaining solvent.

The pre-formed empty SiO$_2$ monoliths with pore sizes of about 1 nm, 5 nm and 11 nm were prepared by this procedure, leading to the confined precipitation of nanoparticles within the matrix. The obtained empty SiO$_2$ monoliths and SNP@SiO$_2$ (1nm pores) samples are shown in Fig. 4.1.
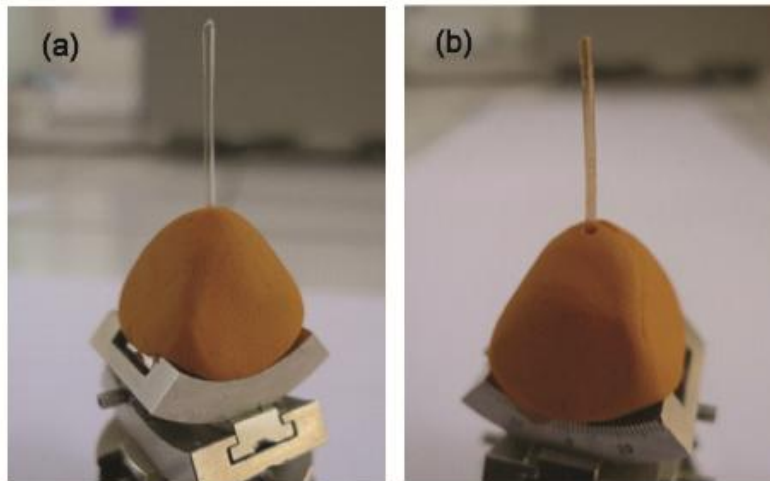


Figure 4.1 Photographs of the synthesized mesoporous silica monoliths: (a) empty SiO$_2$ monolith and (b) SNP@SiO$_2$ nanocomposites.

## 4.1.2    Pre-doping

1.5 ml of TMOS, 1.8 ml of methanol (VWR) and 3.6 ml of distilled water and different amounts of 0.2517 (mol/L) aqueous SNP solutions were mixed and stirred for

about 30 minutes. The total amount of water was kept constant at 3.6 ml. By varying the amount of added SNP solution the concentration of SNP was varied between 12.5 and 625 μmol per gel. After 30 minutes the gels in the glass flasks were covered by parafilm and put into an oven for 1 week at 50 °C in order to allow for complete gelation. Then small holes were pierced into the parafilm in order to allow for a complete evaporation of remaining solvents in about 1 week. Then the parafilm was completely removed and the gel dried for 1 week in an oven at 50 °C. Finally the dried gels were put in desiccators at ca. $10^{-2}$ mbar in order to remove remaining residual solvent.

## 4.2 Average crystal structure of the bulk material $(Na_2[Fe(CN)_5NO] \cdot 2H_2O$

The crystal structure of the Sodium Nitroprusside dihydrate complex $(Na_2[Fe(CN)_5NO].2H_2O$, SNP), has been previously determined from both X-ray and neutron diffraction measurements [16–18]. In order to use the average structural model of this complex in our PDF analysis we have reinvestigated the average crystal structure of SNP from accurate room temperature single crystal X-ray diffraction measurements. More details on the single crystal measurement and structural refinement are given in Annex 1. The asymmetric unit of SNP is shown in Fig 4.2.a and selected structural parameters are given in Table 4.1. The compound crystallizes in the orthorhombic space group Pnnm with cell parameters a=6.2051(4) Å, b= 11.9098(6) Å, c=15.5605(9) Å and V=1149.94(1) Å$^3$. The molecular structure is characterized by distorted octahedral geometry around the iron atom, where the metal center is hexacoordinated by five CN groups and one NO ligand (Fig 4.2.a). The distortion from a perfect octahedral configuration is essentially due to the presence of the NO group and as a consequence the four *cis* CN ligands (related by the pseudo-fourfold axis) are bent down away from the N-O group toward the *trans* CN ligand. This is also marked by the displacement of the Fe atom (0.184(1) Å) out of the plane of the *cis* C atoms towards NO group. It is worth noting that the *cis* Fe—C bond lengths (Fe—C2=1.936(1) Å and Fe—C3 =1.943(1) Å) are slightly longer than the *trans* Fe—C (Fe—C1= 1.928(1) Å). One also notes that the Fe-N4-O4 fragment of the ion is more deviated from linearity compared to the Fe-C*i*-N*i* portions *(i*=1, 2 or 3) (Table 4.1.).
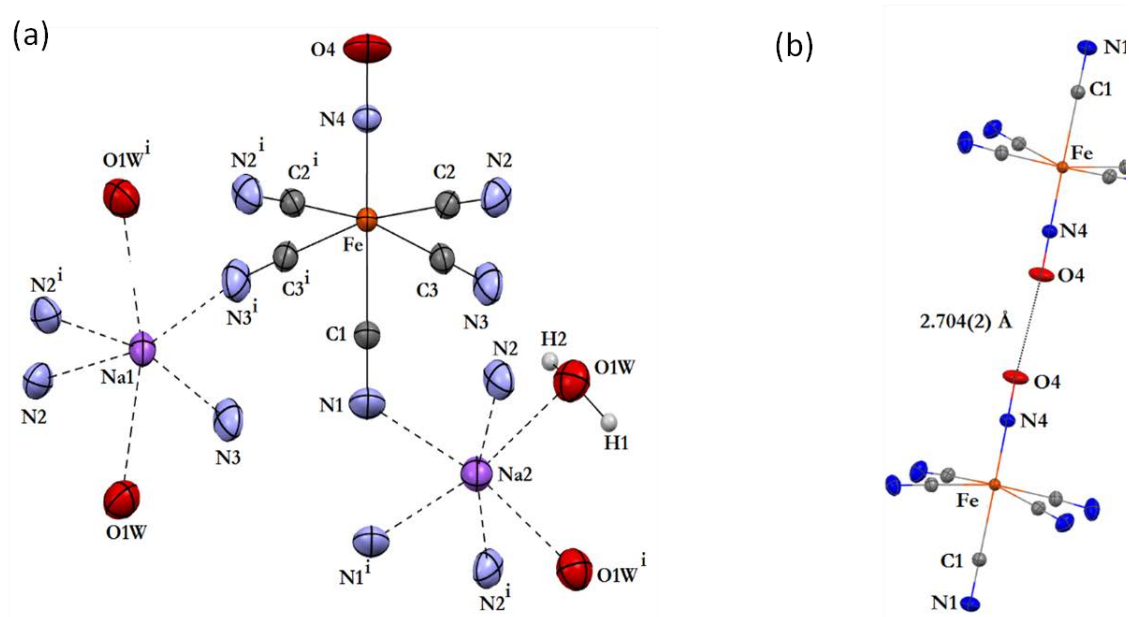
Figure 4.2 (a) A projection of SNP complex, showing the atom-labelling scheme and coordination geometry of Na atoms. Displacement ellipsoids are drawn at the 50% probability level for all non-H atoms. (b) The N—O…O—N anion-anion interactions

**Table4.1**. Selected structural parameters for SNP complex.

| Bond length (Å) | | |
|---|---|---|
| Fe—C1: 1.928(1) | Fe—C2: 1.936(1) | Fe—C3: 1.943(1) |
| C1—N1: 1.144(2) | C2—N2: 1.144(1) | C3—N3: 1.147(1) |
| Fe—N4: 1.660(1) | N4—O4: 1.130(2) | Na1…Na2: 3.7306(6) |
| Fe…Na1:5.5695(6) | Fe…Na2: 4.9293(5) | |
| Bond angles (°) | | |
| N1-C1-Fe:179.8(2) | N2-C2-Fe:176.9(1) | |
| N3-C3-Fe:178.5(1) | O4-N4-Fe: 176.1(1) | |

The crystal packing consists of a three dimensional network of intermolecular interactions involving $[Fe(CN)_5NO]^{2-}$ anions, $Na^+$ cations and water molecules. The cyano moieties are only involved in anion-cation interactions and there is no hydrogen bonding between water molecules and the CN groups. This can be explained by the fact that the water oxygen atoms are tetrahedrally coordinated by sodium cations ($Na1^+$ and $Na2^+$) and therefore water molecules are not close enough to the CN groups to form such hydrogen bonds. Furthermore, the specific configuration of the $[Fe(CN)_5NO]^{2-}$ anions results in shortened anion-anion contacts between two neighbouring NO groups with O…O distance of 2.704(2) Å (Fig 4.2.b).

54

The sodium cations (Na1$^+$ and Na2$^+$) have similar distorted octahedral environment, where each sodium cation is hexacoordinated to two water molecules and four cyano groups (Fig 4.2.a). The Na…N interactions range from 2.487(1) Å to 2.534(1) Å and the Na…O interactions have distances varying from 2.496(1) Å to 2.528(1) Å. It is also noteworthy that the shortest distance between two iron metal centers is 6.6583(4) Å.

The optical excitation of SNP leads to a change in the bond between the central metal atom Fe and the NO ligand which triggers the rotation of the NO group. In the ground state (GS) the nitrosyl ligand is bound via nitrogen (Fe-N-O). The ligand can be totally switched by 180° to an oxygen coordination Fe-O-N (metastable state S1) by irradiation with blue-green light [11]. A subsequent irradiation of light in the near infrared spectral range turns nitrosyl ligands by 90° to a side-on coordination (S2) [6,19,20] as illustrated in Fig. 4.3.
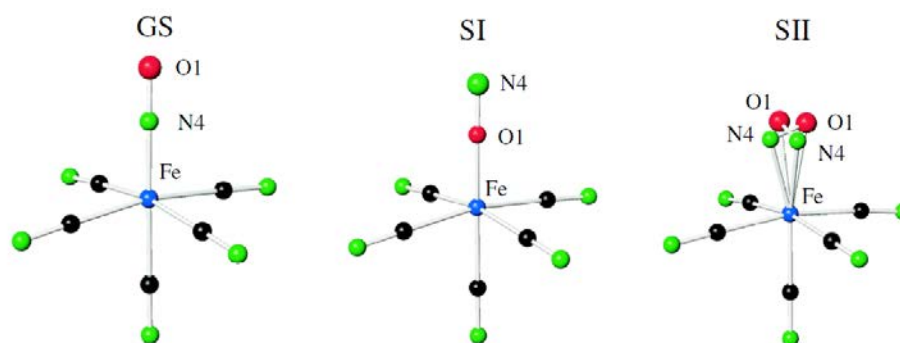


Figure 4.3 Schematic illustration of the photoinduced changes for (Na$_2$[Fe(CN)$_5$NO]. 2H$_2$O) complex [21].

These photoswitchable properties have been evidenced by infrared spectroscopy by the υ(NO) shift under irradiation (λ = 458 nm and 1064 nm) at low temperature (T = 80 K). The reversible transfers in a single crystal from the GS to S1 and GS to S2 are about 45% [11] and 30% [22], respectively. In order to explore the properties of embedded (Na$_2$[Fe(CN)$_5$NO]. 2H$_2$O) complex and the generation conditions of photoinduced linkage isomers in these conditions we studied the electronic structure of SNP embedded in SiO$_2$ xerogels using X-ray diffraction, absorption and infrared spectroscopy.

## 4.3    Evidence of photoswitchable properties

UV-Vis absorption spectroscopy delivers information about the electronic structure of the compound in its different configurations. In the case of photoinduced metastable linkage isomers, the low temperature measurements yield in addition information about the spectral ranges for photoswitching [22]. Fig. 4.4 shows the absorption spectra in the GS at 297 K of SNP@SiO$_2$ with 1 nm pore sizes, with the two absorption bands at 19100 cm$^{-1}$ (I) and 25100 cm$^{-1}$ (II) (deconvolution with Gaussians).

For comparison the two absorption bands in crystalline SNP are found at 19800 cm$^{-1}$ (I) and 25950 cm$^{-1}$ (II) for polarization along a-axis of the crystal [22]. There is thus a slight redshift of about 700 cm$^{-1}$ in the xerogel compared to the crystal, an effect known from SNP embedded in aqueous solutions, where the two bands are found at 19125 cm$^{-1}$ and 25100 cm$^{-1}$, respectively [23]. Also the width of the peaks is in the same range of that found in solution, 4800 cm$^{-1}$ and 6000 cm$^{-1}$ in the silica compared to 3800 cm$^{-1}$ and 6000 cm$^{-1}$ in solution. Consequently the assignment of the absorption bands to the transitions $d_{xy} \rightarrow \pi(NO)$ (I, HOMO-LUMO) and $d_{xz,yz} \rightarrow \pi(NO)$ (II) is the same as found in single crystal and solutions. Furthermore, the fact that the absorption spectrum of SNP@SiO$_2$ resembles the spectrum of an aqueous SNP solution is a first hint that the SNP complexes are embedded as isolated complexes and that the system SNP@SiO$_2$ might be considered as some kind of frozen solution of SNP in a glassy matrix.
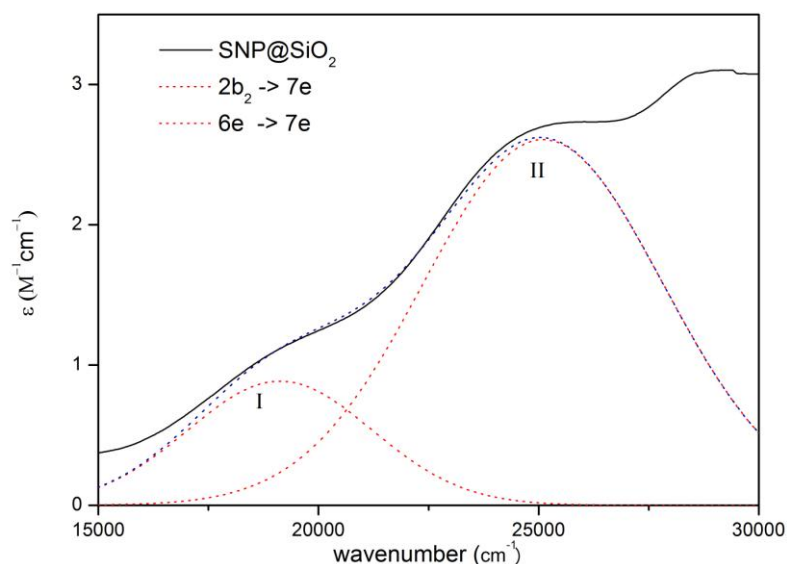


Figure 4.4 UV/vis spectra of SNP@SiO2 (pore sizes of 1 nm) at 297 K using Shimadzu UV-3600 spectrophotometer. The dotted curves I and II denote the Gaussian deconvolution of the spectrum

Infrared spectroscopy (IR) yields information of embedded SNP in the $SiO_2$ matrix, as well as their photoswitchable properties [7,12]. The IR spectrum of the SNP@$SiO_2$ hybrids is a combination of the pure $SiO_2$ spectrum with the pure SNP spectrum and shows both the characteristic bands for the $SiO_2$ gel and SNP. The pure $SiO_2$ has wide bands at 800 cm$^{-1}$ (Si-O stretching) and 970 cm$^{-1}$ (SiOH bending). The Si-O stretching vibrations lead to a very strong and wide band between 1000 and 1200 cm$^{-1}$. At 1660, 1875 and 2000 cm$^{-1}$ weak bands are observed that are identified as combination or overtones of the silicon-oxygen fundamentals [7]. Since $H_2O$ can easily be adsorbed into the pores, the band at 1660 cm$^{-1}$ might also stem from its bending mode (see Fig. 4.5 (a)).

The IR spectrum of crystalline SNP shows peaks corresponding to the nitrosyl stretching mode $\upsilon$(NO) and the cyanide stretching mode $\upsilon$(CN) centered at 1947 cm$^{-1}$ and 2147 cm$^{-1}$, respectively. However, the asymmetric $\upsilon$(CN) band splits into multiple bands (2147 cm$^{-1}$, 2163 cm$^{-1}$, 2168 cm$^{-1}$, and 2177 cm$^{-1}$). After embedding the SNP complexes into $SiO_2$ gel, some of the $SiO_2$ bands overlap the SNP bands. The two characteristic bands of $\upsilon$(NO) and $\upsilon$(CN) are still visible in Fig. 4.5 (b) and (c), which represent samples of post-doping SNP into $SiO_2$ matrices of 1 nm and 5 nm, respectively. If we take a closer look at $\upsilon$(CN) bands, the fourfold splitting is completely smeared out in the samples with 1 nm pore sizes. In the samples with 5 nm pore size this splitting is clearly visible, however it is less pronounced than in the crystalline SNP. These results indicate that the inclusion of SNP in matrices with different pore size leads to different structural arrangement of the SNP complexes inside the pores. While in the small pores (with probably isolated SNP complexes) the effect of the well-ordered crystalline environment seems to be completely absent or at least largely reduced it reappears in the bigger pores, indicating that in these larger pores small crystallites are formed. We note also that the position of the peaks is not changed within experimental error (2cm$^{-1}$) indicating that the structure of the anion is not changed upon embedding.
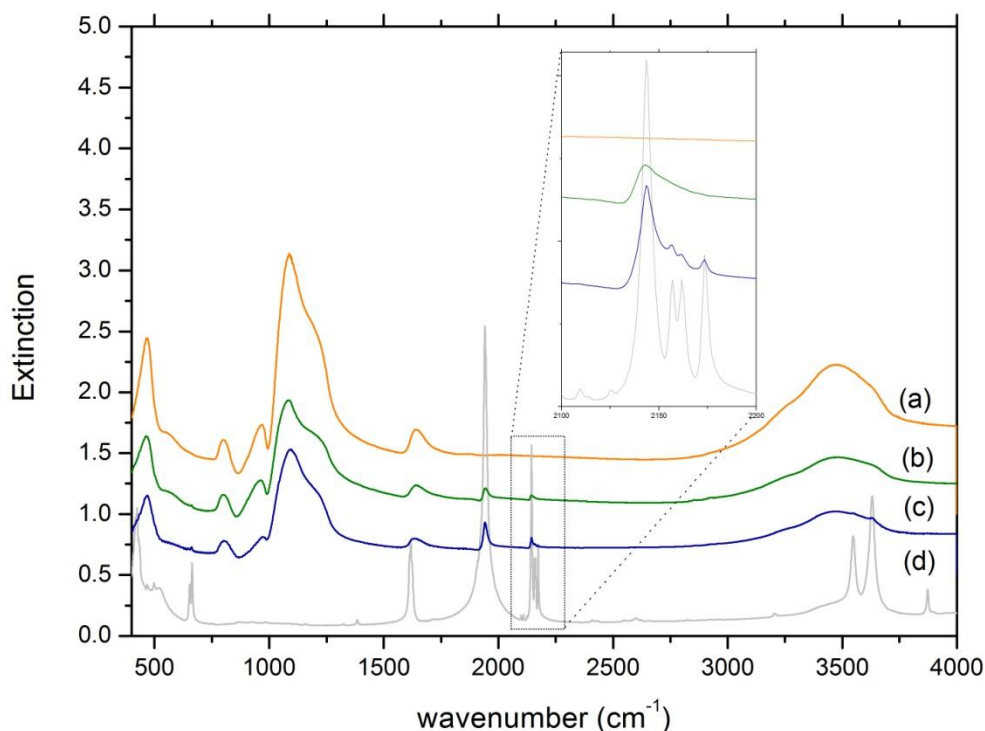
Figure 4.5 Infrared spectra of SNP-silica hybrids in GS: (a) pure/empty silica gel, (b) SNP-silica with pore sizes of 1 nm, (c) SNP-silica with pore sizes of 5 nm, and (d) crystalline SNP. The spectra are shifted vertically for clarity.

The illumination with light in the blue-green spectral range at 80 K generates the metastable state S1, which can be identified by a new $\upsilon$(NO) band appearing at 1828 cm$^{-1}$. The decrease in the area of the GS band at 1947 cm$^{-1}$ yields the amount of transferred molecules, i.e. the population of S1. In the samples with 1 nm pores the populations obtained for S1 are 11(1)% when using 476 nm. The subsequent illumination with 1064 nm transfers the molecules from S1 towards S2 and partially back to GS. As can be seen from Fig. 4.6(a) the S1 band disappears and the GS band increases. The new band of S2 is hidden in the H$_2$O absorption band, but can be identified from a difference spectrum, shown in the inset. The band of S2 is found at 1684 cm$^{-1}$ and the population determined from the GS area is about 7(1)%. Compared to the crystalline SNP, where the $\upsilon$(NO) stretching vibrations of S1 and S2 are found at 1835 and 1664 cm$^{-1}$, respectively, we observe a shift of 7 and 20 cm$^{-1}$ for S1 and S2, respectively. In the case of the samples with 5 nm pores we obtain a population of about 13(1)% and 12(1)% for irradiation with 442 nm and 476 nm, respectively (Fig. 4.6(b)). The transfer with 1064 nm results in a population of 7(1)% for S2. No shifts of the peak with respect to the crystalline SNP are

observed in the samples of 5 nm pores, i.e the bands of S1 and S2 are found at 1835 and 1664 cm$^{-1}$, respectively. Furthermore, we note that there is broad band underneath the S1 peak around 1828 cm$^{-1}$, indicating that there might be also a contribution due to isolate molecules as for the 1 nm sample.

The large width of the two bands in the xerogel samples (1 nm pore size) of 40 and 60 cm$^{-1}$ for S1 and S2 is a clear hint for the disordered arrangement of the molecules within the pores and possibly weak interactions with the matrix, e.g. with OH groups on the pore surfaces. In general we could expect that S2 with its side-on position reacts more sensitively upon small local structural changes that could occur in the isolated complexes in the gel compared to the crystalline packing, which might explain the more pronounced broadening as well as the peak shift of 20 cm$^{-1}$ with respect to the crystal. The population of 13% is in the range of the population achieved in powder samples indicating that the orientation of the fourfold axis of the molecules is statistically distributed in the gel.
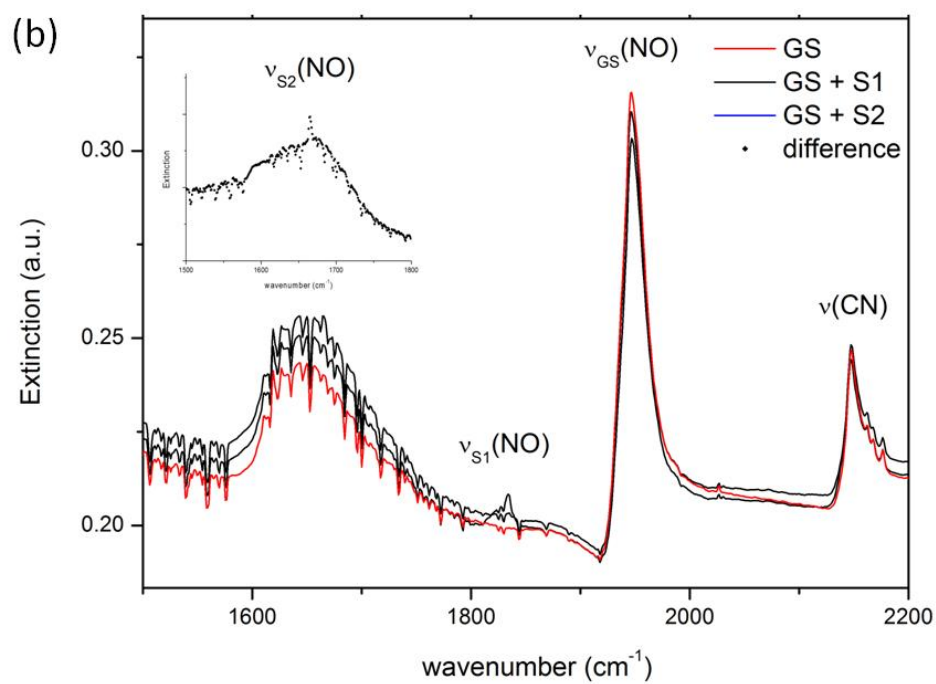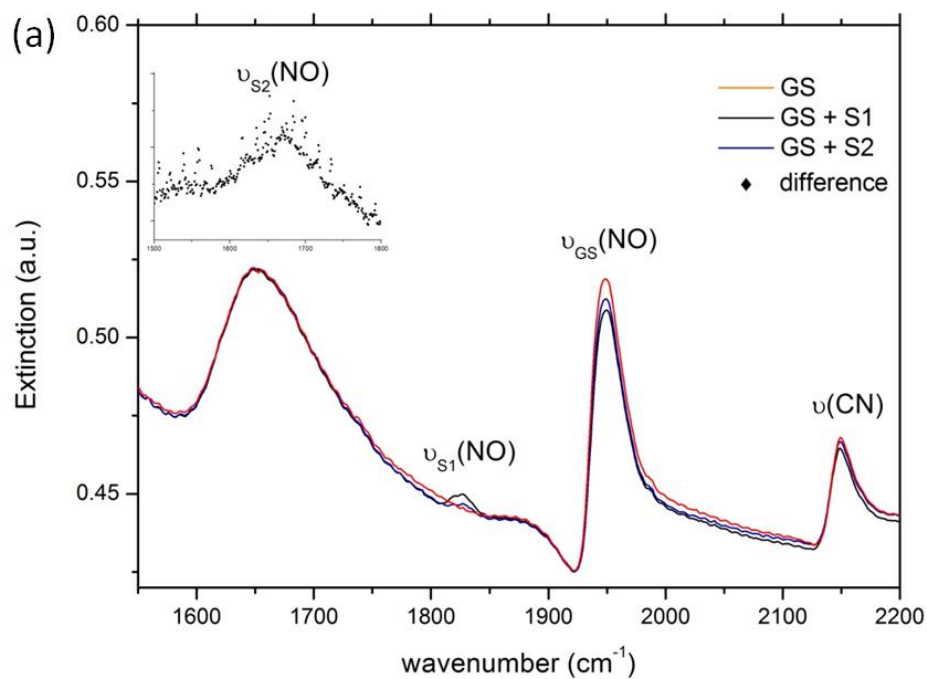
Figure 4.6 Infrared spectra at T = 80 K of SNP@SiO$_2$ hybrids with pore sizes of (a) 1 nm and (b) 5nm. The GS and after irradiation with 458 nm and 1064 nm for S1 and S2, respectively.

## 4.4   The PDF for SNP@SiO2 monolith (1nm)

By the total scattering method, including Debye function analysis (DFA) and Pair distribution function (PDF), not only Bragg peaks but also the diffuse scattering in the whole powder diffraction pattern is measured. In this manner the local atomic environment which may be lost in the average long-range structure analysis can be studied as, e.g., in the case of the isolated complexes embedded in amorphous matrix.

In order to explore the possibilities and limitations of the total scattering measurements coupled to a PDF analysis we first investigated crystalline SNP which serves as a reference substance. Furthermore we used this measurement to compare the PDF analysis of synchrotron data to that of data collected on the laboratory X-ray diffractometer. This allows for studying the effect of $Q_{max}$ on the accuracy of the structural model, and – as a more general conclusion – for the comparison of the quality of laboratory based PDF results to those obtained on synchrotron beamlines for such molecular materials.

### 4.4.1   Bulk structure of SNP

We compare experimental data of bulk SNP collected at E = 24.9866 keV ($\lambda$ = 0.4133 Å) at the MS-beamline (SLS, Paul Scherrer Institut) and using Mo K$\alpha$ radiation ($\lambda$ = 0.7107 Å) at CRM2. Fig. 4.7 illustrates the routine extraction steps, which are followed in order to obtain from raw intensity I(Q) the normalized S(Q), and finally G(r) using the program GudrunX [24].

The X-ray total structure factor falls off sharply with increasing Q resulting in a weak signal at high diffraction angles. This is illustrated in Fig 4.7(a) that shows the raw intensity from bulk SNP. The overall drop-off in intensity follows $<f(Q)>^2$ with very little apparent structure in the scattering at high-Q region. However, when the data are divided by $<f(Q)>^2$, (cf. Eq. 2.10), diffuse scattering becomes apparent in this region (Fig 4.7(c)). It is therefore important to measure the diffracted intensity up to high Q-values with good counting statistics. This does not present a problem when high flux, high-energy sources such as synchrotrons are used. The incident flux at high energies is so intense that, despite the inefficient coherent scattering and $Q_{max}$ value, sufficient statistics can be obtained to yield accurate G(r) (Fig 4.7(e)). On the other hand, on a laboratory source one usually needs to increase data acquisition times at high angle in order to improve statistics. Otherwise it could result in an improper picture of the local-range order below ca. 5 Å in G(r) after Fourier transformation (Fig 4.7(f)).

Comparing the intensity patterns in Fig 4.7(a,b) one immediately recognizes the two main differences in the synchrotron and laboratory pattern: resolution and maximum

accessible Q-range. The synchrotron data exhibit both a higher resolution and a higher $Q_{max}$. By measuring up to 120° a $Q_{max}$ of about 27 $\text{Å}^{-1}$ can be obtained (data are truncated at $Q_{max}$= 25 $\text{Å}^{-1}$ beyond which the signal-to-noise ratio became unfavourable) in the synchrotron data set while on the laboratory source the $Q_{max}$ of about 17 $\text{Å}^{-1}$ can only be obtained when measuring up to 150° in 2θ. Concerning the resolution the shown patterns illustrate the compromise made in the laboratory measurement, where a step size of 0.07° in 2θ was chosen in order to limit the measurement time to approximately 48h, whereas in the synchrotron measurement the resolution can be reached 0.0035° due to the fact that the measurement time of only about 20 minutes is not a limiting factor.

The differences in signal-to-noise ratio are more clearly visible in the S(Q) patterns in Fig 4.7(c,d), from which can be seen that noise remains small up to high Q-values, while for the laboratory pattern the noise starts to increase at about 10$\text{Å}^{-1}$. Note that the difference in scale of the two patterns, S(Q) tends towards 1 in both cases, the count rate simply being much higher in the synchrotron data.

Finally, these differences are transferred to the PDF (Fig 4.7(c,d)), showing a much better resolution in the small-r range and less termination effects due to higher $Q_{max}$, as well as a smaller peak width due to the higher Q-resolution.
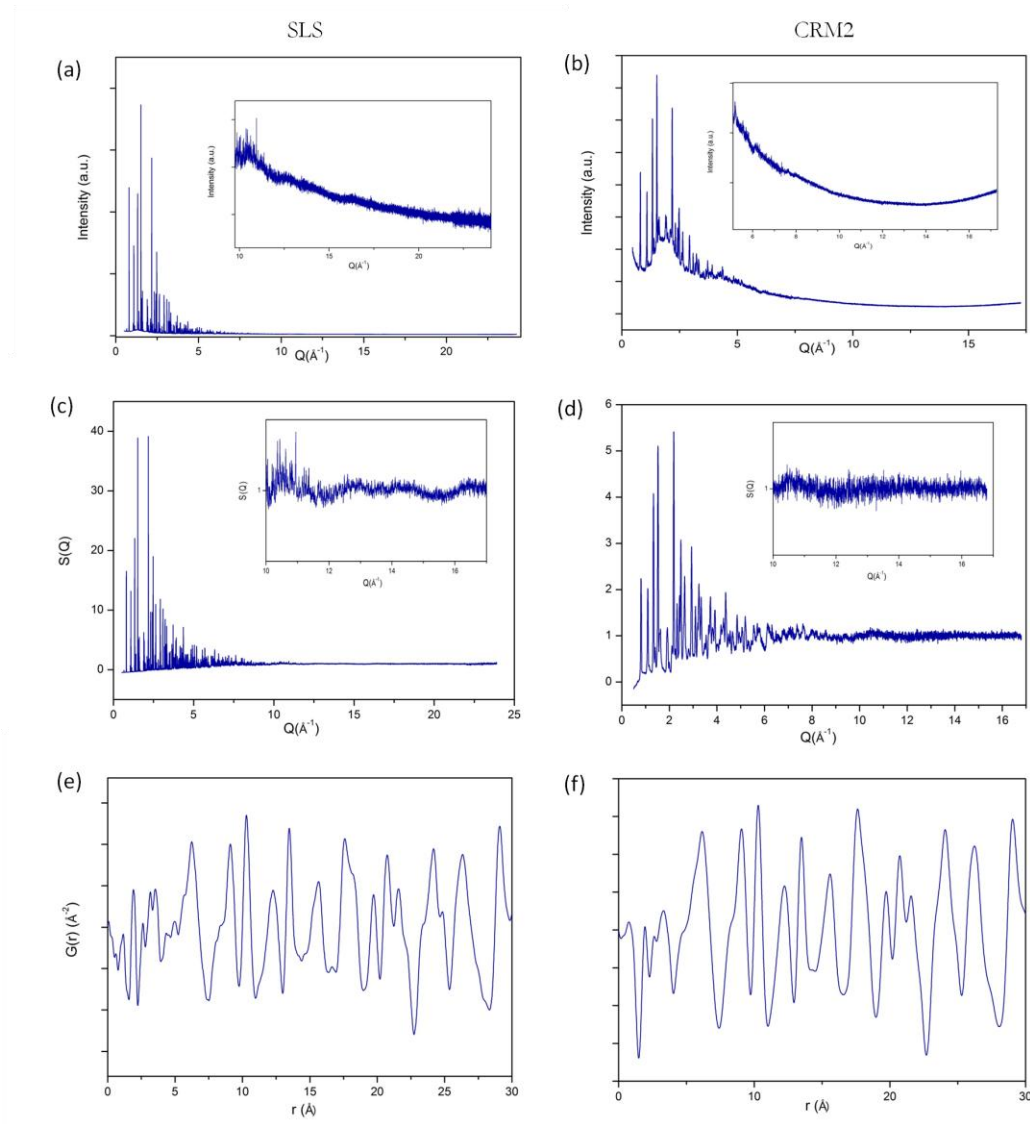
Figure 4.7 Diagrams compare data collected including I(Q), S(Q) and G(r) with synchrotron source (left) and laboratory Mo Kα radiation (right) for bulk SNP powder. From top to the bottom the routine data extraction steps from raw intensity I(Q) to normalized total structure function S(Q), and G(r), respectively, are illustrated. The high-Q region is zoomed on a small window to highlight the presence of diffuse scattering.

In order to better illustrate the differences in the PDF obtained from the two measurements Fig. 4.8. shows the overlapping plot of Fig. 4.7(e,f). We see clearly that the position and relative amplitude of the peaks is the same in the two PDFs, but that the peak width is larger in the laboratory data, and that still in the small-r range (below about 5 Å) the difference is most pronounced.
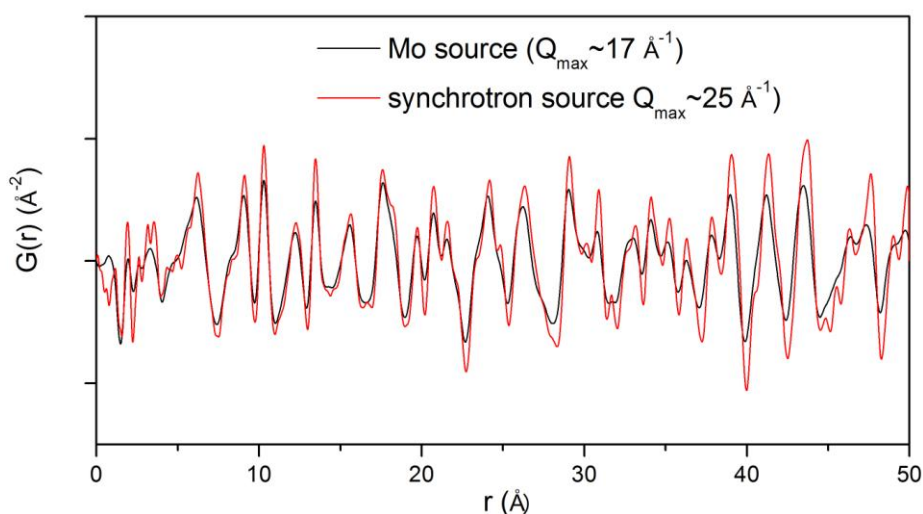
Figure 4.8 Scaled overlap of plots from Fig. 1.7(e,f) for comparison of PDF obtained from laboratory and synchrotron data.

In order to extract structural information from the experimental PDF, it is then possible to refine the experimental PDF with a structural model in direct space in a similar way as Rietveld refinement is used in reciprocal space for crystalline materials. We first used the PDF analysis method to check the average structural model by refining the observed G(r) (Fig 4.7(e)) by using the program PDFgui [25].

To be noted, previous PDF studies have shown that the small-r peaks in experimental PDFs have systematically smaller peak widths than the PDF peaks that have been calculated from a model, as illustrated in Fig 4.9(a). This phenomenon is related to correlated motions of atoms in PDFs [26,27] and more visible in molecular compounds [28]. In order to take this correlated motion into account a cut-off value in r ($r_{cut}$) can be defined which corresponds to the longest intramolecular distances in the studied system. In our case the $[Fe(CN)_5NO]^{2-}$ anion is quite rigid and therefore the displacements of the atoms within this anion are correlated. We therefore introduced the cut-off value of $r_{cut} = 3.25$ Å corresponding to the distances of the central Fe atom to the terminal N atoms of the C-N ligands. The result is shown in Fig 4.9(b).
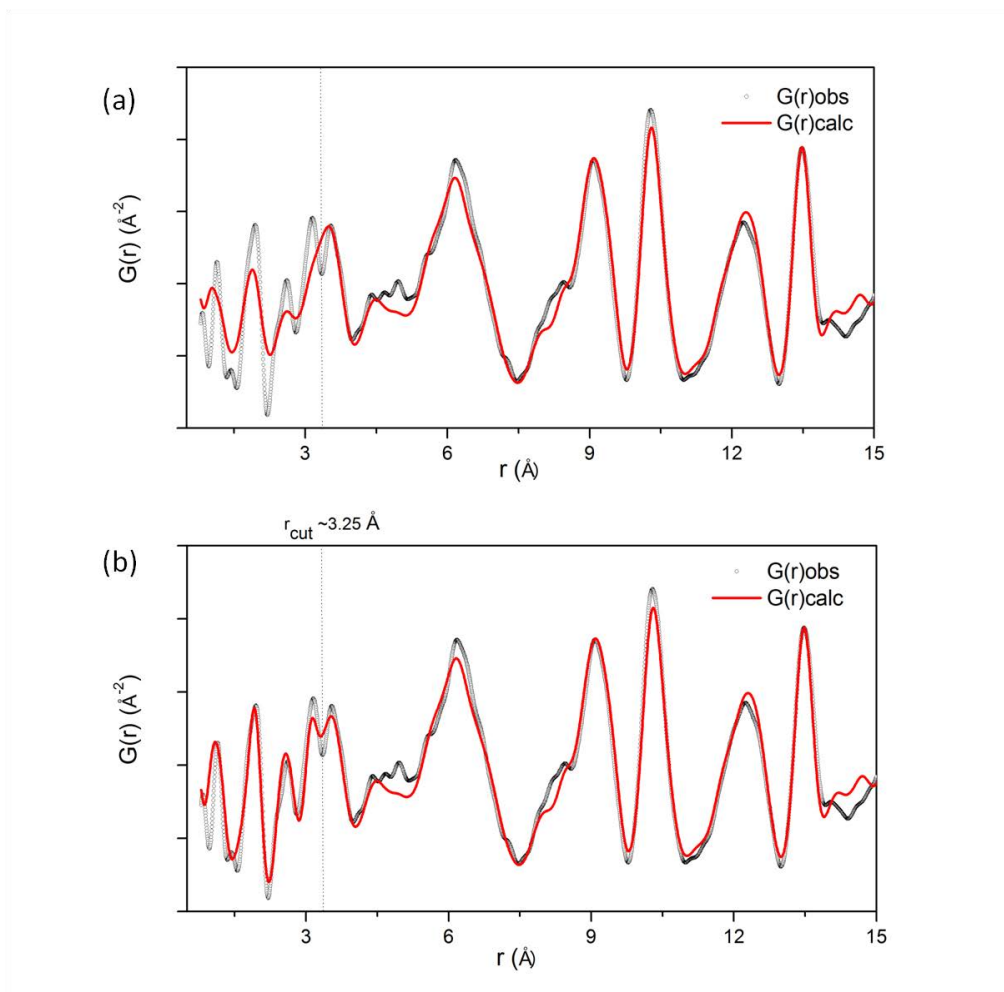
Figure 4.9 Experimental PDF of SNP and calculations from a structural model. (a) No parameter for peak sharpening is used, (b) sharpened PDF defining $r_{cut}$=3.25 Å.

After application of the r-cut correction we performed the PDF refinement in three steps and the final fit result is shown in Fig. 4.10. The initial model is the one that was measured from single crystal data at 297 K. The refinement was carried out from 0.5 Å up to 30 Å. Using the atomic positions fixed to the average structure known from the single crystal study and refining only a scale factor leads already to a reasonable fit result ($R_{WP}$ = 22.44 %). In a second step the parameter $Q_{damp}$, is introduced and fixed to the value obtained from the Si calibration measurement, this takes into account peak broadening due to the instrument configuration. Furthermore the two parameters $Q_{broad}$, describing instrumental peak broadening and broadening due to thermal motion, and $S_{rat}$ describing the effects of correlated motions on peak broading are refined. This fit results in an improved $R_{WP}$ of 19.72%. Finally the lattice parameters are refined resulting in the parameters shown in Table 4.2. This step leads only to a small reduction of the $R_{WP}$ to 19.24% yielding lattice parameters in good agreement with single crystal refinement. If

we further release atom positions and thermal parameters, the $R_{WP}$ improves to 18.28%. However, in this case the atomic positions undergo important change (up to 0.2 Å) compared to the known crystal structure, and the thermal parameters increase for the terminal atoms of the ligands by about a factor of 2. We consider this refinement result as physically not meaningful. In effect, it is most probably due to the fact that the instrumental peak broadening in the PDF is not completely described using the three parameters $Q_{damp}$, $Q_{broad}$, and $S_{rat}$. Thus the remaining broadening effects are accounted by increased thermal parameters and movements in the positional coordinates. This represents thus a limitation of our PDF based analysis of the detailed structure, on the other hand yields information on the precision of our PDF analysis.
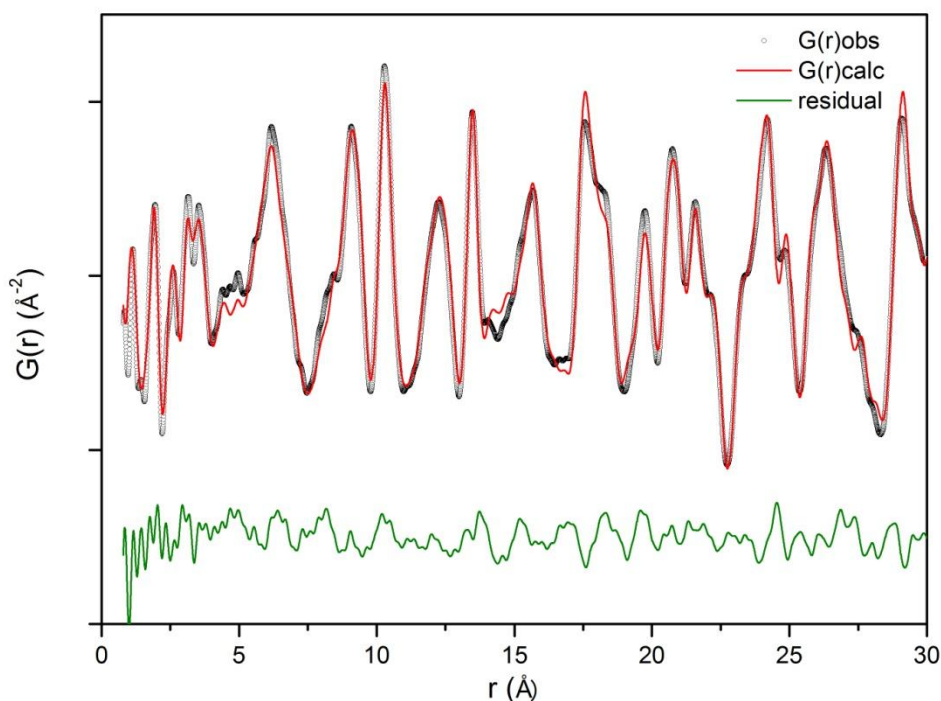


Figure 4.10 Refinement of the PDF for crystalline SNP from 0.5 Å up to 30 Å (agreement factor $R_{WP}$ = 19.24 % for synchrotron data collected at SLS, PSI).

The same refinement procedure has been applied to the laboratory data by using the same $r_{cut}$ value ($r_{cut}$ = 3.25 Å). The result is shown in Fig. 4.11. The experimental PDF is well described by the structural model of SNP. Compared to the synchrotron data we see that the low-r range clearly exhibits larger residuals, which is expected due to the smaller $Q_{max}$. The agreement factor $R_{WP}$ = 29.37 % was obtained by fitting with the instrumental parameters ($Q_{damp}$ and $Q_{broad}$), and improves to $R_{WP}$ = 26.16 % after refining with lattice

parameters. We note that the lattice parameter change with respect to the single crystal measurement.
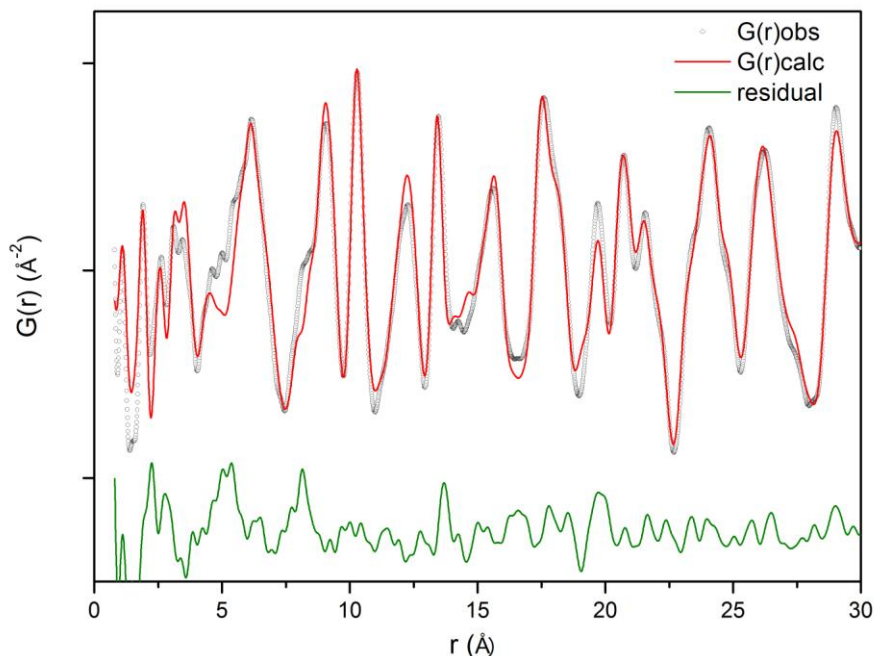


Figure 4.11 Refinement of the PDF for crystalline SNP from 0.5 Å up to 30 Å (agreement factor $R_{WP} = 26.16$ % for laboratory data).

It is worth nothing that the agreement factor $R_{wp}$ used in PDF refinements appears higher when compared to the corresponding $R_{wp}$ factor used in single crystal refinements. This does not indicate an inferior quality of the PDF fit since it yields structural parameters that agree with those obtained by the single crystal refinement. Rather, it reflects the fact that the experimental quantity being fit in real and reciprocal space is not the same.

In summary, the presented results show that from the PDF analysis a good structural description of SNP can be obtained from synchrotron measurements. Using a laboratory X-ray source yields PDF results of similar quality in the range 10-30 Å and a slightly lower precision in the range below 10 Å, provided the necessary care for calibration of the instrument and corrections has been taken. This is crucial to obtain good results in the distances inferior to ~5 Å, which are of interest in our further studies.

**Table 4.2**. Selected parameters for refinement of SNP single crystal model.

| Parameter | Single crystal data | Synchrotron data | Lab data |
|---|---|---|---|
| $Q_{damp}$ ($\text{Å}^{-1}$) | | 0.0071 | 0.0165 |
| $Q_{broad}$ ($\text{Å}^{-1}$) | | 0.0022 | 0.0343 |
| $S_{rat}$ ($r_{cut}$ =3.25 Å) | | 0.7125 | 0.7671 |
| $R_{wp}$ (%) | | 19.72 | 29.37 |
| a (Å) | 6.2051(4) | 6.205 | 6.168 |
| b (Å) | 11.9098(6) | 11.909 | 11.870 |
| c (Å) | 15.5605(9) | 15.582 | 15.545 |
| V ($\text{Å}^3$) | 1149.94(1) | 1151.7 | 1138.3 |
| $R_{wp}$ (%) | | 19.24 | 26.16 |

### 4.4.2    Structure of amorphous $SiO_2$ matrix

For the structural study of the hybrid materials it was first necessary to establish a good model for the amorphous silica matrix. Therefore the amorphous $SiO_2$ monolith was measured on both experimental setups as described above for bulk SNP. Fig. 4.12 illustrates the obtained results. The two data sets yield similar results even though the $Q_{max}$ values are quite different, i.e., $Q_{max}$ = 25 $\text{Å}^{-1}$ for the synchrotron data (left) and $Q_{max}$ = 16.7 $\text{Å}^{-1}$ for the conventional laboratory source (right).

The X-ray diffraction data of the $SiO_2$ monoliths are shown in Fig. 4.12(a,b). Both data sets show the typical silica glass pattern first measured by Mozzi and Warren [29], exhibiting the characteristic broad first sharp diffraction peak (FSDP) at Q~1.64 $\text{Å}^{-1}$, which is associated with the intermediate range ordering. It refers to the ordering of the nearest neighbor in a tetrahedral environment, which occurs with a periodicity of $2\pi/Q$ ~ 3.8 Å. The similar features at higher Q range are more clearly visible in total structure function S(Q) shown in Fig. 4.12(c,d).
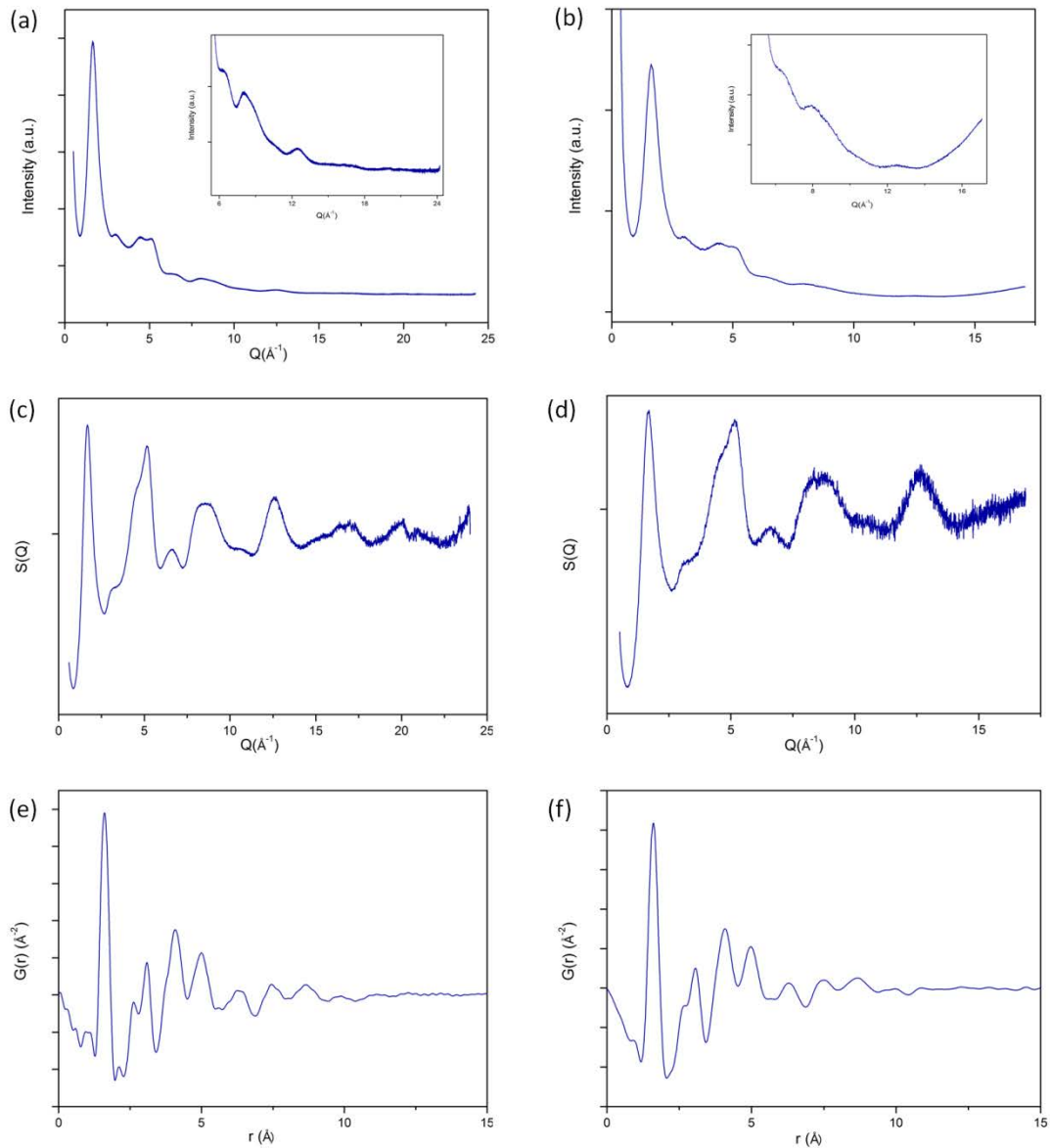
Figure 4.12 Diagrams compare data collected with synchrotron source (left) and laboratory Mo Kα radiation (right) for a monolithic $SiO_2$ rod. From top to the bottom illustrates the routine data extraction steps from raw intensity I(Q) to normalized total structure function S(Q), and G(r), respectively. The high-Q region is zoomed on a small window to highlight the presence of diffuse scattering.

The corresponding atomic PDFs in real space, G(r), are shown in Fig. 4.12(e,f). The expected pair distances for a $SiO_2$ xerogel have been identified and are in agreement with published data of (see e.g. Benmore [30]). The first peak at 1.60 Å in the PDF refers to the Si-O bond length in the silica network. The second G(r) peak at 2.64 Å originates from O-O distances and confirms that the average O-Si-O bond angle is tetrahedral. The third peak in G(r) at 3.08 Å corresponds to Si-Si distances in the configuration of

corner-shearing $SiO_4$ tetrahedral units. This mutual arrangement of the $SiO_4$ tetrahedra can be further described by the $4^{th}$ and $5^{th}$ peaks, respectively, at 4.08 Å and 4.99 Å, corresponding to two Si-O and O-O distances between two adjacent $SiO_4$ units and depending on the two torsion angles describing the rotation of the $SiO_4$ units about the two joined Si-O bonds. The assignment of peaks at higher r values is difficult due to peak overlap.

### 4.4.2.1    Refinement of amorphous $SiO_2$

X-ray diffraction studies have long been used to obtain information on the short and intermediate range structure of liquid and glasses, where the long range order structure is broken. In the amorphous state ordering only persists on the length scale of a few polyhedral units. Amorphous silica is considered as a continuous random network of corner-linked $SiO_4$ tetrahedra as proposed by Zachariasen [31]. (Fig 4.13 and Fig. 4.14)
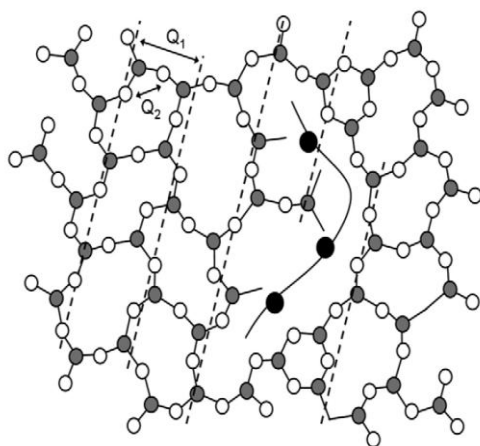


Figure 4.13 Zachariasen 2D network model of a glass in which the structure is random within the steric packing constraints of local units.
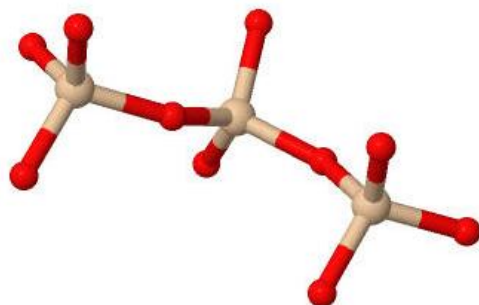


Figure 4.14 Fragments of $SiO_4$ tetrahedral units in an amorphous silica structure. Oxygen atoms are colored red and Silicon atoms are lightly grey.

Structure refinement was then used to build a three dimensional structural model of the $SiO_2$ that is consistent with the experimental data, using the EPSR code [32]. The procedure begins with a Monte Carlo simulation of the system based on a combination of Lennard-Jones and Coulomb potentials. The potential between atoms $\alpha$ and $\beta$ is given by,

$$U_{\alpha\beta}(r) = 4\epsilon_{\alpha\beta}\left[(\frac{\sigma_{\alpha\beta}}{r})^{12} - (\frac{\sigma_{\alpha\beta}}{r})^6\right] + \frac{q_\alpha q_\beta}{4\pi\epsilon_0 r} \qquad (4.1)$$

Where Lorentz-Berthelot mixing rules for calculating $\epsilon_{\alpha\beta} = (\epsilon_\alpha \epsilon_\beta)^{1/2}$, $\sigma_{\alpha\beta} = 0.5(\sigma_\alpha + \sigma_\beta)$, between different types of atom are used.

The simulation was performed in a cubic box of side length 35.2762 Å under periodic boundary conditions. The simulation box contained 1000 silicon atoms and 2000 oxygen atoms at a corresponding local density of 0.0683 atoms $\mathring{A}^{-3}$. Ionic charges have been used on the silicon (+4e) and oxygen (-2e) atoms to mimic their effects in the formation of the local chemical ordering expected in this binary system. All atoms were given a Lennard-Jones potential well depth with Coulomb repulsive potential of atoms. Table 4.3 lists the main parameters used in the Monte Carlo simulations of these materials. The Reverse Monte Carlo procedure is then allowed to continue under this final potential scheme and ensemble average structural information is accumulated for the judgment of $\chi^2$ (cf. Eq. 3.13). Once generated, these average functions can be interrogated to obtain structural information of interest. Fig. 4.15(a) shows the resulting calculated G(r) in comparison to the experimental one.

Table 4.3. Lennard-Jones and charge parameters used in the simulation of SiO$_2$ xerogel. [33]

| Atoms | $\epsilon_\alpha$ (kJ/mol) | $\sigma_\alpha$ $(r_{\alpha\beta})$, (Å) | q (e) | No. of atoms | Box size (Å) |
|-------|------|------|------|------|------|
| Si | 0.800 | 0.760 | 4.000 | 1000 | 35.2762 |
| O | 0.650 | 3.690 | -2.000 | 2000 | |

For a system containing N atom types, there are N(N+1)/2 partial pair distribution functions $G_{\alpha\beta}(r)$. If we take SiO$_2$ xerogel as an example, N=2 and there are three partial distribution function, namely $G_{SiSi}(r)$, $G_{SiO}(r)$ and $G_{OO}(r)$. For SiO$_2$ we have,

$$G_{SiO2}(r) = \frac{c_{Si}^2 f_{Si}^2(Q)G_{SiSi}(r) + 2c_{Si}c_O f_{Si}(Q)f_O(Q)G_{SiO}(r) + c_O^2 f_O^2(Q)G_{OO}(r)}{c_{Si}^2 f_{Si}^2(Q) + 2c_{Si}c_O f_{Si}(Q)f_O(Q) + c_O^2 f_O^2(Q)} \quad (4.2)$$

Given that the atomic concentrations of Si and O are $c_{Si}=1/3$ and $c_O=2/3$ respectively, and that the number of electrons are $f_{Si}=14$ and $f_O=8$ (at $Q=0$ Å$^{-1}$). Eq 4.2 reduces to,

$$G_{SiO2}(r) = 0.218 * G_{SiSi}(r) + 0.498 * G_{SiO}(r) + 0.284 * G_{OO}(r) \quad (4.3)$$

Fig. 4.15(b) shows the three weighted partial PDFs calculated from the total PDF. The good reproduction of these independent partial PDFs suggests that the X-ray diffraction generated model is reasonable.
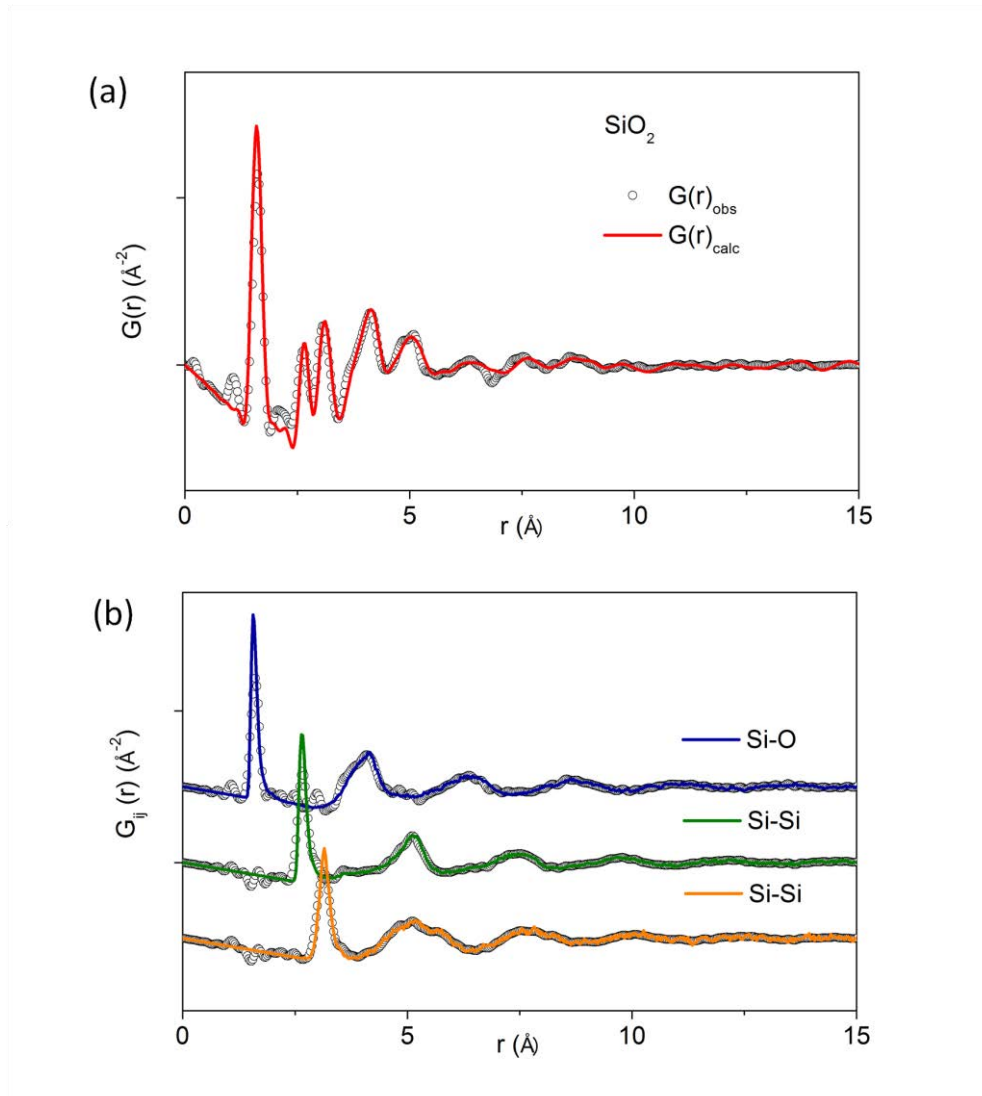


Figure 4.15 (a) Refinement of total pair distribution function G(r), and (b) the three corresponding contributions from partial $G_{\alpha\beta}(r)$, namely Si-O, O-O, and Si-Si for SiO$_2$.

To better understand the local geometry of the $SiO_4$ units within the structure, the coordination numbers N(r) calculated from each partial PDF and the angular distributions are illustrated in Fig. 4.16 and Fig. 4.17, respectively. These indicate that each silicon atom is directly coordinated to 3.9 oxygen atoms with dominant 109° and 140° O–Si–O and Si–O–Si bond angles, respectively, confirming the basic tetrahedral structure of amorphous silica.
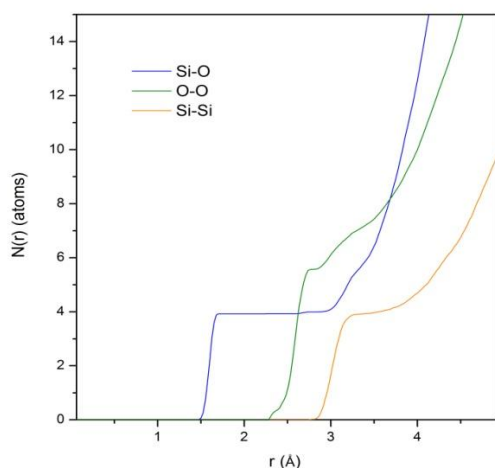


Figure 4.16 Coordination numbers $N_{Si}(r)$, $N_{SiSi}(r)$, and $N_{OO}(r)$.
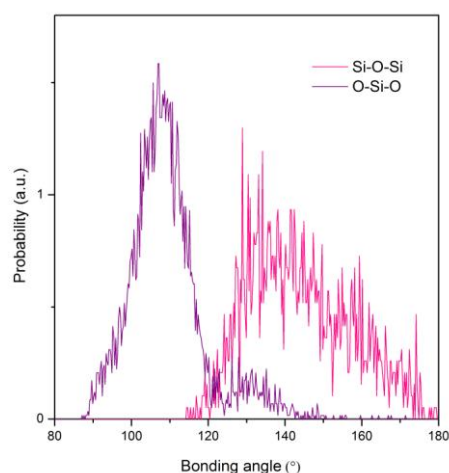
Figure 4.17 Bonding angles distribution of Si-O-Si and O-Si-O.

Fig 4.18 shows the picture of the RMC generated structure $SiO_2$ model obtained from experimental PDFs, it consists of a polyhedral network of $SiO_4$. However, the information of pore size distribution is missing in this model. Such information can be obtained from small angle scattering or adsorption measurements (see Annex 2).
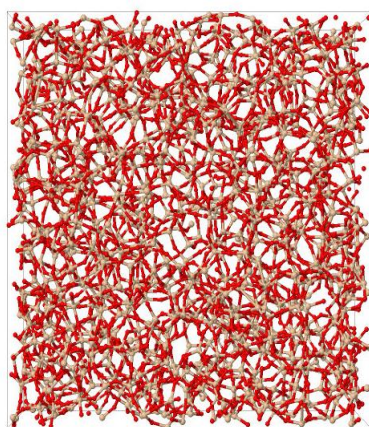


Figure 4.18 A plot showing the central 3000 atoms from the RMC refined model of silica gel. Grey spheres correspond to silicon atoms and red spheres to oxygen atoms.

Summarizing this part, a valid model for the amorphous silica host can be obtained from RMC modeling of the experimental PDF. This validation is important for the calculation of the differential PDF as used in the next section describing the result of the matrices loaded with SNP complexes.

### 4.4.3    Fingerprints of SNP@1 nm SiO$_2$

The X-ray diffraction data of the loaded and unloaded monoliths are shown in Fig.4.19(a). Both data sets confirm the amorphous nature of the silica gel, exhibiting the characteristic broad principal peak at Q~1.64 Å$^{-1}$ [34]. We observe that the main peak has a lower intensity and is slightly broadened in the loaded monolith. This feature has been observed in previous work [12] and indicates the change of the scattering contrast between the empty and filled monoliths. The corresponding atomic PDFs in real space, G(r), are shown in Fig. 4.19(b). Small differences in the PDF between loaded and unloaded monoliths can be clearly observed in the differential PDF corresponding to the direct subtraction G(r)$_{loaded}$ − G(r)$_{unloaded}$, and occur mainly at low r values (x3, Fig. 4.19(b)) up to 7 Å.

The study of differential PDFs allows for the extraction of structural information due to atomic correlation involving the guests, both guest-guest and guest-framework, as well as guest-induced framework perturbations [35]. In the present case the significant structural changes due to the insertion of the SNP complexes are limited to the local scale up to distances of 10 Å indicating well isolated molecules inside the matrix pores.

Fig. 4.20 shows the comparison of the experimental differential PDF obtained by the subtraction G(r)$_{loaded}$ − G(r)$_{unloaded}$ and the G(r) obtained from crystalline SNP (measured under the same experimental conditions). We note that the positions of the peaks below 5 Å are different in the two spectra. They are slightly shifted to each other which is a clear hint for a structural relaxation of the single molecule embedded in nano-pores. However, it can be seen that the main bond lengths of SNP encapsulated in the SiO$_2$ gel correspond to the intramolecular pair correlations found in crystalline samples in the range 1-5 Å, with distances of 1.16 Å (C-N), 1.93 Å (Fe-C), 3.09 Å (Fe-N) and some weaker intra-molecular correlations (C-C, N-N between ligands). The most intense peaks in the G(r) involve the pairs including the strongest scatterers (Fe atom) in this complex as well as the most abundant pairs (five C-N ligands). The absence of sharp features in the d-PDF beyond 5 Å is a strong indication for the absence of any regular ordering around the [Fe(CN)$_5$NO]$^{2-}$ molecules and thus confirms our hypothesis that we are dealing with isolated SNP complexes in the porous network. However, the distances due to intramolecular pair correlations in [Fe(CN)$_5$NO]$^{2-}$ do not account for all the features observed in the d-PDF. In order to obtain more detailed information about a

possible structural relaxation of the SNP complex, the position of the counter ions ($Na^+$), and the interactions with the pore walls of the $SiO_2$ monoliths we performed extensive modelling as detailed below.
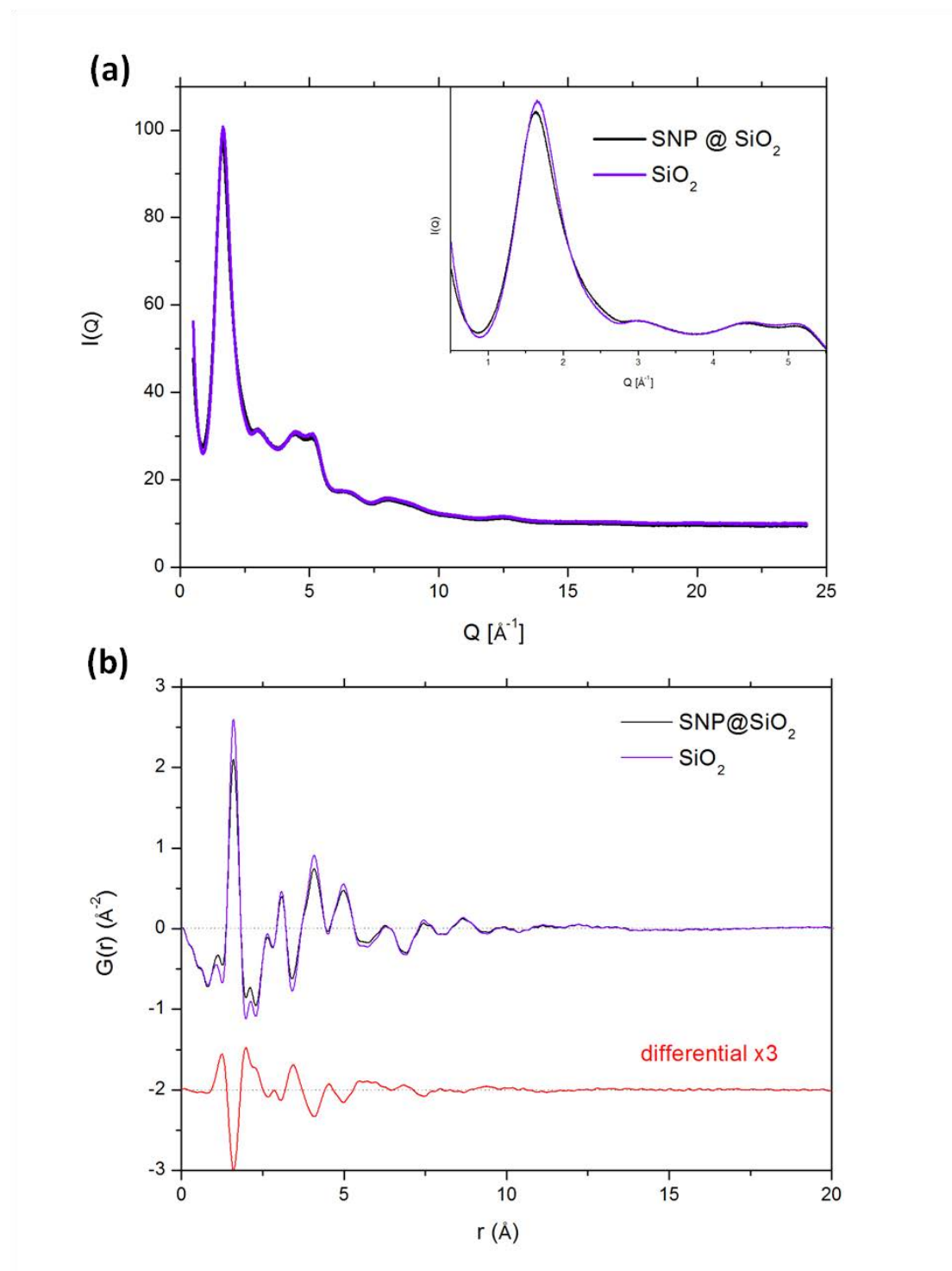


Figure 4.19 (a) Diffraction patterns of unloaded and loaded monoliths. (b) corresponding PDFs, G(r), unloaded (blue) and loaded (black) monoliths, and the subtracted differential-PDF (red) is scaled up for clarity.
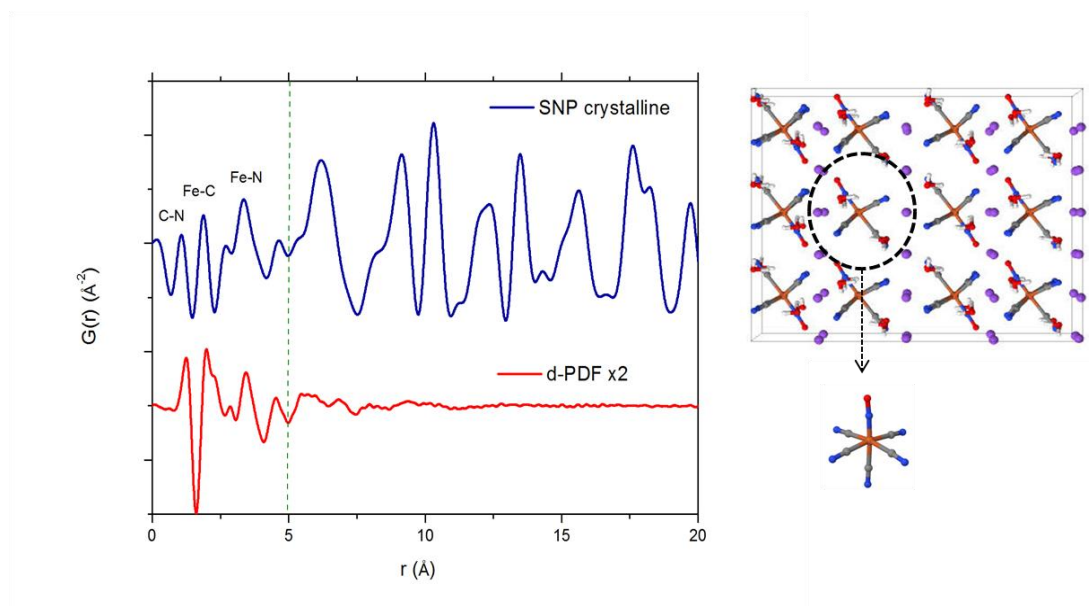
Figure 4.20 Comparison of G(r) of crystalline SNP (crystalline structure illustrated perpendicular to ab plane), and subtracted d-G(r) from embedded SNP which isolates structural information of the molecule in the porous matrix.

The fitting of the differential PDF was accomplished using the "difference modelling" strategy which employs three components: i) a reference PDF of the vacant host, ii) the structure model of the host-guest system, and iii) the experimental differential PDF. An initial structure of the host-guest system was constructed as follows. First, the empty porous $SiO_2$ network was created using the Reverse Monte Carlo (RMC) method which has been described by Keen [36]. The RMC modelling of amorphous $SiO_2$ was developed by using reliable total scattering data to create three dimensional models as described in the previous section. Starting from random configuration of $SiO_2$ groups based on the experimental number density, three geometrical constraints have been applied: Si-O distances ($\sim$1.6 Å) and O-Si-O angle ($\sim$109.5°) which permit to keep the $SiO_4$ tetrahedral configuration, and Si-O-Si angle ($\sim$143.0°) for creating undistorted corner shearing $SiO_4$ tetrahedra to form an amorphous silica network. Then, a credible configuration of the $Na_2[Fe(CN)_5NO]$ complex was taken from single crystal data measured at room temperature. This modelling was performed using the DISCUS program [37].

Fig. 4.21(a) illustrates clearly that pair correlations are mainly dominated by the $[Fe(CN)_5NO]^{2-}$ anion to $\sim$5 Å; Fig. 4.21 (b$\sim$f) show configurations where two $Na^+$ cations are taken into account around the molecule with a fixed radial distance of 5.55 Å. This allows an improved fit of the d-PDF in the region below 8 Å. Fig. 4.21(d) shows the configuration yielding the best fit including the 5-10 Å region. In this configuration the

76

two $Na^+$ anions are in the equatorial plane of the $[Fe(CN)_5NO]^{2-}$ anions, in prolongation of the Fe-C-N direction. Additionally, we have arranged the $Na^+$ positions as given in the single crystal (one equatorial and one near the axial CN ligand) but the $R_{wp}$-value increases (see Fig 4.22). The same increase of $R_{wp}$ was found by varying the radial distance of the $Na^+$ counter ions between 4 - 7 Å. Consequently we can determine by this procedure the position of the two $Na^+$ ions with respect to the $[Fe(CN)_5NO]^{2-}$ anion with reasonable reliability.

On the other hand there are still some features in the differential PDF that are not completely explained by our model, especially the intensity of the peak at 1.3 Å as well as the shoulder at about 2.3 Å. It should be noted here that the low r region (~1.2 Å) of the differential PDF is very critical and may contain some errors due to the limitation of the experimental setup and the processing of the data [38]. Therefore we should be careful in interpreting the intensity of the peak at 1.3 Å. Nevertheless, we tested two hypotheses in order to account for these features: i) hydration, ii) interaction with pore wall. Concerning i) the impregnation of the monoliths was performed from aqueous solutions and NMR measurements indicate that the SNP complex inside the pore is surrounded by water molecules (see details below). It is also known that porous matrices like $SiO_2$ readily uptake humidity. However, fitting the differential PDF with additional $H_2O$ molecules proved to be a very difficult task. Although improvements could be realized the reliability of such fits was quite limited, as different configurations yielded similar results, sometimes with no significant improvement of R-values. We conclude therefore that the presence of water molecules in the pores surrounding the SNP complexes is highly probable but the structural arrangement cannot be obtained from a PDF measurement at this stage. Concerning ii) host-guest interaction: we note that the shoulder at 2.3 Å could stem from such an interaction. However, also in this case the differential PDF did not allow a clear identification of the host-guest interaction. It could stem from Na⋯H-O or N⋯H-O. We note here that an earlier neutron diffraction study on a similar compound GuNP@SiO2 has shown the possibility of such host-guest interactions (Cervellino et al. [13]).
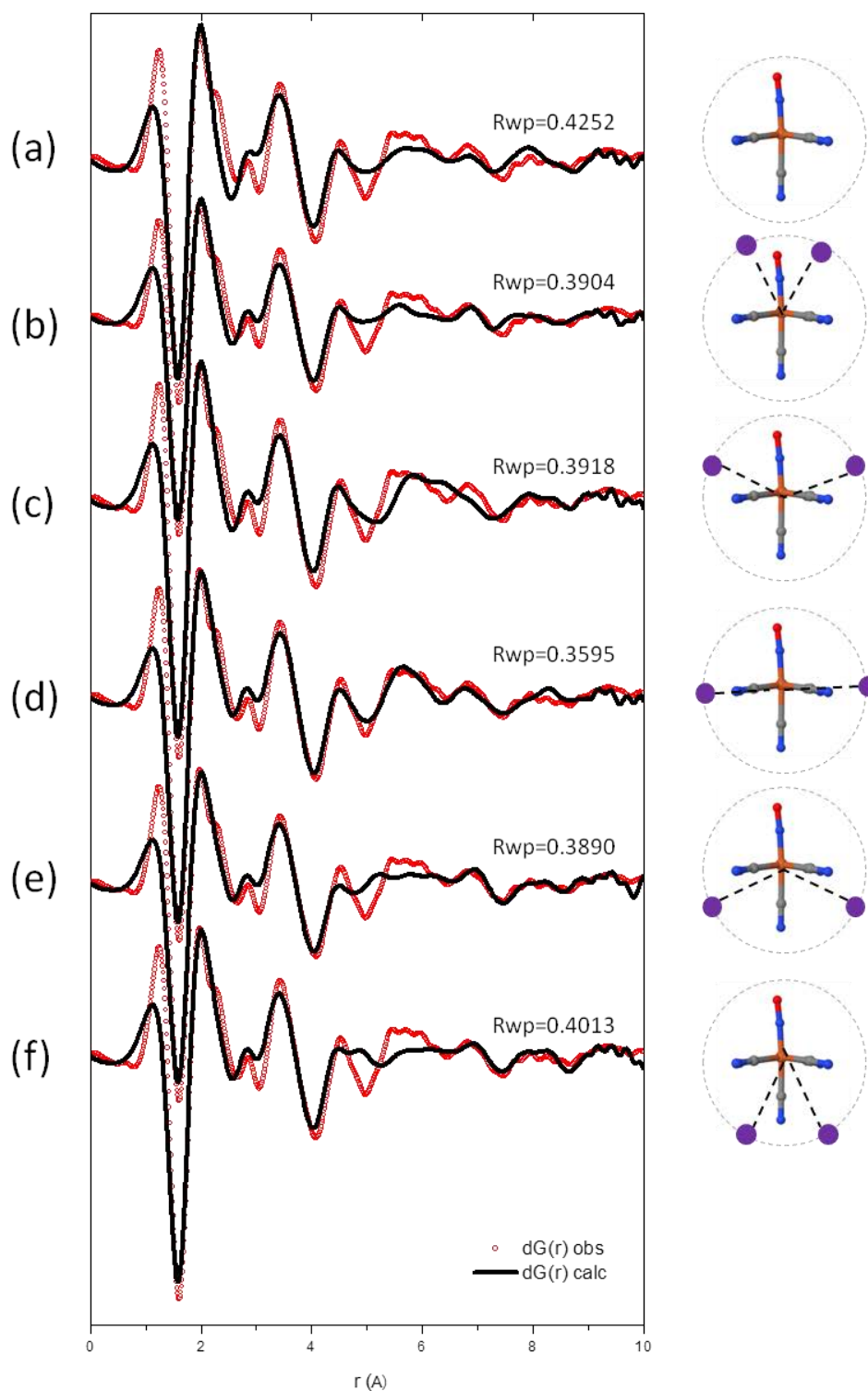
Figure 4.21 d-PDF fits with different configurations of isolated SNP complexes illustrated on the right: (a) one $[Fe(CN)_5NO]^{2-}$ anion within the pores; (b)~(f) considers two $Na^+$ cations placed around $[Fe(CN)_5NO]^{2-}$ to keep electrostatic neutrality. Five configurations are considered for which (d) results in the best fit. In that case the two $Na^+$ cations are placed on the coordination of the cyanide ligands within the equatorial plane of the molecule.
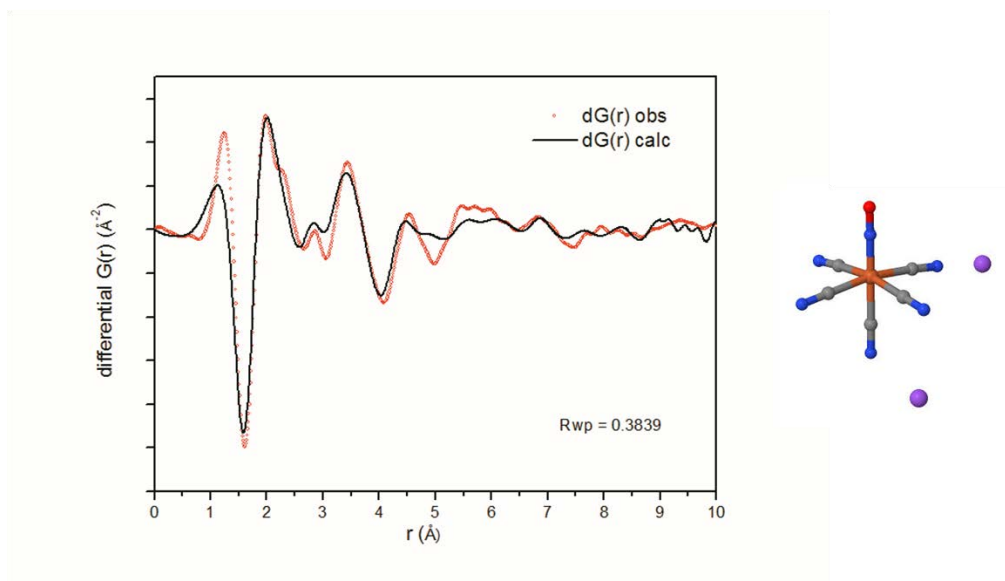
Figure 4.22 Arrangement of $Na^+$ positions are given as in the single crystal (one equatorial and one near the axial CN ligand) but the $R_{wp}$-value increases.

Concluding this first part, total X-ray scattering measurements coupled to analysis of the differential PDF showed that for the silica matrices with 1-3 nm pore sizes isolated SNP complexes are embedded in $SiO_2$ pores. Additionally the structural configuration of cation and anion could be proposed from a difference modelling strategy.

Furthermore, it should be mentioned here that comparable results have been achieved using the data collected on the laboratory setup, even though the attainable Q-range is not as high as with synchrotron radiation. Together with the good results obtained for the amorphous matrix this shows, that for such amorphous molecular compounds the PDF analysis based on laboratory data is feasible and can yield results of similar quality as that obtained using synchrotron data.

## 4.5 The Solid State NMR

Since NMR observables depend on the local environment of the nuclear spins, long range order is not necessary to obtain resolved structural information. This complementary approach is thus well adapted to characterize both the amorphous host and the molecular guest as long as NMR sensitive nuclei are present in both components of the material. Additionally, the anisotropic nuclear interactions typically measured by solid state NMR techniques can also be used to obtain information on molecular dynamics inside the solids.

### 4.5.1    Structure of amorphous $SiO_2$ host

The porous matrix containing the isolated SNP complexes is composed of amorphous $SiO_2$ silica. Both $^{29}Si$ (I = 1/2; 4.7 % natural abundance) and $^{17}O$ (I = 5/2; 0.037% natural abundance) allow NMR studies. However the very low natural abundance and the quadrupole moment of the $^{17}O$ isotope severely reduces its sensitivity and limits the NMR application. We applied $^{29}Si$ MAS NMR to characterize the xerogel matrix. Figure 4.23 presents the $^{29}Si$ MAS NMR spectra of the nanoporous $SiO_2$ xerogel before and after incorporating the SNP molecules. The chemical shifts observed are typical for $Q^n$ $SiO_4$ tetrahedral units; $Q^n$ representing $SiO_4$ tetrahedral of the amorphous network, which form n bonds with neighboring tetrahedral. Both spectra show two major resonances at -101.7ppm and -110.5ppm, corresponding to $Si(OSi)_3(OH)$ ($Q^3$) and $Si(OSi)_4$ ($Q^4$) sites, respectively, and one resonance at -91.8ppm corresponding to $Si(OSi)_2(OH)_2$ ($Q^2$) sites. The absence of $Q^1$ sites and the low ratio of $Q^2$ sites indicate a relatively high degree of condensation of the xerogels. This is especially true since, on the spectra acquired here, this ratio is overestimated because of short experimental repetition times compared to $Q^3$ and $Q^4$ $^{29}Si$ $T_1$ relaxation times.
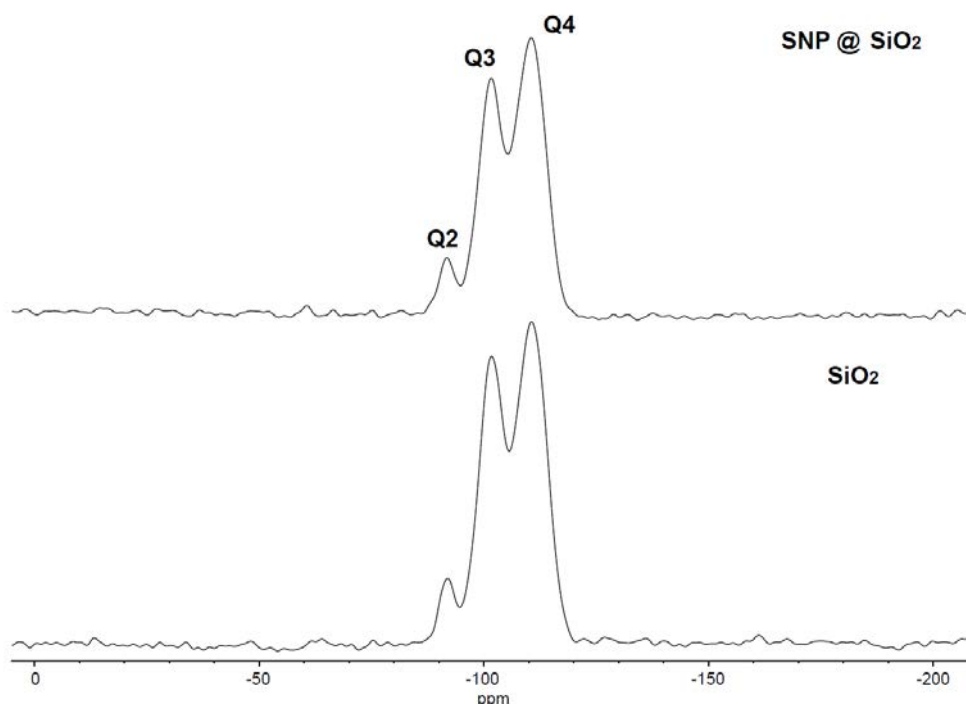


Figure 4.23 $^{29}Si$ MAS NMR spectra ($\nu^{MAS}$ = 12.5 KHz ) of the SNP loaded $SiO_2$ matrix (top) and the empty $SiO_2$ matrix (bottom). No additional sites are observed after loading the matrix with SNP.

A comparison between the spectra of the empty and the SNP loaded matrix shows neither a change of the line widths nor the appearance of additional sites. This indicates that the gel structure is not modified by the embedding procedure of the SNP molecules. This point is very important since it validates the differential PDF (d-PDF) approach described previously. The comparison also doesn't show evidence of strong interactions between the host xerogel and the molecular guest since significant covalent chemisorptions on the silanol groups (by $Na^+$ for example) would generate new chemically shifted $^{29}Si$ sites.

### 4.5.2 Structure and dynamics of the SNP guest

Given the NMR sensitivity of the nuclei present in the SNP salt ($Na_2[Fe(CN)_5NO]$), we applied $^{13}C$ NMR to probe the local environment of the nitroprusside and $^{23}Na$ NMR to probe the environment of the counterions.

The $^{23}Na$ MAS NMR spectrum of the bulk crystal (Fig. 4.24) displays two inequivalent sites with same multiplicity but significantly different quadrupolar coupling constants. The first site $Na_1$ has a quadrupolar constant $C_{Q1} = 1369$ kHz and an asymmetry of $\eta_1 = 0.92$ while the second site $Na_2$ has a smaller constant $C_{Q2} = 615$ kHz and $\eta_2 = 0.33$. The isotropic chemical shifts ($\delta_1^{iso} = -5.74$ ppm and $\delta_2^{iso} = -1.91$ ppm) indicate hexacoordinated sodium atoms and are consistent with the XRD crystal structure, the NMR sites could be assigned by comparison of the Electrical Field Gradient properties with those published from DFT calculations [39].The $^{23}Na$ MAS NMR spectrum of the SNP inside the silica matrix (Fig. 4.24) is very different. This spectrum presents only one $^{23}Na$ site with a chemical shift ($\delta^{iso} = -1.1$ ppm) indicating that the sodium site is coordinated by six water molecules. This means that the crystal structure is not preserved inside the pores of the $SiO_2$ matrix and that the two $^{23}Na$ counterions experience a similar local environment on the ms timescale. Several possibilities can explain the presence of a unique $^{23}Na$ site but consistently with our other measurements we interpret this as motional averaging below the ms timescale due to solvation by surrounding water molecules.

Figure 4.24 $^{23}$Na MAS NMR spectra ($\nu^{MAS}$ = 12.5 KHz ) of the SNP loaded SiO$_2$ matrix (top) and crystalline SNP (bottom). Inside the matrix the quadrupolar interaction is averaged out by rotational diffusion. For the crystalline sample quadrupolar coupling constants and asymmetry parameters could be obtained by fitting the central bands using the Dmfit program [40]. Quadrupolar satellites are marked by asterisks.

The $^{13}$C MAS NMR spectrum of the bulk crystal (Fig. 4.25) displays four resolved sites ($\delta^{iso}$=136.7ppm, 136.2ppm, 135.9ppm, and 135.5ppm) whereas the SNP-silica nanocomposite displays only two ($\delta_{eq}^{iso}$ = 134.7 ppm and $\delta_{ax}^{iso}$ = 133.3 ppm). For the nanocomposite, the isotropic chemical shifts are thus displaced towards the solution state values with a surface ratio of 4:1 typically observed for SNP in solution. Consistently

with the $^{23}$Na results, this means that the crystal structure is not preserved in the nanocomposite. It also indicates that water molecules are present inside the pores and that, for sufficiently high hydration levels, the nitroprussiate is well separated from its sodium counterions. Nevertheless, as will be detailed in the next section, the line width broadening observed for samples stored in relatively dry conditions indicates that the "free" solvation water molecules can quite easily be removed.

In the bulk crystal, both the $^{13}$C and the $^{23}$Na nuclei display anisotropic interactions. Fitting the MAS sideband pattern of the $^{13}$C spectrum informs us about the chemical shift anisotropy. For the crystal we find $\delta^{aniso} = 32$ kHz with a slight asymmetry of $\eta = 0.08$. It's origin is mainly intramolecular and relies on the anisotropic electron distribution of the Fe-C≡N bonding. For the $^{23}$Na spins the dominant interaction is the quadrupolar coupling which can be obtained here by fitting the second order quadrupolar lineshapes of the center bands. These values are $C_{Q1} = 1369$ kHz and $C_{Q2} = 615$ kHz depending on how the nuclear electric quadrupole moment couples to the local electric field gradient. As evidenced on Fig 4.24 and 4.25, both interactions split the MAS NMR signals into spinning sidebands and satellites (respectively) appearing at integer multiples of the sample rotation frequency and spread over a frequency window equivalent to the strength of the interactions. Interestingly these spinning sidebands are no longer present for the nanocomposite powder spectra. This clearly indicates that the embedded SNP performs isotropic motion inside the pores, a motion sufficiently fast to completely average out both types of anisotropic interactions. Hence the characteristic frequency of the motion is higher than those interactions and implies a sub-μs isotropic reorientation. Still, whether or not the nitroprussiate and the counterions move in a correlated manner cannot be inferred from these experiments alone.

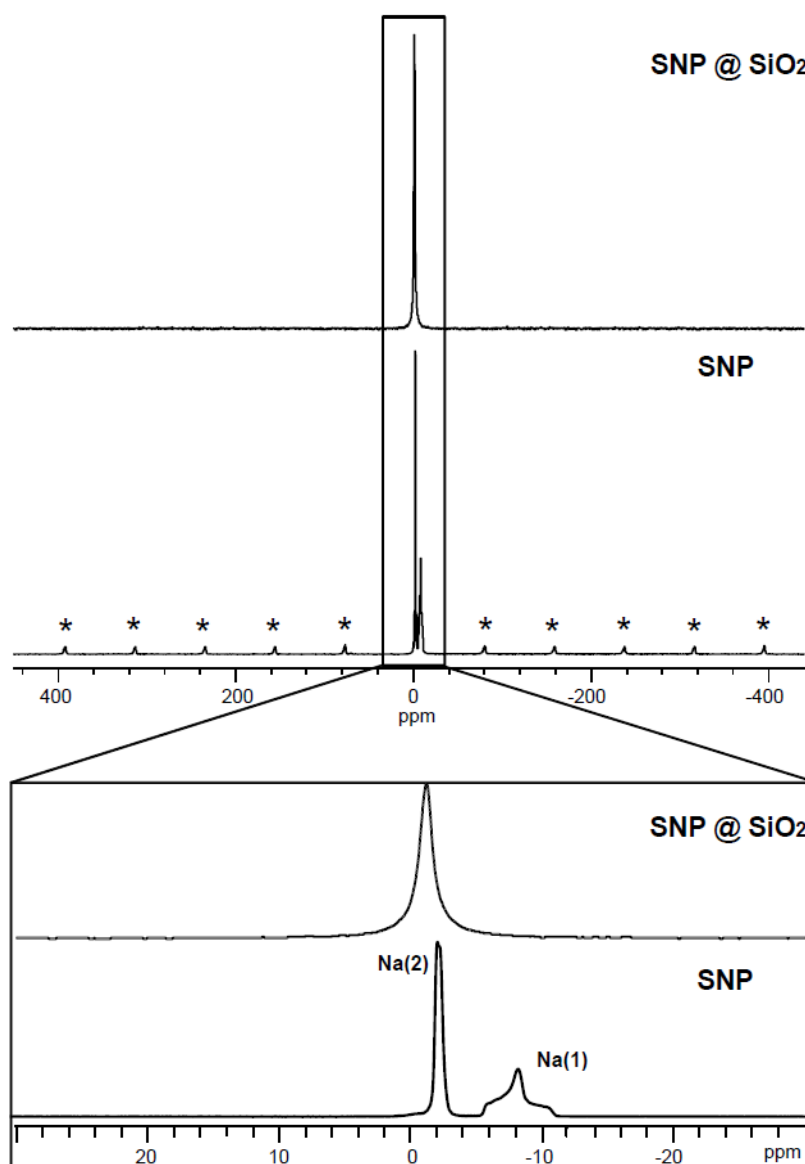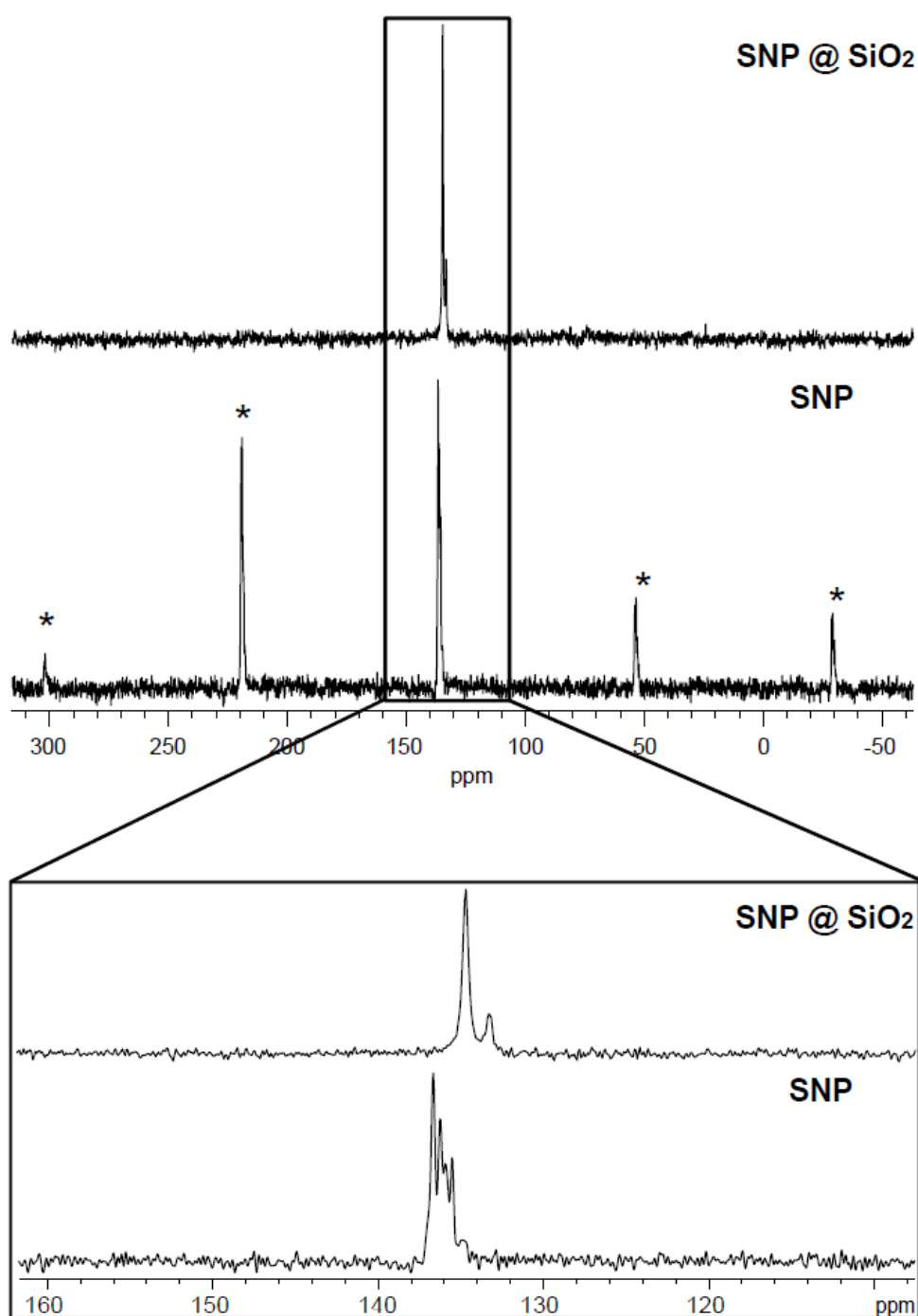Figure 4.25 $^{13}$C MAS NMR spectra ($\nu^{MAS} = 12.5$ KHz ) of the SNP loaded SiO$_2$ matrix (top) and crystalline SNP (bottom). Inside the matrix the CSA interaction is averaged out by rotational diffusion. For the crystalline sample CSA and asymmetry parameters could be obtained by fitting the spinning sideband pattern using the Dmfit program [40]. Spinning sidebands are marked by asterisks.

### 4.5.3   Hydration of the nanocomposite SNP@SiO$_2$ xerogel

To study how hydration influences the structure and dynamics of the SNP complex inside the SiO$_2$ matrix, the NMR samples have been stored in three different environments of 6%, 29% and 85% relative humidity. $^1$H, $^{13}$C, $^{23}$Na MAS NMR spectra (Fig. 4.26) were subsequently acquired to observe how the different components of the material were influenced by hydration.
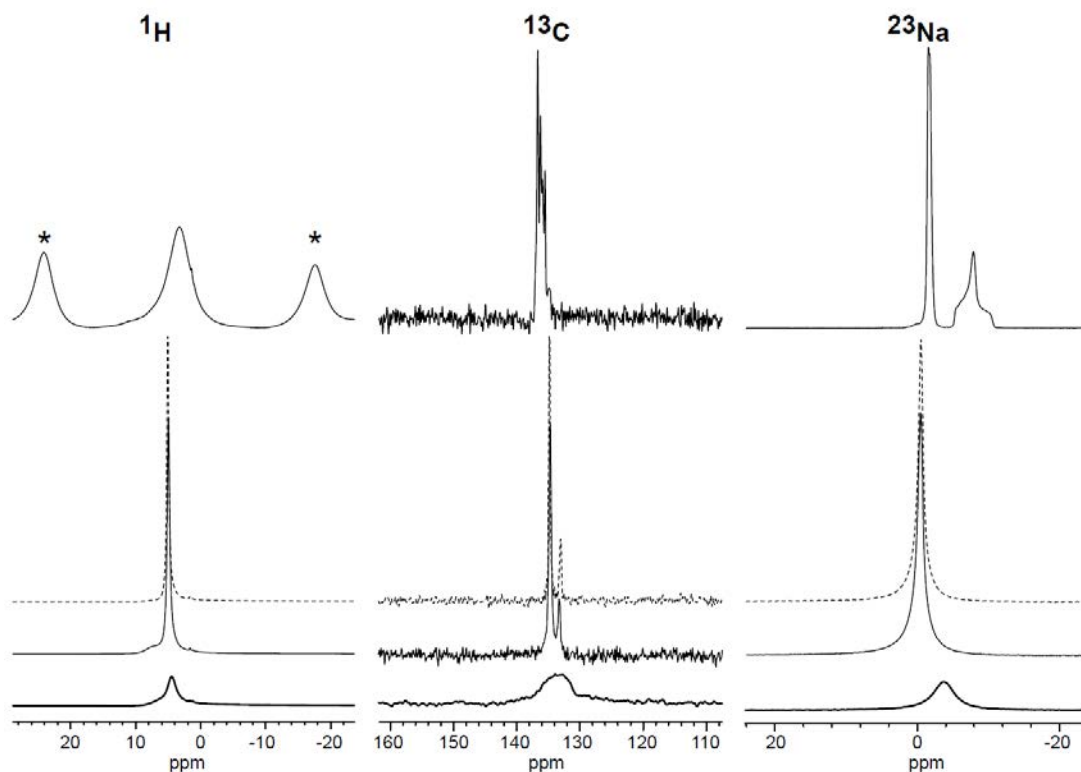


Figure 4.26 Effect of hydration on the $^1$H, $^{13}$C and $^{23}$Na spectra (respectively from left to right) of the SNP@SiO$_2$ hybrid xerogel. For reference, the upper spectra are acquired on crystalline SNP. The spectra below correspond to SNP loaded xerogels that have been stored overnight at 84%, 29% and 6% relative humidity (broken, fine and bold line respectively). MAS spinning sidebands are marked with asterisks ($v^{MAS}$ = 12.5 KHz ).

The signals observed on the $^1$H spectra originate principally from water molecules that can exchange protons with silanols groups. The series of $^1$H spectra shows how the pore water content diminishes with the relative humidity levels. The spectra are composed of a dominating signal between 4.5ppm and 4ppm that is reduced, broadened and shifted upfield when the relative humidity is lowered. This signal reflects relatively mobile water molecules present inside the pores of the matrix. When the humidity is decreased, the "free" water is removed and only the first hydration layers remain.

Therefore the remaining signal is shifted and broadened because of the stronger adsorption of the protons and their exchange between liquid water, physisorbed water and silanols [42].

The $^{13}C$ and $^{23}Na$ spectra (Fig. 4.24) focus on the SNP guest. Both series behave comparably and show that all anisotropic interactions remain motionally averaged even at a low hydration level (no MAS sidebands or satellites even at 6% relative humidity). Additionally, the removal of water molecules does not induce chemical shift changes towards those observed for crystalline SNP. This indicates that even when most of the water inside the nanopore cavity is removed, the SNP maintains its strong dynamic properties and does not take a bulk-like nanocrystalline structure. We also observe an upfield shifting of the $^{23}Na$ signal which is consistent with an elongation of the average coordination distance [43]. Nevertheless, both $^{13}C$ and $^{23}Na$ signals become considerably broadened for samples stored at 6% RH. This broadening cannot be refocused by spin echo type sequences; it is therefore from the homogeneous type which means that it is not due to a distribution of chemical shifts. Since both the nitroprusside and the sodium counterions display sub-$\mu$s dynamics, we speculate that the broadening originates from their mutual interaction rather than from physisorption to the pore surface.

## 4.6 Multiscale structural analysis of SNP@SiO2 (1nm, 5nm, 11nm): the structural aspect-pore size and organisation relationship

In the previous sections, we have discussed the structure of isolated $Na_2[Fe(CN)_5NO]$ complexes incorporated in silica monoliths with pore sizes in the range of 1~3 nm using the PDF approach. In the following we will study the inclusion of SNP into $SiO_2$ with larger pore dimensions of 5 nm and 11 nm. In this case the post-doping of the SNP is expected to generate nanoparticles within the matrix where the particle size is limited by the pore size.

### 4.6.1 Problems of SNP crystallized on monolith surface

As a first observation and in contrast to the samples with smaller pore sizes, we observe sharp Bragg peaks in the diffraction pattern in the samples of pore sizes 5 and 11 nm. These sharp Bragg peaks are an indication that SNP crystallites of dimensions that exceed the dimensions of the pores are formed. This suggests that at least a fraction of SNP has crystalllized outside the pores, yielding an inhomogeneous composite material. (Fig 4.27)

A more detailed analysis of the total structure functions (Fig 4.28) clearly demonstrates that 2 different cluster sizes of SNP have formed: large crystals as indicated

by the sharp Bragg peaks and isolated complexes as indicated by the broader oscillations. However, the SNP@SiO$_2$ of 5 nm pore sizes exhibits stronger broad oscillations of S(Q), indicating a higher number of isolated [Fe(CN)$_5$NO]$^{2-}$ complexes within the pores (Fig 4.29). By comparing the intensities of peaks corresponding to isolated molecules (low-r region < 8 Å) and nanoparticles (medium to long range region).
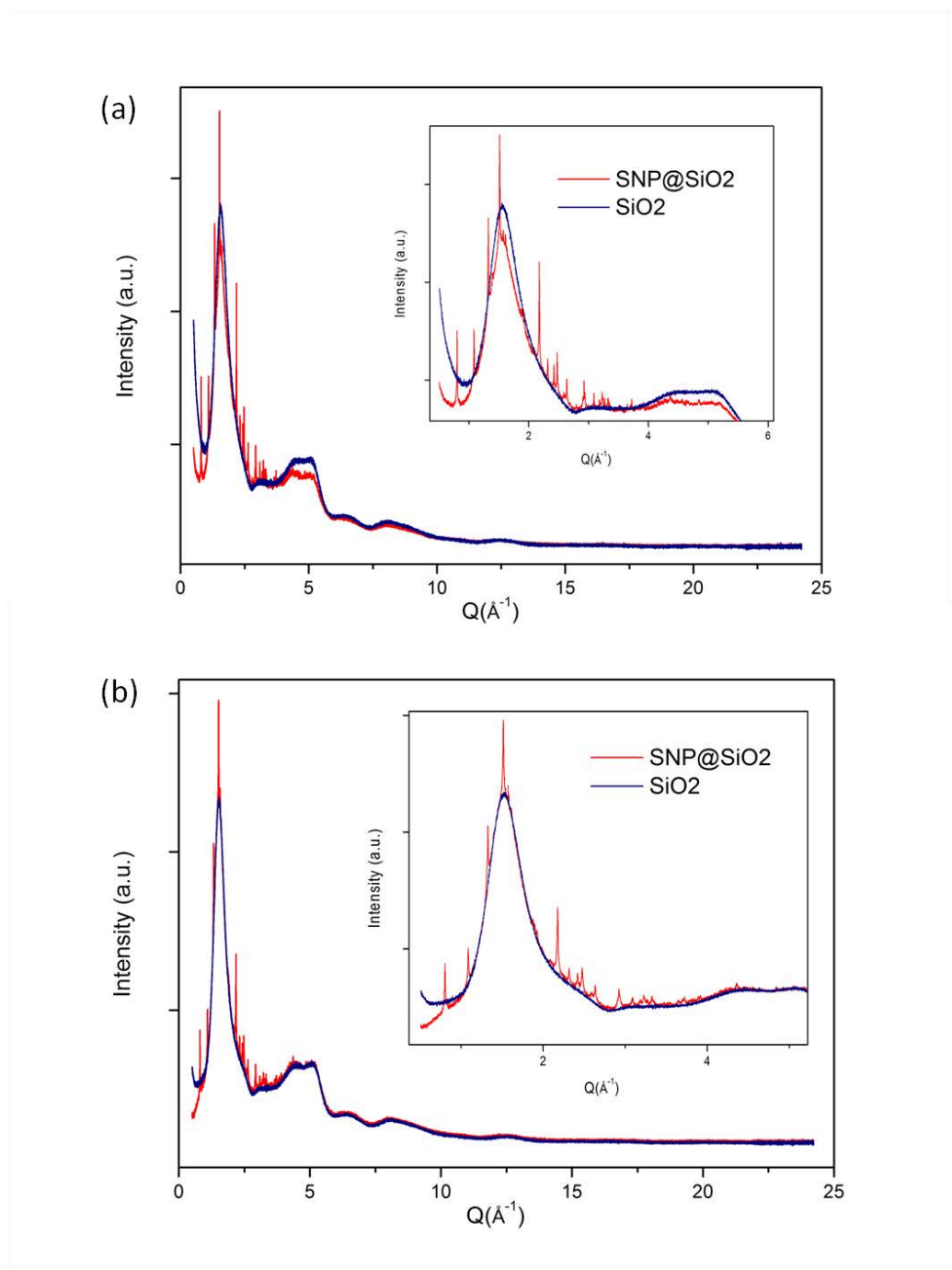


Figure 4.27 diffraction pattern of SNP@SiO$_2$ doping in pore size of (a) 5 nm and (b) 11 nm.
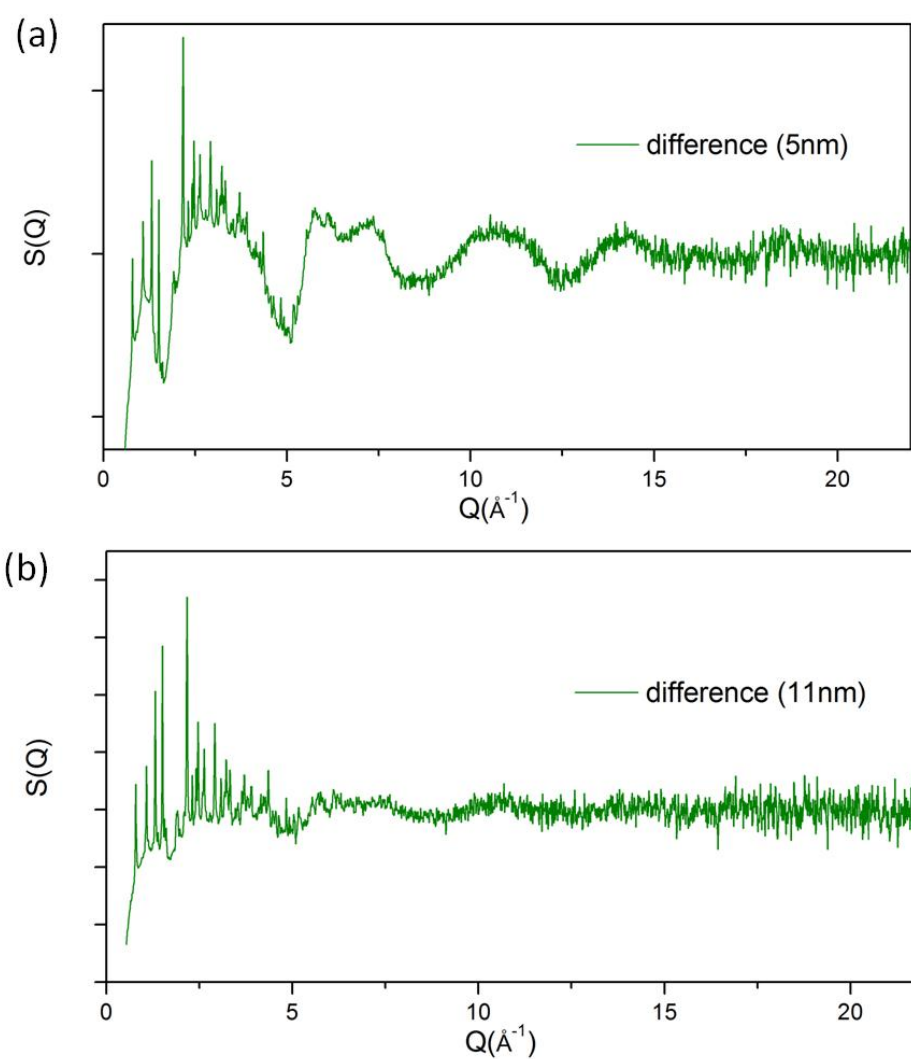
Figure 4.28 Total structure function of difference (loaded - unloaded) subtracted from Fig 4.27 SNP@SiO$_2$ doping in pore size of (a) 5 nm and (b) 11 nm.
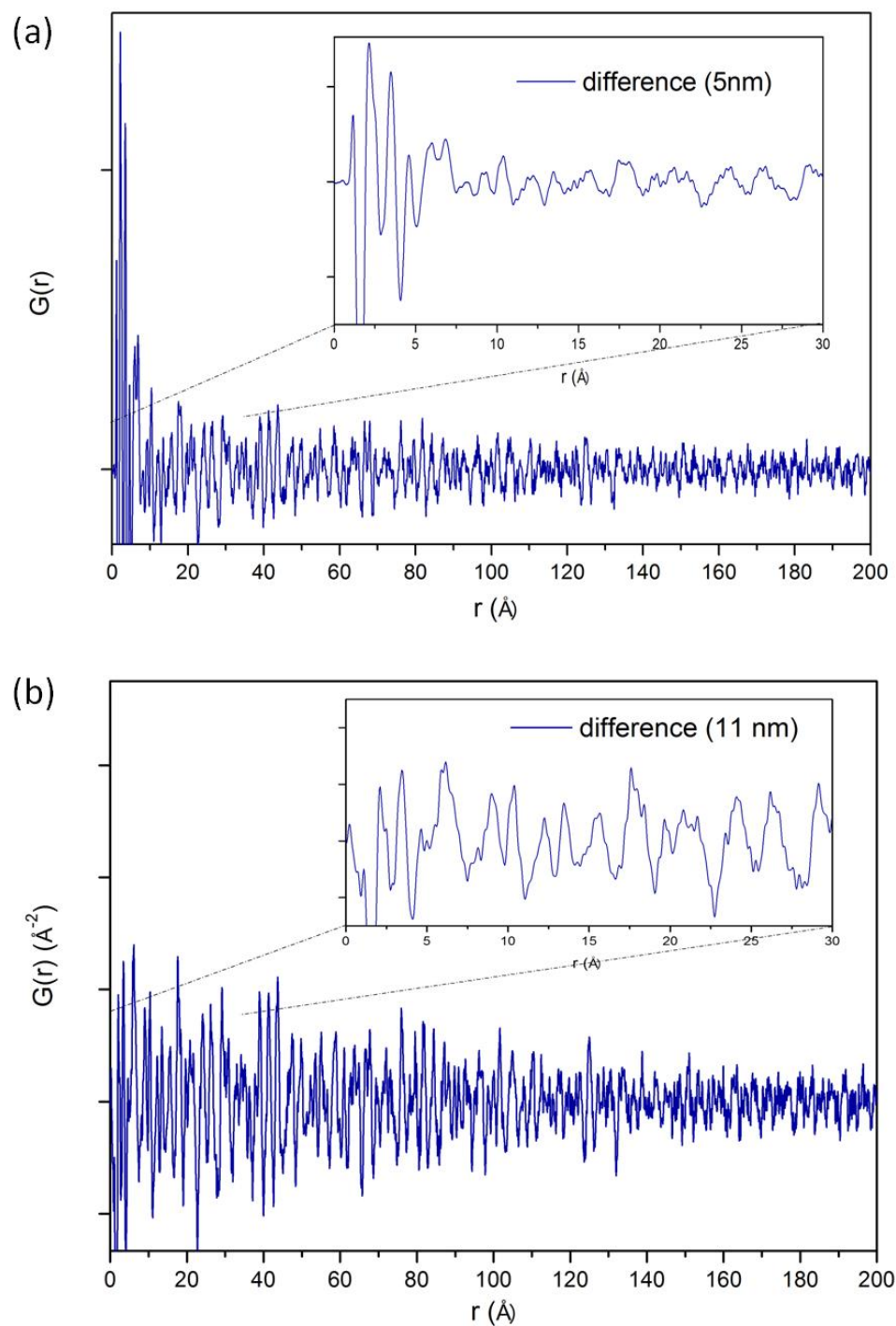
Figure 4.29 Difference PDFs (loaded - unloaded) are Fourier transformed from Fig 4.28. SNP@SiO$_2$ doping in pore size of (a) 5 nm and (b) 11 nm.

In order to avoid the extra signal that most probably stems from larger crystallites that have formed on the monolith surface, we slightly polished the surface of monolith and then measured again the SNP@SiO$_2$ sample with 5 nm pore sizes.

### 4.6.2    SNP@SiO$_2$ (5nm)

The PDF measurements of the polished samples was performed at ESRF (60keV, λ=0.22299 Å, ID11) using a Perkin Elmer flat panel detector to record diffraction pattern to high momentum transfer (Q~24 Å$^{-1}$). Raw images were processed using Fit-2D and PDFs were extracted by GudrunX as described previously.

The diffraction pattern of the empty monolith exhibits the typical amorphous silica features (Fig 4.30). Inspection of the diffraction pattern of the loaded monolith indicates the amorphous SiO$_2$ phase, as well as additional rather broad peaks due to a nanocrystalline SNP phase (Fig 4.27). The rather large width of the diffraction peaks indicates clearly the formation of SNP nanoparticles. The evaluation of the broadening according to Scherrer's formula yields a particle size of ca. 7.5 nm. Note that this particle size corresponds to an average particle size.
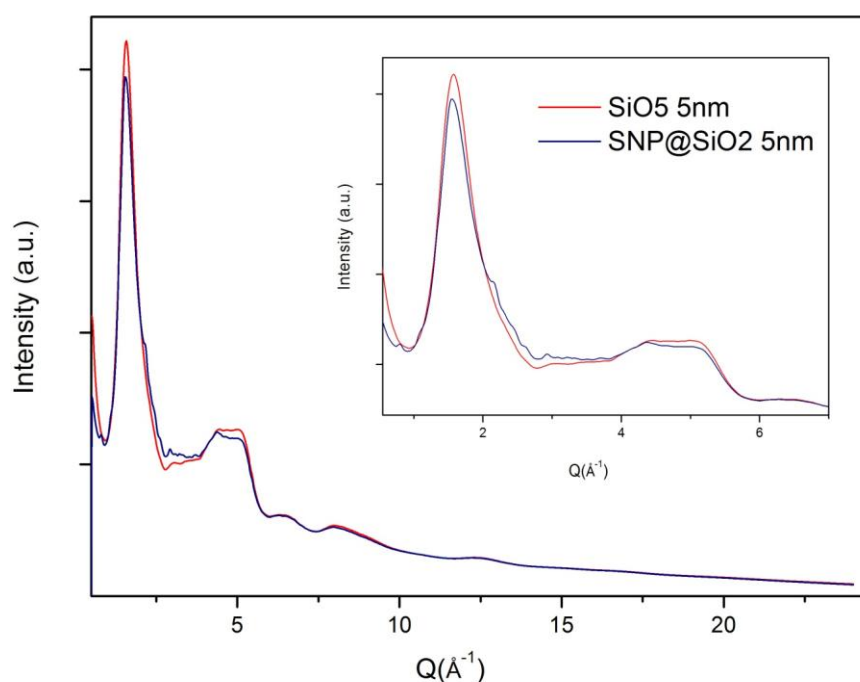


Figure 4.30 X-ray diffraction pattern of SNP@SiO$_2$ with pores size of 5 nm. The porous empty SiO$_2$ indicates an amorphous silica phase, and the loaded samples present several weak peaks corresponding to the confined SNP nanoparticles.

The difference intensity was then calculated after absorption correction of both samples (Fig 4.31(a)). In this manner the information of the embedded nanoparticles can be extracted. While the presence of SNP peaks indicative of nanoparticles is clearly visible in the difference pattern, the total scattering function S(Q) (Fig 4.31(b)) reveals a further contribution from an incorporated guest. In order to determine the origin of this second contribution we need to analyze in detail the PDF (Fig 4.31(c)). In the case of the PDF of a nanoparticle, the extent of atom-atom distribution is influenced by the particle diameter, beyond which the PDF drops to zero. Effectively G(r) is rather structureless beyond 5 nm, we therefore refer to the confined SNP particles as 5 nm in diameter. On the other hand, two strong and sharp peaks are present in the r-range below 8 Å, which cannot be explained by the 5 nm particles and might be due to the formation of a second phase of SNP confined in the porous environment.

As a first model we compared the PDF calculated from a 5 nm spherical model of SNP to the experimental d-PDF, as shown in Fig 4.32(a). The modelling of the SNP particles was based on the structural model of the bulk material at 297 K, and by applying a spherical shape function up to 50 Å (Fig 4.32(b)). The particle size is a little bit larger than 5 nm as shown in the inset, Thus the final refinement of the SNP particles was then carried out in the medium to long-range from 8 to 70 Å, thereby we avoid the overlapping of peaks with the second phase in the low-r region. The particle size was refined to 6.7 nm in diameter, and lattice parameters were refined to a= 6.23(1) Å, b=11.93(2) Å, and c=15.60(2) Å. This corresponds to about 0.3 % of lattice expansion for the confined SNP nanoparticles compared to the bulk.

The particle sizes estimated from the PDFs (~6.7 nm) or Scherrer equation (~7.5 nm) are systematically larger than those which are obtained from the BET measurement (~5 nm). It could be explained by different shape of embedded particles. The porous environment is not ideally spherical in shape and furthermore connected by tunnels. We could thus expect the formation of, e.g. elliptical particles with one dimension longer than 5 nm, or even interconnected particles via tunnels. We note furthermore that the BET analysis is also based on a spherical pore model and therefore yields limited accuracy. Finally 5 nm corresponds to an average pore size, i.e. larger pores of 6-7 nm are present and might be filled with nanoparticles.

(a)

difference Intensity (a.u.)

I (loaded - unloaded)

Q(Å$^{-1}$)

(b)

S(Q)

S(Q), loaded - unloaded

Q(Å$^{-1}$)

(c)

G(r) (Å$^{-2}$)

G(r) loaded - unloaded

5 nm ?

r (Å)
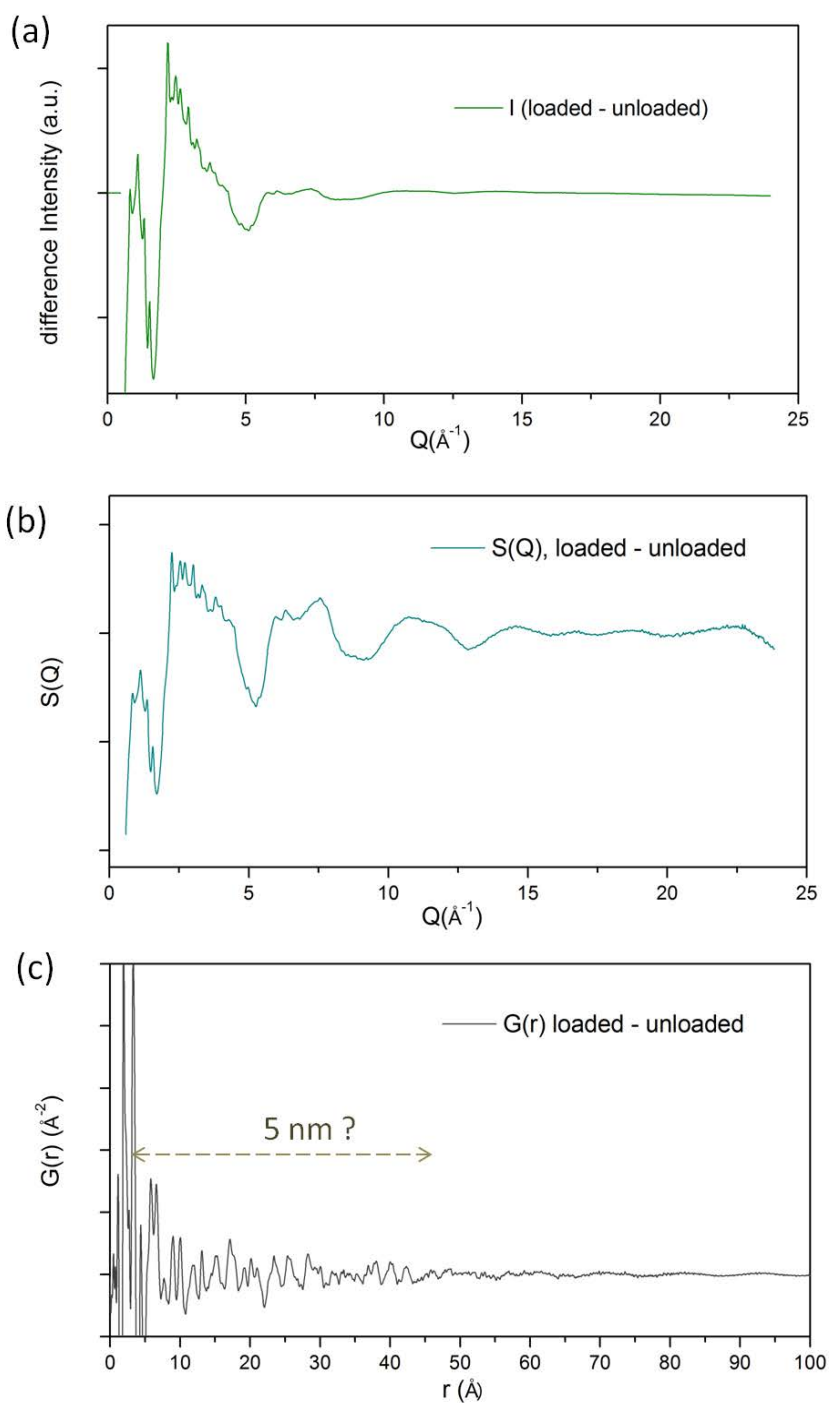
Figure 4.31 (a) Difference intensity subtracted from $I_{loaded} - I_{unloaded}$ after absorption correction, (b) the total structure function S(Q), and (c) the corresponding PDFs where the atomic pair distribution tends to zero beyond ~50 Å.
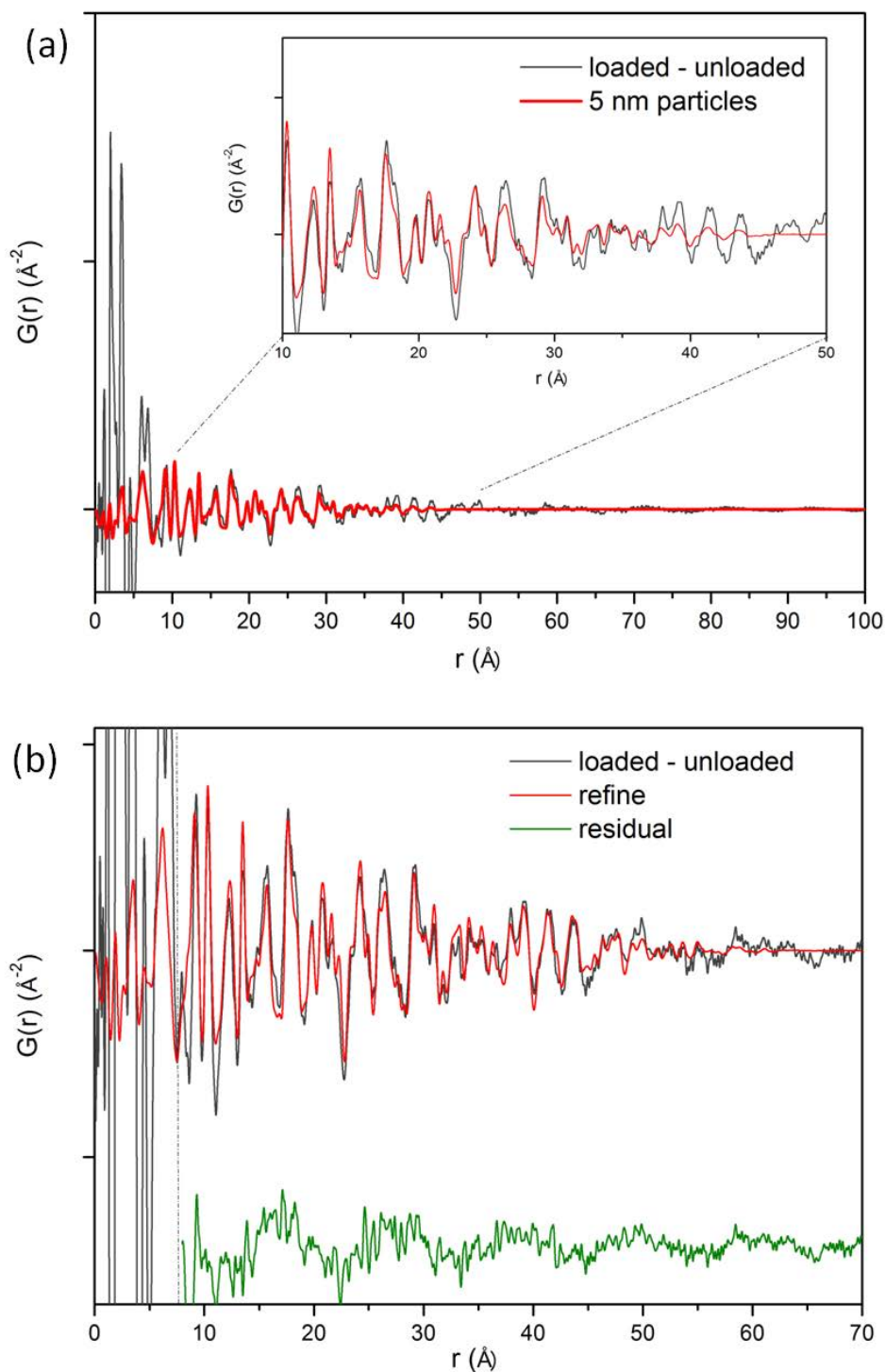
Figure 4.32 (a) Comparison between PDFs obtained from difference data and simulation from a spherical particle model (d=5 nm) using crystal structure, and (b) refinement of lattice parameters a, b, c and the particle size in the medium to long-range from 8 to 70 Å.

Having determined the contribution of the 5 nm particles, we can address the second phase that is visible in the low-r region of the differential PDFs. The subtraction of the PDF modelled with the 5 nm particles from the experimental PDFs as shown in Fig 4.33 allows for a more detailed investigation. Two sharp peaks are located inferior to 5 Å, which resemble very much the PDF of the isolated $Na_2[Fe(CN)_5NO]$ complexes in the $SiO_2$ monolith with pore sizes of about 1 nm (see section 4.4.3). However, in the range of 5 to 8 Å, there are some differences to the signature of the isolated molecules, which might be due to the perturbation of counter-ions or different porous environments. Further, broad features (oscillations with a period of ~11 Å) in the long-range region of the PDFs might be due to intermolecular distances including molecules in neighboring pores.
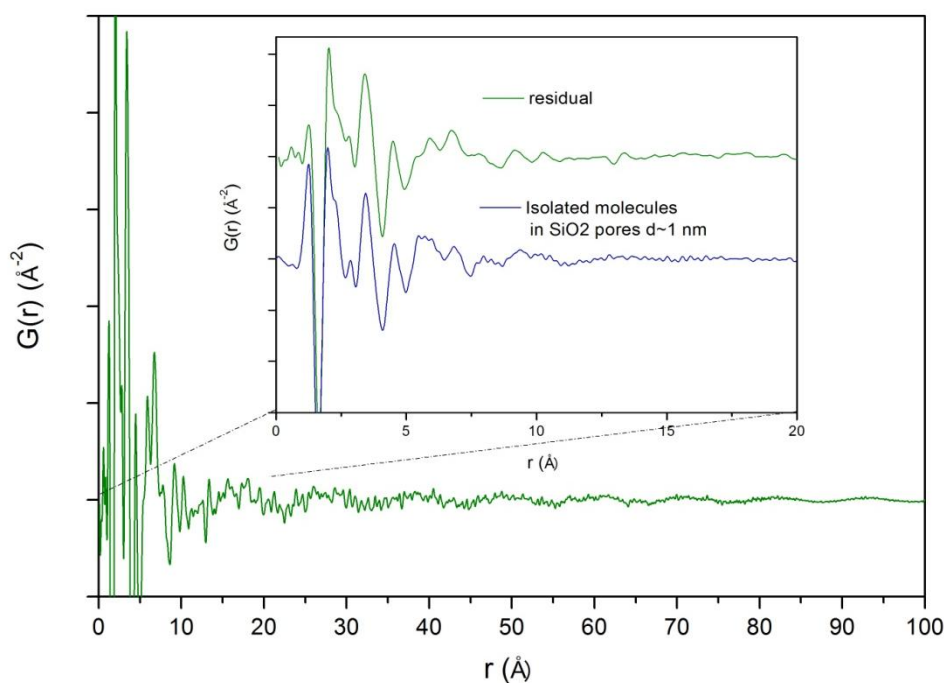


Figure 4.33 Subtraction of experimental PDFs by the refined SNP nanoparticles from Fig 1.32 (b). The "fingerprint" of isolated SNP was also presented at low-r region, the same as we have observed in $SiO_2$ of 1 nm pore sizes.

Concluding this part we found that in the samples of $SNP@SiO_2$ with pore sizes ~5nm, SNP nanoparticles of about 6 nm are formed and that the lattice parameters in the SNP nanoparticles are slightly expanded in comparison to bulk SNP. Furthermore, the PDF analysis indicates the presence of a second phase of SNP in the form of isolated $Na_2[Fe(CN)_5NO]$ complexes inside the porous network. However it is difficult to quantify accurately the contribution of these two phases from such analysis.

94

Additional Solid State NMR experiments confirm the presence of two types of SNP structures. The $^{23}$Na NMR spectrum acquired under magic angle spinning ($\nu_{MAS}$=12,5kHz) is shown on Fig. 4.34. It can be deconvoluted into three different sites. The two sites presented in purple correspond to the sites present in the published crystal structure [44]. The third site (in red) is not present in the bulk crystalline material and its chemical shift is sensitive to the hydration level of the sample. Therefore this site reflects the presence of smaller molecular clusters where the number of SNP complexes is not sufficient to allow for ideal crystallization. In those assemblies the sodium counterions are partially coordinated by water molecules to replace the missing Nitroprusside molecules. These results are therefore consistent with the PDF analysis since they show the presence of properly crystallized nanoparticles as well as additional structures that probably correspond to smaller assemblies. These additional sites correspond to less than 30% of all $^{23}$Na atoms.
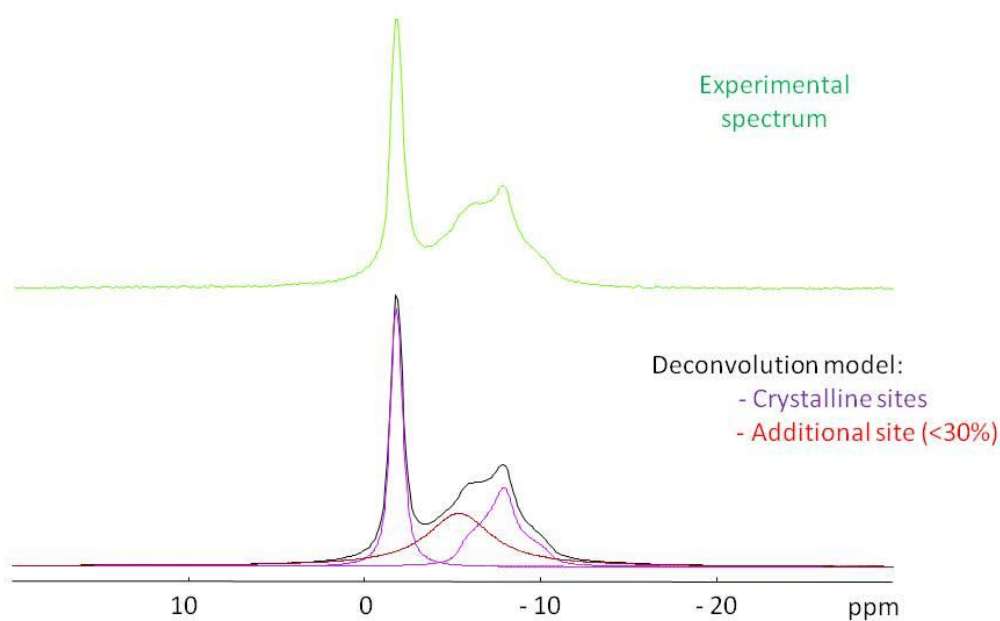


Figure 4.34 Central band of the $^{23}$Na spectrum from the L5 sample. Experimental spectrum (top) and the corresponding deconvoluted model (bottom). The spectral components are represented in purple and red whereas the sum is overlaid in black

### 4.6.3 Pre-doping SNP@SiO2 nanocomposites

A second possibility to prepare xerogels with isolated SNP complexes and/or SNP nanoparticles is the pre-doping procedure (see section 4.1.2). In the pre-doping samples the particle size can be influenced by the initial concentration of the dopant. In order to study the structure and size of the SNP (nano)particles formed by this procedure we performed total scattering experiments coupled to PDF analysis as described for the post-doped samples. Fig 4.35 illustrates the XRD patterns from pure $SiO_2$ xerogel and doped samples for different concentrations of the SNP salt (see Table 4.4). For the samples of Pre-4 to Pre-7, broadened Bragg peaks are clearly visible and indicate the presence of embedded crystalline SNP particles within the gel. The evaluation of the broadening according to Scherrers formula yields a particle size in a range of 83 nm to 143 nm. In the samples with lower doping concentration (samples Pre-1 to Pre-3) no traces of Bragg peaks appear. In this case the structural information can be obtained by subtracting the intensity of loaded – unloaded samples following the procedures described earlier. Fig 4.36 shows the total scattering functions S(Q) of difference intensities from Fig 4.35. The oscillations of isolated $Na_2[Fe(CN)_5NO]$ complexes become visible for the samples with lower concentrations. For the samples with higher concentrations we observe two phases: the nanocrystalline one reflected already in the Bragg peaks but also a huge population of isolated complexes within the gel (Fig 4.36), which are listed in the Table 4.4.
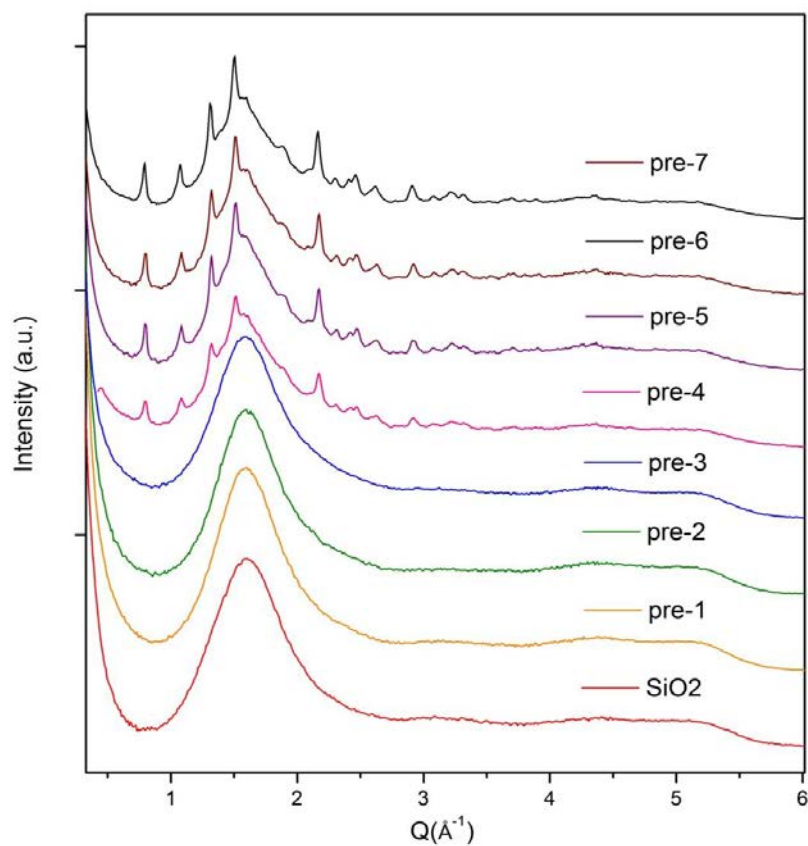
Figure 4.35 XRD patterns of SNP@SiO$_2$ series of samples synthesized by pre-doping method.

Table 4.4. Pre-doping samples of SNP@SiO$_2$ with different concentrations.

| Samples | Number of SNP in gel (μmol) | Estimated embedded SNP phases (%) | |
|---|---|---|---|
| | | Isolated complexes | Particles |
| Pure SiO$_2$ | 0 | 0 | 0 |
| Pre-1 | 12.5 | 100 | 0 |
| Pre-2 | 62.5 | 100 | 0 |
| Pre-3 | 187.5 | 100 | 0 |
| Pre-4 | 312.5 | 92.5 | 7.5 |
| Pre-5 | 437.5 | 90.3 | 9.7 |
| Pre-6 | 500.0 | 88.2 | 11.8 |
| Pre-7 | 625.0 | 86.7 | 13.3 |
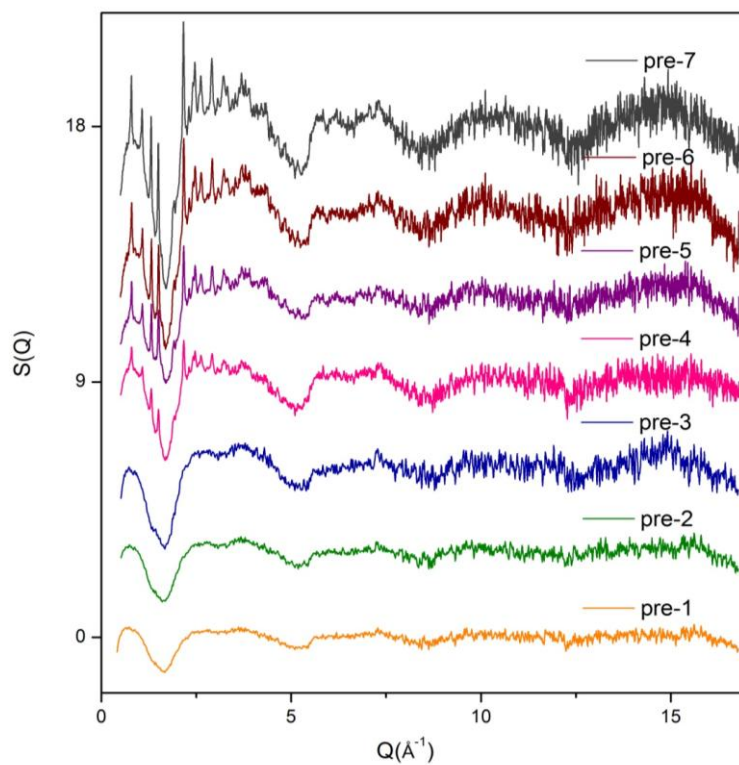
Figure 4.36 Total structure function of difference (loaded - unloaded) subtracted from Fig 4.35.
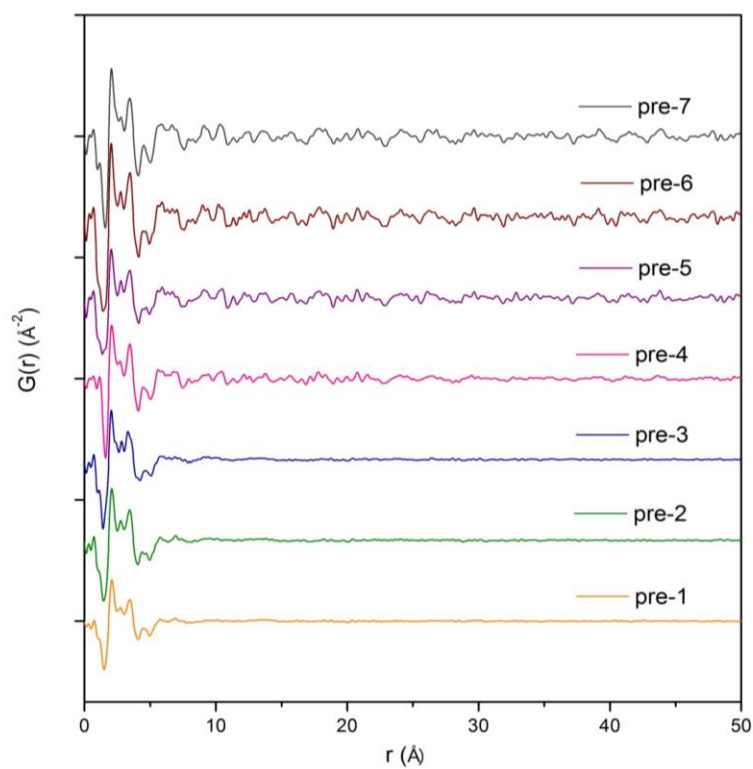


Figure 4.37 PDFs of difference (loaded - unloaded) obtained from Fig 1.36.

## 4.7    Conclusion

We have studied the influence of embedding SNP in porous silica xerogels with different pore sizes on its structure. The high energy X-ray total scattering experiments coupled to experimental differential PDF analysis, together with Solid State NMR techniques, allow us to investigate structural properties of isolated SNP molecules incorporated in the silica nanopores. The atomic d-PDF and the modelling approaches provide direct structural evidence on the local cation and anion arrangement of the SNP complexes and show that the SNP complexes are well isolated as single molecules inside the matrix pores in the case of $SiO_2$ matrices with pore sizes in the range of 1-3 nm. The corresponding analysis of SNP encapsulated in hosts with 5 nm pores sizes (average value !) reveals the presence of both isolated molecules as in the previous case and of nanoparticles of SNP with an estimated diameter of 6 nm.

The multi-nuclei Solid State NMR investigation provides information on both the amorphous host and the molecular guest and adds a dynamic dimension to the classical static structural characterization. $^{29}$Si MAS NMR measurements show that the gel matrix structure is not modified by the SNP embedding procedure.

$^{13}$C and $^{23}$Na MAS NMR measurements show that inside the matrix pores the SNP neither takes a crystalline like structure nor does it adhere to the pore surface in agreement with the d-PDF results. We surprisingly find evidence that the confined complex adopts solution like structure and dynamics with isotropic reorientation below the μs timescale. Additional experiments at different relative humidity levels show the presence of weakly interacting water molecules inside the pores. These water molecules can easily be removed to some extent, nevertheless the strong isotropic motion of the SNP is still preserved even for low hydration levels. Globally, the SNP complexes behave as "free" isolated molecules inside the matrix pores. The fact that the local arrangement of cation and anion and their dynamic can be proposed from a model obtained by using d-PDF and solid state NMR multiscale approach allows for future systematic investigations of structure-property relationship in such hybrid organic-inorganic nanocomposites.

Furthermore, we have verified that SNP retains its interesting optical properties. Especially the photoisomerisation of the nitrosyl group is still possible, and it was shown that the main characteristics of this photoswitching (spectral sensitivity, population of the isomers, ...) are independent of the particle sizes, indicating the truly molecular nature of the nitrosyl isomerisation.

A second important conclusion of this study concerns the methodology. In fact we have seen through this example, that good PDFs yielding proper structural information

can be obtained using a laboratory setup with limited Q-range (17 $\text{Å}^{-1}$). The comparison with PDF analysis based on synchrotron data shows, that using (much) longer counting times a sufficient signal-to-noise ratio for meaningful structure analysis can be obtained on a laboratory source. We note that this observation is especially true for amorphous molecular compounds, which have limited diffraction power at high Q-values, thus yielding the parameter $Q_{max}$ less important for the structure interpretation.

## Annex 1: Single crystal measurement of SNP complex

Table. X-ray data collection and refinement details for SNP complex

| | |
|---|---|
| Chemical formula | $Na_2[Fe(CN)_5NO]. 2H_2O$ |
| Formula weight | 297.97 |
| Temperature | 293(2) K |
| Crystal system, Space group | Orthorhombic, Pnnm |
| Unit cell dimensions (Å): a, b, c | 6.2051(4), 11.9098(6), c = 15.5605(9) |
| V ($Å^3$) | 1149.94(12) |
| Z | 4 |
| Radiation type, Wavelength | Mo K$\alpha$, 0.71073 Å |
| Density (calculated) | 1.721 $Mg/m^3$ |
| Absorption coefficient | 1.390 $mm^{-1}$ |
| F(000) | 592 electrons/unit cell |
| Crystal size | 0.12 x 0.12 x 0.1 $mm^3$ |
| **Data collection** | |
| Diffractometer | Oxford SuperNova Dual with an Atlas detector |
| Theta range for data collection | 3.53 to 30.00°. |
| Index ranges | -8<=h<=8, -16<=k<=16, -21<=l<=21 |
| Reflections collected | 36985 |
| Absorption correction | Analytical [CrysAlis PRO, Oxford Diffraction, 2009] |
| $T_{min}$, $T_{max}$ | 0.681 and 0.768 |
| Independent reflections | 1731 [$R_{int}$ = 0.045] |
| Completeness to theta = 30.00° | 99.7 % |
| **Refinement** | |
| Refinement method | Full-matrix least-squares on $F^2$ |
| Data / restraints / parameters | 1731 / 0 / 89 |
| Goodness-of-fit on $F^2$ | 1.072 |
| Final R indices [$F^2>2\sigma(F^2)$], $w$R($F^2$) | R1 = 0.022, 0.064 |
| R indices (all data) | R1 = 0.025, 0.065 |
| $\Delta\rho_{max}$, $\Delta\rho_{min}$ (e.$Å^{-3}$) | 0.255 and -0.246 |

## Data Collection and Reduction

Accurate single crystal X-ray diffraction experiment was performed at room temperature (T=293(2) K) with an Oxford Diffraction SuperNova Dual Wavelength Microfocus diffractometer equipped with a 135 mm Atlas CCD detector, using Mo K$\alpha$ radiation ($\lambda$

= 0.71073 Å). In order to ensure high redundancies, the intensity data were accurately collected using ω oscillation scans of 1° per frame repeated at different φ positions. The radiation exposure time was 20 s per frame. Coverage of reciprocal space was more than 99% complete to ($\sin\theta_{max}/\lambda$) of 0.704 Å$^{-1}$. The unit cell determination and data integration were carried out using the *CrysAlis Pro* program suite [45]. Absorption effects were corrected by numerical methods based on multifaceted crystal model. The different sets of measured reflections were subsequently merged and scaled using SORTAV [46]. A total of 36985 reflections intensities were merged into 1731 unique reflections. The internal agreement factor for all data is $R_{Int}(I)$ = 0.045 with an average redundancy of 21.3.

### Crystal structures Determination and refinements

The structure was solved by direct methods and successive Fourier difference syntheses and refined against F$^2$ by weighted full-matrix least-squares methods using the SHELXL97 program [47]. All calculations were carried out using the WinGX software package [48].

**Annex 2. Brunauer-Emmett-Teller (BET) results**
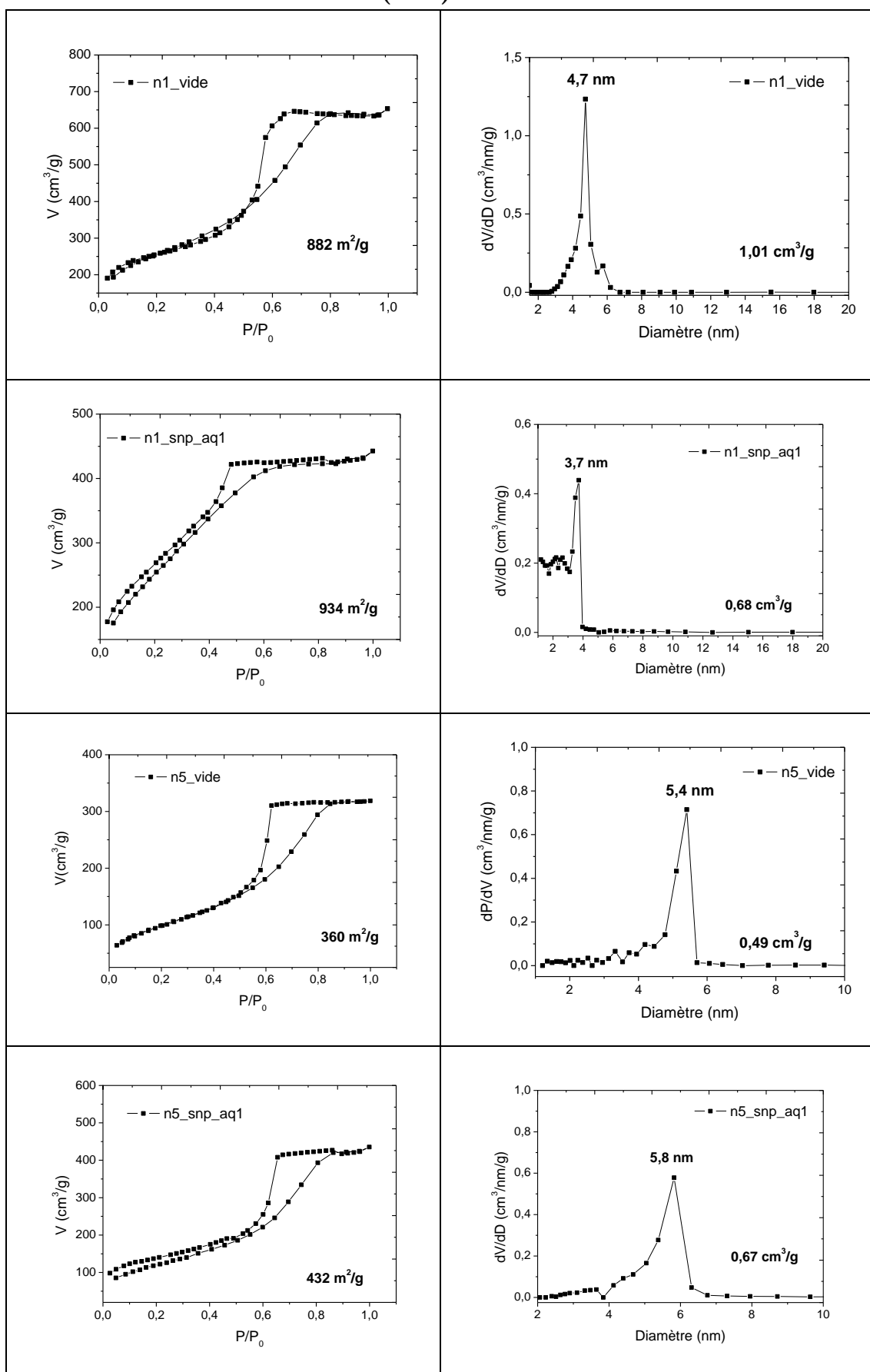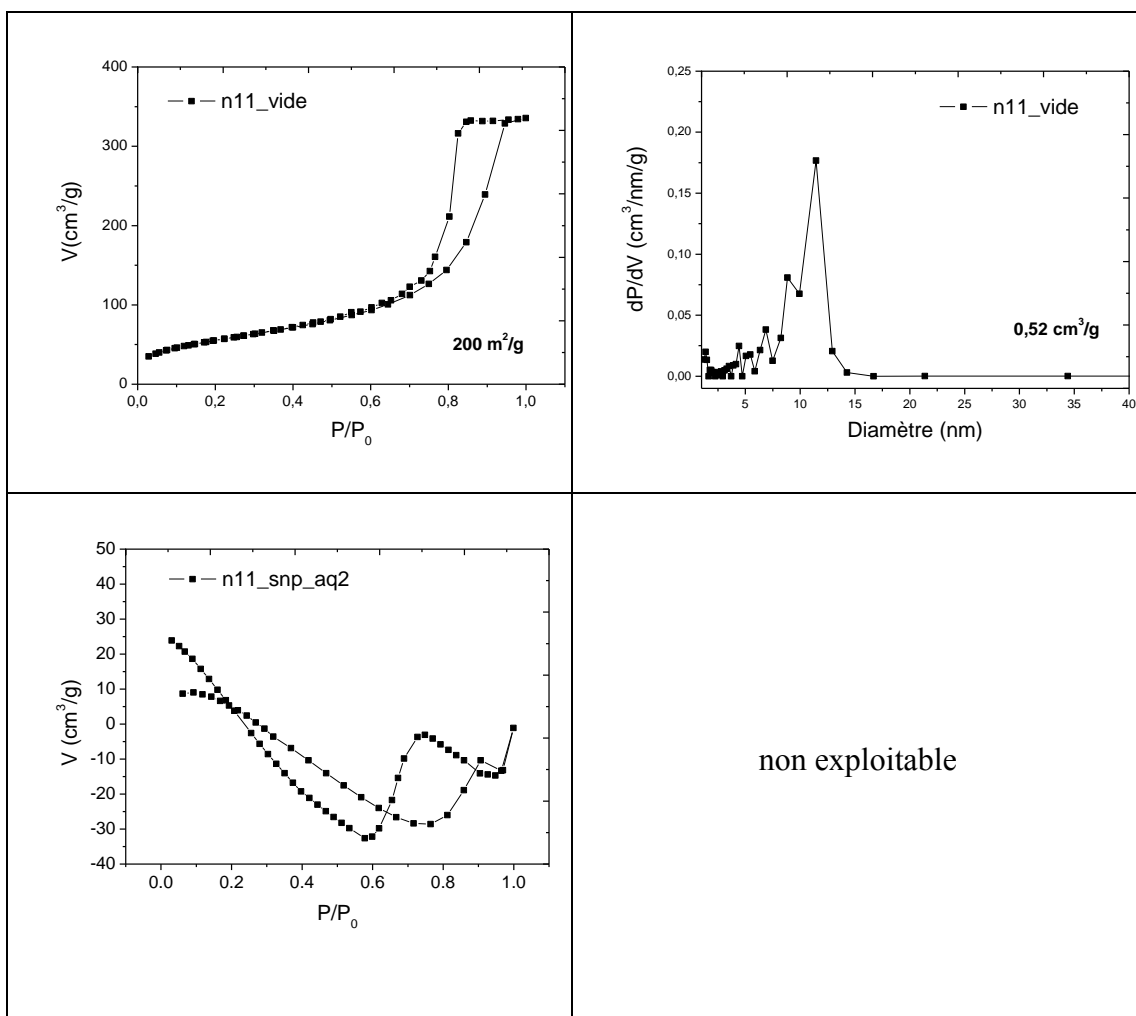
| Samples | Specific Surface (m²/g) | Porous Volume (cm³/g) | Average sizes of pores (nm) |
|---|---|---|---|
| SiO₂ (1nm) | 882 | 1.01 | 4.7 |
| SNP@SiO₂ (1nm) | 934 | 0.68 | 3.7 |
| SiO₂ (5nm) | 360 | 0.49 | 5.4 |
| SNP@SiO₂ (5nm) | 432 | 0.67 | 5.8 |
| SiO₂ (11nm) | 200 | 0.52 | 11.4 |
| SNP@SiO₂ (11nm) | - | - | - |

# Bibliography

[1]    V. Dieckmann, S. Eicke, K. Springfeld, and M. Imlau, Materials **5**, 1155 (2012).

[2]    D. Schaniel, M. Imlau, T. Weisemoeller, T. Woike, K. W. Krämer, and H.-U. Güdel, Adv. Mater. **19**, 723 (2007).

[3]    M. Goulkov, D. Schaniel, and T. Woike, J. Opt. Soc. Am. B **27**, 927 (2010).

[4]    T. Woike, W. Kirchner, G. Schetter, T. Barthel, K. Hyung-sang, and S. Haussühl, Opt. Commun. **106**, 6 (1994).

[5]    P. Coppens, I. Novozhilova, and A. Kovalevsky, Chem. Rev. **102**, 861 (2002).

[6]    D. Schaniel and T. Woike, Phys. Chem. Chem. Phys. **11**, 4391 (2009).

[7]    A. Schuy, T. Woike, and D. Schaniel, J. Sol-Gel Sci. Technol. **50**, 403 (2009).

[8]    C. Seidel, U. Ruschewitz, A. Schuy, T. Woike, and D. Schaniel, Z. Für Anorg. Allg. Chem. **634**, 2018 (2008).

[9]    V. Dieckmann, M. Imlau, D. H. Taffa, L. Walder, R. Lepski, D. Schaniel, and T. Woike, Phys. Chem. Chem. Phys. **12**, 3283 (2010).

[10]   B. Delley, J. Schefer, and T. Woike, J. Chem. Phys. **107**, 10067 (1997).

[11]   D. Schaniel, T. Woike, J. Schefer, V. Petříček, K. W. Krämer, and H. U. Güdel, Phys. Rev. B **73**, 174108 (2006).

[12]   Z. Tahri, R. Lepski, K.-Y. Hsieh, E.-E. Bendeif, S. Pillet, P. Durand, T. Woike, and D. Schaniel, Phys. Chem. Chem. Phys. **14**, 3775 (2012).

[13]   A. Cervellino, J. Schefer, L. Keller, T. Woike, and D. Schaniel, J. Appl. Crystallogr. **43**, 1040 (2010).

[14]   L. L. Hench and S. H. Wang, Phase Transitions **24-26**, 785 (1990).

[15]   H. El Hamzaoui, L. Courthéoux, V. N. Nguyen, E. Berrier, A. Favre, L. Bigot, M. Bouazaoui, and B. Capoen, Mater. Chem. Phys. **121**, 83 (2010).

[16]   F. Bottomley and P. S. White, Acta Crystallogr. B **35**, 2193 (1979).

[17]   A. Navaza, G. Chevrier, P. M. Alzari, and P. J. Aymonino, Acta Crystallogr. C **45**, 839 (1989).

[18]   P. T. Manoharan and W. C. Hamilton, Inorg. Chem. **2**, 1043 (1963).

[19]   P. Coppens, D. V. Fomitchev, M. D. Carducci, and K. Culp, J. Chem. Soc. Dalton Trans. 865 (1998).

[20]   D. Schaniel, T. Woike, J. Schefer, and V. Petříček, Phys. Rev. B **71**, 174112 (2005).

[21]   D. Schaniel, Structural Investigations of High Knowledge Content Materials, [s.n.], 2003.

[22]   D. Schaniel, J. Schefer, B. Delley, M. Imlau, and T. Woike, Phys. Rev. B **66**, 085103 (2002).

[23]   M. S. Lynch, M. Cheng, B. E. Van Kuiken, and M. Khalil, J. Am. Chem. Soc. **133**, 5255 (2011).

[24] A. K. Soper and E. R. Barney, J. Appl. Crystallogr. **44**, 714 (2011).

[25] C. L. Farrow, P. Juhas, J. W. Liu, D. Bryndin, E. S. Božin, J. Bloch, T. Proffen, and S. J. L. Billinge, J. Phys. Condens. Matter **19**, 335219 (2007).

[26] I.-K. Jeong, T. Proffen, F. Mohiuddin-Jacobs, and S. J. L. Billinge, J. Phys. Chem. A **103**, 921 (1999).

[27] I.-K. Jeong, R. H. Heffner, M. J. Graf, and S. J. L. Billinge, Phys. Rev. B **67**, 104301 (2003).

[28] N. Rademacher, L. L. Daemen, E. L. Chronister, and T. Proffen, J. Appl. Crystallogr. **45**, 482 (2012).

[29] R. L. Mozzi and B. E. Warren, J. Appl. Crystallogr. **2**, 164 (1969).

[30] C. J. Benmore and P. J. M. Monteiro, Cem. Concr. Res. **40**, 892 (2010).

[31] W. H. Zachariasen, J. Am. Chem. Soc. **54**, 3841 (1932).

[32] A. K. Soper, Phys. Rev. B **72**, 104204 (2005).

[33] A. K. Soper, J. Phys. Condens. Matter **22**, 404210 (2010).

[34] H. F. Poulsen, J. Neuefeind, H.-B. Neumann, J. R. Schneider, and M. D. Zeidler, J. Non-Cryst. Solids **188**, 63 (1995).

[35] K. W. Chapman, P. J. Chupas, and C. J. Kepert, J. Am. Chem. Soc. **127**, 11232 (2005).

[36] D. A. Keen, Phase Transitions **61**, 109 (1997).

[37] T. Proffen and R. B. Neder, J. Appl. Crystallogr. **32**, 838 (1999).

[38] B. H. Toby and T. Egami, Acta Crystallogr. A **48**, 336 (1992).

[39] P. Blaha, K. Schwarz, W. Faber, and J. Luitz, Hyperfine Interactions **126**, 389 (2000).

[40] D. Massiot, F. Fayon, M. Capron, I. King, S. Le Calvé, B. Alonso, J.-O. Durand, B. Bujoli, Z. Gan, and G. Hoatson, Magn. Reson. Chem. **40**, 70 (2002).

[41] A. R. Butler, C. Glidewell, A. R. Hyde, and J. McGinnis, Inorg Chem **24**, 2931 (1985).

[42] J. Trébosc, J. W. Wiench, S. Huh, V. S.-Y. Lin, and M. Pruski, J. Am. Chem. Soc. **127**, 3057 (2005).

[43] X. Xue and J. F. Stebbins, Phys. Chem. Miner. **20**, 297 (1993).

[44] K.-Y. Hsieh, E.-E. Bendeif, G. Axel, P. Sbestien, S. Dominik, and W. Theo, Phys. Chem. Chem. Phys. (2013).

[45] *Oxford Diffraction, CrysAlis CCD and CrysAlis RED* (Oxford Diffraction Ltd, Yarnton, Oxfordshire, England, 2009).

[46] R. H. Blessing, J. Appl. Crystallogr. **30**, 421 (1997).

[47] G. M. Sheldrick, Acta Crystallogr. A **64**, 112 (2007).

[48] L. J. Farrugia, J. Appl. Crystallogr. **45**, 849 (2012).

# Chapter 5

# Structural investigation and photoluminescent properties of embedded neodymium complex

# Chapter 5

# Structural investigation and

# photoluminescent properties of

# embedded neodymium complex

Luminescent rare earth (RE) materials are very promising for a variety of photonic applications, such as IR lasers, as a source for optical communication networks or as light-emitting diodes; and they are very suitable for photovoltaic devices [1–7]. The trivalent ions of the RE series are characterized by a gradual filling of the 4f orbitals, from $4f^0$ ($La^{3+}$) to $4f^{14}$ ($Lu^{3+}$). One of the most interesting features of these ions is their photoluminescence, whose emission is due to transitions inside the 4f shell, thus intraconfigurational f-f transitions. The shielding of the partially filled 4f shell is responsible for the specific properties of RE luminescence, particularly for the narrowband emission and the long lifetimes of the excited states. Several RE-doped silica materials show luminescence in the visible or near-infrared spectral regions upon irradiation with ultraviolet radiation. In this respect, the $Nd^{3+}$ based materials are among the most investigated systems and have attracted a major interest owing to their near-infrared photoluminescence behaviour [4,5].

Recently, many theoretical and experimental studies have been devoted to $Nd^{3+}$ ($4f^4$) based materials, aiming at defining the relevant parameters which control the luminescent properties [8–11]. It was found that the spectroscopic and the photonic properties of $Nd^{3+}$ based complexes are strongly affected by the arrangement of the ligands around the RE sites *(i.e., the local structure at the RE sites)* [12,13]. Furthermore, the neodymium hydroxychlorides complexes have been investigated by various scientists [2-6] owing to their interesting structural and optical properties. By investigating the correlation of the structural and spectroscopic properties of the $Nd(OH)_2Cl$ complex [5], it has been shown that the highly linked three-dimensional network seems to contribute to the remarkable inertness of this material in near neutral aqueous environments, which could be one of the key properties for the potential application of actinide bis-hydroxychlorides as nuclear waste forms. Although the characterisation of the optical properties of $Nd^{3+}$ based complexes has thoroughly been performed and are quite well documented [17,18], reports on their structural behaviour are still rather scarce and quite disparate.

In this chapter we present a detailed structural characterization of neodymium complexes embedded into $SiO_2$ xerogels with pore sizes of 1 nm, 5 nm and 11 nm, as well as their optical properties (absorption and luminescence) as a function of the host pore size.

## 5.1   Sample Preparation

The transparent silica monolith was prepared by a low temperature sol-gel route, which forms average pore sizes of around 1~3 nm, 5 nm, and 11 nm.

In order to immobilize the luminescent complexes into the $SiO_2$ matrix, the prepared silica monolith was impregnated in $NdCl_3$. $6H_2O$ aqueous solution of 1.411 [mol/L] that contains a fairly high concentration of Nd complexes. During 1 day of immersion, the complex was diffused into the channels or pores of the monolith that became homogeneous colored in mauve (Fig 5.1). As a final drying step the loaded monolith was kept at 50 °C in an oven, and then left in a desiccator for one week in order to remove the remaining solvent.
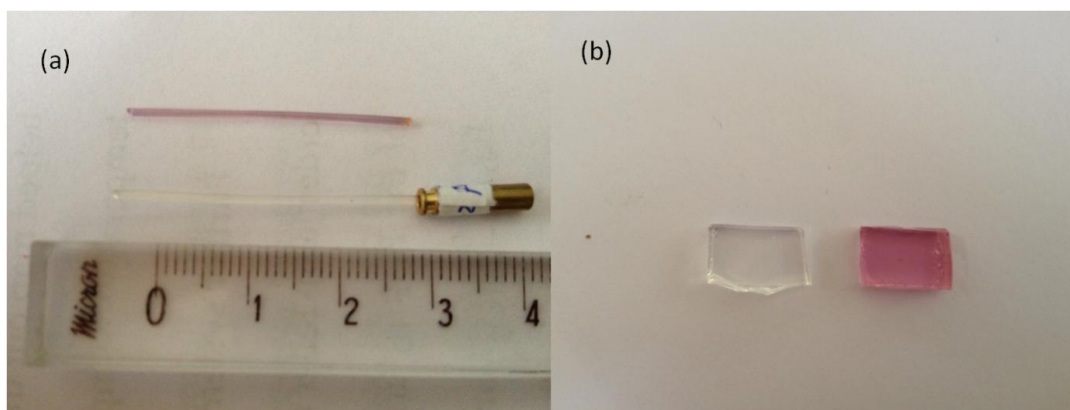


Figure 5.1 Photographs of the synthesized unloaded (transparent) and loaded (colored) Nd silica monoliths: (a) $Nd@SiO_2$ monolith rod with pore sizes of 1~3 nm, and (b) $Nd@SiO_2$ with pore sizes of about 5 nm.

## 5.2   Average crystal structure of the bulk material    $[NdCl_2(H_2O)_6]Cl^-$

The crystal structure of the photoluminescent compound hexaaquadichlorido-neodymium(III), $[NdCl_2(H_2O)_6, Cl]$, was first determined by Habenschuss & Spedding (1980) [19] to be isostructural with the $[LuCl_3.6H_2O]$ complex [20]. Nevertheless, the 12 H atoms (six of them symmetry-independent) were not identified, which prevents a clear interpretation of the crystal packing; so no detailed structural discussion was presented. A more complete crystallographic analysis of this compound is therefore of great interest to get better insights into its structural properties. In this context, we reinvestigate the crystal structure of the $[NdCl_2(H_2O)_6, Cl]$ complex from single-crystal X-ray diffraction data at

100 K, with the aim of providing an accurate structural model for the bulk crystalline material. In addition we calculate the PDF in order to discuss the local structure which will serve as a reference model for the structural studies of neodymium complex encapsulated in the different mesoporous silica matrices. Crystal data, data collection and structure refinement details are summarized in Table 1 (Annex 1).

Fig.5.2 shows the crystal structure of the studied compound, $[NdCl_2(H_2O)_6, \cdot Cl]$, along with the numbering scheme. The detailed examination of the arrangement around the neodymium ion reveals a distorted square antiprism geometry, where each neodymium ion ($Nd^{3+}$) is located on a twofold axis and is eight-fold coordinated by six water molecules and two inner sphere chlorines atoms (Table 1). The Nd1—$H_2O$ bond lengths range from 2.437(1) Å to 2.465(1) Å with an average value of 2.453(1) Å and are significantly shorter than the Nd1—Cl1 [2.8180 (4) Å]. The third chloride ion (Cl2) is located on a twofold axis, at much greater distance of 5.0638(2) Å from the $Nd^{3+}$ cation, without any evidence for direct Nd1…Cl2 interaction. These interatomic distances are clearly visible in the calculated atomic Pair distribution Function (PDF) diagram (Fig. 5.3).
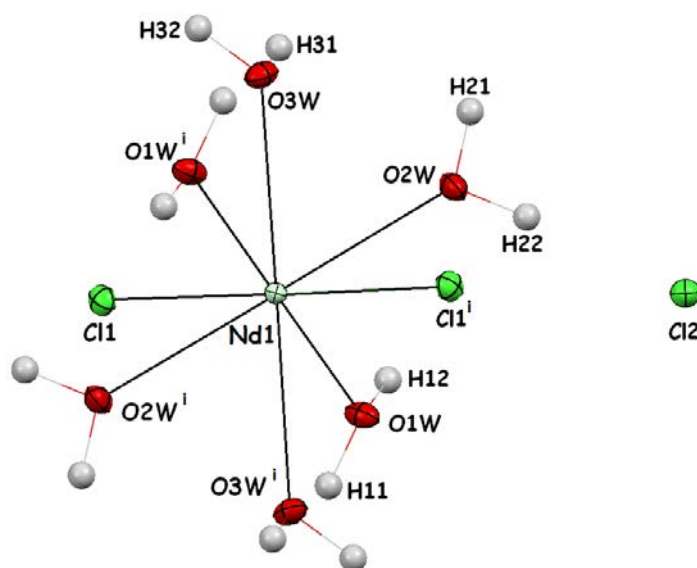


Figure 5.2 A projection of $[NdCl_2(H_2O)_6, Cl]$, showing the atom-labelling scheme. Displacement ellipsoids are drawn at the 50% probability level. [Symmetry code: (i) *-x + 3/2, y, -z +3/2.*]

In Fig. 5.3 we illustrate the calculated PDF up to 10 Å obtained from the crystal structure described herein (solid line) and that from the previously reported structure

(Habenschuss & Spedding, (1980)) (open circles). The most intense peaks in the $G(r)$ function correspond to atomic pairs between the strongest atomic scatterers in this complex, $Nd^{3+}$ cations, as well as the most abundant pairs (six water molecules). Moreover, the examination of the short scale region in the PDF diagram, below ~10 Å, gives information on the first few coordination spheres and therefore yields extensive information about the local atomic arrangement in the vicinity of the $Nd^{3+}$ sites.

Table 2: Selected geometric parameters for $[NdCl_2(H_2O)_6,\cdot Cl]$ complex.

| Bond length (Å) | | |
|---|---|---|
| Nd1—O1W: 2.437(1) | Nd1—O3W: 2.465(1) | Nd1—O2W: 2.457(1) |
| Nd1—Cl1 2.8180(4) | Nd1…Cl2: 5.0638(2) | Cl1…Cl2: 4.1821(5) |
| Bond angles (°) | | |
| O1W-Nd1-O1W[i]: 83.19(6) | O3W[i]-Nd1-O3W:148.49(6) | O1W-Nd1-O2W:69.41(4) |
| O1W-Nd1-Cl1: 142.94(3) | O1W[i]-Nd1-O2W: 75.13(4) | O1W[i]-Nd1-Cl1: 108.22(3) |
| O2W-Nd1-O2W[i]: 132.01(6) | O2W-Nd1-Cl1: 147.07(3) | O1W-Nd1-O3W[i]: 70.06(4) |
| O2W[i]-Nd1-Cl1: 76.39(3) | O1W[i]-Nd1-O3W[i]: 138.34(4) | O3W[i]-Nd1-Cl1: 79.32(3) |
| O2W-Nd1-O3W[i]: 120.76(4) | O3W-Nd1-Cl1: 77.41(3) | O2W[i]-Nd1-O3W[i]: 73.11(4) |
| | Cl1-Nd1-Cl1[i]:84.10(2) | |

Symmetry code: (i) *-x + 3/2, y, -z +3/2.*
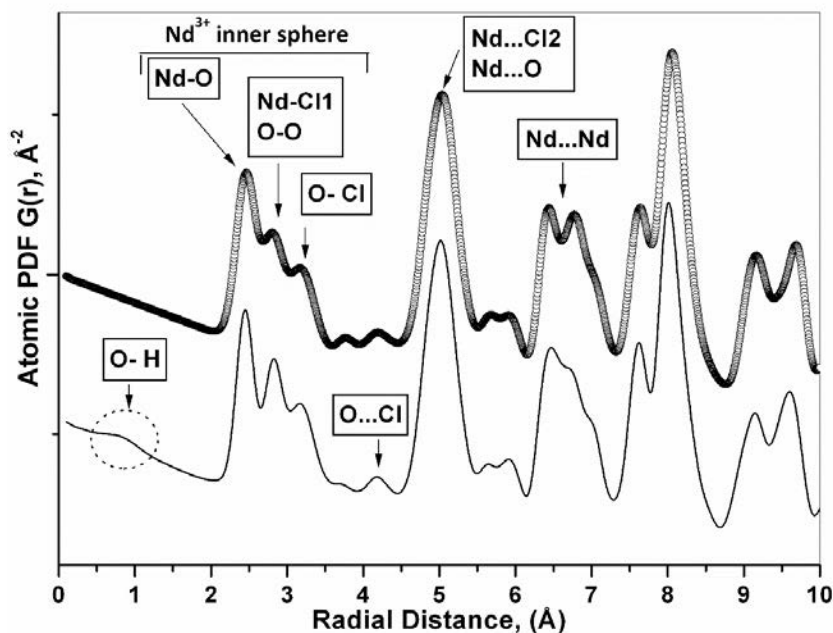
Figure 5.3 Comparison of PDFs calculated from the crystal structure obtained in this work (solid line) and that determined from previously reported structure (open circles). The PDF diagrams were calculated using the program PDFgui [21]

The PDF peak at 2.45 Å corresponds to the Nd1—O bond lengths whereas the peak at 2.82 Å is due to both the Nd1—Cl1 pairs and the intraprism $H_2O…H_2O$ interactions. The peaks at 3.15 Å and 4.18 Å originate from the intramolecular Cl1…$H_2O$ interactions and the intense G(r) peak near 5.1 Å can be assigned to the Nd…Cl2 interactions, together with a significant number of next nearest Nd…O pairs. As can be seen in Fig.5.3, the calculated PDFs are quite similar. As a notable difference a small peak near 1 Å, definitely corresponding to the O—H bond length, is only observed in the PDF profile obtained from the results reported in this work. This is obviously due to the fact that all hydrogen atoms (12 atoms) were successfully located in Fourier difference maps in our study. Furthermore, we note that the structural parameters reported here are more precise than those communicated previously due to the different experimental conditions (low temperature, experimental data collection setup).

The crystal structure of $[NdCl_2(H_2O)_6,·Cl]$ is made up of a network of three different neodymium pairs linked by O—H…Cl1 interactions ranging from 3.134(1) Å to 3.162 (1) Å (Fig. 5.4). These pairs are also characterized by significantly different Nd1…Nd1 pairs with distances ranging from 6.3739(3) Å to 6.7491(3) Å which are clearly visible in the

PDF diagram (Fig 5.3) in the 6.13-7.26 Å regions. The chloride ion (Cl2) is in contact with six neighboring $[NdCl_2(H_2O)_6]^+$ cations, four in the *ab* plane and two directed almost along the crystallographic *c* axis. Anions Cl1 and Cl2 are both involved in the highly linked three-dimensional network of the intermolecular interactions connecting the different pairs of neodymium-centred cations (Table3, Annex 1). It is also noteworthy that the O—H…Cl2 interactions are only slightly longer (from 3.170(1) Å to 3.233(1) Å) compared to the O—H…Cl1 interactions and the shortest Cl1…Cl2 interaction is of 4.1821(5) Å.
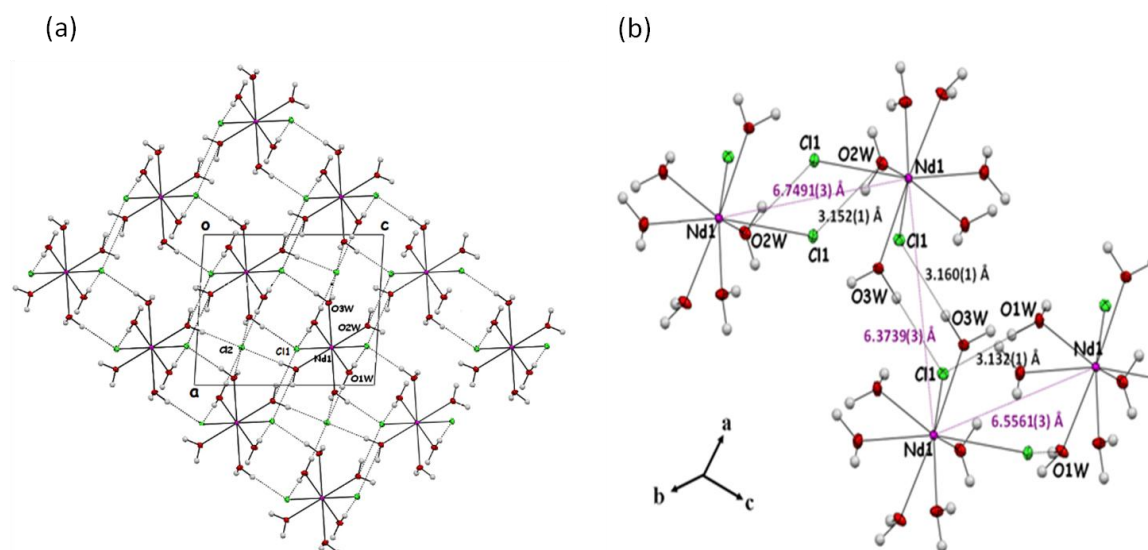


Figure 5.4 (a) Packing diagram of $[NdCl_2(H_2O)_6, \cdot Cl]$ in the ac plane showing dimers linked by the three dimensional network of O—H…Cl intermolecular interactions. (b) A detailed view of the different Nd1...Nd1 pairs.

## 5.3    Optical properties

We investigated the influence of the particle size on the optical properties of the $Nd^{3+}$ complexes embedded in the silica matrix using spectroscopic techniques including UV/Vis, IR, and photoluminescence. The crystalline $[NdCl_2(H_2O)_6, \cdot Cl]$ compound was also characterized and will serve as a reference sample. The $Nd^{3+}$characteristic absorption bands are clearly shown on the UV/Vis spectra. The IR measurements give useful information on both the $SiO_2$ glass and the embedded $Nd^{3+}$ species, namely the characteristic vibrations of Si—OH and Nd—O bonds in the matrix. The inclusion of the $Nd^{3+}$ complex within the silica pores was also confirmed from the characteristic luminescent bands of the $Nd^{3+}$cation at 920, 1080, and 1320 nm.

### 5.3.1  UV-visible spectroscopy

**Fig. 5.5** shows the absorption spectra of crystalline $[NdCl_2(H_2O)_6, \cdot Cl]$, aqueous solution of $[NdCl_2(H_2O)_6, \cdot Cl]$, and the loaded and unloaded $SiO_2$ gel, respectively. One can clearly observe that the absorption spectra of the $Nd^{3+}$ doped-silica composite differs significantly from that of the crystalline $[NdCl_2(H_2O)_6, \cdot Cl]$ complex but resembles very much the absorption spectrum of the aqueous solution of $[NdCl_2(H_2O)_6, \cdot Cl]$. This result suggests that the embedded $Nd^{3+}$ species did not crystallize within the matrix pores and that the $Nd^{3+}$ cations might have a local structure closely related to that found in aqueous solution.

The absorption spectra of the different Nd-compounds that are shown in Fig. 5.5 in the range 200-900 nm show several transitions from the ground state ($^4I_{9/2}$) to various excited states. Karraker [22] has shown that the intensities and peak shapes of the transitions at ~800 nm ($^4I_{9/2} \rightarrow \ ^4F_{5/2}, \ ^2H_{9/2}$), ~740 nm ($^4I_{9/2} \rightarrow \ ^4S_{3/2}, \ ^4F_{7/2}$), ~580 nm ($^4I_{9/2} \rightarrow \ ^4G_{5/2}, \ ^2G_{7/2}$), and ~520 nm ($^4I_{9/2} \rightarrow \ ^4G_{7/2}$) are sensitive to the coordination of the $Nd^{3+}$ ion. The transition at 580 nm is often referred to as "hypersensitive transition" [22–24] while the three remaining transitions are sometimes referred to as "insensitive transitions" [24]. From these studies it was inferred that the coordination number of $Nd^{3+}$ in aqueous solution is 9, a fact that was later confirmed by analysis of the radial distribution function obtained from x-ray diffraction experiments [27]. The fact, that the corresponding peaks in the absorption spectrum of $Nd@SiO_2$ resemble those of the aqueous solution, is thus a strong indication that the $Nd^{3+}$ is nonacoordinated within the xerogel.
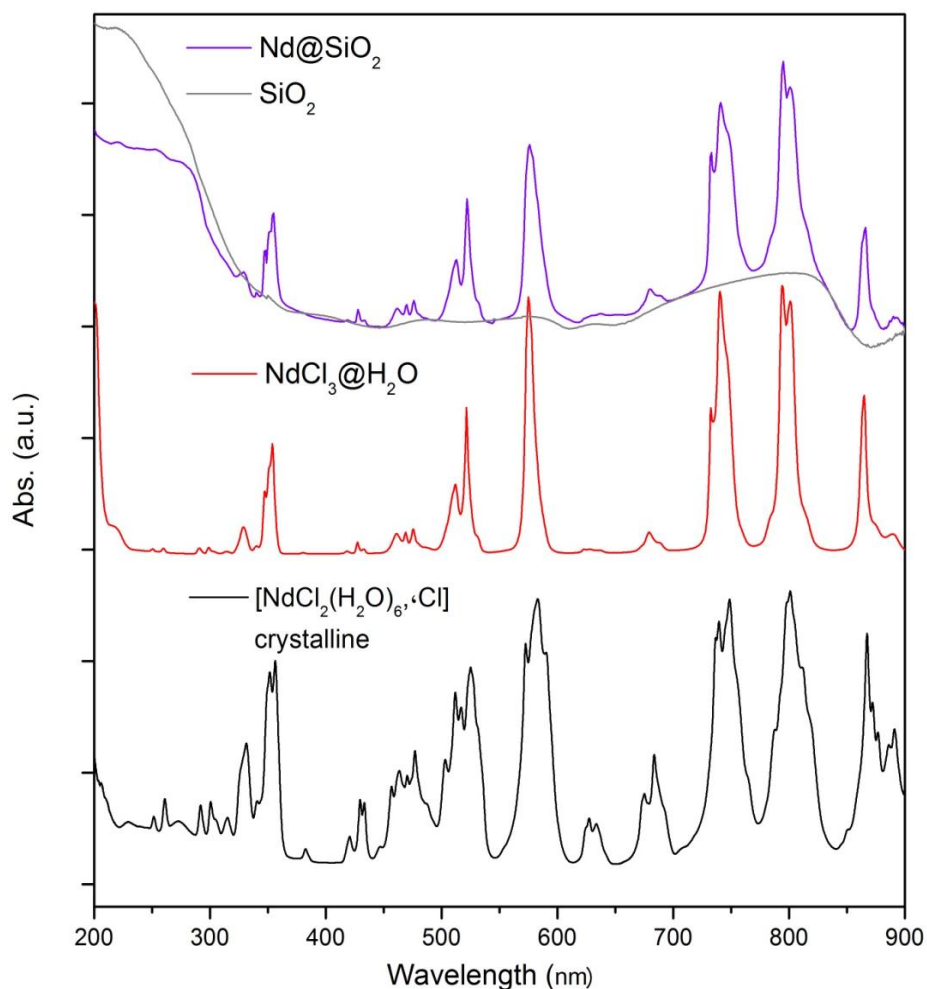
Figure 5.5 UV/vis spectra of loaded and unloaded $SiO_2$, aqueous $NdCl_3$ solution, and the $[NdCl_2(H_2O)_6,\cdot Cl]$ crystalline, respectively.

### 5.3.2 IR spectroscopy

IR spectra of empty $SiO_2$ and Nd@$SiO_2$ are shown in Fig 5.6(a). The $SiO_2$ network exhibits the absorption bands at ~1090 cm$^{-1}$ (antisymmetric Si-O-Si stretch, transverse optic mode, with the shoulder at ~1200 cm$^{-1}$ arising from the longitudinal optic mode), ~970 cm$^{-1}$ (Si-OH), ~800 cm$^{-1}$ (symmetric Si-O-Si stretch). In addition, peaks at ~3400 cm$^{-1}$ and 1660 cm$^{-1}$ arise from hydroxyl groups associated with the silica.

For the Nd@$SiO_2$ gel the absorption bands at ~3400 cm$^{-1}$ and ~1660 cm$^{-1}$ seem more intense compared to the bulk crystalline complex $[NdCl_2(H_2O)_6,\cdot Cl]$ (see Fig 5.6(b)). This effect is associated with the $Nd^{3+}$ doping as was also reported for other Re complexes [24,25] and might indicate an increase of the concentration of the hydroxyl

groups in the Nd@SiO$_2$ hybrid material. This is probably due to the presence of an important amount of water molecules in the vicinity of the Nd$^{3+}$ cations within the matrix pores. To verify that, we calculated the ratio between such absorption bands, ~3400 cm$^{-1}$ and ~1660 cm$^{-1}$, in both cases (the difference curve as well as the bulk crystalline material). We find that this ratio is 2.5 larger in the case of the doped monolith compared to that obtained in the crystalline material, confirming the presence of a larger amount of water molecules in the Nd@SiO$_2$ composite.
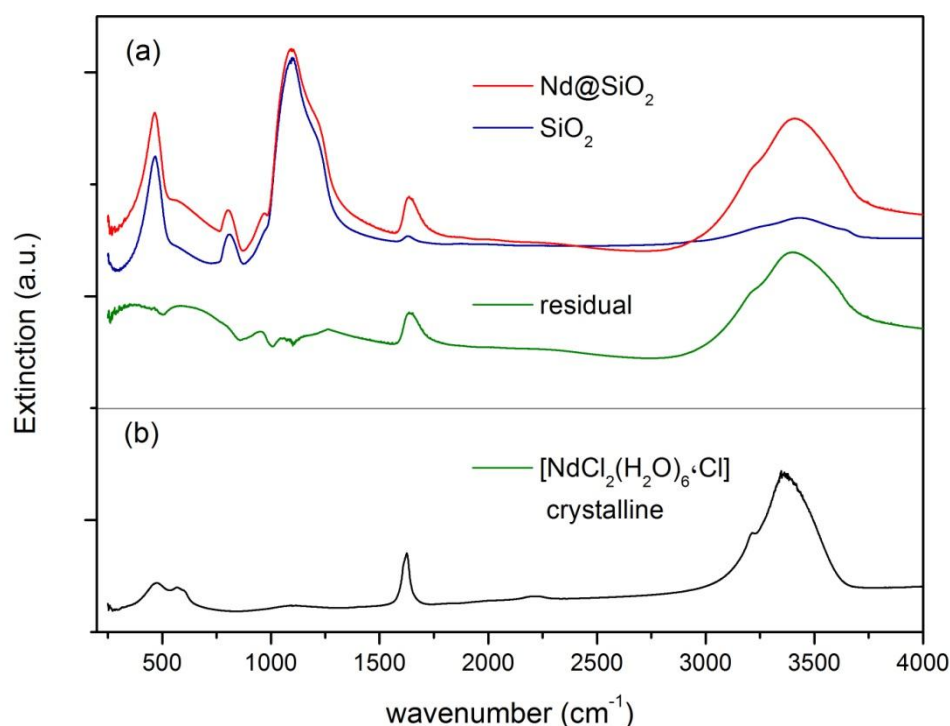


Figure 5.6 IR spectra of (a) unloaded and loaded Nd@SiO$_2$ gel and the corresponding difference pattern. (b) Crystalline [NdCl$_2$(H$_2$O)$_6$,·Cl] complex for comparison.

### 5.3.3    Photoluminescence

The photoluminescence spectrum was obtained through excitation at room temperature with λ = 325 nm in a range of 800-1200 nm. The empty SiO$_2$ xerogel shows the characteristic wide PL band around 800 nm, which overlaps with the bands around 920 nm of the loaded Nd@SiO$_2$. We used a filter of 600 μm to avoid it.

The characteristic PL emissions of Nd$^{3+}$ are observed at 920, 1050 and 1320 nm and correspond to the transitions $^4F_{3/2} \rightarrow$ $^4I_{9/2}$, $^4I_{11/2}$, and $^4I_{13/2}$, respectively, as shown in **Fig 5.7**. The spectra of Nd@SiO$_2$ exhibit changes in line shapes and positions of the luminescent bands compared with crystalline [NdCl$_2$(H$_2$O)$_6$,·Cl]. Most notably the $^4F_{3/2} \rightarrow$ $^4I_{9/2}$ transition found at 920 nm in [NdCl$_2$(H$_2$O)$_6$,·Cl] crystals are shifted by about 40 nm to 880 nm in the Nd@SiO$_2$ samples. A similar position (emission band at 860-920 nm) for this transition was found in a neodymium monochloroacetate single crystal, where the Nd$^{3+}$ is coordinated by 9 (2 sites) or 10 (1 site) oxygen atoms with average bond lengths of 2.501 Å and 2.486 Å (coordination number 9) and 2.552 Å (coordination number 10) [26]. Furthermore we note that the positions and peak shapes of the three different gel samples do not differ, only the luminescence intensity decreases with increasing pore size. This indicates that there is probably no formation of [NdCl$_2$(H$_2$O)$_6$,·Cl] nanocrystals inside the pores.
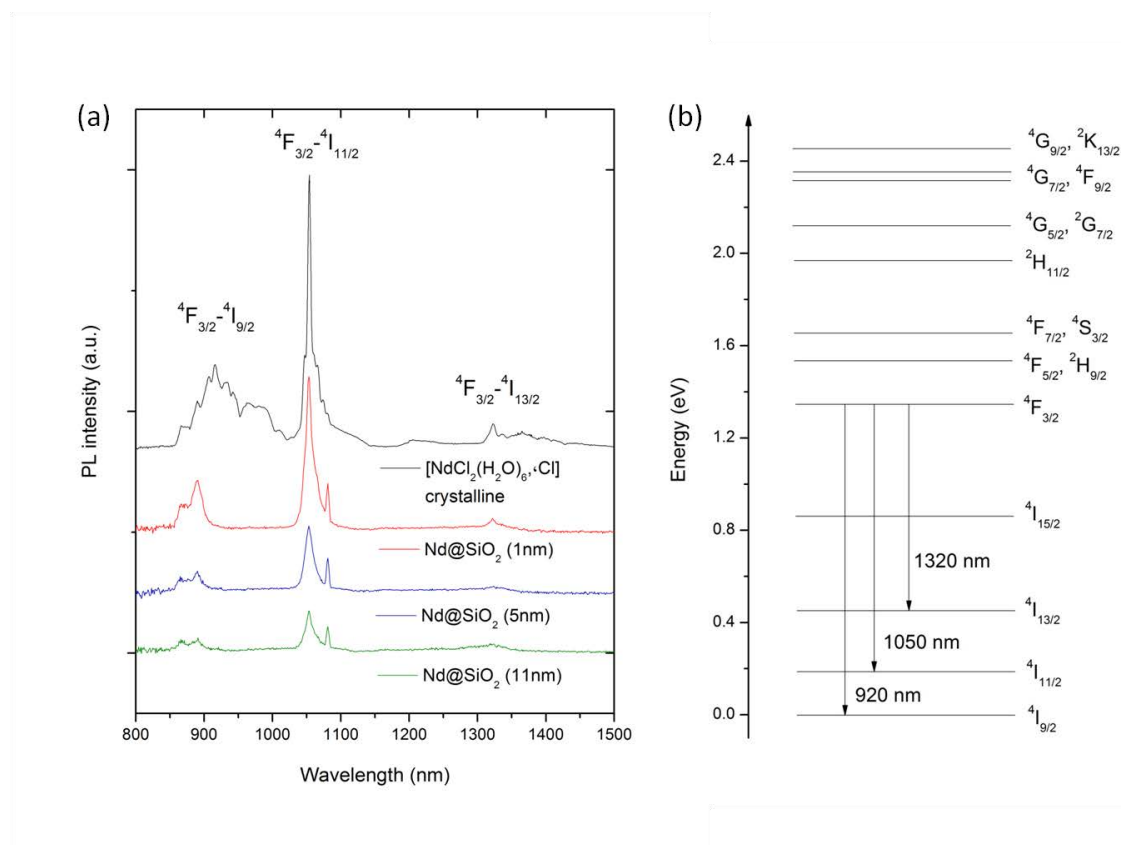


Figure 5.7 (a) Emission spectra of [NdCl$_2$(H$_2$O)$_6$,·Cl] crystalline and Nd@SiO$_2$ monoliths with pore sizes 1 nm, 5 nm, and 11 nm, respectively. (b) Energy level diagram of Nd$^{3+}$ ions and three radioactive intra-4f transitions.

In order to investigate the structural details, especially the coordination number of the embedded $Nd^{3+}$ complexes and their cluster size as a function of pore size, we perform total scattering experiments coupled to PDF and Debye Function Analysis.

## 5.4 Total scattering methods

The structural characterizations of the neodymium doped monoliths ($Nd@SiO_2$) were carried out by using two complementary approaches namely, the PDF technique and the Debye analysis. The total scattering data of empty $SiO_2$ monoliths with pores sizes of 1 nm, 5 nm, and 11 nm and post-doping $Nd@SiO_2$ nanocomposite were recorded, similar to $SNP@SiO_2$ samples, on the powder diffractometer of the MS beamline of the Swiss Light Source (SLS) at the Paul Scherrer Institute (Villigen, Switzerland). Several data sets were collected at room temperature up to $Q_{max}= 24.2$ Å$^{-1}$ using a monochromatic beam of wavelength $\lambda = 0.4962$ Å (energy E = 24.9866 keV) with Debye-Scherrer geometry.

The diffraction patterns of loaded and unloaded $Nd@SiO_2$ xerogels and the corresponding patterns (loaded – unloaded) are shown in Fig 5.8. Interestingly, the difference patterns of the three samples (1 nm, 5 nm, 11 nm pore size) are very similar, exhibiting three main broad Q peaks at about 0.798 Å$^{-1}$, 1.482 Å$^{-1}$, and 2.797 Å$^{-1}$ respectively. Given the strong similarities of the three experimental PDFs resulting in equivalent structural models for the three samples, we will present in the following only the details of the structural analysis of the 1 nm doped sample.
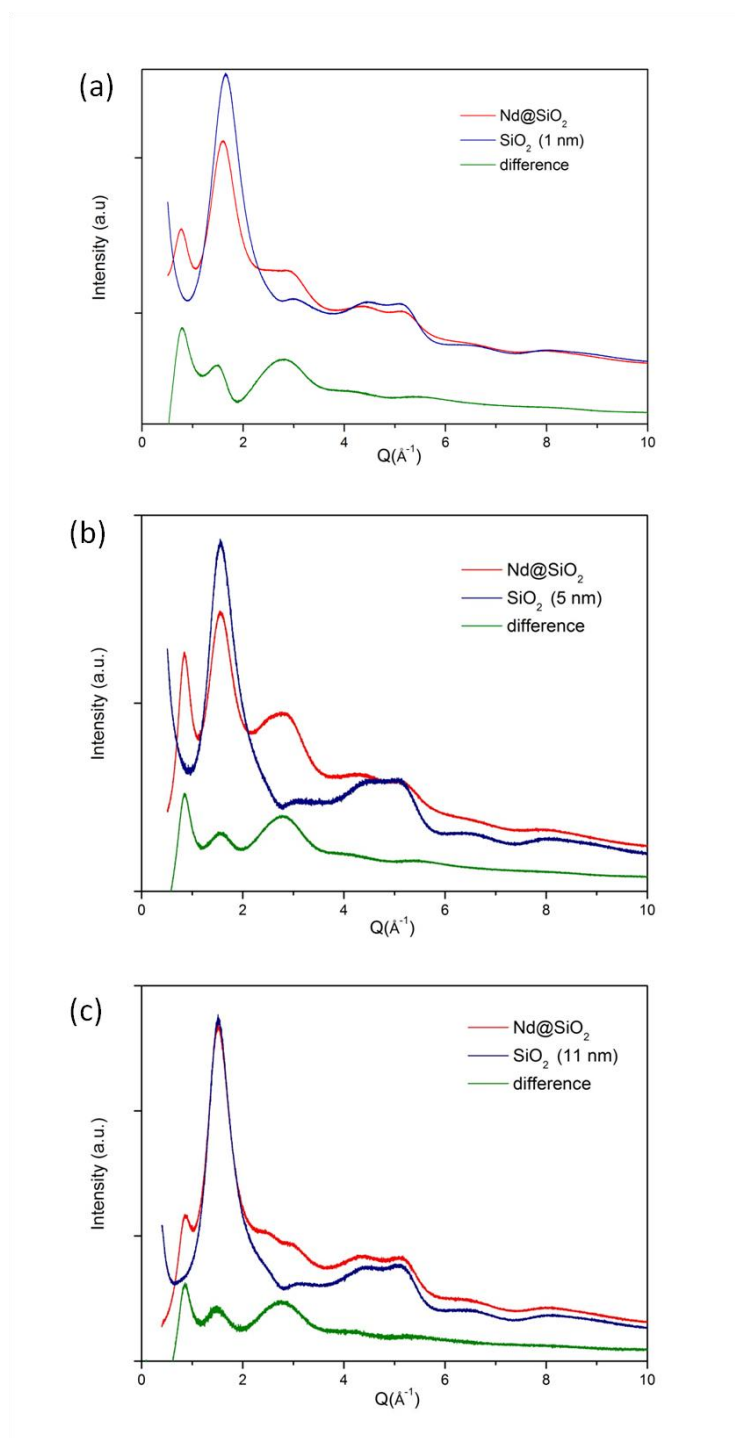
Figure 5.8 Total scattering patterns of Nd-doped monoliths with pore sizes of (a) 1 nm, (b) 5 nm, and (c) 11 nm, respectively. The difference patterns (loaded – unloaded) (green lines) show similar features for the three samples.

### 5.4.1 Differential patterns

In contrast to the example we have seen in chapter 4 the scattering contrast between the unloaded $SiO_2$ and loaded $Nd@SiO_2$ hybrid materials is rather large yielding neat difference patterns (Fig 5.8(a)). This difference is mainly due to the scattering power of the $Nd^{3+}$. The X-ray scattering factor of Neodymium ($f_{Nd}(0) \sim 22.684$ Å$^{-1}$) is dominant with respect to $SiO_2$ ($f_{Si}(0) \sim 6.292$ Å$^{-1}$, $f_O(0) \sim 3.049$ Å$^{-1}$). By comparing the scattering patterns of the empty $SiO_2$ gels and the $Nd@SiO_2$ hybrid materials (Fig 5.9(a)) one can clearly observe that the $Nd@SiO_2$ hybrid materials show additional features at Q=0.84 and 2.77 Å$^{-1}$, that give information on the embedded $Nd^{3+}$ species. This is also reflected by a more pronounced second peak in the total structure function, S(Q) (Fig 5.9(b) and results in an intense peak ~2.56 Å in the PDF diagram(Fig 5.9(c)). This peak can be assigned to the Nd—O pairs in agreement with the PDF results we obtained for crystalline $[NdCl_2(H_2O)_6, \cdot Cl]$.

Fig 5.10 shows the difference patterns (loaded - unloaded) of the patterns shown in Fig 5.9. The structure function, S(Q), shown in Fig 5.10(b) displays two oscillations corresponding to the sin(Qr)/(Qr) in the Debye formula. The main oscillation evident throughout the curve gives rise to the first peak in the PDFs ~2.56 Å, which can be attributed to the Nd—O pairs. The remaining oscillations are due to the second or third nearest neighbor interactions and are dominated by the interactions between the $Nd^{3+}$ cations and the Cl$^-$ ions.

The difference PDF (Fig 5.10(c)) shows three prominent interaction distances below 5 Å at approximately 2.51, 3.12, and 4.81 Å. The region below the first significant peak, *i.e.* low r region (0-~1.4 Å), is often very critical and may contain some errors due to the limitation of the experimental setup and the processing of the data. The broad features of the d-PDF beyond 5 Å might be attributed to the third nearest neighbor distances or intermolecular interactions. Beyond about 12 Å the G(r) function becomes featureless.
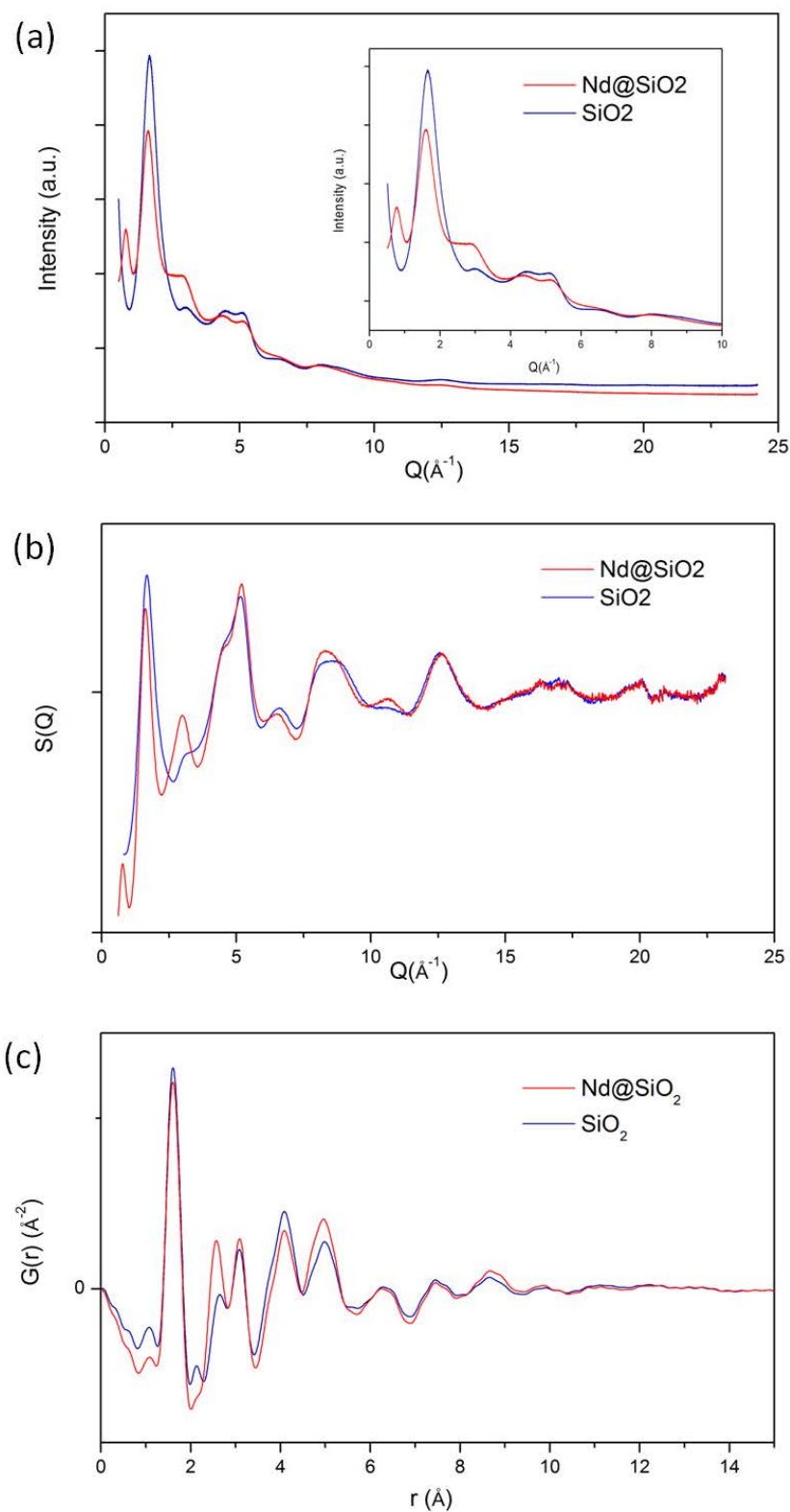
Figure 5.9 The empty $SiO_2$ and $Nd@SiO_2$:(a) X-ray powder diffraction patterns, (b) the total structure function, S(Q), and (c) the corresponding PDFs.
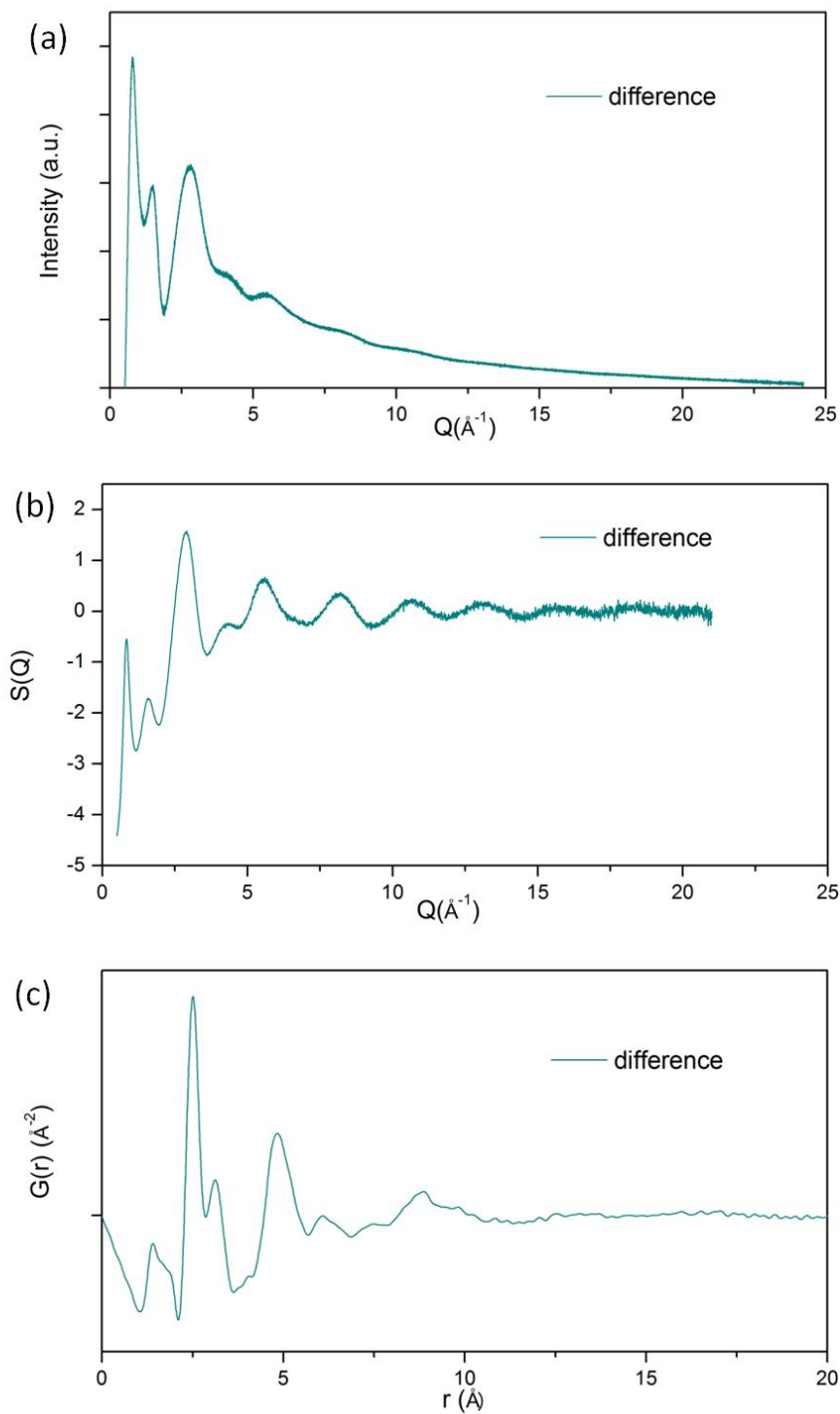
Figure 5.10 (a)The difference pattern subtracted from **Fig 5.9**:, (b) the total structure function, S(Q), and (c) the corresponding PDF.

### 5.4.2 Structure of embedded $Nd^{3+}$ complexes

It is straightforward to verify that the differential G(r) of the embedded $Nd^{3+}$ complexes is different from the initial crystalline configuration, *i.e.* $[NdCl_2(H_2O)_6]^+$ cations. Fig 5.11(a) shows the difference diffraction pattern (loaded – unloaded) in comparison to those of crystalline $[NdCl_2(H_2O)_6 \cdot Cl]$ and an aqueous solution of $[NdCl_2(H_2O)_6 \cdot Cl]$. It becomes clear that the embedded $Nd^{3+}$ complex has a similar diffraction pattern as found for the aqueous solution of $[NdCl_2(H_2O)_6 \cdot Cl]$. This indicates that the local arrangement of the $Nd^{3+}$ cations undergoes a drastic change in the solution before entering into the $SiO_2$ matrix and that it does not recrystallize in its original form within the matrix. As a result, the distance between the $Nd^{3+}$ cations and $Cl^-$ anions (~2.818 Å) in the inner sphere of the crystalline salt disappears in the liquid state, as well as for the embedded $Nd^{3+}$ complexes (sees Fig 5.11(b)). Therefore, we can assume that the embedded $Nd^{3+}$ species have a similar inner coordination sphere as $Nd^{3+}$ in aqueous solution of $[NdCl_2(H_2O)_6 \cdot Cl]$. This local structural rearrangement around the $Nd^{3+}$ cations was also observed in other rare-earth based systems [27–29].

Steele and Wertz have first reported the X-ray diffraction studies on aqueous solution of $LaCl_3$, $LaBr_3$, and $GdCl_3$, with different chloride solutions concentrations. They showed that the Re sites may adopt either 8 fold $[Re(H_2O)_8]^{3+}$ or $[ReCl(H_2O)_7]^{3+}$ configurations depending on the nature and the concentration of the solvent [20]. Habenschuss and Spedding [27–29] have reported a series of local structural studies of rare earth ions in aqueous chloride solutions. It has been shown that the inner coordination spheres for the $La^{3+}$, $Pr^{3+}$, and $Nd^{3+}$ cations are dominated by the nonaaquo $[Re(H_2O)_9]^{3+}$ complex and the octaaquo $[Re(H_2O)_8]^{3+}$ complex is the predominant hydration species for the cations $Tb^{3+}$ through $Lu^{3+}$. Furthermore, in these systems the average $Re^{3+} \cdots Cl^-$ ion pair distances are located on the second sphere shell at about 5 Å.

Based on these literature results, we tested different configurations such as $[NdCl_2(H_2O)_6]^+$, $[Nd(H_2O)_9]^{3+}$ and $[Nd(H_2O)_9]Cl_3$ for describing the inner coordination sphere of the embedded $Nd^{3+}$ complex. For this purpose we used the derived radial distribution function, R(r), instead of the total pair distribution function G(r). It is noteworthy that compared to the G(r) function, the R(r) function is very useful for peak fitting and is more suitable to overcome the difficulties that might arise from the normalization process [30]. The fitting results of the radial distribution function R(r) based on the three models are illustrated in Fig 5.12. One can clearly observe that the bulk crystalline configuration, $[NdCl_2(H_2O)_6]^+$ (Fig 5.12.a), is not appropriate as it produces a

supplementary intense peak at about 2.8 Å corresponding to the Nd-Cl inner sphere interaction which is absent in the experimental data. We can thus conclude that the inner coordination sphere of the embedded $Nd^{3+}$ complex can be described either by a 9-fold $[Nd(H_2O)_9]^{3+}$ or $[Nd(H_2O)_9]Cl_3$ geometry instead of the 8-fold $[NdCl_2(H_2O)_6]^+$ configuration of the crystalline solid state (Fig 5.12.b and c).
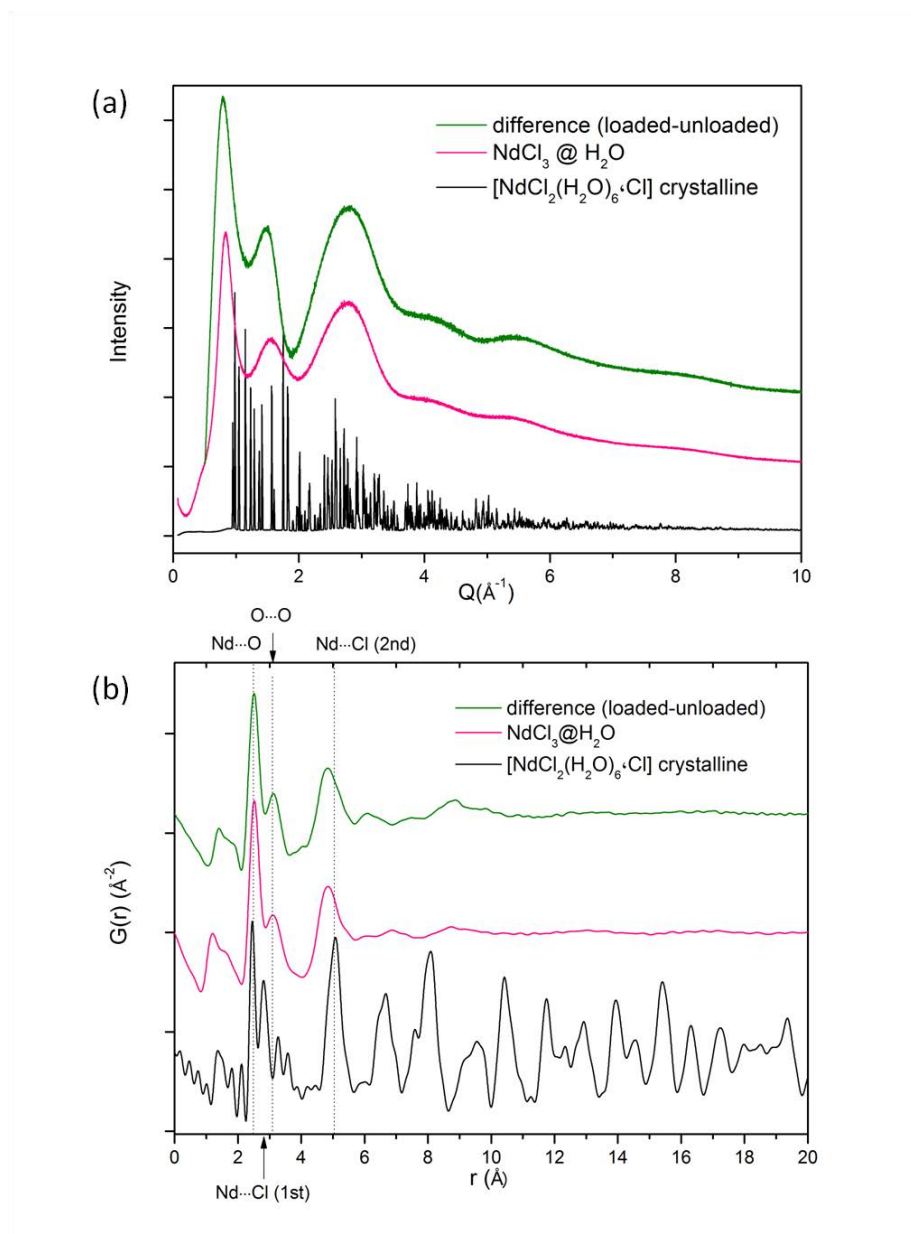


Figure 5.11 (a) X-ray diffraction of difference pattern (loaded - unloaded), aqueous solution of $NdCl_3$ salt, and hydrate $[NdCl_2(H_2O)_6,\cdot Cl]$ crystalline. (b) The corresponding PDFs., where embedded $Nd^{3+}$ complexes show a remarkable change in intensity at ~2.818 Å comparing to $[NdCl_2(H_2O)_6,\cdot Cl]$ crystalline.
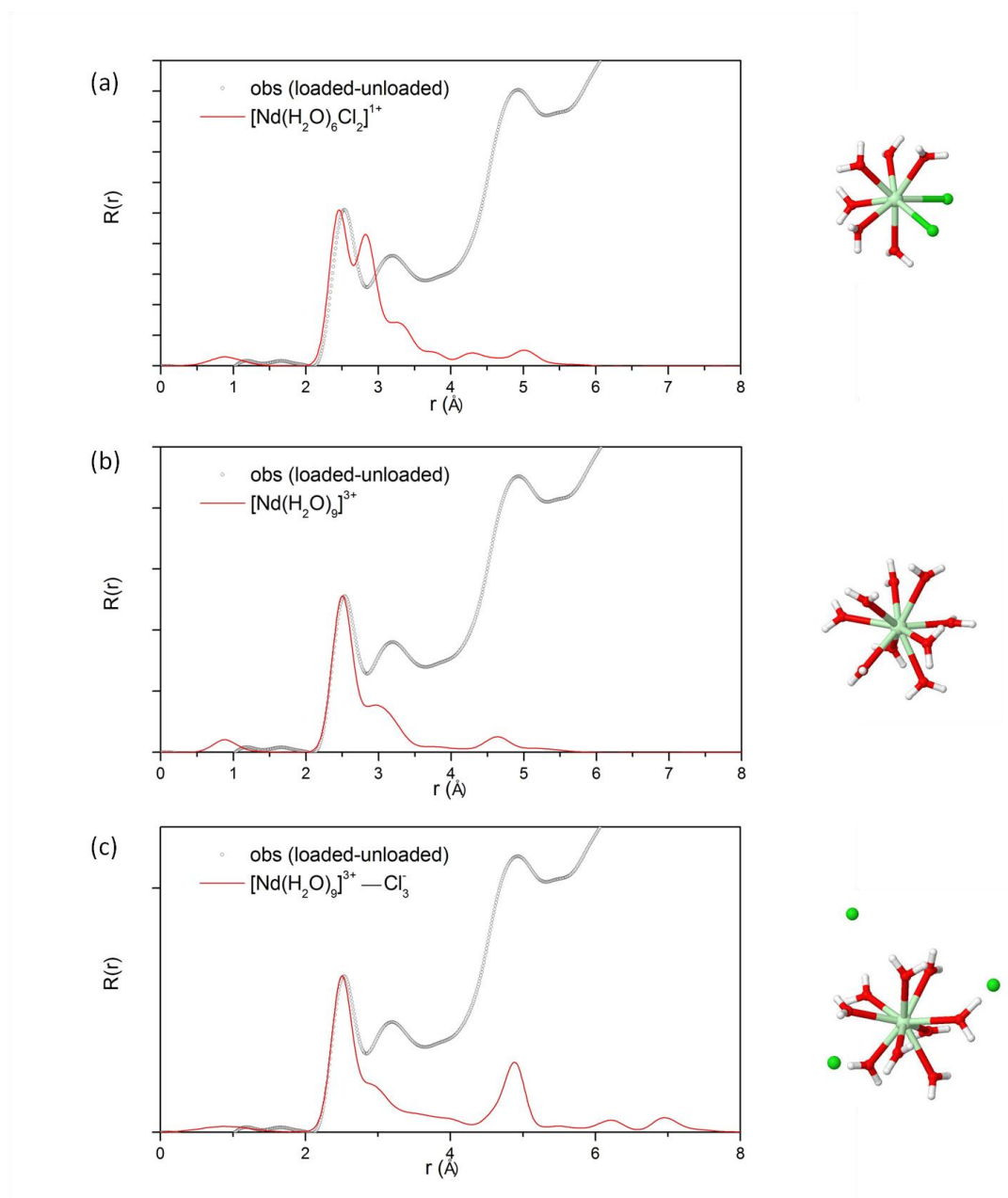
Figure 5.12 Fitting of the R(r) function by different local configuration of the Nd$^{3+}$ cation: (a) 8 fold [NdCl$_2$(H$_2$O)$_6$]$^+$ geometry, (b) 9 fold [Nd(H$_2$O)$_9$]$^{3+}$ configuration, and (c) [Nd(H$_2$O)$_9$]$^{3+}$···3 Cl$^-$ ion pairs model.

Furthermore, the analysis of the remaining peaks was accomplished by fitting the R(r) by Gaussian distributions up to 5 Å. For this, we first assume that the Nd—O interactions corresponding to the first peak ~2.56 Å have an approximate Gaussian distribution, that can be deconvoluted from the rest of the RDF by means of the least squares fit. Then, we

used four additional Gaussian distributions to fit the RDFs up to 5 Å (see Fig 1.13). The second peak ~ 3.12 Å could be deconvoluted by two contributions corresponding to 4~5 $H_2O \cdots H_2O$ inner sphere interactions plus 7~8 $Cl^- \cdots H_2O$ interactions for each $Cl^-$ anion [28], and serve to approximate these interactions reasonably well. Finally, the RDF peak near 4.8 Å was deconvoluted by taking into account the $Nd^{3+} \cdots Cl^-$ outer sphere interactions.
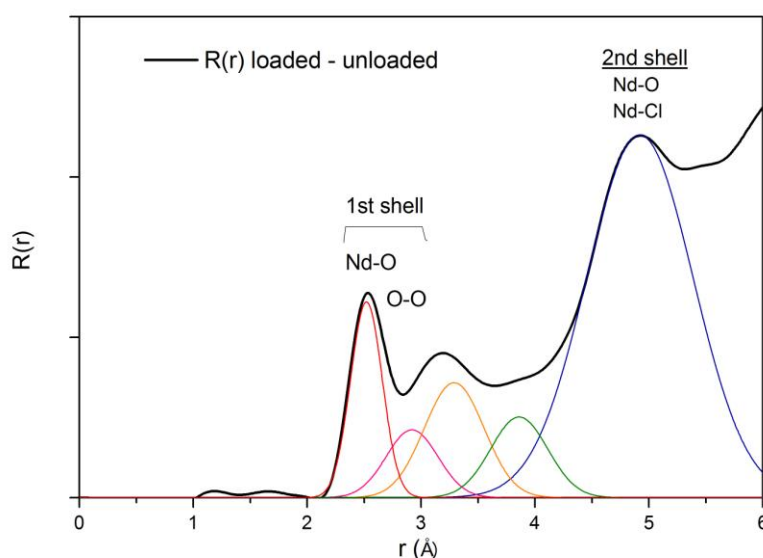


Figure 5.13 The radial distribution function, R(r), fited with four Gaussian distributions up to 5 Å

This deconvoluted model is based on the fact that the embedded $Nd^{3+}$ complexes have very similar local structure as in aqueous solution of $[NdCl_2(H_2O)_6 \cdot Cl]$ salts. Qualitatively, the likely interactions of the nearest neighbour in the $Nd@SiO_2$ hybrid materials are: $O \cdots H$, $Nd^{3+} \cdots H_2O$, $H_2O \cdots H_2O$, $Cl^- \cdots H_2O$, and possibly $Nd^{3+} \cdots Cl^-$. The $O \cdots H$ interaction is very difficult to detect due to the weak scattering power of the hydrogen atoms and will be ignored. The peak at~2.56 Å can be attributed to the $Nd^{3+} \cdots H_2O$ distance. If we assume that no chloride anions penetrate the inner coordination sphere of the rare earth one can expect that the $Nd^{3+}$ cation is coordinated by 9 water molecules (Fig 5.14). As a result, the $H_2O \cdots H_2O$ distances will be near ~2.85 Å and the $Cl^- \cdots H_2O$ interactions vary from 3.1 to 3.3 Å in agreement with the results found in other studies [31]. It is noteworthy that we might estimate the number of $Cl^- \cdots H_2O$

interactions from the deconvoluted contributions (7~8 $Cl^-\cdots H_2O$ interactions), however the analysis of the contributions of $H_2O\cdots H_2O$ interactions is more complicated. In fact, the majority of the $H_2O\cdots H_2O$ interactions should be nearest neighbour distances. However, the water molecules in the hydration sphere would have a distribution of $H_2O\cdots H_2O$ distances varying from normal $H_2O\cdots H_2O$ distances to $H_2O\cdots H_2O$ distances across the $Nd^{3+}$ water complex. This would cause the distribution of $H_2O\cdots H_2O$ distances to trail to longer distances and might cause different position in the PDF. Four to 11 water nearest neighbours have been reported for $Cl^-$ ions in various studies [32,33]. It has been found that the $H_2O\cdots H_2O$ coordination distance for pure water is around 4.4 Å and the number of water nearest neighbours for water molecules in the rare earth chloride hydrates is around 4-5 Å.

The peak near 4.8 Å is due to an array of second nearest neighbour interactions. One of the larger contributions to this peak is from the $Nd^{3+}\cdots Cl^-$ outer sphere ion pairs because of the large scattering power of these ions. The dependence of the position of this peak on the rare earth ion confirms this view. Note that, in the $[NdCl_2(H_2O)_6,\cdot Cl]$ crystalline the shortest outer sphere $Nd^{3+}\cdots Cl^-$ interaction occurs at 5.0638(2) Å.
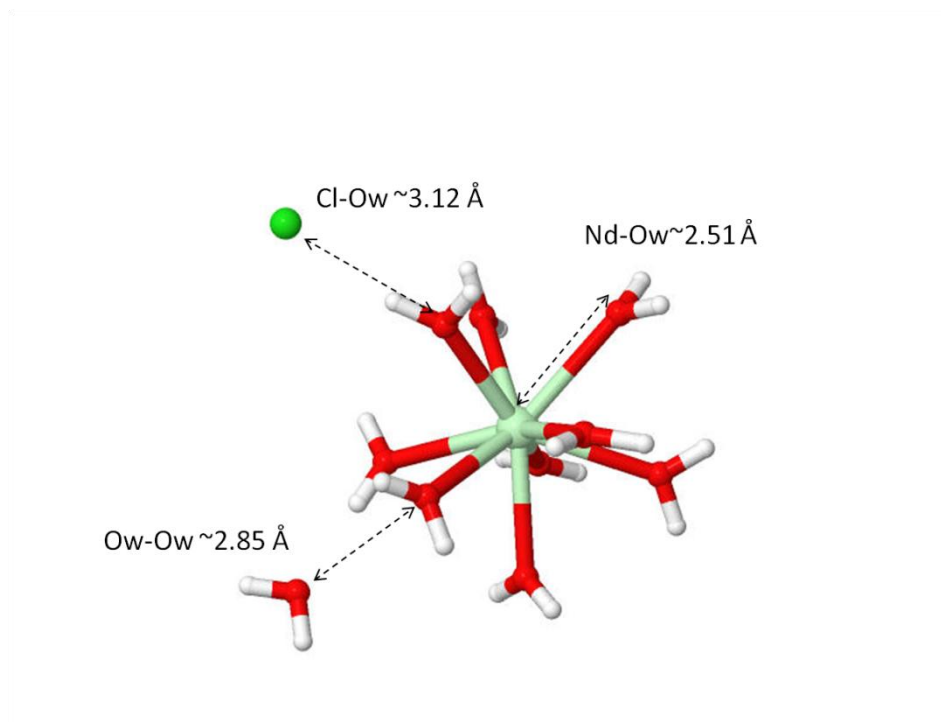


Figure 5.14 The local geometry of 9 fold $[Nd(H_2O)_9]^{3+}$ complex, where $Cl^-$ ion pairs are located on the second shell.

In summary, the embedded $Nd^{3+}$ complexes have similar inner coordination sphere as for aqueous solution of $[NdCl_2(H_2O)_6,\cdot Cl]$. The local structural arrangement of the $Nd^{3+}$ cation can be appropriately described by a 9 fold $[Nd(H_2O)_9]^{3+}$ model with $Nd^{3+}\cdots Cl^-$ outer sphere interactions in contrast to the $[NdCl_2(H_2O)_6,\cdot Cl]$ crystalline, where the $Nd^{3+}$ is eight-fold coordinated by six water molecules and two inner sphere chlorine atoms.

### 5.4.3 Debye function analysis

In view of the difficulty of the d-PDF analysis due to modeling in liquid state, it is worth to verify the same data set by Debye function analysis (DFA) in reciprocal space. For this, an appropriate Q range should be determined, that depends on the average size of the embedded substance. For small clusters of one or two molecules, it is best to choose $Q_{min} = 2\pi/D$ and $Q_{max} = 2\pi/d$, where D is the cluster diameter and d the nearest-neighbor distance [34]. Here the wide angle region ($2 \leqq Q \leqq 6$ Å$^{-1}$) has been chosen for small clusters of one $[Nd(H_2O)_9]^{3+}$ complex. The fit is taken into account by adding a linearly increasing background.

Fig 5.15 shows the subtracted and corrected scattering intensity, together with three different calculated patterns based on three different geometries of the $Nd^{3+}$ complexes. The main peak at Q~2.76 Å$^{-1}$ represents the $\sin(Qr)/(Qr)$ contributions from the inner sphere of complexes, e.g. interactions between Nd—O and O$\cdots$O . For the 8 fold $[NdCl_2(H_2O)_6]^+$ complex, two Chlorine atoms lead to a slight shifting of this peak to lower Q region due to the longer Nd—Cl distances. On the contrary, the 9 fold $[Nd(H_2O)_9]^{3+}$ complex remains on the same position. However, those two models do not account for a small broad peak at ~4.21 Å$^{-1}$, which is principally contributed by the second maximum of the oscillation due Nd$\cdots$Cl pairs (around 4.9 Å). The assumption of ion pairing and 9 fold $[Nd(H_2O)_9]^{3+}$ complex improved the fit quality in the region from 2 to 6 Å$^{-1}$, and even extended to Q>6 Å$^{-1}$ where the data might be influenced by the correlated motions of atoms.

In the previous work of Cervellino [34] further guest-host interaction in the small angle region have been discussed as an explanation for peaks in this range. However, the two extra peaks at Q ~1.53 Å$^{-1}$ and ~0.81 Å$^{-1}$ in the subtracted pattern in our samples are also observed in the aqueous solution (Fig. 5.11a). Thus assigning the peak at Q~1.53 Å$^{-1}$ to a hydration shell of $Nd^{3+}$ complexes, corresponding to the 4$^{th}$ and 5$^{th}$ Gaussian peaks in the R(r) in Fig 5.13 is justified. The position at Q~0.81 Å$^{-1}$ seems to be due to inter-complexes interactions, and corresponds to the broad peaks at r~8.5 Å in the PDFs [29]. The exact

position of this peak in PDFs is modulated by the amount of solvent separating the hydrated $Nd^{3+}$ ions, depending on the concentration. It also appears that the position of this peak is consistent with approximately one layer of water molecules separating the hydrated $Nd^{3+}$ ions on the average.
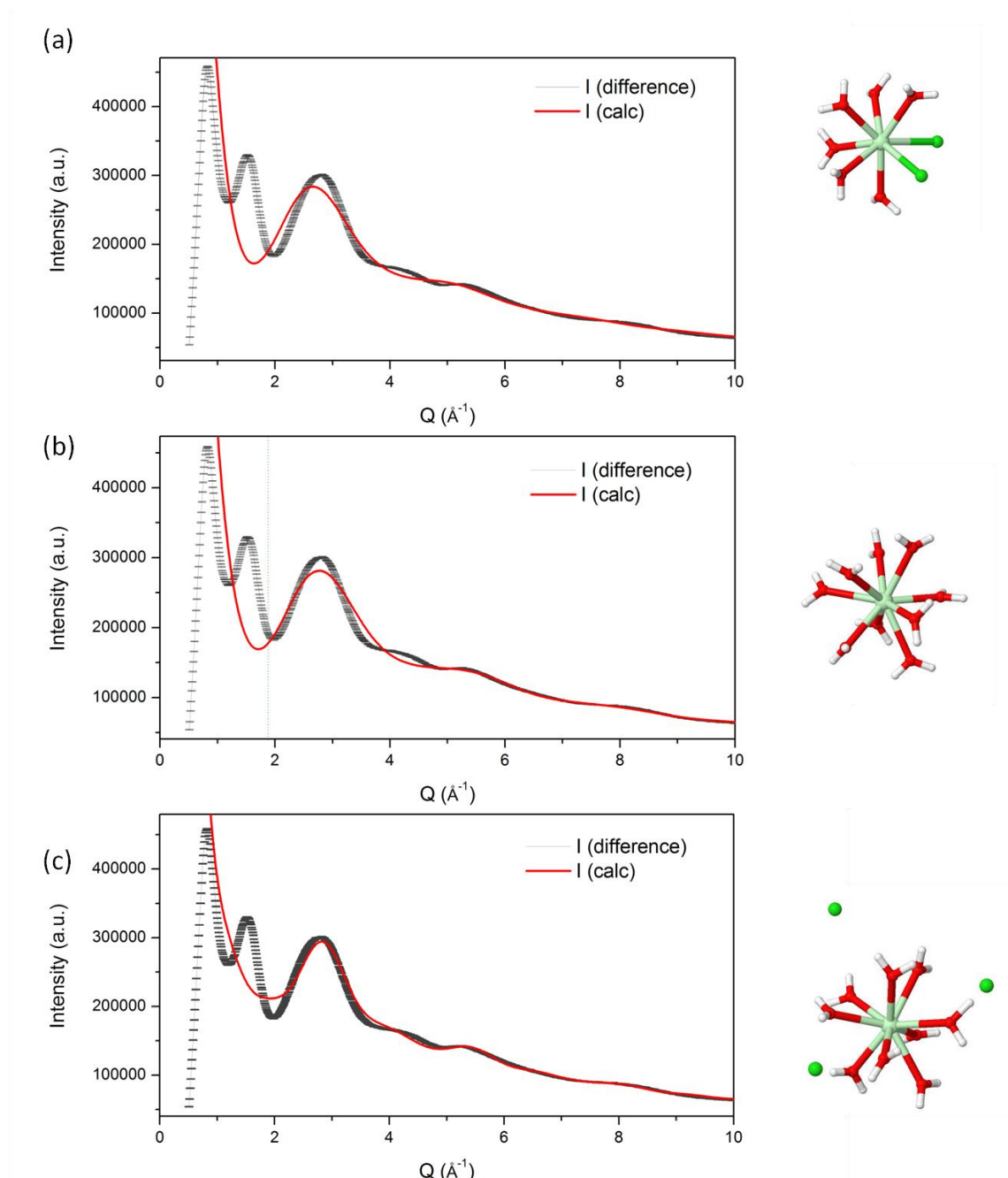


Figure 5.15 Fitting of R(r) by two different geometries: (a) 8 fold $[NdCl_2(H_2O)_6]^+$ complex, and (b) 9 fold $[Nd(H_2O)_9]^{3+}$ complex.

## 5.5 Conclusion

In the crystal structure of [(NdCl$_2$(H$_2$O)$_6$, Cl] complex, the Nd$^{3+}$ cation is eight-coordinated: six water molecules and two chlorine atoms build the inner coordination sphere. The average value of the inner sphere Nd—O$_w$ distance is 2.453(1) Å and is significantly shorter than the Nd—Cl$^-$ distance [2.8180(4) Å]. The outer sphere chloride anion is located at much greater distance of 5.0638(2) from the Nd$^{3+}$ cation without any evidence for direct Nd···Cl$^-$ interaction. The crystal packing consists of three different neodymium pairs linked by a three-dimensional network of O—H···Cl intermolecular interactions.

In aqueous solution of [NdCl$_2$(H$_2$O)$_6$,·Cl] salt, the Nd$^{3+}$ cation is nonacoordinated by water molecules and forms the [Nd(H$_2$O)$_9$]$^{3+}$ species. The average Nd···O$_w$ distance is 2.56 Å in the inner sphere which adopts a local geometric configuration of a tricapped trigonal prism (TTP) about the trivalent Nd. Further, an average Nd$^{3+}$···Cl$^-$ ion pair distance of 4.88 Å is found for the second sphere (i.e. the Cl$^-$ anions).

In the porous host the Nd$^{3+}$ cation adopts also the nonacoordinated configuration like in solution. Further there is evidence from both the d-PDF (R(r) deconvolution) and the DFA that the Cl$^-$ anions are embedded in a second hydration shell around the [Nd(H$_2$O)$_9$]$^{3+}$ cations with an average distance of 4.9 Å, very similar to the structural arrangement in aqueous solution. Note that there is no significant difference in the structures of the embedded complexes for the three different host matrices (1, 5, and 11 nm pore size). Furthermore, absorption and luminescence spectra are in agreement with the interpretation of the embedded complex as a nonacoordinated [Nd(H$_2$O)$_9$]$^{3+}$ with Nd$^{3+}$···Cl$^-$ outer sphere interactions.

This example shows that the DFA can be used to obtain structural information on molecular clusters embedded in porous host matrices. The results are in good agreement with the interpretation based on the R(r) analysis. DFA has the advantage that the refinement is performed in reciprocal space, it thus does not require high Q-values which is needed for a good quality PDF in real space. However, we note also the limitations of both approaches in modeling the second coordination sphere. This is most probably due to the dynamics of the water molecules in the pores, which were not taken into account in our static model.

# Annex 1: Single crystal measurement of [NdCl$_2$(H$_2$O)$_6$, Cl] complex

**Table 1**. X-ray data collection and refinement details for [NdCl$_2$(H$_2$O)$_6$, Cl] complex

| | |
|---|---|
| Chemical formula | NdCl$_2$(H$_2$O)$_6$, Cl |
| Formula weight | 358.69 |
| Temperature | 100(2) K |
| Crystal system, Space group | Monoclinic, *P2/n* |
| Unit cell dimensions (Å): a, b, c | 7.9850(3), 6.5561(2), 9.6727(4) |
| β(°) | 93.655(4) |
| V (Å$^3$) | 505.34(3) |
| Z | 2 |
| Radiation type, Wavelength | Mo Kα, 0.71073 Å |
| Density (calculated) | 2.357 Mg/m$^3$ |
| Absorption coefficient | 5.91 mm$^{-1}$ |
| F(000) | 592 electrons/unit cell |
| Crystal size | 0.06 x 0.04 x 0.01 mm$^3$ |
| **Data collection** | |
| Diffractometer | Oxford SuperNova Dual with an Atlas detector |
| Theta range for data collection | 3.11 to 32.89°. |
| Index ranges | -12<=h<=12, -9<=k<=9, -14<=l<=14 |
| Reflections collected | 8593 |
| Absorption correction | Analytical [CrysAlis PRO, Oxford Diffraction, 2009] |
| T$_{min}$, T$_{max}$ | 0.712 and 0.943 |
| Independent reflections | 1731 [R$_{int}$ = 0.032] |
| Completeness to theta = 30.00° | 99.9 % |
| **Refinement** | |
| Refinement method | Full-matrix least-squares on F$^2$ |
| Data / restraints / parameters | 1793 / 6 / 71 |
| Goodness-of-fit on F$^2$ | 1.03 |
| Final R indices [F$^2$>2σ(F$^2$)], *w*R(F$^2$) | R1 = 0.016, 0.030 |
| R indices (all data) | R1 = 0.017, 0.030 |
| Δρ$_{max}$, Δρ$_{min}$ (e.Å$^{-3}$) | 0.57 and -0.57 |

**Table 3**. Interatomic distances (Å) and bond angles (°) for Hydrogen bonds in the [NdCl$_2$(H$_2$O)$_6$, Cl] complex

| D—H⋯A | D—H | H⋯A | D⋯A | D—H⋯A |
|---|---|---|---|---|
| O1W—H11⋯Cl2[ii] | 0.81(2) | 2.39(1) | 3.194(1) | 171(2) |
| O1W—H12⋯Cl1[iii] | 0.81(2) | 2.33(1) | 3.134 (1) | 177(3) |
| O2W—H21⋯Cl1[iv] | 0.80(2) | 2.38(1) | 3.153 (1) | 163(1) |
| O2W—H22⋯Cl2 | 0.81(2) | 2.36(1) | 3.170 (1) | 171(2) |
| O3W—H31⋯Cl2[v] | 0.82(2) | 2.44(1) | 3.233 (1) | 163(2) |
| O3W—H32⋯Cl1[vi] | 0.79(2) | 2.37(1) | 3.162 (1) | 176(2) |

Symmetry codes: (ii) $-x+2, -y+2, -z+2$; (iii) $-x+3/2, y+1, -z+3/2$; (iv) $x-1/2, -y+1, z+1/2$; (v) $-x+1, -y+1, -z+2$; (vi) $-x+1, -y+1, -z+1$.

## Data Collection and Reduction

To investigate the crystal structure of hexaaquadichloridoneodymium(III) chloride [(NdCl$_2$(H$_2$O)$_6$, Cl], accurate single crystal X-ray diffraction experiment was performed at 100K with an Oxford Diffraction SuperNova Dual Wavelength Microfocus diffractometer equipped with a 135 mm Atlas CCD detector, using Mo Kα radiation ($\lambda$ = 0.71073 Å). The temperature of the sample was controlled with a liquid-nitrogen Oxford Cryostream cooling device. In order to ensure high redundancies, the intensity data were accurately collected using ω oscillation scans of 1° per frame repeated at different φ positions. The radiation exposure time was 30 s per frame. Coverage of reciprocal space was more than 99.9% complete to (sin$\theta_{max}/\lambda$) of 0.704 Å$^{-1}$. The unit cell determination and data integration were carried out using the *CrysAlis Pro* program suite [35]. Absorption effects were corrected by numerical methods based on multifaceted crystal model. The different sets of measured reflections were subsequently merged and scaled using SORTAV [36]. A total of 8593 reflections intensities were merged into 1793 unique reflections. The internal agreement factor for all data is $R_{Int}(I)$ = 0.032 with an average redundancy of 5.

## Crystal structures Determination and refinements

The structure was solved by direct methods and successive Fourier difference syntheses and refined against F$^2$ by weighted full-matrix least-squares methods using the SHELXL97 program [37]. The electron density of the H atoms was clearly identified in a difference Fourier map, and their atomic coordinates and isotropic displacement parameters were refined with O—H distances restrained to 0.84(2) Å. All calculations were carried out using the WinGX software package [38].

# Bibliography

[1]     K. Binnemans, Chem. Rev. **109**, 4283 (2009).

[2]     K.-Y. Hsieh, E.-E. Bendeif, S. Pillet, A. Doudouh, D. Schaniel, and T. Woike, Acta Crystallogr. C **69**, 1002 (2013).

[3]     L. H. Slooff, A. Polman, F. Cacialli, R. H. Friend, G. A. Hebbink, F. C. J. M. van Veggel, and D. N. Reinhoudt, Appl. Phys. Lett. **78**, 2122 (2001).

[4]     K. Kuriki, S. Nishihara, Y. Nishizawa, A. Tagaya, Y. Koike, and Y. Okamoto, J. Opt. Soc. Am. B **19**, 1844 (2002).

[5]     Z. Li, J. Yu, L. Zhou, R. Deng, and H. Zhang, Inorg. Chem. Commun. **12**, 151 (2009).

[6]     S. I. Klink, L. Grave, D. N. Reinhoudt, F. C. J. M. van Veggel, M. H. V. Werts, F. A. J. Geurts, and J. W. Hofstraat, J. Phys. Chem. A **104**, 5457 (2000).

[7]     R. J. Reeves, C. Polley, and J. S. Choi, J. Lumin. **129**, 1673 (2009).

[8]     A. Mussot, M. L. Parquier, B. Berrier, M. Perard, and P. Szriftgiser, Opt. Commun. **282**, 988 (2009).

[9]     E. O. Serqueira, N. O. Dantas, G. H. Silva, V. Anjos, M. J. V. Bell, and M. A. Pereira-da-Silva, Chem. Phys. Lett. **504**, 67 (2011).

[10]   J. C. Pivin, A. Podhorodecki, R. Kudrawiec, and J. Misiewicz, Opt. Mater. **27**, 1467 (2005).

[11]   E. Steveler, H. Rinnert, and M. Vergnat, J. Appl. Phys. **110**, 113518 (2011).

[12]   Ehrt D., Ebendorff-Heidepriem H., and Seeber W., J. Non-Cryst. Solids **183**, 191 (1995).

[13]   S. Tanabe, K. Hirao, and N. Soga, J. Non-Cryst. Solids **142**, 148 (1992).

[14]   V. I. Bukin, Dokl Akad Nauk SSSR **207**, 1332 (1972).

[15]   L. N. Dem'yanets and E. N. Emel'yanova, Kristallografiya **14**, 753 (1969).

[16]   R. A. Zehnder, D. L. Clark, B. L. Scott, R. J. Donohoe, P. D. Palmer, W. H. Runde, and D. E. Hobart, Inorg. Chem. **49**, 4781 (2010).

[17]   J. Pisarska, J. Mol. Struct. **887**, 201 (2008).

[18]   I. A. Sokolov, I. V. Murin, N. A. Mel'nikova, and A. A. Pronkin, Glass Phys. Chem. **29**, 291 (2003).

[19]   A. Habenschuss and F. H. Spedding, Acta Crystallogr. C **9**, 71 (1980).

[20]   M. L. Steele and D. L. Wertz, Inorg. Chem. **16**, 1225 (1977).

[21] C. L. Farrow, P. Juhas, J. W. Liu, D. Bryndin, E. S. Božin, J. Bloch, T. Proffen, and S. J. L. Billinge, J. Phys. Condens. Matter **19**, 335219 (2007).

[22] D. G. Karraker, Inorg. Chem. **7**, 473 (1968).

[23] K. Gatterer, G. Pucker, H. . Fritzer, and S. Arafa, J. Non-Cryst. Solids **176**, 237 (1994).

[24] C. C. Perry and S. Aubonnet, J. Sol-Gel Sci. Technol. **13**, 593 (1998).

[25] R. M. Almeida, X. Orignac, and D. Barbier, J. Sol-Gel Sci. Technol. **2**, 465 (1994).

[26] G. Oczko, J. Alloys Compd. **300–301**, 414 (2000).

[27] A. Habenschuss and F. H. Spedding, J. Chem. Phys. **70**, 3758 (1979).

[28] A. Habenschuss and F. H. Spedding, J. Chem. Phys. **70**, 2797 (1979).

[29] A. Habenschuss and F. H. Spedding, J. Chem. Phys. **73**, 442 (1980).

[30] D. A. Keen, J. Appl. Crystallogr. **34**, 172 (2001).

[31] C. Kepert, B. Skelton, and A. White, Aust. J. Chem. **47**, 385 (1994).

[32] A. H. Narten and H. A. Levy, J. Chem. Phys. **55**, 2263 (1971).

[33] A. H. Narten and H. A. Levy, Science **165**, 447 (1969).

[34] A. Cervellino, J. Schefer, L. Keller, T. Woike, and D. Schaniel, J. Appl. Crystallogr. **43**, 1040 (2010).

[35] *Oxford Diffraction, CrysAlis CCD and CrysAlis RED* (Oxford Diffraction Ltd, Yarnton, Oxfordshire, England, 2009).

[36] R. H. Blessing, J. Appl. Crystallogr. **30**, 421 (1997).

[37] G. M. Sheldrick, Acta Crystallogr. A **64**, 112 (2007).

[38] L. J. Farrugia, J. Appl. Crystallogr. **45**, 849 (2012).

# General conclusion and perspectives

Molecular hybrid materials have been prepared by embedding photofunctional molecules into porous silica hosts with different pore sizes. Two main strategies, based on the sol-gel procedure, have been developed in this work for the incorporation of the molecular guest into the silica matrix, namely, *post-doping* and *pre-doping*. We have focused our investigations in this work on two different photoactive complexes: the photo-isomerisable $(Na_2[Fe(CN)_5NO] \cdot 2H_2O$, SNP) complex and the luminescent $[NdCl_2(H_2O)_6]Cl$ compound.

In the case of SNP@SiO$_2$ the wet-impregnation technique resulted in the formation of isolated molecules when using hosts with pore sizes in the range of 1-3 nm and of small nanoparticles of about 6-7 nm (value determined from PDF analysis) for silica matrices with pore sizes of about 5-6 nm (value determined from BET analysis). The detailed structural analysis of these materials has been performed by using appropriate multiscale approach combining the solid state NMR and pair distribution function analysis based on total X-ray scattering data. The differential PDF modelling allowed for the structural description of the encapsulated SNP complexes. It could be shown that the SNP complex is included as isolated guest in the 1-3 nm pores and the mutual arrangement of $[Fe(CN)_5NO]^{2-}$ anion and $Na^+$ cation could be inferred from the comparison of model structures and experimental PDF. The multi-nuclei solid state NMR experiments have provided evidence that the gel matrix structure is not modified by the SNP embedding process. Furthermore, the NMR investigations confirmed the isolated nature of the guest complex and indicated in addition that the SNP guests are highly mobile in the pores (rotational movement below the μs timescale). In the sample with 5 nm pores two types of structural arrangement are taken: besides the small SNP

nanoparticles with diameter of about 6-7 nm a second SNP population is present, exhibiting the same signature as the isolated SNP complexes found in the 1 nm pores. Again NMR measurements confirm the presence of these two SNP populations and furthermore allow estimate the fraction of the second phase to be lower than 30%. Moreover, using infrared spectroscopy we could show that the embedded SNP retains its interesting optical properties and that its photoswitching characteristics are independent of the particle size. Further solid state NMR measurements coupled to PDF analysis over a wide range of temperature will shed light on the motional regimes present inside the pore which allows obtaining more relevant structural information.

As a second example the $SiO_2$ matrices were impregnated with an aqueous solution of $[NdCl_2(H_2O)_6]Cl$ salt. In this case the complex changes its coordination upon embedding and adopts the nona-coordinated $[Nd(H_2O)_9]^{3+}$ configuration surrounded by a hydration shell containing several water molecules and the three $Cl^-$ counter ions. The coordination of $Nd^{3+}$ by 9 water molecules could be unambiguously determined from the PDF analysis as well as from the Debye function analysis. The modeling of the hydration shell is more complicated: while a static model accounts for the remaining peaks in the experimental patterns, it is not suitable to perform complete refinements. In fact one would probably need to simulate a dynamical model of the $[Nd(H_2O)_9]^{3+}$ - $H_2O$- $Cl^-$ system in order to explain the clearly visible distances in the short range and to account for their washing out in the medium to long range distances. Furthermore, in this system the impregnation of the matrices with 1-3 nm, 5 nm and 11 nm resulted in a very similar diffraction pattern suggesting that in all three cases the same structural configuration is adopted. Thus in this case the impregnation did not yield nanoparticles for the larger pore sizes. The absorption and luminescence properties are in agreement with the structural interpretation as a nona-coordinated neodymium complex. Interestingly, the photoluminescence measurements show that the luminescence intensity decreases with increasing pore size. This behavior can be induced either by the decrease of the neodymium species ( *i.e., decrease of $Nd^{3+}$ ions number*) within the matrix pores or by the concentration quenching effect that results from non-radiative energy transfer processes between $Nd^{3+}$ ions. In this respect, time dependent PL measurements will be very beneficial to determine the origin of such behavior.

From a methodological point of view the two structural studies of SNP and $[NdCl_2(H_2O)_6]Cl$ embedded into silica matrices yielded some interesting results. On the example of SNP@$SiO_2$ we could show that the PDF obtained from laboratory data with

a significantly lower $Q_{max}$ (17 Å$^{-1}$ compared to 25 Å$^{-1}$ for the synchrotron data) allows extracting the same structural information, although with lower precision especially in the range below 5 Å. It is noteworthy that the difference in quality of fit between synchrotron and laboratory measurement is smaller for the amorphous samples (empty $SiO_2$ host and SNP@$SiO_2$) compared to the crystalline reference (SNP powder).

The example with the rare earth compound shows that the refinement in reciprocal space using the Debye Function yields results of comparable quality as the refinement in real space using the R(r) analysis. We note here that in this exemplary case we deal with limited cluster sizes, which is in favor of the DFA. Finally, we see in this example also the limitations of both approaches in modeling the second coordination sphere of a dynamical system. In view of this, the molecular structure will be greatly complemented by using locale probe techniques such as solid state NMR and therefore more extensive and accurate structural properties can be obtained.

# List of publications related to this work

- Z. Tahri, R. Lepski, **K.-Y. Hsieh**, E.-E. Bendeif, S. Pillet, P. Durand, T. Woike, and D. Schaniel, Phys. Chem. Chem. Phys. **14**, 3775 (2012), "Properties of metastable linkage NO isomers in Na2[Fe(CN)5NO]·2H2O incorporated in mesopores of silica xerogels"

- **K.-Y. Hsieh**, E.-E. Bendeif, S. Pillet, A. Doudouh, D. Schaniel, and T. Woike, Acta Crystallogr. C **69**, (2013), "Structural reinvestigation of the photoluminescent complex [NdCl2(H2O)6, Cl]"

- **K.-Y. Hsieh**, E.-E. Bendeif, A. Gansmuller, S. Pillet, D. Schaniel, and T. Woike, RSC Advances, (2013), "Structure and dynamics of single molecules confined in a mesoporous silica matrix: a joint NMR and PDF characterisation", accepted.

# Conference & School

- Hercules: Neutron and Synchrotron Radiation (Session A: Physics and Chemistry of Condensed Matter):
  Poster, Grenoble, 2011/2/27

- Journées Philip Coppens
  Oral, Nancy, 2011/9/20

- ADD workshop: Analysis of Diffraction Data in Real Space
  Poster, Grenoble, 2011/10/12,

- Laue Day and 20th Annual Meeting of the German Crystallographic Society (DGK)
  Poster, Munich (Germany), 2012/03/12,

- DISCUS simulation package workshop
  Erlangen (Germany), 2012/09/13

- Ecole Doctorale de Chimie et Physique Moléculaires (Journée Scientifique)
  Oral, Metz, 2012/11/08

- GDR MCM-2 : Magnétisme et Commutation Moléculaires
  Oral, Dourdan, 2012/12/15

# PCCP

www.rsc.org/pccp

**PAPER**

# Properties of metastable linkage NO isomers in Na$_2$[Fe(CN)$_5$NO]·2H$_2$O incorporated in mesopores of silica xerogels

**Zakaria Tahri,[a] Robert Lepski,[b] Kuan-Ying Hsieh,[a] El-Eulmi Bendeif,[a] Sebastien Pillet,[a] Pierrick Durand,[a] Theo Woike[c] and Dominik Schaniel*[a]**

We study the properties of photoinduced metal–nitrosyl linkage isomers in sodium nitroprusside (SNP) as a function of particle size. By embedding the molecular complex at various concentrations into mesopores of silica xerogels the size of the particles can be adjusted. The ground state is characterized by X-ray diffraction, absorption and infrared spectroscopy. The physical properties of the photoswitched molecules were analysed by steady-state low-temperature absorption, infrared spectroscopy and by nanosecond transient absorption spectroscopy. The electronic structure as well as the activation energies of the metastable linkage isomers are independent of the particle size down to single isolated molecules, indicating that the SNP complexes are quasi-free inside the pores of the gel.

## 1 Introduction

The generation of photoinduced nitrosyl linkage isomers in Na$_2$[Fe(CN)$_5$NO]·2H$_2$O (SNP) is connected with a photochromic and photorefractive response of the material which renders it interesting for optical applications.[1–6] Such applications would demand a more robust and industrial processing than growing single crystals. A potential route to applicable materials is the embedding of the complex into polymers or sol–gel based materials like silica or titania matrices or the deposition on functionalized surfaces.[7–20] From a fundamental point of view it is interesting to study the properties of the complex and its photoinduced linkage isomers as a function of particle size and variation of the environment. First studies of (CN$_3$H$_6$)$_2$[Fe(CN)$_5$NO] embedded in bulk silica xerogels indicated that the structure of the complex remains close to that found in single crystals[21] and that the [Fe(CN)$_5$NO]-molecule retains its ability to form linkage isomers.[11] In the case where the molecule is electrostatically attached to thin films of mesoporous TiO$_2$ deposited on silicon, the photofunctionality is changed towards a release of the NO and CN ligands upon irradiation.[13] These different functionalities depend on the electronic structure and on the characteristics of the potential energy surface. The generation of linkage isomers in such X$_n$[ML$_5$NO]$y$H$_2$O complexes with different transition metals M such as nickel,[23,24] ruthenium,[25–29] osmium,[30] iron,[31] platinum,[32,33] different ligands

L such as F, Cl, Br, I, OH, CN, NH$_3$, NO$_2$, pyridine, different counter ions X$_n$ such as (CN$_3$H$_6$), alkali, earth alkali, halogen, NH$_4$, and different amounts $y$ of crystal water[34] can be described in a generalized potential scheme as illustrated in Fig. 1.[22] The optical excitation leads to a change in the bond between the central metal atom M and the NO ligand which triggers the rotation of the NO group. If the excited state potential possesses a minimum close to the saddle point of the ground state surface between the ground state (GS) and the metastable state S1 or S2 or crosses that surface, the relaxation towards S1 or S2 can occur. It was recently shown that the relaxation into S2 occurs with a time constant of 200 femtoseconds.[35] The NO ligand rotates from the N-bound

$^a$ *CRM2 UMR 7036, Institut Jean Barriol, Université de Lorraine, BP 70239, 54506 Vandoeuvre les Nancy, France.*
  *E-mail: dominik.schaniel@crm2.uhp-nancy.fr;*
  *Fax: 0033 383 684300; Tel: 0033 383 684889*
$^b$ *I. Physikalisches Institut, Universität zu Köln, Zülpicher Str. 77, 50674 Köln, Germany*
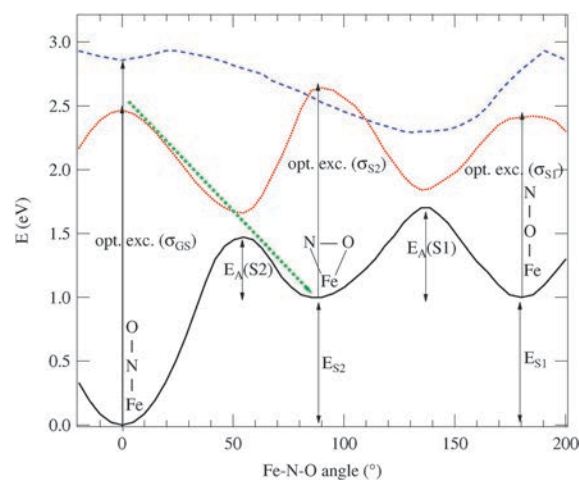$^c$ *Institut für Strukturphysik, TU Dresden, Zellescher Weg 16, Dresden, Germany*

**Fig. 1** Potential scheme illustrating the characteristic points of the potential surface and relaxation pathways during generation of linkage isomers in ML$_5$NO compounds.[22]

This journal is © the Owner Societies 2012

*Phys. Chem. Chem. Phys.*, 2012, **14**, 3775–3781 | 3775

configuration (M–N–O) in GS either to the O-bound configuration M–O–N (S1) by nearly 180° or by about 90° to the side-on bound configuration $M\underset{N}{\overset{O}{<}}$ (S2).[36–38] These new structures correspond to two different potential minima (S1, S2) in the relaxed GS potential.[22,39,40] In SNP the linkage isomers are separated from the GS by potential barriers of $E_A = 0.68$ eV (S1) and $E_A = 0.47$ eV (S2), so that at low temperatures they exhibit lifetimes $t > 10^6$ s.[41] At low temperature the population, *i.e.* number of transferred molecules into S1 or S2, depends on the absorption cross sections $\sigma_{GS,S1,S2}$ for population and depopulation that establish the photostationary state. In order to explore the properties of isolated $ML_5NO$ molecules and the generation conditions of photoinduced linkage isomers in these conditions we studied the electronic structure and potential energy surface of SNP embedded in silica xerogels using X-ray diffraction, absorption and infrared spectroscopy, and transient transmission measurements.

## 2 Experimental details

### 2.1 Synthesis of silica–SNP hybrids

Silica–SNP hybrids were prepared following the two slightly different procedures described hereafter.

(1) Procedure A: 1.5 ml of tetramethoxysilane (TMOS, 98% purity, Fluka), 1.8 ml of methanol (VWR) and 3.6 ml of distilled water were mixed and stirred for 5 minutes which allowed the solution to gel. Then 3.1 ml of two different concentrations (0.1 mol l$^{-1}$ and 0.01 mol l$^{-1}$) of aqueous SNP solutions were added and stirred for another 5 minutes in a glass dish. The mixtures were kept at 50 °C for 7 days in an oven and dried at room temperature in air for 1 week. The resulting SNP concentrations were 310 and 31 μmol per gel.

(2) Procedure B: 1.5 ml of TMOS, 1.8 ml of methanol (VWR) and 3.6 ml of distilled water and different amounts of 0.25 mol l$^{-1}$ aqueous SNP solutions were mixed and stirred for about 30 minutes. The amount of water was kept constant at 3.6 ml, *e.g.*, when 2.0 ml of aqueous SNP solution was added only 1.6 ml of pure $H_2O$ was added. By varying the amount of added SNP solution the concentration of SNP was varied between 12.5 and 875 μmol per gel. After 30 minutes the gels in the glass dish were covered by parafilm or a cap and put into a dry chamber for 1 week at 50 °C in order to allow for complete gelation. Then small holes were pierced into the parafilm or the cap in order to allow for a complete evaporation of remaining solvents in about 1 week. Then the parafilm or cap was completely removed and the gel dried for further 4–8 weeks in the dry cabinet. Finally the dried gels were put in an exsiccator at $10^{-3}$ mbar in order to remove remaining solvent molecules.

### 2.2 X-Ray diffraction

X-Ray powder diffraction measurements were performed on a PANalytical XPert system equipped with a reflection spinner, scanning $2\theta$ from 5 to 68° using Cu K$\alpha_1$ radiation ($\lambda = 1.5406$ Å). The particle size $L$ of embedded nanoparticles of SNP was determined from the broadening of the Bragg peaks according to Scherrer's formula $\Delta(2\theta) = K/L\cos\theta_0$ using the Scherrer factor $K = 0.9$ for the Bragg peak at $2\theta_0 = 30.9°$ corresponding to $Q = 4\pi\sin\theta_0/\lambda = 2.173$ Å$^{-1}$ (see Fig. 2).
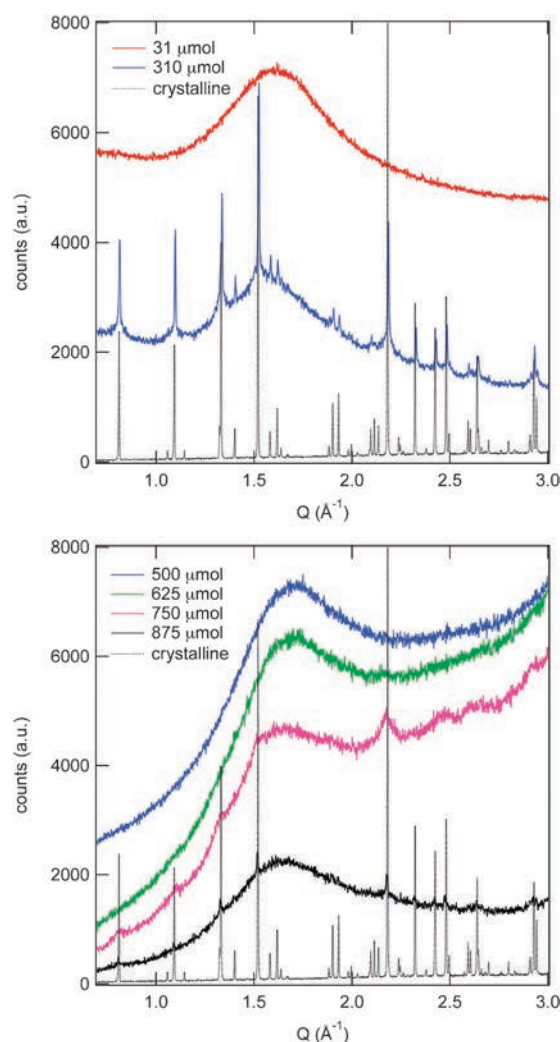


**Fig. 2** X-Ray diffraction pattern of xerogels with different concentrations of SNP synthesized according to procedures A (top) and B (bottom). With decreasing concentration the particle size of the embedded SNP decreases as can be seen from the broadening and subsequent disappearance of the Bragg peaks. The dotted line indicates the powder diffraction pattern of crystalline SNP.

### 2.3 UV/Vis and infrared spectroscopy

UV-Vis absorption spectra were recorded using a Shimadzu UV-3600 UV-Vis-NIR spectrophotometer. For the low-temperature measurements a home-built cryostat was used, where the sample was positioned in a $N_2$ gas atmosphere. The double-walled cryostat is equipped with glass windows that allow for measurement and *in situ* illumination of the samples. The molar extinction coefficient $\varepsilon(\lambda)$ was determined according to the Lambert–Beer law $E(\lambda) = -\log(I/I_0) = \alpha(\lambda)d = \varepsilon(\lambda)cd$, where $E(\lambda)$ denotes the measured absorption, $I$ and $I_0$ the intensity of the probe and reference beam, $c$ the concentration of SNP complexes in the sample, and $d$ the thickness of the sample. Knowing the volume of the prepared disk-like samples (procedure B), $V_{Gel} = \pi r^2 d$, $r$ being the radius of the disk and $d$ the thickness, the concentration of samples is given by $c = n/V_{Gel}$, $n$ being the number of moles per gel, as indicated above. The infrared spectra were collected using a Nicolet 5700 FTIR

spectrometer with a resolution of 2 cm$^{-1}$. The samples were finely ground, mixed with KBr, and pressed to pellets. To ensure good thermal contact for the low-temperature measurements the pellets were contacted with silver paste on the cold finger of a home-built cryostat. The samples were cooled to liquid nitrogen temperature (80 K) in the evacuated sample chamber (10$^{-6}$ mbar). The cryostat is equipped with CsI windows allowing for collection of spectra in the range 8000–260 cm$^{-1}$ and for *in situ* illumination with lasers. The excitation of the samples at low temperature was performed with different laser sources with wavelengths ranging from 325 nm up to 1064 nm.

### 2.4 Time-resolved transmission measurements

The generation and relaxation of light-induced metastable states at different temperatures in a SNP crystal and the different SNP gels are measured by transient absorption spectroscopy with nanosecond time resolution. The pump pulses that excite the sample were provided by a Surelite™ laser with wavelength $\lambda_p$ = 532 nm corresponding to the frequency doubled pulse of the fundamental at $\lambda$ = 1064 nm, with a pulse duration of $\tau_p$ = 5 ns. This pump pulse is guided by two mirrors and focussed by a lens in order to obtain a diameter of about $d_p$ = 0.4 cm on the sample surface and an energy of 35 mJ per pulse. The pump laser pulse is delivered on demand by an external control. The probe light was provided by a cw He–Ne laser centred at 632.8 nm that was focussed by a lens to a spot size much smaller than the pump pulse in order to ensure proper overlap of the probe and pump pulse on the sample position. The probe light is detected by a 200 MHz Si-Pin diode from Femto Messtechnik GmbH. The output voltage of the detector is sampled using a 1.5 GHz oscilloscope (Lecroy Wavepro 715zi). The trigger is obtained from another fast Si-Pin diode (Thorlabs PE310) that detects a part of the reflected light from the first guiding mirror. In order to block the pump light a color filter RG610 (FGL610 Thorlabs) and an interference filter IR632.8 (Coherent, FWHM = 10 nm) are mounted in front of the probe diode, attenuating the 532 nm light by a factor of 10$^{-6}$. The measurements are performed as a function of temperature in the range 190–290 K. For this reason, the samples are mounted on the cold finger of an Oxford Instruments cryostat in a sample holder sandwiched between two thin glass plates to ensure good thermal contact and plane surfaces. The optical absorption changes induced due to the excitation of metastable states are measured as $\alpha_{li}$ = (1/$d$)ln($I(t = 0)/I(t)$), where $d$ is the thickness of the sample and $I(t)$ and $I(t = 0)$ are, respectively, the intensity of the probe beam measured after and before the pulse irradiation. A typical trace is obtained by averaging 100 acquisitions in order to improve the signal to noise ratio.

## 3 Experimental results and discussion

### 3.1 Structural characterization

The synthesized xerogels with embedded SNP were characterized by X-ray diffraction. The top panel of Fig. 2 shows the powder diffraction patterns of the two samples prepared according to procedure A. For the sample with higher concentration ($c$ = 0.1 mol l$^{-1}$ corresponding to 310 µmol SNP in the gel) Bragg peaks are clearly visible and can be attributed to the

structure of SNP (orthorhombic, space group *Pnnm*).[36] The reference diffraction pattern of a SNP powder sample is indicated by dashed lines in Fig. 2. The peak positions of the particles formed within the gel and that of the crystalline reference sample coincide perfectly, clearly showing that the embedded particles exhibit the same structure as the crystalline phase of SNP. The peaks of the SNP xerogel sample are broadened and the evaluation of the broadening according to Scherrer's formula yields a particle size of 83 nm. Note that this particle size corresponds to an average particle size. In fact the peaks exhibit an even more broadened base indicating the presence of particles smaller than 83 nm in the gel. The broad peak at $Q$ = 1.6 Å$^{-1}$ is due to the amorphous SiO$_2$ matrix. For the sample with a ten times lower concentration ($c$ = 0.01 mol l$^{-1}$ corresponding to 31 µmol SNP in the gel) no traces of Bragg peaks could be detected, indicating that SNP is embedded as isolated complexes in the pores of the xerogel.[21] It is worth noting in this case that the amount of water used in the synthesis is identical for the two samples with different SNP concentrations; the porosity of the corresponding formed xerogel is thus expected to be quite similar and of the order of 1 nm.[21] As a consequence, the size of the embedded particles is independent of the pore size, indicating that the nanoparticles are formed before the xerogel matrix has become too rigid.

The bottom panel of Fig. 2 shows the powder diffraction patterns of four samples prepared according to procedure B at concentrations of 875, 750, 625, and 500 µmol per gel. The average particle sizes determined from the peak broadenings are 200 nm for a concentration of 875 µmol SNP per gel and 11 nm for 750 µmol SNP per gel. In the sample with 625 µmol SNP per gel the peaks are so broad that the analysis becomes difficult. An estimate yields particles of size 2–3 nm. At concentrations of 500 µmol and less SNP per gel no traces of Bragg peaks could be detected indicating again that SNP is embedded in the form of isolated complexes.

These structural measurements clearly show that the initial concentration of SNP in the gel solution determines the particle size. For low enough concentrations the SNP complexes occur isolated in the pores of the xerogels, a result that is in agreement with previous studies.[11,21] We note however that different procedures of sol–gel production lead to different results with respect to the size of embedded particles. By procedure A a concentration of 310 µmol SNP in the gel produces rather large particles of 83 nm, while the same concentration in procedure B results in isolated molecules in the gel. In procedure A the amount of H$_2$O used in the synthesis was superior compared to that in the procedure B (6.7 ml *vs.* 3.1 ml). It is known that the gelation is slowed down when the amount of H$_2$O in the starting solution is increased. The SNP guest has thus more time to crystallize in procedure A, a fact which explains the observed larger particle sizes for lower concentrations obtained in procedure A compared to B. It would be thus important to measure the particle size within each synthesized sample, as small variations in the sol–gel process can lead to quite different results.

### 3.2 Properties of linkage isomers

Infrared spectroscopy is a fast and efficient tool to identify the photoinduced linkage isomers, which is suitable also for the characterization of molecules embedded in silica matrices.[11]

Fig. 3 shows the infrared spectra collected at 80 K in the range 1550–2250 cm$^{-1}$ in a gel with 375 µmol SNP that was synthesized using procedure B. This corresponds to a concentration where SNP is embedded as an isolated complex in the pores of the silica matrix. In the GS we can clearly identify the $\nu$(NO) and $\nu$(CN) stretching vibrations at 1947 and 2149 cm$^{-1}$, respectively. The band at 1650 cm$^{-1}$ is the deformation mode $\delta(H_2O)$ of water, which is very broad due to the disordered position of the $H_2O$ molecules and possibly the presence of hydrogen bonds within the pores. Compared to crystalline SNP, where the $\nu$(NO) and $\nu$(CN) stretching vibrations are found at 1947 and 2147 cm$^{-1}$, respectively,[42] no significant shifts are observed. However the fourfold splitting of the $\nu$(CN) stretching vibrations (2147, 2163, 2168, 2177 cm$^{-1}$) present in crystalline SNP has disappeared in the gel. This and the broadening of all vibrations are due to the lack of the crystalline environment in the gel and a consequence of the disordered arrangement and the environment of isolated molecules in the mesopores of the xerogel.

The illumination with 458 nm at 80 K generates the metastable state S1, which can be identified by a new $\nu$(NO) band appearing at 1828 cm$^{-1}$. The decrease in the area of the GS band at 1947 cm$^{-1}$ yields the amount of transferred molecules, i.e. the population of S1, of 17%. A subsequent illumination with 1064 nm transfers the molecules from S1 towards S2 and partially back to GS. As can be seen from Fig. 3 the S1 band disappears and the GS band increases. The new band of S2 is hidden in the $H_2O$ absorption band, but can be identified from a difference spectrum, shown as the inset. The band of S2 is found at 1684 cm$^{-1}$ and the population determined from the GS area is about 7%. Compared to the crystalline SNP, where the $\nu$(NO) stretching vibrations of S1 and S2 are found at 1835 and 1664 cm$^{-1}$, respectively, we observe a shift of 7 and 20 cm$^{-1}$ for S1 and S2, respectively. The large width of the two bands in the xerogel samples of 40 and 60 cm$^{-1}$ for S1 and S2 is a clear hint for the disordered arrangement of the molecules within the pores and possibly weak interactions with the matrix, e.g. with OH groups on the pore surfaces. In general we could expect that S2 with its side-on position reacts more sensitively upon small local structural changes that could occur in the isolated complexes in the gel
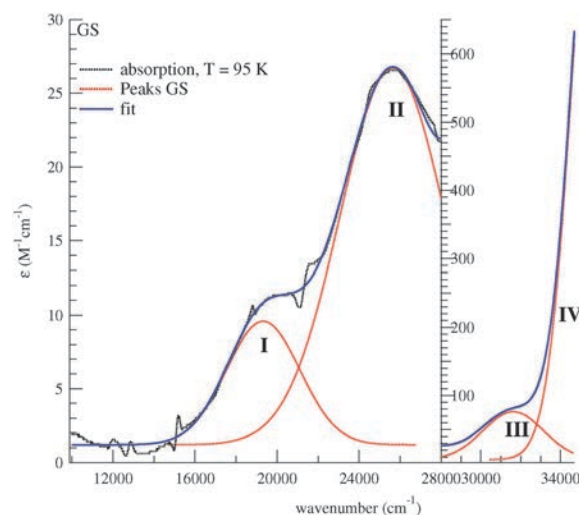


Fig. 4 Absorption spectrum of SNP embedded in silica xerogels at 95 K. The concentrations of SNP are 400 µmol (left) and 62.5 µmol (right), such that SNP is embedded in the form of isolated complexes in the mesopores of the silica host. The dotted curves I–IV denote the Gaussian deconvolution of the spectrum.

compared to the crystalline packing,[21] which might explain the more pronounced broadening. The population of 17% is in the range of the population achieved in powder samples indicating that the orientation of the fourfold axis of the molecules is statistically distributed.

UV-Vis absorption spectroscopy delivers information about the electronic structure of the compound in its different configurations. In the case of photoinduced metastable linkage isomers, the low temperature measurements yield in addition information about the spectral ranges for photoswitching.[43] Fig. 4 shows the absorption spectra in the GS at 95 K for two SNP silica xerogel hybrids. Both have concentrations below the threshold for nanoparticle formation, i.e. less than 500 µmol SNP per gel synthesized according to procedure B. The left part of Fig. 4 shows the absorption spectrum of a 400 µmol SNP gel with the two absorption bands at 19 300 cm$^{-1}$ (I) and 25 600 cm$^{-1}$ (II) with molar extinction coefficients of $\varepsilon$(I) = 8 M$^{-1}$ cm$^{-1}$ and $\varepsilon$(II) = 25 M$^{-1}$ cm$^{-1}$ (deconvolution with Gaussian bands). The right hand side shows the absorption spectrum of a 62.5 µmol SNP gel for illustration of the high-energy bands at 31 600 cm$^{-1}$ (III) and 37 000 cm$^{-1}$ (IV). The lower concentration simply allows for measuring up to higher energies. The molar extinction coefficients are $\varepsilon$(III) = 70 M$^{-1}$ cm$^{-1}$ and $\varepsilon$(IV) = 900 M$^{-1}$ cm$^{-1}$ (estimated value). For comparison the four absorption bands in crystalline SNP are found at 19 800 cm$^{-1}$ (I), 25 950 cm$^{-1}$ (II), 31 750 cm$^{-1}$ (III), and 37 600 cm$^{-1}$ (IV) for polarization along the crystallographic $a$-axis.[43] There is thus only a slight redshift of maximal 500 cm$^{-1}$ in the xerogel compared to the crystal, an effect known from SNP in solutions.[44,45] Consequently the assignment of the absorption bands to the transitions $d_{xy} \rightarrow \pi$(NO) (I, HOMO–LUMO), $d_{xz,yz} \rightarrow \pi$(NO) (II), $d_{xy} \rightarrow d_{z^2}$ (III) and $d_{xz,yz} \rightarrow d_{z^2}$ (IV) is the same as found in single crystals[43] and solutions.[44]

In order to explore the electronic structure of S1 and S2 we performed absorption measurements at low temperature after illumination with 488 nm and subsequent illumination with
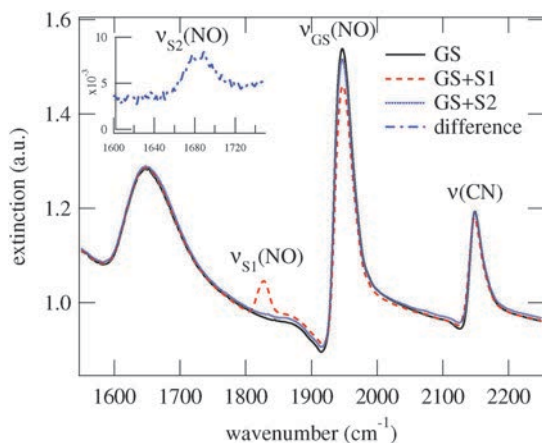


Fig. 3 Infrared spectra at $T$ = 80 K of a SNP xerogel in GS and after irradiation with 458 nm and 1064 nm for S1 and S2, respectively.
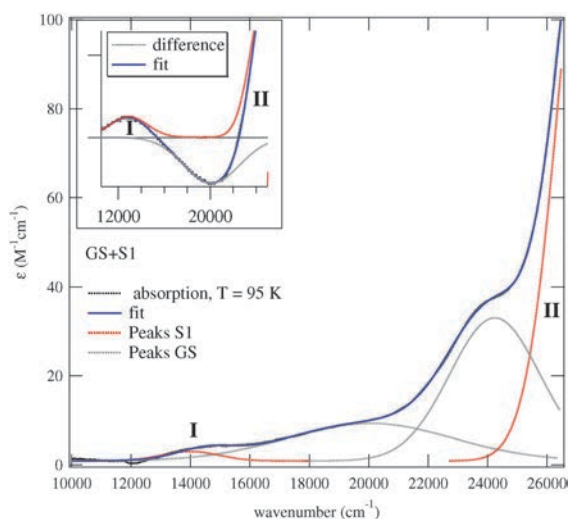
**Fig. 5** Absorption spectrum of GS + S1 after illumination with 488 nm at $T = 95$ K. I and II denote novel absorption bands due to the generation of S1. The inset shows the difference spectrum (GS + S1) − GS.

1064 nm. The results on the gel with 375 μmol SNP are shown in Fig. 5 and 6 for S1 and S2, respectively. Two bands attributed to S1 are found at 13 000 cm$^{-1}$ with $\varepsilon$(I) = 1.5 M$^{-1}$ cm$^{-1}$ and at 29 300 cm$^{-1}$ with $\varepsilon$(II) = 640 M$^{-1}$ cm$^{-1}$ (from the fit). For S2 two bands are found at 14 300 cm$^{-1}$ with $\varepsilon$(I) = 0.68 M$^{-1}$ cm$^{-1}$ and at 16 200 cm$^{-1}$ with $\varepsilon$(II) = 0.75 M$^{-1}$ cm$^{-1}$ (from the fit). The corresponding populations for S1 and S2 shown in Fig. 5 and 6 are 17(1)% and 6(1)%, respectively. Novel bands appear in the NIR both in S1 and S2, *i.e.* the HOMO–LUMO transition is shifted to lower energies. This is in agreement with the single crystal study[43] where the corresponding transitions were found at 13 050 cm$^{-1}$ (I) and 29 300 cm$^{-1}$ (II) for S1 and at 14 000 cm$^{-1}$ (I) and 16 350 cm$^{-1}$ (II) for S2 where the reduction of symmetry lifts the degeneracy of the $\pi$(NO) orbital. For S1 the values are identical within errors, while for S2 a slight blueshift of the low-lying absorption at 14 000 cm$^{-1}$ is observed in the gel. This
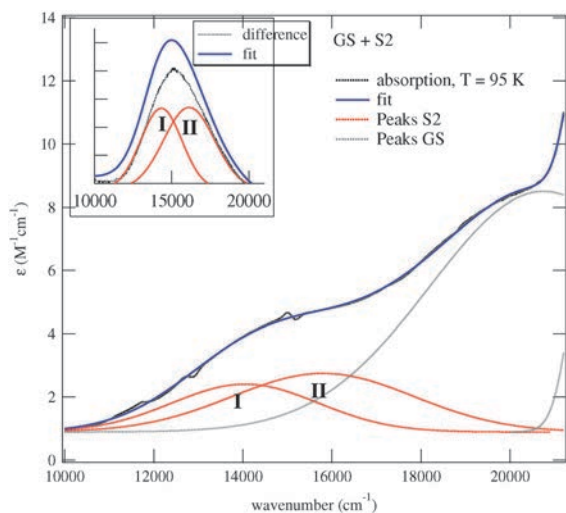


**Fig. 6** Absorption spectrum of GS + S2 after illumination with 488 nm and subsequently 1064 nm at $T = 95$ K. I and II denote novel absorption bands due to the generation of S2. The inset shows the difference spectrum (GS + S2) − S2.

apparent blueshift most probably is due to the fact that in the crystal the low-lying transition of S2 measured along the *c*-axis is found at 17 000 cm$^{-1}$ and we thus would have to consider an average position of the transitions in the gel due to the disordered complexes. Overall we find that the generation of S1 and S2 in SNP embedded in xerogels (as isolated complexes) occurs in the same manner as in single crystals. Furthermore the electronic structure is almost identical within errors. Only small shifts of the absorption bands towards lower energies are observed, but less pronounced than found in solutions. This indicates that the electronic properties of the linkage isomers on a single molecule scale embedded in a porous host remain unaffected.

A further important characteristic of the photoinduced linkage isomers is the energy barrier that separates them from the ground state. These activation energies can be detected by Differential Scanning Calorimetry in single crystals.[41] Unfortunately, DSC is not applicable to the case of the low concentrations embedded in the xerogel host, because the heatflow released is too small and blurred by the thermal isolation properties of the surrounding host material. However, as was shown in an earlier study[46] the activation energy (for S2) can be determined by time-resolved transmission measurements after pulsed excitation at high temperatures. S2 has a lifetime in the range of 100 ns at room temperature to milliseconds at 200 K.[46] We therefore performed a temperature dependent study of the lifetime of S2 excited with nanosecond laser pulses in the temperature range 200–300 K. Fig. 7 shows the temporal decay of the light-induced metastable state after excitation with a pulse energy of $E = 35$ mJ at $T = 220$ K and concentrations of SNP of 310 μmol (top) and 31 μmol (bottom). For all measured temperatures the decay of $\alpha_{li}(t)$ is mono-exponential. The open circles and squares are the thinned data points and the solid line corresponds to a fit of $\alpha_{li}(t) = \alpha_{li}^0 \exp(-t/\tau)$ where $\tau$ is the relaxation time (lifetime) and $\alpha_{li}^0$ is the amplitude of the light-induced absorption at $t = 0$. The amplitude of the light-induced absorption $\alpha_{li}^0(t)$ probed at 632 nm in the xerogels is 6.3 m$^{-1}$ and 0.8 m$^{-1}$ for the two samples with 310 and 31 μmol SNP per gel, respectively.

From the temperature dependence of the relaxation time $\tau$ of the monoexponential decay the activation energy $E_A$ and the frequency factor $Z$ are obtained *via* the Arrhenius relation: $\tau = Z^{-1}\exp(E_A/k_B T)$. Fig. 8 shows the natural logarithm of the inverse relaxation time $\tau^{-1}$ as a function of the inverse temperature for the xerogels. The linear fit yields the activation energy $E_A = 0.36(3)$ eV and the frequency factor $Z = 1 \times 10^{13}$ s$^{-1}$ for both samples. The data and fit for lifetimes measured on a SNP single crystal are also shown in Fig. 8. For the crystal an activation energy of $E_A = 0.38(3)$ eV and a frequency factor of $Z = 2 \times 10^{13}$ s$^{-1}$ are obtained. This shows that the size reduction to nanoparticles of 83 nm (310 μmol SNP per gel) and to single molecules in mesopores (31 μmol per gel) does not affect the activation energy and thus the potential energy surface. In comparison with an earlier study on single crystals in the temperature range 260–340 K[46] where $E_A = 0.43(3)$ eV and $Z = 7 \times 10^{13}$ s$^{-1}$ were found, we observe a slight deviation. This can be explained by the inaccuracy of our temperature measurements (the temperature is measured on the cold finger of the cryostat). The thermal contact of the crystal sandwiched between two glass plates as well as the thermal contact of the embedded complexes through the silica xerogel to the coldfinger of the cryostat is far from being perfect. Assuming a temperature gradient
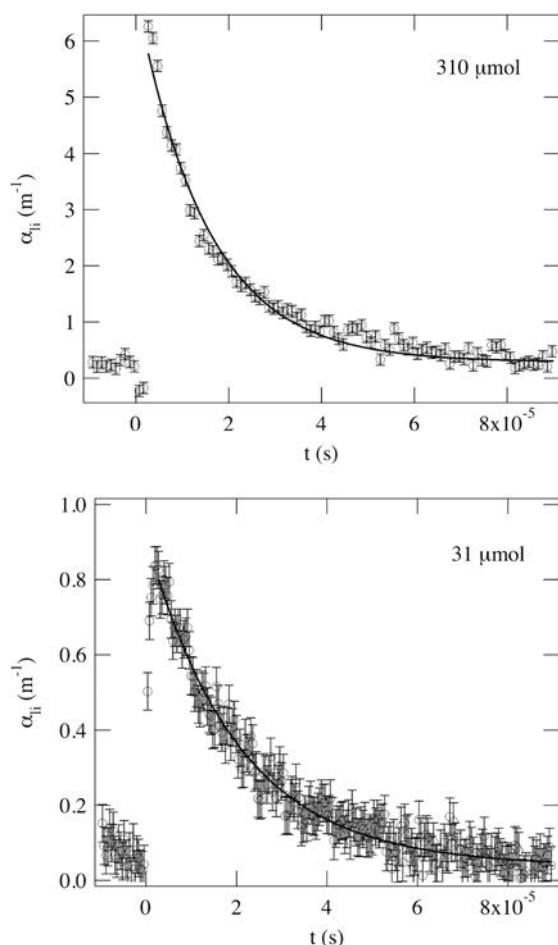
Fig. 7 Light-induced absorption $\alpha_{li}(t)$ after pulsed excitation with nanosecond laser pulses (35 mJ per pulse at 532 nm) for two hybrid xerogels with 310 µmol (top) and 31 µmol (bottom) SNP per gel and thickness $d = 0.8$ mm and $d = 1.9$ mm, respectively. The absorption is probed at 632 nm and 220 K. The solid line corresponds to a mono-exponential fit with relaxation times $\tau = 2 \times 10^{-5}$ s.

yielding a 10 °C higher temperature in the sample we can re-evaluate our data and find activation energies of $E_A = 0.40(3)$ eV and $Z = 2 \times 10^{13}$ s$^{-1}$ for the two xerogel samples and $E_A = 0.42(3)$ eV and $Z = 4 \times 10^{13}$ s$^{-1}$ for the single crystal, which correspond perfectly to the results obtained in ref. 46.

Overall we find that in SNP the electronic and energetic properties of the photoinduced linkage isomers are almost identical for isolated complexes or nanoparticles embedded in xerogel matrices compared to single crystals. The activation energy and thus the lifetime of the metastable linkage isomers remain the same. The electronic transitions and especially the HOMO–LUMO transition remain unaffected as well and consequently the spectral ranges for transfer between the three NO configurations remain the same as in single crystals, except that in the gel there is no possibility to choose the polarization along a specific direction of the $[Fe(CN)_5NO]$ molecule. These results underline the local nature of the linkage isomerism in these nitrosyl complexes. While the change of counter ions or of molecular composition, *e.g.* through the substitution of ligands, significantly affects the properties of the linkage isomers,[26–29] the bare isolation of the complex (still with the presence of the
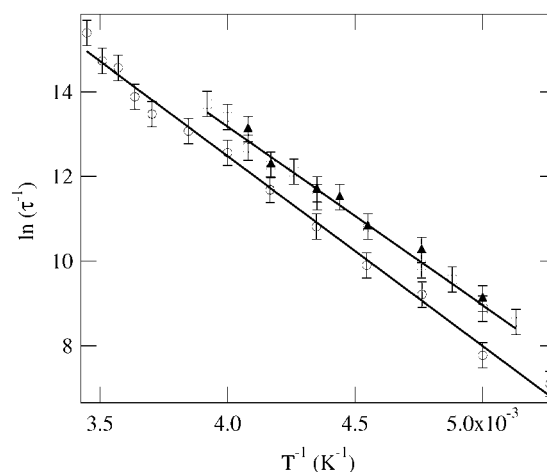


Fig. 8 Arrhenius plot of the relaxation times for two xerogels with 310 µmol (empty squares) and 31 µmol (full triangles) SNP per gel, respectively. Empty circles denote the relaxation times found in a single crystal of SNP. The absorption is probed at 632 nm. The solid line corresponds to linear fits yielding the activation energies $E_A = 0.36(3)$ eV for the xerogel hybrids and $E_A = 0.38(3)$ eV for the SNP crystal. The frequency factors are $Z = 1 \times 10^{13}$ s$^{-1}$ and $Z = 2 \times 10^{13}$ s$^{-1}$ for the xerogel hybrids and the crystal, respectively.

counter ion) has nearly no influence. Furthermore this study supports the structural investigations on the relative guanidinium nitroprusside, isolated in xerogels, where it was found that the counter ions remain at the nearly identical position with respect to the $[Fe(CN)_5NO]$ molecule in the gel as in the crystal.[21] With respect to potential applications these results are encouraging, as they show us that we can produce sol–gel materials with homogeneously embedded nanoparticles or isolated molecules that retain their photosensitive properties.

## 4 Conclusion

We have studied the influence of the embedding of SNP in mesoporous silica xerogels on the properties of the photoinduced nitrosyl linkage isomers in SNP. Statistically distributed molecules as well as nanoparticles of SNP can be incorporated or grown in the silica matrix depending on the gelation procedures. The generation and relaxation of the metastable states as well as their electronic and nuclear structure are not significantly changed by the size of SNP particles/clusters (or local concentration of the SNP) confined in the silica matrices. In conclusion, this approach allows us to obtain photochromic nitrosyl complexes in the form of nano-objects or isolated complexes that retain their interesting properties as an internal molecular effect almost isolated from the surrounding atoms of the matrix.

## References

1 T. Woike, W. Kirchner, G. Schetter, T. Barthel, K. Hyung-Sang and S. Haussühl, *Opt. Commun.*, 1994, **106**, 6–10.
2 S. Haussühl, G. Schetter and T. Woike, *Opt. Commun.*, 1995, **114**, 219–222.
3 T. Woike, M. Imlau, S. Haussühl, R. Rupp and R. Schieder, *Phys. Rev. B: Condens. Matter*, 1998, **58**, 8411–8415.

4  T. Woike, S. Haussühl, B. Sugg, R. Rupp, J. Beckers, M. Imlau and R. Schieder, *Appl. Phys. B: Lasers Opt.*, 1996, **63**, 243–248.

5  D. Schaniel, M. Imlau, T. Weisemöller, T. Woike, K. Krämer and H. U. Güdel, *Adv. Mater.*, 2007, **19**, 723–726.

6  M. Goulkov, D. Schaniel and T. Woike, *J. Opt. Soc. Am. B*, 2010, **27**, 927–931.

7  D. Levy, *Chem. Mater.*, 1997, **9**, 2666–2670.

8  K. Moller and T. Bein, *Chem. Mater.*, 1997, **10**, 2950–2963.

9  K. Ariga, *Coord. Chem. Rev.*, 2007, **251**, 2562–2591.

10  G. Schulz-Ekloff, D. Wöhrle, B. van Duffel and R. A. Schoonheydt, *Microporous Mesoporous Mater.*, 2002, **51**, 91–138.

11  A. Schuy, T. Woike and D. Schaniel, *J. Sol-Gel Sci. Technol.*, 2009, **50**, 403–408.

12  B. Cormary, I. Malfant and L. Valade, *J. Sol-Gel Sci. Technol.*, 2009, **52**, 19–23.

13  V. Dieckmann, M. Imlau, D. H. Taffa, L. Walder, R. Lepski, D. Schaniel and T. Woike, *Phys. Chem. Chem. Phys.*, 2010, **12**, 3283–3288.

14  R. Pardo, M. Zayat and D. Levy, *J. Mater. Chem.*, 2009, **19**, 6756–6760.

15  C. Schomburg, M. Wark, Y. Rohlfing, G. Schulz-Ekloff and D. Wöhrle, *J. Mater. Chem.*, 2001, **11**, 2014–2021.

16  B. Schaudel, C. Guermeur, C. Sanchez, K. Nakatani and J. A. Delaire, *J. Mater. Chem.*, 1997, **7**, 61–65.

17  S. Wagner, F. Leyssner, C. Kördel, S. Zarwell, R. Schmidt, M. Weinelt, K. Rück-Braun, M. Wolf and P. Tegeder, *Phys. Chem. Chem. Phys.*, 2009, **11**, 6242–6248.

18  P. G. Zanichelli, R. L. Sernaglia and D. W. Franco, *Langmuir*, 2006, **22**, 203–208.

19  F. G. Doro, U. P. Rodrigues-Filho and E. Tfouni, *J. Colloid Interface Sci.*, 2007, **307**, 405–417.

20  F. Chaput, J. Biteau, K. Lahlil, J. P. Boilot, B. Darracq, Y. Levy, J. Peretti, V. I. Safarov, G. Parent, A. Fernandez-Acebes and J.-M. Lehn, *Mol. Cryst. Liq. Cryst.*, 2000, **334**, 77–82.

21  A. Cervellino, J. Schefer, L. Keller, T. Woike and D. Schaniel, *J. Appl. Crystallogr.*, 2010, **43**, 1040–1045.

22  D. Schaniel and T. Woike, *Phys. Chem. Chem. Phys.*, 2009, **11**, 4391–4395.

23  D. Fomitchev, T. R. Furlani and P. Coppens, *Inorg. Chem.*, 1998, **37**, 1519–1526.

24  P. Schaiquevich, J. Guida and P. Aymonino, *Inorg. Chim. Acta*, 2000, **303**, 277–281.

25  D. Fomitchev, P. Coppens, T. Li, K. A. Bagley, L. Chen and G. B. Richter-Addo, *Chem. Commun.*, 1999, 2013–2014.

26  K. Ookubo, Y. Morioka, H. Tomizawa and E. Miki, *J. Mol. Struct.*, 1996, **379**, 241–247.

27  P. Coppens, I. Novozhilova and A. Kovalevsky, *Chem. Rev.*, 2002, **102**, 861–883.

28  D. Schaniel, B. Cormary, I. Malfant, L. Valade, T. Woike, B. Delley, K. Krämer and H. U. Güdel, *Phys. Chem. Chem. Phys.*, 2007, **9**, 3717–3724.

29  D. Schaniel, T. Woike, B. Delley, D. Biner, K. Krämer and H. U. Güdel, *Phys. Chem. Chem. Phys.*, 2005, **7**, 1164–1170.

30  J. Guida, O. Piro and P. Aymonino, *Inorg. Chem.*, 1995, **34**, 4113–4116.

31  P. Gütlich, Y. Garcia and T. Woike, *Coord. Chem. Rev.*, 2001, **219–221**, 839–879.

32  D. Schaniel, T. Woike, B. Delley, D. Biner, K. Krämer and H. U. Güdel, *Phys. Chem. Chem. Phys.*, 2007, **9**, 5149–5157.

33  D. Schaniel, T. Woike, N. R. Behrnd, J. Hauser, K. Krämer, T. Todorova and B. Delley, *Inorg. Chem.*, 2009, **48**, 11399–11406.

34  H. Zöllner, W. Krasser, T. Woike and S. Haussühl, *Chem. Phys. Lett.*, 1989, **161**, 497–501.

35  D. Schaniel, M. Nicoul and T. Woike, *Phys. Chem. Chem. Phys.*, 2010, **12**, 9029–9033.

36  M. Carducci, M. Pressprich and P. Coppens, *J. Am. Chem. Soc.*, 1997, **119**, 2669–2678.

37  D. Schaniel, J. Schefer, T. Woike and V. Petříček, *Phys. Rev. B: Condens. Matter Mater. Phys.*, 2005, **71**, 174112.

38  D. Schaniel, J. Schefer, T. Woike and V. Petříček, *Phys. Rev. B: Condens. Matter Mater. Phys.*, 2006, **73**, 174108.

39  B. Delley, J. Schefer and T. Woike, *J. Chem. Phys.*, 1997, **107**, 10067–10074.

40  M. Buchs, C. Daul, P. T. Manoharan and C. W. Schläpfer, *Int. J. Quantum Chem.*, 2002, **91**, 418–431.

41  D. Schaniel, T. Woike, L. Tsankov and M. Imlau, *Chem. Phys.*, 2005, **429**, 19–23.

42  J. B. Bates and R. K. Khanna, *Inorg. Chem.*, 1970, **9**, 1376.

43  D. Schaniel, J. Schefer, B. Delley, M. Imlau and T. Woike, *Phys. Rev. B: Condens. Matter*, 2002, **66**, 085103.

44  P. Manoharan and H. Gray, *J. Am. Chem. Soc.*, 1965, **87**, 3340–3347.

45  M. Lynch, M. Cheng, E. Van Kuiken and M. Khalil, *J. Am. Chem. Soc.*, 2010, **133**, 5255–5262.

46  D. Schaniel, T. Woike, C. Merschjann and M. Imlau, *Phys. Rev. B: Condens. Matter Mater. Phys.*, 2005, **72**, 195119.

# Structural reinvestigation of the photoluminescent complex [NdCl$_2$(H$_2$O)$_6$]Cl

**Kuan-Ying Hsieh, El-Eulmi Bendeif, Sebastien Pillet, Abdelatif Doudouh, Dominik Schaniel and Theo Woike**
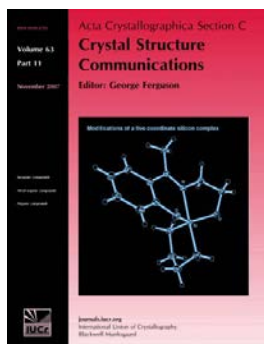
*Acta Crystallographica Section C: Crystal Structure Communications* specializes in the rapid dissemination of high-quality studies of crystal and molecular structures of interest in fields such as chemistry, biochemistry, mineralogy, pharmacology, physics and materials science. The numerical and text descriptions of each structure are submitted to the journal electronically as a Crystallographic Information File (CIF) and are checked and typeset automatically prior to peer review. The journal is well known for its high standards of structural reliability and presentation. *Section C* publishes approximately 1000 structures per year; readers have access to an archive that includes high-quality structural data for over 10000 compounds.

**Crystallography Journals Online** is available from **journals.iucr.org**

# inorganic compounds

# Structural reinvestigation of the photoluminescent complex [NdCl₂(H₂O)₆]Cl

Kuan-Ying Hsieh,[a] El-Eulmi Bendeif,[a]* Sebastien Pillet,[a] Abdelatif Doudouh,[a] Dominik Schaniel[a] and Theo Woike[b]

[a]Laboratoire de Cristallographie, Résonance Magnétique et Modélisations (CRM2, UMR CNRS 7036), Institut Jean Barriol, Université de Lorraine, BP 70239, Boulevard des Aiguillettes, 54506 Vandoeuvre-lès Nancy, France, and [b]Institut für Strukturphysik, TU Dresden, Zellescher Weg 16, Dresden, Germany
Correspondence e-mail: el-eulmi.bendeif@crm2.uhp-nancy.fr

The structure of the photoluminescent compound hexaaquadichloridoneodymium(III) chloride has been redetermined from single-crystal X-ray diffraction data at 100 K, with the aim of providing an accurate structural model for the bulk crystalline material. The crystal structure may be described as a network of [NdCl₂(H₂O)₆]⁺ cations with distorted square-antiprism geometry around the Nd$^{III}$ centre. The Nd$^{III}$ cation and the nonbonded Cl⁻ anion are both located on twofold symmetry axes. The crystal packing consists of three different neodymium pairs linked by a three-dimensional network of O—H⋯Cl intermolecular interactions. The pair distribution function (PDF) calculated from the experimentally determined structure is used for the discussion of the local structure.

## 1. Introduction

Luminescent rare earth (RE) materials have been extensively studied over recent decades for both fundamental and application purposes. These compounds possess narrow emission lines and are very promising for a variety of photonic applications, such as IR lasers, as a source for optical communication networks or as light-emitting diodes; and they are very suitable for photovoltaic devices (Slooff et al., 2001; Kuriki et al., 2002; Klink et al., 2000; Li et al., 2009; Reeves et al., 2009). In this respect, the Er³⁺- and Nd³⁺-based materials are among the most investigated systems and have attracted major interest owing to their photoluminescence behaviour. Recently, many theoretical and experimental studies have been devoted to Nd³⁺-based materials, aiming to define the relevant parameters which control the luminescent properties

(Mussot et al., 2009; Serqueira et al., 2011; Pivin et al., 2005; Steveler et al., 2011). It was found that the spectroscopic and photonic properties of Nd³⁺-based complexes are strongly affected by the coordination environments of the RE sites (Ebendorff-Heidepriem et al., 1995; Tanabe et al., 1992). Although the characterization of their optical properties has been performed thoroughly and is quite well documented (Pisarska, 2008; Sokolov et al., 2003), reports on their structural behaviour are still rather scarce and quite disparate.

The synthesis and X-ray single-crystal structural studies of neodymium hydroxychloride complexes have been described by various workers (Bukin, 1972; Dem'yanets & Emel'yanova, 1969; Habenschuss & Spedding, 1980). Recently, Zehnder et al. (2010) established a correlation between the structural and spectroscopic properties of the complex [NdCl(OH)₂], showing that the highly linked three-dimensional network seems to contribute to the remarkable inertness of this material in near-neutral aqueous environments. This could be one of the key properties for the potential application of actinide bis-hydroxychlorides as nuclear waste materials.

The title compound was originally determined by Habenschuss & Spedding (1980) as isostructural with the [LuCl₃·6H₂O] complex (Habenschuss & Spedding, 1979). Nevertheless, the 12 H atoms (six of them symmetry-independent) were not identified, which prevents a clear interpretation of the crystal packing; so no detailed structural discussion was presented. A more complete crystallographic analysis of this compound is therefore of interest for gaining better insight into its structural properties.

## 2. Experimental

### 2.1. Synthesis and crystallization

Crystals of [NdCl₂(H₂O)₆]·Cl were obtained by slow evaporation of an aqueous solution ($10^{-3}$ M) of [NdCl₃(H₂O)₆] powder (99.9% purity, Fluka AG) kept at room temperature. After a few weeks, small colourless single crystals appeared.

### 2.2. Refinement

Crystal data, data collection and structure refinement details are summarized in Table 1. The electron density of the H atoms was clearly identified in a difference Fourier map, and their atomic coordinates and isotropic displacement parameters were refined with O—H distances restrained to 0.84 (2) Å.

## 3. Results and discussion

Fig. 1 shows the structure of the asymmetric unit of the title compound, [NdCl₂(H₂O)₆]Cl, along with the atom-numbering scheme. Selected bond lengths and angles are listed in Table 2. A detailed examination of the coordination of the Nd$^{III}$ cation reveals a distorted square-antiprism geometry, where each Nd$^{III}$ cation is located on a twofold axis and eight-fold coordinated by six water molecules and two inner-sphere Cl atoms

## Table 1
Experimental details.

| | |
|---|---|
| **Crystal data** | |
| Chemical formula | $[NdCl_2(H_2O)_6]Cl$ |
| $M_r$ | 358.69 |
| Crystal system, space group | Monoclinic, $P2/n$ |
| Temperature (K) | 100 |
| $a, b, c$ (Å) | 7.9850 (3), 6.5561 (2), 9.6727 (4) |
| $\beta$ (°) | 93.655 (4) |
| $V$ (Å$^3$) | 505.34 (3) |
| $Z$ | 2 |
| Radiation type | Mo $K\alpha$ |
| $\mu$ (mm$^{-1}$) | 5.91 |
| Crystal size (mm) | $0.06 \times 0.04 \times 0.01$ |
| | |
| **Data collection** | |
| Diffractometer | Oxford SuperNova Dual (Cu at zero, with an Atlas detector) diffractometer |
| Absorption correction | Analytical [*CrysAlis PRO* (Oxford Diffraction, 2009); analytical numerical absorption correction using a multifaceted crystal model based on expressions derived by Clark & Reid (1995)] |
| $T_{min}, T_{max}$ | 0.712, 0.943 |
| No. of measured, independent and observed [$I > 2\sigma(I)$] reflections | 8593, 1793, 1710 |
| $R_{int}$ | 0.032 |
| $(\sin \theta/\lambda)_{max}$ (Å$^{-1}$) | 0.764 |
| | |
| **Refinement** | |
| $R[F^2 > 2\sigma(F^2)]$, $wR(F^2)$, $S$ | 0.016, 0.030, 1.03 |
| No. of reflections | 1793 |
| No. of parameters | 71 |
| No. of restraints | 6 |
| H-atom treatment | All H-atom parameters refined |
| $\Delta\rho_{max}, \Delta\rho_{min}$ (e Å$^{-3}$) | 0.57, −0.57 |

Computer programs: *CrysAlis PRO* (Oxford Diffraction, 2009), *SHELXS97* (Sheldrick, 2008), *SHELXL97* (Sheldrick, 2008), *WinGX* (Farrugia, 2012), *ORTEPIII* (Burnett & Johnson, 1996), *ORTEP-3 for Windows* (Farrugia, 2012) and *enCIFer* (Allen *et al.*, 2004).

(Fig. 1 and Table 2), the twofold symmetry axis bisecting the Cl1—Nd—Cl1 and O*i*W—Nd—O*i*W ($i$ = 1, 2 or 3) angles. The
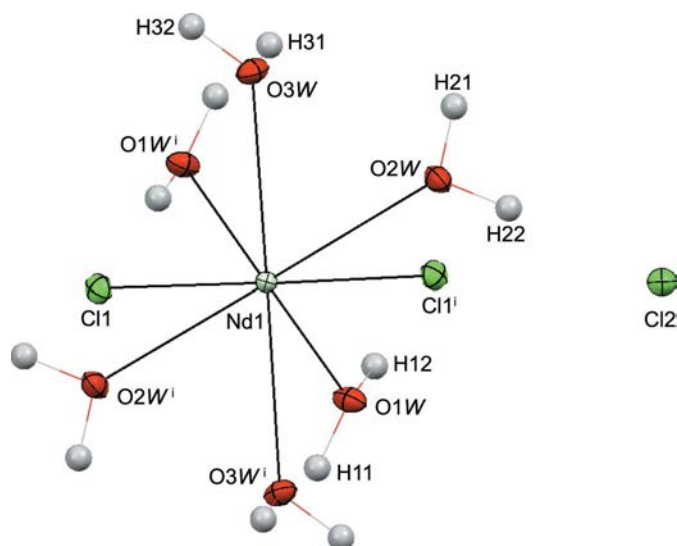


**Figure 1**
A projection of the title compound, showing the atom-labelling scheme. Displacement ellipsoids are drawn at the 50% probability level for all non-H atoms. [Symmetry code: (i) $-x + \frac{3}{2}, y, -z + \frac{3}{2}$.]
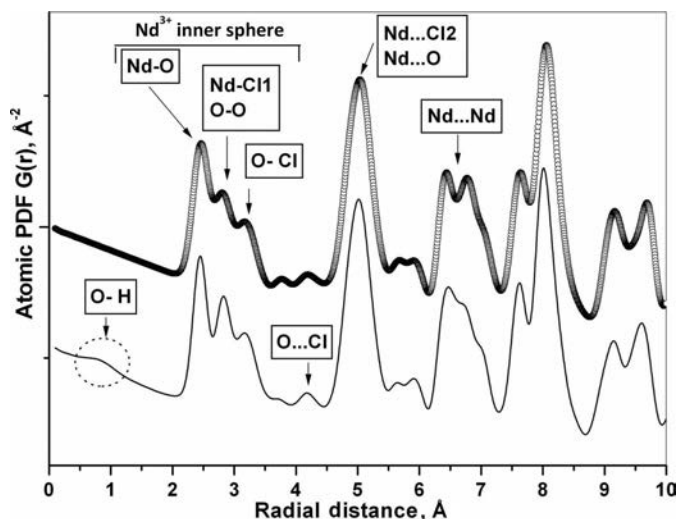


**Figure 2**
Comparison of the PDF [$G(r)$ function] calculated from the crystal structure obtained in this work (solid line) and that determined from the previously reported structure (open circles) (Habenschuss & Spedding, 1980). The PDF diagrams were calculated using the program *PDFgui* (Farrow *et al.*, 2007).

Nd1—O bond lengths range from 2.4371 (12) to 2.4653 (11) Å, with an average value of 2.453 (14) Å, and are significantly shorter than Nd1—Cl1 [2.8180 (4) Å].

Chloride ion Cl2 is located on a twofold axis, at a much greater distance of 5.0638 (2) Å from the Nd$^{III}$ cation, without any evidence for a direct Nd1···Cl2 interaction. These interatomic distances are clearly visible in the calculated atomic pair distribution function (PDF) diagram (Fig. 2), since peaks in the PDF pattern correspond to distances between atomic pairs and so describe the atomic arrangement in a material (Egami & Billinge, 2003; Billinge, 2007). In Fig. 2 we illustrate the calculated PDF up to 10 Å obtained from the crystal structure described herein (solid line) and that from the previously reported structure (Habenschuss & Spedding, 1980) (open circles). The highest peaks in the $G(r)$ function correspond to atomic pairs between the strongest atomic scatterers in this complex, the Nd$^{III}$ cations, as well as the most abundant pairs (six water molecules). Moreover, examination of the short-scale region in the PDF diagram gives information on the first few coordination spheres and therefore yields extensive information about the local atomic arrangement in

## Table 2
Selected geometric parameters (Å, °).

| | | | |
|---|---|---|---|
| Nd1—O1W | 2.4371 (12) | Nd1—O3W | 2.4653 (11) |
| Nd1—O2W | 2.4569 (12) | Nd1—Cl1 | 2.8180 (4) |
| | | | |
| O1W—Nd1—O1W$^i$ | 83.19 (6) | O3W$^i$—Nd1—O3W | 148.49 (6) |
| O1W—Nd1—O2W | 69.41 (4) | O1W—Nd1—Cl1 | 142.94 (3) |
| O1W$^i$—Nd1—O2W | 75.13 (4) | O1W$^i$—Nd1—Cl1 | 108.22 (3) |
| O2W—Nd1—O2W$^i$ | 132.01 (6) | O2W—Nd1—Cl1 | 147.07 (3) |
| O1W—Nd1—O3W$^i$ | 70.06 (4) | O2W$^i$—Nd1—Cl1 | 76.39 (3) |
| O1W$^i$—Nd1—O3W$^i$ | 138.34 (4) | O3W$^i$—Nd1—Cl1 | 79.32 (3) |
| O2W—Nd1—O3W$^i$ | 120.76 (4) | O3W—Nd1—Cl1 | 77.41 (3) |
| O2W$^i$—Nd1—O3W$^i$ | 73.11 (4) | Cl1—Nd1—Cl1$^i$ | 84.099 (16) |

Symmetry code: (i) $-x + \frac{3}{2}, y, -z + \frac{3}{2}$.
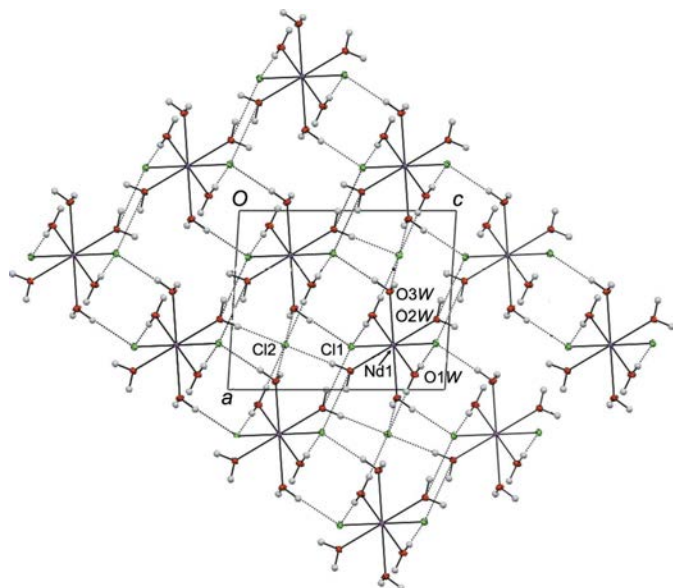
**Figure 3**
A packing diagram for $[NdCl_2(H_2O)_6]Cl$, viewed in the *ac* plane, showing neodymium pairs linked by the three-dimensional network of O—H$\cdots$Cl intermolecular interactions (dotted lines).

**Table 3**
Hydrogen-bond geometry (Å, °).

| $D-H\cdots A$ | $D-H$ | $H\cdots A$ | $D\cdots A$ | $D-H\cdots A$ |
|---|---|---|---|---|
| O1W—H11$\cdots$Cl2$^{ii}$ | 0.812 (16) | 2.389 (2) | 3.1937 (12) | 171 (2) |
| O1W—H12$\cdots$Cl1$^{iii}$ | 0.808 (16) | 2.327 (2) | 3.1339 (12) | 177 (3) |
| O2W—H21$\cdots$Cl1$^{iv}$ | 0.800 (15) | 2.380 (2) | 3.1531 (13) | 163 (1) |
| O2W—H22$\cdots$Cl2 | 0.813 (16) | 2.364 (2) | 3.1703 (13) | 171 (2) |
| O3W—H31$\cdots$Cl2$^{v}$ | 0.819 (16) | 2.438 (2) | 3.2333 (13) | 163 (2) |
| O3W—H32$\cdots$Cl1$^{vi}$ | 0.793 (16) | 2.370 (2) | 3.1617 (13) | 176 (2) |

Symmetry codes: (ii) $-x+2, -y+2, -z+2$; (iii) $-x+\frac{3}{2}, y+1, -z+\frac{3}{2}$; (iv) $x-\frac{1}{2}, -y+1, z+\frac{1}{2}$; (v) $-x+1, -y+1, -z+2$; (vi) $-x+1, -y+1, -z+1$.

also noteworthy that the O—H$\cdots$Cl2 interactions are only slightly longer [3.1703 (12)–3.2333 (13) Å] than the O—H$\cdots$Cl1 interactions and that the shortest Cl1$\cdots$Cl2 interaction is 4.1821 (5) Å.

## References

Allen, F. H., Johnson, O., Shields, G. P., Smith, B. R. & Towler, M. (2004). *J. Appl. Cryst.* **37**, 335–338.
Billinge, S. J. L. (2007). *Z. Kristallogr. Suppl.* **26**, 17–26.
Bukin, V. I. (1972). *Dokl. Akad. Nauk SSSR*, **207**, 1332–1335.
Burnett, M. N. & Johnson, C. K. (1996). *ORTEPIII*. Report ORNL-6895. Oak Ridge National Laboratory, Tennessee, USA.
Clark, R. C. & Reid, J. S. (1995). *Acta Cryst.* A**51**, 887–897.
Dem'yanets, L. N. & Emel'yanova, E. N. (1969). *Kristallografiya*, **14**, 753–754.
Ebendorff-Heidepriem, H., Seeber, W. & Ehrt, D. (1995). *J. Non-Cryst. Solids*, **183**, 191–200.
Egami, T. & Billinge, S. J. L. (2003). *Underneath the Bragg Peaks: Structural Analysis of Complex Materials*, edited by R. W. Cahn, p. 138. Oxford: Pergamon Press.
Farrow, C. L., Juhás, P., Liu, J. W., Bryndin, D., Božin, E. S., Bloch, J., Proffen, Th. & Billinge, S. J. L. (2007). *J. Phys. Condens. Matter*, **19**, 335219.
Farrugia, L. J. (2012). *J. Appl. Cryst.* **45**, 849–854.
Habenschuss, A. & Spedding, F. H. (1979). *J. Chem. Phys.* **70**, 2797–2806.
Habenschuss, A. & Spedding, F. H. (1980). *Cryst. Struct. Commun.* **9**, 71–75.
Klink, S. I., Grave, L., Reinhoudt, D. N. & van Veggel, F. C. J. M. (2000). *J. Phys. Chem. A*, **104**, 5457–5468.
Kuriki, K., Koike, Y. & Okamoto, Y. (2002). *Chem. Rev.* **102**, 2347–2356.
Li, Z., Yu, J., Zhou, L., Deng, R. & Zhang, H. (2009). *Inorg. Chem. Commun.* **12**, 151–153.
Mussot, A., Le Parquier, M., Berrier, B., Perard, M. & Szriftgiser, P. (2009). *Opt. Commun.* **282**, 988–991.
Oxford Diffraction (2009). *CrysAlis CCD* and *CrysAlis RED*. Oxford Diffraction Ltd, Yarnton, Oxfordshire, England.
Pisarska, J. (2008). *J. Mol. Struct.* **887**, 201–204.
Pivin, J. C., Podhorodecki, A., Kudrawiec, R. & Misiewicz, J. (2005). *Opt. Mater.* **27**, 1467–1470.
Reeves, R. J., Polley, C. & Choi, J. C. (2009). *J. Lumin.* **129**, 1673–1676.
Serqueira, E. O., Dantas, N. O. & Bell, M. J. V. (2011). *Chem. Phys. Lett.* **508**, 125–129.
Sheldrick, G. M. (2008). *Acta Cryst.* A**64**, 112–122.

the vicinity of the Nd$^{III}$ sites. The PDF peak at 2.45 Å corresponds to the Nd1$\cdots$O bonds, whereas the peak at 2.82 Å is present due to both the Nd1$\cdots$Cl1 pairs and the intraprism $H_2O\cdots H_2O$ interactions. The peaks at 3.15 and 4.18 Å originate from the intramolecular Cl1$\cdots H_2O$ interactions and the intense $G(r)$ peak near 5.1 Å can be assigned to the Nd$\cdots$Cl2 interactions, together with a significant number of next-nearest Nd$\cdots$O pairs. As can be seen in Fig. 2, the calculated PDFs are quite similar, exhibiting almost the same features. However, appreciable differences must be noted between the PDF obtained from the present structure analysis (solid line) and that from the previously reported structure (open circles). Firstly, a small peak near 1 Å, definitely corresponding to the O—H bonds, is only observed in the PDF profile obtained from the results reported in this work, as all 12 H atoms were successfully located in a difference Fourier map in our study. Furthermore, we note that the structural parameters reported here are more precise than those communicated previously, due to the different experimental conditions (low temperature and experimental data-collection set-up).

The crystal structure of $[NdCl_2(H_2O)_6]Cl$ is made up of three different neodymium pairs linked by O—H$\cdots$Cl1 interactions ranging from 3.1339 (13) to 3.1617 (13) Å (Fig. 3 and Table 3). These pairs are also characterized by significantly different Nd1$\cdots$Nd1 distances, ranging from 6.3739 (3) to 6.7491 (3) Å, which are clearly visible in the PDF diagram (Fig. 2) in the 6.13–7.26 Å region.

Chloride ion Cl2 is in contact with six neighbouring $[NdCl_2(H_2O)_6]^+$ cations, four in the *ab* plane and two almost directed along the crystallographic *c* axis. Anions Cl1 and Cl2 are both involved in the highly linked three-dimensional network of intermolecular interactions connecting the different pairs of neodymium-centred cations (Table 3). It is

Slooff, L. H., Polman, A., Cacialli, F., Friend, R. H., Hebbink, G. A., van Veggel, F. C. J. M. & Reinhoudt, D. N. (2001). *Appl. Phys. Lett.* **78**, 2122–2124.

Sokolov, I. A., Murin, I. V., Mel'nikova, N. A. & Pronkin, A. A. (2003). *Glass Phys. Chem.* **29**, 291–299.

Steveler, E., Rinnert, H. & Vergnat, M. (2011). *J. Appl. Phys.* **110**, 113518.

Tanabe, S., Hirao, K. & Soga, N. (1992). *J. Non-Cryst. Solids*, **142**, 148–154.

Zehnder, R. A., Clark, D. L., Scott, B. L., Donohoe, R. J., Palmer, P. D., Runde, W. H. & Hobart, D. E. (2010). *Inorg. Chem.* **49**, 4781–4790.

# supplementary materials

# Structural reinvestigation of the photoluminescent complex [NdCl$_2$(H$_2$O)$_6$]Cl

**Kuan-Ying Hsieh, El-Eulmi Bendeif, Sebastien Pillet, Abdelatif Doudouh, Dominik Schaniel and Theo Woike**

## Computing details

Data collection: *CrysAlis PRO* (Oxford Diffraction, 2009); cell refinement: *CrysAlis PRO* (Oxford Diffraction, 2009); data reduction: *CrysAlis PRO* (Oxford Diffraction, 2009); program(s) used to solve structure: *SHELXS97* (Sheldrick, 2008); program(s) used to refine structure: *SHELXL97* (Sheldrick, 2008) and *WinGX* (Farrugia, 2012); molecular graphics: *ORTEPIII* (Burnett & Johnson, 1996) and *ORTEP-3 for Windows* (Farrugia, 2012); software used to prepare material for publication: *enCIFer* (Allen *et al.*, 2004).

### (Hexaaquadichlorido)neodymium(III) chloride

*Crystal data*

[NdCl$_2$(H$_2$O)$_6$]·Cl
$M_r$ = 358.69
Monoclinic, $P2/n$
Hall symbol: -P 2yac
$a$ = 7.9850 (3) Å
$b$ = 6.5561 (2) Å
$c$ = 9.6727 (4) Å
$\beta$ = 93.655 (4)°
$V$ = 505.34 (3) Å$^3$
$Z$ = 2

$F(000)$ = 342
$D_x$ = 2.357 Mg m$^{-3}$
Mo $K\alpha$ radiation, $\lambda$ = 0.71073 Å
Cell parameters from 8593 reflections
$\theta$ = 3.1–32.9°
$\mu$ = 5.91 mm$^{-1}$
$T$ = 100 K
Plate, colourless
0.06 × 0.04 × 0.01 mm

*Data collection*

Oxford SuperNova Dual
 diffractometer, Cu at zero, with an Atlas
 detector
Radiation source: SuperNova (Mo) X-ray
 source
Mirror monochromator
Detector resolution: 10.4508 pixels mm$^{-1}$
$\omega$ scans

Absorption correction: analytical
 [*CrysAlis PRO* (Oxford Diffraction, 2009);
 analytical numerical absorption correction using
 a multifaceted crystal model based on
 expressions derived by Clark & Reid (1995)]
$T_{min}$ = 0.712, $T_{max}$ = 0.943
8593 measured reflections
1793 independent reflections
1710 reflections with $I > 2\sigma(I)$
$R_{int}$ = 0.032
$\theta_{max}$ = 32.9°, $\theta_{min}$ = 3.1°
$h$ = −12→12
$k$ = −9→9
$l$ = −14→14

*Refinement*

| | |
|---|---|
| Refinement on $F^2$ | Secondary atom site location: difference Fourier map |
| Least-squares matrix: full | |
| $R[F^2 > 2\sigma(F^2)] = 0.016$ | Hydrogen site location: difference Fourier map |
| $wR(F^2) = 0.030$ | All H-atom parameters refined |
| $S = 1.03$ | $w = 1/[\sigma^2(F_o^2) + (0.0097P)^2 + 0.0698P]$ |
| 1793 reflections | where $P = (F_o^2 + 2F_c^2)/3$ |
| 71 parameters | $(\Delta/\sigma)_{max} < 0.001$ |
| 6 restraints | $\Delta\rho_{max} = 0.57$ e Å$^{-3}$ |
| Primary atom site location: structure-invariant direct methods | $\Delta\rho_{min} = -0.57$ e Å$^{-3}$ |

*Special details*

**Geometry**. All s.u.'s (except the s.u. in the dihedral angle between two l.s. planes) are estimated using the full covariance matrix. The cell s.u.'s are taken into account individually in the estimation of s.u.'s in distances, angles and torsion angles; correlations between s.u.'s in cell parameters are only used when they are defined by crystal symmetry. An approximate (isotropic) treatment of cell s.u.'s is used for estimating s.u.'s involving l.s. planes.

**Refinement**. Refinement of $F^2$ against ALL reflections. The weighted $R$-factor $wR$ and goodness of fit $S$ are based on $F^2$, conventional $R$-factors $R$ are based on $F$, with $F$ set to zero for negative $F^2$. The threshold expression of $F^2 > 2\sigma(F^2)$ is used only for calculating $R$-factors(gt) *etc*. and is not relevant to the choice of reflections for refinement. $R$-factors based on $F^2$ are statistically about twice as large as those based on $F$, and $R$-factors based on ALL data will be even larger.

*Fractional atomic coordinates and isotropic or equivalent isotropic displacement parameters (Å$^2$)*

| | $x$ | $y$ | $z$ | $U_{iso}*/U_{eq}$ |
|---|---|---|---|---|
| Nd1 | 0.7500 | 0.647838 (16) | 0.7500 | 0.00558 (4) |
| Cl1 | 0.75958 (5) | 0.32866 (5) | 0.55554 (4) | 0.01015 (7) |
| Cl2 | 0.7500 | 0.87674 (8) | 1.2500 | 0.01062 (10) |
| O1W | 0.91551 (15) | 0.92584 (18) | 0.85559 (13) | 0.0112 (2) |
| O2W | 0.60535 (15) | 0.80024 (18) | 0.94150 (13) | 0.0113 (2) |
| O3W | 0.45290 (14) | 0.54572 (18) | 0.71823 (13) | 0.0115 (2) |
| H11 | 1.003 (2) | 0.963 (4) | 0.825 (2) | 0.034 (7)* |
| H12 | 0.873 (3) | 1.030 (3) | 0.880 (2) | 0.031 (6)* |
| H21 | 0.512 (2) | 0.762 (4) | 0.953 (2) | 0.028 (6)* |
| H22 | 0.645 (3) | 0.833 (3) | 1.0179 (18) | 0.029 (7)* |
| H31 | 0.420 (3) | 0.431 (3) | 0.736 (2) | 0.029 (6)* |
| H32 | 0.398 (3) | 0.581 (4) | 0.651 (2) | 0.031 (7)* |

*Atomic displacement parameters (Å$^2$)*

| | $U^{11}$ | $U^{22}$ | $U^{33}$ | $U^{12}$ | $U^{13}$ | $U^{23}$ |
|---|---|---|---|---|---|---|
| Nd1 | 0.00511 (6) | 0.00594 (5) | 0.00569 (6) | 0.000 | 0.00049 (4) | 0.000 |
| Cl1 | 0.01099 (17) | 0.00977 (16) | 0.00978 (17) | −0.00071 (12) | 0.00144 (14) | −0.00203 (13) |
| Cl2 | 0.0090 (2) | 0.0122 (2) | 0.0107 (2) | 0.000 | 0.00065 (19) | 0.000 |
| O1W | 0.0088 (5) | 0.0099 (5) | 0.0153 (6) | −0.0016 (4) | 0.0027 (5) | −0.0043 (5) |
| O2W | 0.0100 (6) | 0.0140 (5) | 0.0102 (6) | −0.0019 (4) | 0.0031 (5) | −0.0028 (5) |
| O3W | 0.0086 (5) | 0.0118 (6) | 0.0139 (6) | −0.0016 (4) | −0.0018 (5) | 0.0023 (5) |

*Geometric parameters (Å, º)*

| | | | |
|---|---|---|---|
| Nd1—O1W | 2.4371 (12) | Nd1—Cl1<sup>i</sup> | 2.8180 (4) |
| Nd1—O1W<sup>i</sup> | 2.4371 (11) | O1W—H11 | 0.812 (16) |
| Nd1—O2W | 2.4569 (12) | O1W—H12 | 0.808 (16) |
| Nd1—O2W<sup>i</sup> | 2.4569 (12) | O2W—H21 | 0.800 (15) |
| Nd1—O3W | 2.4653 (11) | O2W—H22 | 0.813 (16) |
| Nd1—O3W<sup>i</sup> | 2.4653 (11) | O3W—H31 | 0.819 (16) |
| Nd1—Cl1 | 2.8180 (4) | O3W—H32 | 0.793 (16) |
| | | | |
| O1W—Nd1—O1W<sup>i</sup> | 83.19 (6) | O3W<sup>i</sup>—Nd1—Cl1 | 79.32 (3) |
| O1W—Nd1—O2W | 69.41 (4) | O3W—Nd1—Cl1 | 77.41 (3) |
| O1W<sup>i</sup>—Nd1—O2W | 75.13 (4) | O1W—Nd1—Cl1<sup>i</sup> | 108.22 (3) |
| O1W—Nd1—O2W<sup>i</sup> | 75.13 (4) | O1W<sup>i</sup>—Nd1—Cl1<sup>i</sup> | 142.94 (3) |
| O1W<sup>i</sup>—Nd1—O2W<sup>i</sup> | 69.41 (4) | O2W—Nd1—Cl1<sup>i</sup> | 76.39 (3) |
| O2W—Nd1—O2W<sup>i</sup> | 132.01 (6) | O2W<sup>i</sup>—Nd1—Cl1<sup>i</sup> | 147.07 (3) |
| O1W—Nd1—O3W<sup>i</sup> | 70.06 (4) | O3W<sup>i</sup>—Nd1—Cl1<sup>i</sup> | 77.41 (3) |
| O1W<sup>i</sup>—Nd1—O3W<sup>i</sup> | 138.34 (4) | O3W—Nd1—Cl1<sup>i</sup> | 79.32 (3) |
| O2W—Nd1—O3W<sup>i</sup> | 120.76 (4) | Cl1—Nd1—Cl1<sup>i</sup> | 84.099 (16) |
| O2W<sup>i</sup>—Nd1—O3W<sup>i</sup> | 73.11 (4) | Nd1—O1W—H11 | 121.9 (17) |
| O1W—Nd1—O3W | 138.34 (4) | Nd1—O1W—H12 | 121.8 (17) |
| O1W<sup>i</sup>—Nd1—O3W | 70.06 (4) | H11—O1W—H12 | 104 (2) |
| O2W—Nd1—O3W | 73.11 (4) | Nd1—O2W—H21 | 117.4 (17) |
| O2W<sup>i</sup>—Nd1—O3W | 120.76 (4) | Nd1—O2W—H22 | 128.3 (17) |
| O3W<sup>i</sup>—Nd1—O3W | 148.49 (6) | H21—O2W—H22 | 105 (2) |
| O1W—Nd1—Cl1 | 142.94 (3) | Nd1—O3W—H31 | 123.1 (16) |
| O1W<sup>i</sup>—Nd1—Cl1 | 108.22 (3) | Nd1—O3W—H32 | 120.0 (18) |
| O2W—Nd1—Cl1 | 147.07 (3) | H31—O3W—H32 | 106 (2) |
| O2W<sup>i</sup>—Nd1—Cl1 | 76.39 (3) | | |

Symmetry code: (i) −*x*+3/2, *y*, −*z*+3/2.

*Hydrogen-bond geometry (Å, º)*

| *D*—H⋯*A* | *D*—H | H⋯*A* | *D*⋯*A* | *D*—H⋯*A* |
|---|---|---|---|---|
| O1*W*—H11⋯Cl2<sup>ii</sup> | 0.81 (2) | 2.39 (1) | 3.194 (1) | 171 (2) |
| O1*W*—H12⋯Cl1<sup>iii</sup> | 0.81 (2) | 2.33 (1) | 3.134 (1) | 177 (3) |
| O2*W*—H21⋯Cl1<sup>iv</sup> | 0.80 (2) | 2.38 (1) | 3.153 (1) | 163 (1) |
| O2*W*—H22⋯Cl2 | 0.81 (2) | 2.36 (1) | 3.170 (1) | 171 (2) |
| O3*W*—H31⋯Cl2<sup>v</sup> | 0.82 (2) | 2.44 (1) | 3.233 (1) | 163 (2) |
| O3*W*—H32⋯Cl1<sup>vi</sup> | 0.79 (2) | 2.37 (1) | 3.162 (1) | 176 (2) |

Symmetry codes: (ii) −*x*+2, −*y*+2, −*z*+2; (iii) −*x*+3/2, *y*+1, −*z*+3/2; (iv) *x*−1/2, −*y*+1, *z*+1/2; (v) −*x*+1, −*y*+1, −*z*+2; (vi) −*x*+1, −*y*+1, −*z*+1.

## PAPER

# Structure and dynamics of single molecules confined in a mesoporous silica matrix: a joint NMR and PDF characterisation†

Kuan-Ying Hsieh,[a] El-Eulmi Bendeif,*[a] Axel Gansmuller,[a] Sebastien Pillet,[a] Theo Woike[b] and Dominik Schaniel[a]

We present an experimental approach to study the structure and dynamics of molecular functional complexes in porous host matrices. Combining the results of Solid-State NMR and pair distribution function analysis based on total X-ray scattering data the structural arrangement and dynamical behaviour of $Na_2[Fe(CN)_5NO] \cdot 2H_2O$ (SNP) embedded in amorphous $SiO_2$ matrix is investigated. We show that the SNP complexes are embedded as isolated complexes within the $SiO_2$ pores and propose a structural model for the cation and anion arrangement. Additionally the NMR results demonstrate the rotational dynamics of the SNP complexes.

## 1. Introduction

In recent years, the sol–gel process has emerged as a promising strategy to design nanocomposites in which mesoporous silica matrices serve as templates for the confinement of various types of functional molecules leading to hybrid organic–inorganic nanocomposites. Such nanocomposite materials combine the properties of the guest functional molecules with those of inorganic materials (high stability, transparency, convenient processing and shaping), and have attracted considerable interest owing to their potential applications, such as the fabrication of next-generation molecular-based devices including plasmonic waveguides, photonic crystals, memory storage devices, photovoltaics.[1-6] Embedding photoswichable molecules into porous hosts opens the possibility to complement the molecular optical properties with the chemical and mechanical stability of the host.[7,8] We are especially interested in the inclusion of photoswitchable mononitrosyl complexes $[ML_5NO]^x$ (M = metal, L = ligand) into porous silica matrices in order to exploit their interesting optical properties for applications such as holography or information storage.[9-12] In this class of compounds the nitrosyl ligand can undergo photoinduced linkage isomerisation[13,14] resulting in changes of the colour and the refractive index of the compounds. Since the linkage isomerism is a molecular property these complexes are suitable candidates for

embedding them into hosts materials such as silica gels[15] and metal–organic frameworks[16] or electrostatic attachment on surfaces.[17] The study of the prototype complex $Na_2[Fe(CN)_5NO] \cdot 2H_2O$ (sodiumnitroprusside, SNP) embedded in silica matrices showed that the properties of the metastable linkage isomers are independent of the pore and particle size.[1] Furthermore this study indicated that at low doping levels the SNP guest might be included as isolated molecules in the mesopores of the $SiO_2$ host. This finding is in agreement with the results of a neutron diffraction study on a $(CN_3H_6)_2[Fe(CN)_5NO]$ complex embedded in a silica host,[18] which allowed for the identification of the structural fingerprint of isolated molecules in the porous network. In this case however the properties of the linkage isomerisation change insofar that the achievable population is increased in the gel matrix compared to the crystalline material. In order to be able to derive a structure–functionality relationship and to proceed to a more targeted design of such hybrid complexes, a detailed description of the structural organisation of the guest species and of their immediate surrounding (i.e. silica wall, solvent and counter-ions) is thus absolutely mandatory. We show here that detailed structural information can be obtained by using an appropriate multiscale approach combining various experimental techniques such as X-ray total scattering coupled to atomic pair distribution function (PDF) and solid-state NMR spectroscopy. This multiscale approach does provide more extensive and accurate structural information. As the pioneering work of Toby & Egami (1992)[19] and several subsequent studies[20-23] have shown, the PDF approach is ideally suited for structural characterisation of crystalline materials as well as nanostructured and disordered materials. The PDF is the instantaneous atomic density–density correlation function which describes the atomic arrangements in real space without any crystallographic assumption. Simply speaking, the PDF function

[a]Laboratoire de Cristallographie, Résonance Magnétique et Modélisations, CRM2, UMR CNRS 7036, Institut Jean Barriol, Université de Lorraine, BP 70239, 54506 Vandoeuvre les Nancy, France. E-mail: el-eulmi.bendeif@crm2.uhp-nancy.fr; Fax: +33 (0)3 83 68 43 00; Tel: +33 (0)3 83 68 48 70

[b]Institut für Strukturphysik, TU Dresden, Zellescher Weg 16, Dresden, Germany

is another representation of total scattered X-ray intensities and reflects both the long-range atomic structure, manifested in the sharp Bragg peaks, and the local structural imperfections, manifested in the diffuse components of the total scattering pattern. A significant advantage of the PDF approach is that, unlike EXAFS spectroscopy, the relevant structural information persists over a long distances range. Thus, the structural properties are described at different scale orders in real space. However, the structural studies, based on PDFs obtained from total X-ray scattering data, of amorphous organic–inorganic nanocomposites is a challenging task because of their weak scattering power that contributes to the magnitude of the correlations in the PDF diagrams. Accordingly, it is important to combine different complementary approaches to provide an accurate structural description of these hybrid organic–inorganic nanocomposites. As such, solid state NMR spectroscopy and PDF analysis are very complementary techniques that are increasingly being combined for structural characterisation of heterogeneous, nanocrystalline, and even disordered materials.[24–29] The PDF method can deliver atomic resolution structural information that extends to distances of several nanometers, and thus fill the important gap between short range NMR and long range X-ray Bragg diffraction methods. Additionally, solid-state NMR techniques are element selective, chemically resolved and can provide further information on molecular motion.

In this study we establish a structural characterisation strategy of mononitrosyl complexes $[ML_5NO]^x$ embedded in porous silica matrices and apply it to observe how confinement in the nanopores affects the structure of a SNP guest. A prerequisite for NMR characterization is the presence of NMR sensitive nuclei in the components studied. This condition is fulfilled here since the $[Fe(CN)_5NO]^{2-}$ ions can be studied by natural abundance (1%) $^{13}C$ NMR. The sodium counterion corresponds to 100% abundant and sensitive $^{23}Na$, and the $SiO_2$ matrix can be characterized by natural abundance (4.7%) $^{29}Si$ NMR. The high resolution necessary for interpretation of the spectra is provided by Magic Angle Spinning[30] (MAS) of the samples that partially averages out the anisotropic interactions present in the solid state. Solid State NMR has already been widely applied to characterize crystalline and amorphous silica matrices.[31–38] $^{29}Si$ MAS NMR allows to characterize the degree of condensation of the gel matrix[31,32,34,38–40] whereas $^{29}Si$ CPMAS and $^1H$ MAS NMR provide information on the speciation of silanol groups and the arrangement of water molecules inside the pores.[32,34,37,41,42] Although many structural studies of SNP have been published,[43–50] until now NMR has been applied only in the solution state,[51,52] or single crystals.[53] In this study we apply $^{13}C$ and $^{23}Na$ MAS NMR on crystalline and encapsulated SNP@$SiO_2$ to assess how the porous confinement influences the structure of the complex. As mentioned earlier solid state NMR can also probe molecular motions. This feature relies on the fact that anisotropic NMR interactions depend on the orientation of their tensors with respect to the static magnetic field. When the anisotropic tensors reorient because of molecular dynamics, NMR measurements of the tensor properties are specifically averaged depending on motional amplitude, symmetry and correlation time. Even when the averaging

cannot be characterized directly, the influence of the fluctuating interaction tensors on the different NMR relaxation times is correlated to the characteristics of the dynamics.[54–56] As a consequence NMR is increasingly applied to study dynamics in confined porous environments[57–65] mostly by measuring the effect on quadrupolar interactions from isotopically deuterated molecules. In this study, we use the $^{13}C$ Chemical Shift Anisotropy (CSA) and $^{23}Na$ quadrupolar couplings to probe rotational diffusion of the complex inside the nanopores.

## 2. Experimental

### 2.1. Sample preparation

**2.1.1. Synthesis of porous silica monoliths.** The porous silica matrices were obtained following a procedure published earlier resulting in transparent monolith with pores size in the range of 1–2 nm:[1,15,66] 1.5 ml of tetramethoxysilane (TMOS, 98% purity, Fluka), 1.8 ml of methanol (VWR) and 3.6 ml of distilled water were mixed and stirred at room temperature for about 5 minutes which allowed the solution to gel. The mixture was then placed in a glass tube at 50 °C for 3 weeks in a conventional oven to dry and solidify the obtained gels. Cylindrical transparent rods with a diameter of about 1.0 mm were obtained after the drying and gelation–solidification processes.

**2.1.2. Synthesis of SNP–silica hybrid.** The SNP–silica nanocomposites were prepared by impregnating the porous $SiO_2$ monoliths with an aqueous solution (0.877 mol l$^{-1}$) of SNP salt ($Na_2[Fe(CN)_5NO]\cdot2H_2O$). The $SiO_2$ matrices were slowly introduced into the SNP solution in order to prevent any cracking. The monoliths, initially colourless, then became progressively more and more brown-orange indicating the diffusion of the SNP complexes into the silica pore network. After about 24 hours the monoliths displayed homogeneous colouring and were kept at 50 °C for 7 days in an oven. A final drying step was performed at room temperature in desiccators coupled to vacuum (10$^{-2}$ mbar) for about 3 days in order to remove the remaining solvent. The obtained empty $SiO_2$ monoliths and SNP@$SiO_2$ nanocomposite samples are shown in Fig. 1.

### 2.2. Total scattering measurement

The experiments were performed on the powder diffractometer of the Material Science beamline of the Swiss Light Source
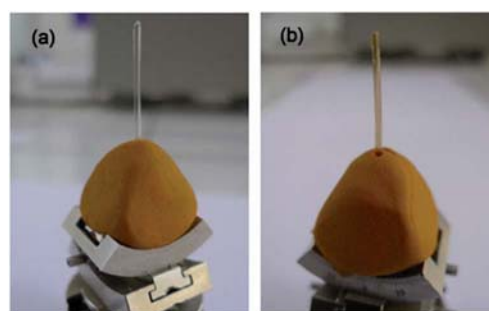


**Fig. 1** Photographs of the synthesized mesoporous silica monoliths: (a) empty $SiO_2$ monolith and (b) SNP–silica nanocomposites.

synchrotron facility (SLS) at the Paul Scherrer Institute (Villigen, Switzerland). Data were collected using a monochromatic beam of wavelength $\lambda = 0.4962$ Å (energy $E = 24.9866$ keV) and the second generation microstrip detector Mythen II covering 120° with 0.0037° resolution. Due to the relatively low absorption coefficient of unloaded and loaded $SiO_2$ monoliths, Debye–Scherrer transmission set up was used. The used photon energy combined with an appropriate data collection strategy enable data to be recorded over a sufficiently high wave vector $Q$ ($Q = 4\pi \sin \theta/\lambda$) to provide the necessary resolution in real-space for quantitative structural analysis to be attempted. Two total scattering data sets have been collected at room temperature up to $Q_{max} = 24.2$ Å$^{-1}$ corresponding to a $d$ spacing of 0.26 Å for the unloaded and the loaded monoliths under the exact same experimental conditions, which is of utmost importance to derive the d-PDF described below. Using the impregnation method described above (post-loading of SNP complexes into the solidified monolith), ensures that the porous silica network is not altered between loaded and unloaded sample.[18,66] This approach allows for calculation of the differential PDF by simple subtraction of the two corresponding $G(r)$ (loaded–unloaded). The $G(r)$ function is defined in the next section. We note here that similar data collections have been conducted (under the same experimental conditions) for the bulk microcrystalline SNP powder. The PDF obtained from the crystalline SNP will serve as a reference for the structural modelling of the loaded $SiO_2$ monoliths.

### 2.3. Data reduction and calculation of the PDF

The data were corrected for absorption, multiple scattering, polarization, Compton scattering and Laue diffuse scattering. To obtain the total scattering structure function $S(Q)$ the data were normalized by the incident flux and the number of scatterers. The experimental atomic pair distribution function $G(r)$ in real space was then obtained by a direct sine Fourier transformation of the resulting total scattering structure function $S(Q)$ according to:

$$G(r) = \frac{2}{\pi} \int_{Q_{min}}^{Q_{max}} Q[S(Q) - 1]\sin(Qr)\mathrm{d}Q$$

The scattering signal from the air and the experimental set up was measured independently under the exact same conditions as the sample and subtracted as a background in the data reduction procedure. In the Fourier transformation step for obtaining the experimental atomic pair distribution function $G(r)$ from $S(Q)$, the data were truncated at a finite maximum value of $Q_{max} = 23.2$ Å$^{-1}$ beyond which the signal-to-noise ratio became unfavourable. All data processing was done using the program GudrunX.[67]

### 2.4. Solid state NMR spectroscopy

All experiments were carried out on a high-field Bruker NMR Avance III spectrometer operating at 14 T ($^1$H NMR frequency of 600 MHz) with a Bruker 4 mm MAS triple-resonance probe. MAS spinning speed was set to 12.5 kHz. For $^{29}$Si experiments the

rf-field strength applied for the $^{29}$Si pulse was set to 45 kHz, with an excitation pulse length of 1.85 µs. During acquisition, SPINAL-64[68] heteronuclear decoupling was applied at an rf-field strength of 80 kHz. The interscan delay was set to 10 s; 1536 scans were accumulated for a total experimental time of about 4.5 h.

For $^{13}$C MAS experiments the rf-field strength applied for the $^{13}$C pulse was set to 51 kHz, leading to a 90° pulse length of 4.9 µs. During acquisition, SPINAL-64[68] heteronuclear decoupling was applied at an rf-field strength of 80 kHz. For the crystalline SNP sample the interscan delay was set to 19 s and 4608 scans were accumulated for a total experimental time of about 24 h; for the hybrid SNP@SiO$_2$ sample the interscan delay was set to 3 s and 6144 scans were accumulated for a total experimental time of about 5 h.

For $^{23}$Na MAS experiments the rf-field strength applied for the $^{23}$Na pulse was set to 76 kHz, leading to a 90° pulse length of 3.3 µs. During acquisition, SPINAL-64[68] heteronuclear decoupling was applied at an rf-field strength of 80 kHz. The interscan delay was set to 3 s; 128 scans were accumulated for a total experimental time of about 6 min.

For $^1$H MAS experiments the rf-field strength applied for the $^1$H pulse was set to 80 kHz, leading to a 90° pulse length of 3.1 µs. The interscan delay was set to 3 s; 32 scans were accumulated for a total experimental time of 1.6 min.

For the hydration study (Fig. 7) the open NMR rotors were stored overnight with saturated solutions of LiBr, CaCl$_2$ and KCl salts stabilizing the atmosphere at 6%, 29% and 85% relative humidity (25 °C) respectively. For all experiments, the temperature at the stator output was stabilized at 298 K.

The Dmfit[69] program was used to fit $^{13}$C chemical shift anisotropy based on spinning sideband patterns and to fit the second order quadrupolar effects on the lineshapes of the $^{23}$Na central peaks. All spectra were processed with the GSim program developed by V. Zorin.[70]

## 3. Results and discussion

### 3.1. Total X-ray scattering approach

3.1.1. Experimental PDF and d-PDF. The X-ray diffraction data of the loaded and unloaded monoliths are shown in Fig. 2a. Both data sets confirm the amorphous nature of the silica gel, exhibiting the characteristic broad principal peak at $Q \sim 1.64$ Å$^{-1}$.[71] We observe that the main peak has a lower intensity and is slightly broadened in the loaded monolith. This feature has been observed in previous work[1] and reflect the change of the scattering contrast between the empty and filled monoliths.

The corresponding atomic PDFs in real space, $G(r)$, are shown in Fig. 2b. The expected pair distances for a $SiO_2$ xerogel have been identified and are in agreement with published data (see e.g. Benmore[72]). The second peak at 1.60 Å in the PDF refers to the Si–O bond length in the silica network. The third $G(r)$ peak at 2.64 Å originates from O–O distances and confirms that the average O–Si–O bond angle is tetrahedral. The fourth peak in $G(r)$ at 3.08 Å corresponds to Si–Si distances in the configuration of corner-sharing $SiO_4$ tetrahedral units. This mutual arrangement of the $SiO_4$ tetrahedra can be further described by
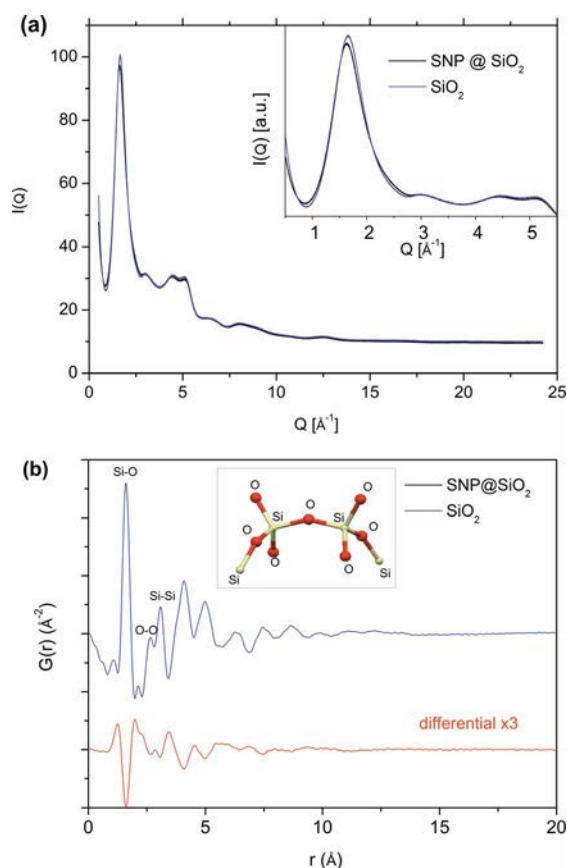
**Fig. 2** (a) Diffraction patterns of unloaded and loaded monoliths. (b) Corresponding PDFs, $G(r)$, for unloaded (blue) and loaded (black) monoliths, and the differential-PDF (red) which is scaled up for clarity.

the 5th and 6th peaks, respectively, at 4.08 Å and 4.99 Å, corresponding to two Si–O and O–O distances between two adjacent SiO₄ units and depending on the two torsion angles describing the rotation of the SiO₄ units about the two joined Si–O bonds. The assignment of peaks at higher $r$ values is difficult due to peak overlap. Small differences in the PDF between loaded and unloaded monoliths can be clearly observed in the differential PDF corresponding to the direct subtraction $G(r)_{loaded}$ − $G(r)_{unloaded}$, and occur mainly at low $r$ values up to 7 Å (Fig. 2).

The study of differential PDFs allows for the extraction of structural information due to atomic correlation involving the guests, both guest–guest and guest-framework, as well as guest-induced framework perturbations.[73] In the present case the significant structural changes due to the insertion of the SNP complexes are limited to the local scale up to distances of 10 Å indicating well isolated molecules inside the matrix pores.

Fig. 3 shows the comparison of the experimental differential PDF obtained by the subtraction $G(r)_{loaded}$ − $G(r)_{unloaded}$ and the $G(r)$ obtained from crystalline SNP (measured under the same experimental conditions). The positions of the peaks (corresponding to atom–atom distances) in the differential PDF are slightly shifted with respect to the crystal structure indicating a minor structural relaxation of the molecule embedded in nanopores. However, it can be seen that the main bond lengths of SNP encapsulated in the SiO₂ gel correspond to the

intramolecular pair correlations found in crystalline samples in the range 1–5 Å, with distances of 1.16 Å (C–N), 1.93 Å (Fe–C), 3.09 Å (Fe–N) and some weaker intra-molecular correlations (C–C, N–N between ligands). The most intense peaks in the $G(r)$ involve the pairs including the strongest scatterers (Fe atom) in this complex as well as the most abundant pairs (five C–N ligands). The absence of sharp features in the d-PDF beyond 5 Å is a strong indication of the absence of any regular ordering around the $[Fe(CN)_5NO]^{2-}$ molecules and thus confirms our hypothesis that we are dealing with isolated SNP complexes in the porous network. However, the distances due to intra-molecular pair correlations in $[Fe(CN)_5NO]^{2-}$ do not account for all the features observed in the d-PDF. In order to obtain more detailed information about a possible structural relaxation of the SNP complex, the position of the counter ions (Na⁺), and the interactions with the pore walls of the SiO₂ monoliths, we performed extensive modelling as detailed below.

**3.1.2. Modelling.** The fitting of the differential PDF was accomplished using the "difference modelling" strategy which employs three components: (i) a reference PDF of the vacant host, (ii) the structure model of the host–guest system, and (iii) the experimental differential PDF. An initial structure of the host–guest system was constructed as follows. First, the empty porous SiO₂ network was created using the Reverse Monte Carlo (RMC) method which has been described by Keen.[74] The RMC modelling of amorphous SiO₂ was developed by using reliable total scattering data to create three dimensional models. Starting from random configuration of SiO₂ groups based on the experimental number density, three geometrical constraints have been applied: Si–O distances (∼1.6 Å) and O–Si–O angle (∼109.5°) which permit to keep the SiO₄ tetrahedral configuration, and Si–O–Si angle (∼143.0°) for creating undistorted corner shearing SiO₄ tetrahedra to form an amorphous silica network. Then, a credible configuration of the $[Fe(CN)_5NO]^{2-}$ anion was taken from single crystal data measured at room temperature. This modelling was performed using the DISCUS program.[75]

Fig. 4 shows the results of the fitting of the experimental d-PDFs up to 10 Å together with the corresponding configurations of the SNP complexes. In order to keep electrical neutrality, the configurations were chosen such that one
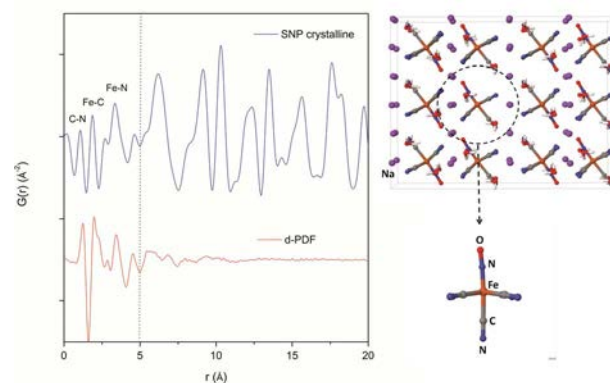


**Fig. 3** Comparison of $G(r)$ of crystalline SNP (crystal structure illustrated perpendicular to *ab* plane), and differential-PDF from embedded SNP which isolates structural information of molecule in the porous matrix.

[Fe(CN)$_5$NO]$^{2-}$ anion is associated with 2 Na$^+$ cations in one nanopore. The two Na$^+$ cations are placed on five different positions with respect to the [Fe(CN)$_5$NO]$^{2-}$ anion.

For judging the quality of the fit we used the weighted R-value;

$$R_{\mathrm{wp}} = \sqrt{\frac{\sum_j w_j \left(G_{\mathrm{obs},j} - G_{\mathrm{calc},j}\right)^2}{\sum_j w_j G_{\mathrm{obs},j}{}^2}}$$

where $w_j$ is the weighting, $G_{\mathrm{obs},j}$ and $G_{\mathrm{calc},j}$ are observed and calculated $G(r)$, respectively, for each point $j$ of the PDF curve.

Fig. 4a illustrates clearly that pair correlations are mainly dominated by the [Fe(CN)$_5$NO]$^{2-}$ anion up to ~5 Å; Fig. 4b–f show configurations where two Na$^+$ cations are taken into account around the molecule with a fixed radial distance of 5.55 Å. This allows for an improved fit of the d-PDF in the region below 8 Å. Fig. 4d shows the configuration yielding the best fit including the 5–10 Å region. In this configuration the two Na$^+$ anions are in the equatorials plane of the [Fe(CN)$_5$NO]$^{2-}$ anions, in prolongation of the Fe–C–N direction. Additionally, we have
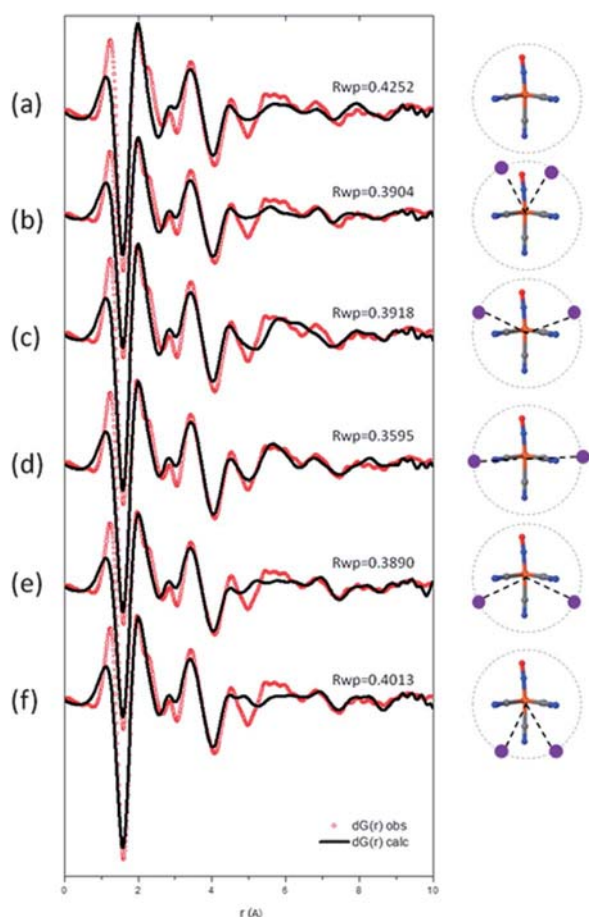


**Fig. 4** d-PDF fits with different configurations of isolated SNP complexes illustrated on the right: (a) one [Fe(CN)$_5$NO]$^{2-}$ anion within the pores; (b)–(f) considers two Na$^+$ cations placed around [Fe(CN)$_5$NO]$^{2-}$ to keep electrostatic neutrality. Five configurations are considered for which (d) results in the best fit. In that case the two Na$^+$ cations in the equatorial plane of the [Fe(CN)$_5$NO]$^{2-}$ anions, in prolongation of the Fe–C–N direction.

arranged the Na$^+$ positions as given in the single crystal (one equatorial and one near the axial CN ligand, not shown here) but for this configuration the $R_{\mathrm{wp}}$-value increases. The same increase of $R_{\mathrm{wp}}$ was found by varying the radial distance of the Na$^+$ counter ions between 4 and 7 Å. Consequently we can determine by this procedure the position of the two Na$^+$ ions with respect to the [Fe(CN)$_5$NO]$^{2-}$ anion with reasonable reliability.

On the other hand there are still some features in the d-PDF that are not completely explained by our model, especially the intensity of the peak at 1.3 Å as well as the shoulder at about 2.3 Å. It should be noted here that the low $r$ region (0 to ~1.2 Å) of the d-PDF is very critical and may contain some errors due to the limitation of the experimental setup and the processing of the data.[19] Therefore the interpretation of the interactions contributing to the intensity of the peak at 1.3 Å has to be taken with care. However we tested two hypotheses in order to account for these features: i) interaction with pore wall, and ii) hydration. Concerning i) host–guest interaction: even though an earlier neutron diffraction study on a similar compound GuNP@SiO$_2$ has shown the possibility of host–guest interactions (Cervellino et al.)[18], the NMR results don't show any evidence for such interactions, neither on the Si nor on the Na$^+$ side. Concerning ii), the impregnation of the monoliths was performed from aqueous solutions and it is also known that porous matrices like SiO$_2$ readily uptake humidity. Additionally, NMR measurements indicate that the SNP complex inside the pore is surrounded by water molecules (see details below). However, fitting the d-PDF with additional H$_2$O molecules proved to be a very difficult task. Although improvements could be realized, the reliability of such fits was quite limited, as different configurations yielded similar results, sometimes with no significant improvement of $R$-values. Thus, although the presence of water molecules surrounding the SNP complexes in the pores is shown by NMR, the structural arrangement cannot be obtained from a PDF measurement at this stage.

Concluding this first part, total X-ray scattering measurements coupled to d-PDF analysis showed that isolated SNP complexes are embedded in SiO$_2$ pores. Additionally the structural configuration of cation and anion could be proposed from a difference modelling strategy.

### 3.2. Solid State NMR approach

Since NMR observables depend on the local environment of the nuclear spins, long range order is not necessary to obtain resolved structural information. This complementary approach is thus well adapted to characterise both the amorphous host and the molecular guest as long as NMR sensitive nuclei are present in both components of the material. Additionally, the anisotropic nuclear interactions typically measured by Solid State NMR techniques can also be used to obtain information on molecular dynamics inside the solids.

**3.2.1. Structure of the amorphous SiO$_2$ host.** The porous matrix containing the isolated SNP complexes is composed of amorphous SiO$_2$ silica. Both $^{29}$Si ($I = 1/2$; 4.7% natural abundance) and $^{17}$O ($I = 5/2$; 0.037% natural abundance) allow NMR

studies, however the very low natural abundance and the quadrupole moment of the $^{17}O$ isotope severely reduce its sensitivity and make its NMR application difficult. Therefore we applied $^{29}Si$ MAS NMR to characterise the xerogel matrix. Fig. 5 presents the $^{29}Si$ MAS NMR spectra of the porous $SiO_2$ xerogel before and after incorporating the SNP molecules. The chemical shifts observed are typical for $Q^n$ $SiO_4$ tetrahedra units;[31] $Q^n$ representing $SiO_4$ tetrahedra of the amorphous network, which form $n$ bonds with neighboring tetrahedral. Both spectra show two major resonances at −101.7 ppm and −110.5 ppm, corresponding to $Si(OSi)_3(OH)$ ($Q^3$) and $Si(OSi)_4$ ($Q^4$) sites, respectively, and one resonance at −91.8 ppm corresponding to $Si(OSi)_2(OH)_2$ ($Q^2$) sites. The absence of $Si(OSi)(OH)_3$ ($Q^1$) sites and the low ratio of $Q^2$ sites indicate a relatively high degree of condensation of the xerogels. This is especially true since, on the spectra acquired here, this ratio is overestimated because of short experimental repetition times compared to $Q^3$ and $Q^4$ $^{29}Si$ $T_1$ relaxation times.

A comparison between the spectra of the empty and the SNP loaded matrix shows neither an increase of the line widths nor the appearance of additional sites. This indicates that the gel structure is not modified by the embedding procedure of the SNP molecules. This point is very important since it validates the differential PDF (d-PDF) approach described previously. The comparison also does not show evidence of strong interactions between the host xerogel and the molecular guest since significant covalent chemisorptions on the silanol groups (by $Na^+$ for example) would generate new chemically shifted $^{29}Si$ sites.

**3.2.2. Structure and dynamics of the SNP guest.** Given the NMR sensitivity of the nuclei present in the SNP salt, we applied $^{13}C$ NMR to probe the local environment of the $[Fe(CN)_5NO]^{2-}$ anions and $^{23}Na$ NMR to probe the environment of the counterions.

The $^{23}Na$ MAS NMR spectrum of the bulk crystal (Fig. 6) displays two inequivalent sites with same multiplicity but significantly different quadrupolar coupling constants. The first site $Na_1$ has a quadrupolar constant $C_{Q^1} = 1369$ kHz and an asymmetry of $\eta_1 = 0.92$ while the second site $Na_2$ has a smaller

constant $C_{Q^2} = 615$ kHz and $\eta_2 = 0.33$. The isotropic chemical shifts ($\delta_1^{iso} = -5.74$ ppm and $\delta_2^{iso} = -1.91$ ppm) indicate hex-accoordinated sodium atoms[76] and are consistent with the XRD crystal structure;[48,49] the NMR sites can be assigned to the inequivalent crystallographic positions by comparing the Electrical Field Gradient properties with those published from DFT calculations.[77] The $^{23}Na$ MAS NMR spectrum of the SNP inside the silica matrix (Fig. 6) is very different. This spectrum presents only one $^{23}Na$ site with a chemical shift ($\delta^{iso} = -1.1$ ppm) indicating that the sodium site is coordinated by mostly water molecules.[78] This means that the crystal structure is not preserved inside the pores of the $SiO_2$ matrix and that the two $^{23}Na$ counterions experience identical local environments on the ms timescale. Several possibilities can explain the presence of a unique $^{23}Na$ site but consistently with our other measurements we interpret this as motional averaging below the ms timescale due to solvation by surrounding water molecules.

The $^{13}C$ MAS NMR spectrum of the bulk crystal (Fig. 7) displays four resolved sites ($\delta^{iso} = 136.7$ ppm, 136.2 ppm, 135.9 ppm, and 135.5 ppm) whereas the SNP@$SiO_2$ nanocomposite displays only two ($\delta_{equatorial}^{iso} = 134.7$ ppm and $\delta_{axial}^{iso} = 133.3$ ppm). For the nanocomposite, the isotropic chemical shifts are thus displaced towards the solution state values[52] with a surface ratio of 4 : 1 typically observed for SNP in solution.



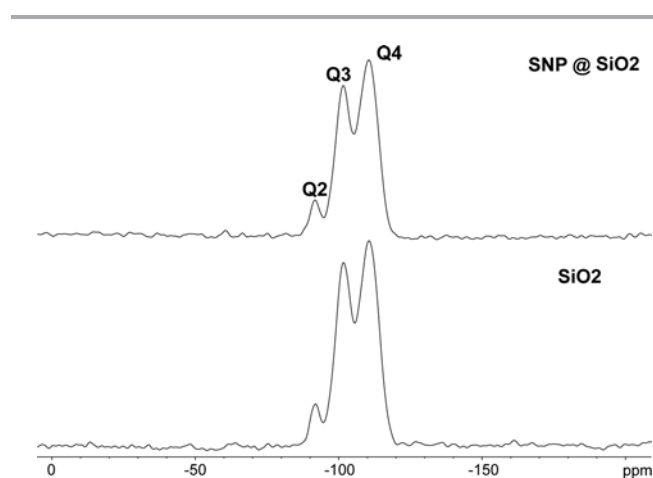**Fig. 5** $^{29}Si$ MAS NMR spectra ($\nu^{MAS} = 12.5$ kHz) of the SNP loaded $SiO_2$ matrix (top) and the empty $SiO_2$ matrix (bottom).
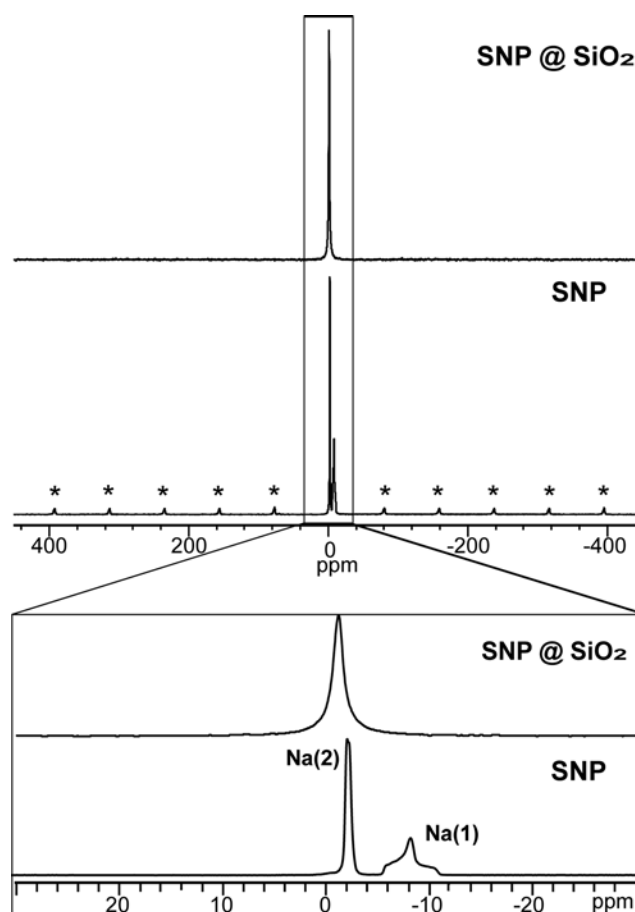


**Fig. 6** $^{23}Na$ MAS NMR spectra ($\nu^{MAS} = 12.5$ kHz) of the SNP loaded $SiO_2$ matrix (top) and crystalline SNP (bottom). Quadrupolar satellites are marked by asterisks.

Consistently with the $^{23}$Na results, this means that the crystal structure is not preserved in the nanocomposite. It also indicates that water molecules are present inside the pores and that, for sufficiently high hydration levels, the nitroprussiate is well separated from its sodium counterions. Nevertheless, as will be detailed in the next section, the line width broadening observed for samples stored in relatively dry conditions indicates that the "free" solvation water molecules can quite easily be removed.

In the bulk crystalline state, both the $^{13}$C and the $^{23}$Na nuclei display anisotropic interactions. Fitting the MAS sideband pattern of the $^{13}$C spectrum informs us about the chemical shift anisotropy. For the crystal we find a relatively strong anisotropy $\delta^{aniso} = 32$ kHz with a slight asymmetry of $\eta = 0.08$. Its origin is essentially intramolecular and relies on the anisotropic electron distribution of the Fe–C≡N bonding. For the $^{23}$Na spins the dominant interaction is the quadrupolar coupling which can be obtained here by fitting the second order quadrupolar lineshapes of the center bands. These values are $C_{Q^1} = 1369$ kHz and $C_{Q^2} = 615$ kHz depending on how the nuclear electric quadrupole moment couples to the local electric field gradient. As evidenced on Fig. 6 and 7, the CSA and quadrupolar interactions split the MAS NMR signals into spinning sidebands and satellites (respectively) appearing at integer multiples of the sample rotation frequency and spread over a frequency window

equivalent to the strength of the interactions.[79] Interestingly the sidebands and satellites are no longer present for the nanocomposite powder spectra. This clearly indicates that the embedded SNP performs isotropic reorientation inside the pores, a motion sufficiently fast to completely average out both types of anisotropic interactions. Hence the characteristic frequency of the motion is higher than those interactions and implies a sub-µs isotropic reorientation. Since the NMR chemical shifts are identical for all equatorial $^{13}$C sites, and the d-PDF modelling results suggest that the Na$^+$ cations are located in the prolongation of the equatorial C≡N bonds, then [Fe(CN)$_5$NO]$^{2-}$ must also experience a C$_4$ rotation around the Fe–N–O axis with respect to the Na$^+$ cation. The correlation time of this rotation has to be shorter than the NMR measurement timescale (ms).

This last point will be further investigated in a subsequent NMR study dedicated to quantitative characterisation of the SNP dynamics inside the SiO$_2$ matrix. CSA and relaxation time measurement at different temperatures and hydration levels will be necessary to characterise the motional correlation between the nitroprusside and its counterion.

**3.2.3. Hydration of the nanocomposite SNP@SiO$_2$ xerogel.** To study how hydration influences the structure and dynamics of the SNP complex inside the SiO$_2$ matrix, the NMR samples have been stored in three different environments of 6%, 29% and 85% relative humidity (RH). $^1$H, $^{13}$C, $^{23}$Na MAS NMR spectra (Fig. 8) were subsequently acquired to observe how the different components of the material were influenced by hydration.

The signals observed on the $^1$H spectra originate principally from water molecules that can exchange protons with silanols groups. The series of $^1$H spectra shows how the pore water content diminishes with the relative humidity levels. The spectra are composed of a dominating signal between 4.5 ppm and 4 ppm that is reduced, broadened and shifted upfield when the relative humidity is lowered. This signal reflects relatively
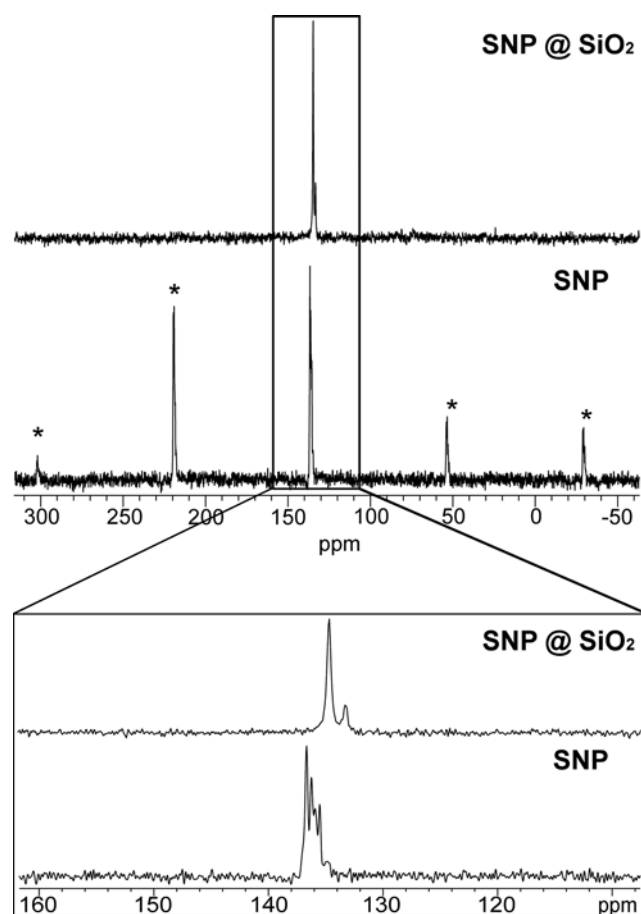


**Fig. 7** $^{13}$C MAS NMR spectra ($\nu^{MAS} = 12.5$ kHz) of the SNP loaded SiO$_2$ matrix (top) and crystalline SNP (bottom). Spinning sidebands are marked by asterisks.
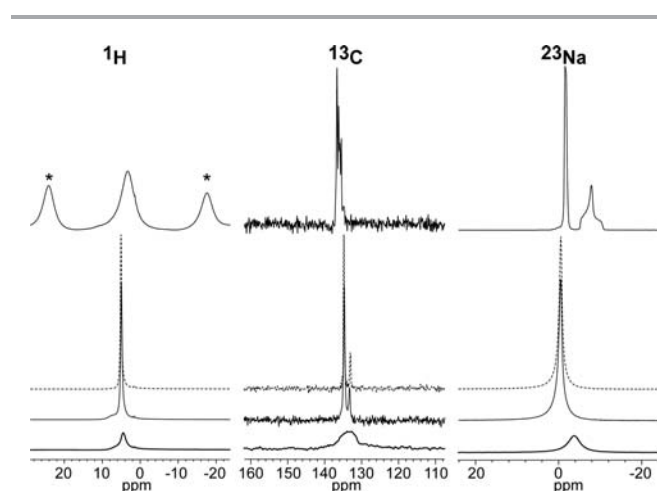


**Fig. 8** Effect of hydration on the $^1$H, $^{13}$C and $^{23}$Na spectra (respectively from left to right) of the SNP@SiO$_2$ hybrid xerogel. For reference, the upper spectra are acquired on crystalline SNP. The spectra below correspond to SNP loaded xerogels that have been stored overnight at 84%, 29% and 6% relative humidity (broken, fine and bold line respectively). MAS spinning sidebands are marked with asterisks ($\nu^{MAS} = 12.5$ kHz).

mobile water molecules present inside the pores of the matrix. When the humidity is decreased, the "free" water is removed and only the first hydration layers remain. Therefore the remaining signal is shifted and broadened because of the stronger adsorption of the water and the proton exchange between liquid water, physisorbed water and silanols.[42]

The ^{13}C and [23]Na spectra (Fig. 8) focus on the SNP guest. Both series behave comparably and show that all anisotropic interactions remain motionally averaged even at a low hydration level (no MAS sidebands or satellites even at 6% relative humidity). Additionally, the removal of water molecules does not induce chemical shift changes towards those observed for crystalline SNP. This indicates that even when most of the water inside the nanopore cavity is removed, the SNP maintains its strong dynamic properties and does not take a nanocrystalline structure. We also observe an upfield shifting of the [23]Na signal which is consistent with an elongation of the average coordination distance.[76] Nevertheless, both ^{13}C and [23]Na signals become considerably broadened for samples stored at 6% RH. This broadening cannot be refocused by spin echo type sequences; it is therefore from the homogeneous type. This means that it is not due to a distribution of chemical shifts but to a decrease of $T_2^*$ transverse relaxation time. Since both the $[Fe(CN)_5NO]^{2-}$ anions and the sodium counterions display sub-μs dynamics, we speculate that the relaxation mechanism originates from fluctuating ion–counterion interactions rather than from interactions with the pore surface. A more quantitative description of the molecular motion inside the pores will be addressed elsewhere by a dedicated NMR study.

## 4.   Conclusion and future outlook

High energy X-ray total scattering coupled with experimental differential PDF analysis, together with Solid State NMR techniques, allows us to investigate structural properties of isolated SNP molecules incorporated in the silica nanopores. The atomic d-PDF and the modelling approaches provide direct structural evidence on the local cation and anion arrangement of the SNP complexes and show that the SNP complexes are embedded in the form of isolated molecules inside the matrix pores. The multi-nuclei Solid State NMR investigation provides information on both the amorphous host and the molecular guest and adds a dynamic dimension to the classical static structural characterisation. ^{29}Si MAS NMR measurements show that the gel matrix structure is not modified by the SNP embedding procedure. ^{13}C and ^{23}Na MAS NMR measurements show that inside the matrix pores the SNP neither takes a crystalline like structure nor does it adhere to the pore surface in agreement with the d-PDF results. Additionally, we surprisingly find evidence that the confined complex adopts solution like structure and dynamics with isotropic reorientation below the μs timescale. Subsequent NMR experiments at different relative humidity levels show the presence of weakly interacting water molecules inside the pores. This explains, to some extent, the differences on the d-PDF curves observed between the experimental and the suggested model. These water molecules can easily be removed to some extent, nevertheless the strong

isotropic motion of the SNP is still preserved even for low hydration levels. Globally, the SNP complexes behave as "free" isolated molecules inside the matrix pores. The fact that the local arrangement of cation and anion and their dynamic can be proposed from a model obtained by using d-PDF and Solid State NMR multiscale approach allows for future systematic investigations of structure–property relationship in such hybrid organic–inorganic nanocomposites.

## Notes and references

1 Z. Tahri, R. Lepski, K.-Y. Hsieh, E.-E. Bendeif, S. Pillet, P. Durand, T. Woike and D. Schaniel, *Phys. Chem. Chem. Phys.*, 2012, **14**, 3775–3781.

2 P. Durand, S. Pillet, E.-E. Bendeif, C. Carteret, M. Bouazaoui, H. E. Hamzaoui, B. Capoen, L. Salmon, S. Hébert, J. Ghanbaja, L. Aranda and D. Schaniel, *J. Mater. Chem. C*, 2013, **1**, 1933–1942.

3 K. Ariga, A. Vinu, J. P. Hill and T. Mori, *Coord. Chem. Rev.*, 2007, **251**, 2562–2591.

4 K. Moller and T. Bein, *Chem. Mater.*, 1998, **10**, 2950–2963.

5 C. Sanchez and B. Lebeau, *MRS Bull.*, 2001, **26**, 377–387.

6 C. Sanchez, B. Lebeau, F. Chaput and J.-P. Boilot, *Adv. Mater.*, 2003, **15**, 1969–1994.

7 U. Ruschewitz and D. Hermann, *Z. Anorg. Allg. Chem.*, 2010, **636**, 2068.

8 D. Hermann, H. Emerich, R. Lepski, D. Schaniel and U. Ruschewitz, *Inorg. Chem.*, 2013, **52**, 2744–2749.

9 V. Dieckmann, S. Eicke, K. Springfeld and M. Imlau, *Materials*, 2012, **5**, 1155–1175.

10 D. Schaniel, M. Imlau, T. Weisemoeller, T. Woike, K. W. Krämer and H.-U. Güdel, *Adv. Mater.*, 2007, **19**, 723–726.

11 M. Goulkov, D. Schaniel and T. Woike, *J. Opt. Soc. Am. B*, 2010, **27**, 927–932.

12 T. Woike, W. Kirchner, G. Schetter, T. Barthel, K. Hyung-sang and S. Haussühl, *Opt. Commun.*, 1994, **106**, 6–10.

13 P. Coppens, I. Novozhilova and A. Kovalevsky, *Chem. Rev.*, 2002, **102**, 861–884.

14 D. Schaniel and T. Woike, *Phys. Chem. Chem. Phys.*, 2009, **11**, 4391–4395.

15 A. Schuy, T. Woike and D. Schaniel, *J. Sol-Gel Sci. Technol.*, 2009, **50**, 403–408.

16 C. Seidel, U. Ruschewitz, A. Schuy, T. Woike and D. Schaniel, *Z. Anorg. Allg. Chem.*, 2008, **634**, 2018.

17 V. Dieckmann, M. Imlau, D. H. Taffa, L. Walder, R. Lepski, D. Schaniel and T. Woike, *Phys. Chem. Chem. Phys.*, 2010, **12**, 3283–3288.

18 A. Cervellino, J. Schefer, L. Keller, T. Woike and D. Schaniel, *J. Appl. Crystallogr.*, 2010, **43**, 1040–1045.

19 B. H. Toby and T. Egami, *Acta Crystallogr., Sect. A: Found. Crystallogr.*, 1992, **48**, 336–346.

20 R. B. Neder and T. Proffen, *Diffuse Scattering and Defect Structure Simulations*, Oxford University Press, 2008.

21 T. Proffen, S. J. L. Billinge, T. Egami and D. Louca, *Z. Kristallogr.*, 2003, **218**, 132–143.

22 T. Egami and S. J. L. Billinge, *Underneath the Bragg Peaks: Structural Analysis of Complex Materials*, Pergamon, 2nd edn, 2012.

23 S. J. L. Billinge and M. G. Kanatzidis, *Chem. Commun.*, 2004, 749–760.

24 F. Pourpoint, X. Hua, D. S. Middlemiss, P. Adamson, D. Wang, P. G. Bruce and C. P. Grey, *Chem. Mater.*, 2012, **24**, 2880–2893.

25 B. Key, M. Morcrette, J.-M. Tarascon and C. P. Grey, *J. Am. Chem. Soc.*, 2011, **133**, 503–512.

26 F. Atassi, C. Mao, A. S. Masadeh and S. R. Byrn, *J. Pharm. Sci.*, 2010, **99**, 3684–3697.

27 Y.-I. Kim, S. Cadars, R. Shayib, T. Proffen, C. S. Feigerle, B. F. Chmelka and R. Seshadri, *Phys. Rev. B: Condens. Matter Mater. Phys.*, 2008, **78**, 195205.

28 M. Shatnawi, G. Paglia, J. L. Dye, K. C. Cram, M. Lefenfeld and S. J. L. Billinge, *J. Am. Chem. Soc.*, 2007, **129**, 1386–1392.

29 J. Breger, N. Dupre, P. J. Chupas, P. L. Lee, T. Proffen, J. B. Parise and C. P. Grey, *J. Am. Chem. Soc.*, 2005, **127**, 7529–7537.

30 E. Andrew, A. Bradbury and R. Eades, *Nature*, 1958, **182**, 1659.

31 E. Lippmaa, M. Maegi, A. Samoson, G. Engelhardt and A. R. Grimmer, *J. Am. Chem. Soc.*, 1980, **102**, 4889–4893.

32 I. S. Chuang, D. R. Kinney and G. E. Maciel, *J. Am. Chem. Soc.*, 1993, **115**, 8695–8705.

33 H. El Rassy, P. Buisson, B. Bouali, A. Perrard and A. C. Pierre, *Langmuir*, 2002, **19**, 358–363.

34 E. Framery and P. H. Mutin, *J. Sol-Gel Sci. Technol.*, 2002, **24**, 191–195.

35 D. H. Brouwer, R. J. Darton, R. E. Morris and M. H. Levitt, *J. Am. Chem. Soc.*, 2005, **127**, 10365–10370.

36 C. A. Fyfe and D. H. Brouwer, *J. Am. Chem. Soc.*, 2006, **128**, 11860–11871.

37 G. Hartmeyer, C. Marichal, B. Lebeau, S. Rigolet, P. Caullet and J. Hernandez, *J. Phys. Chem. C*, 2007, **111**, 9066–9071.

38 W. Lutz, D. Täschner, R. Kurzhals, D. Heidemann and C. Hübert, *Z. Anorg. Allg. Chem.*, 2009, **635**, 2191–2196.

39 C. Cannas, M. Casu, A. Musinu and G. Piccaluga, *J. Non-Cryst. Solids*, 2005, **351**, 3476–3482.

40 H. El Rassy and A. C. Pierre, *J. Non-Cryst. Solids*, 2005, **351**, 1603–1610.

41 J. Walia, J. Crone, J. Liang, M. Niknam, C. Lemaire, R. Terry Thompson and H. Peemoeller, *Solid State Nucl. Magn. Reson.*, 2013, **49–50**, 26–32.

42 J. Trébosc, J. W. Wiench, S. Huh, V. S.-Y. Lin and M. Pruski, *J. Am. Chem. Soc.*, 2005, **127**, 3057–3068.

43 P. T. Manoharan and W. C. Hamilton, *Inorg. Chem.*, 1963, **2**, 1043–1047.

44 F. Bottomley and P. S. White, *Acta Crystallogr., Sect. B: Struct. Crystallogr. Cryst. Chem.*, 1979, **35**, 2193–2195.

45 M. Y. Antipin, V. Tsirelson, M. P. Flyugge, Y. T. Struchkov and R. P. Ozerov, *Russ. J. Coord. Chem.*, 1987, **13**, 67–75.

46 A. Navaza, G. Chevrier, P. M. Alzari and P. J. Aymonino, *Acta Crystallogr., Sect. C: Cryst. Struct. Commun.*, 1989, **45**, 839–841.

47 D. Schaniel, T. Woike, J. Schefer and V. Petříček, *Phys. Rev. B: Condens. Matter Mater. Phys.*, 2005, **71**, 174112.

48 M. D. Carducci, M. R. Pressprich and P. Coppens, *J. Am. Chem. Soc.*, 1997, **119**, 2669–2678.

49 B. Delley, J. Schefer and T. Woike, *J. Chem. Phys.*, 1997, **107**, 10067–10074.

50 A. J. Schultz, B. N. Figgis and A. N. Sobolev, *Acta Crystallogr., Sect. C: Cryst. Struct. Commun.*, 2000, **56**(Pt 11), 1289–1291.

51 H. E. Toma, J. A. Vanin and J. M. Malin, *Inorg. Chim. Acta*, 1979, **33**, L157–L159.

52 A. R. Butler, C. Glidewell, A. R. Hyde and J. McGinnis, *Inorg. Chem.*, 1985, **24**, 2931–2934.

53 D. Gross, N. Pislewski, U. Haeberlen and K. H. Hausser, *J. Magn. Reson.*, 1983, **54**, 236–252.

54 H. W. Spiess, *Macromolecules*, 2010, **43**, 5479–5491.

55 D. A. Torchia, *J. Magn. Reson.*, 2011, **212**, 1–10.

56 M. R. Hansen, R. Graf and H. W. Spiess, *Acc. Chem. Res.*, 2013, **46**(9), 1996–2007.

57 J. Zhang and J. Jonas, *J. Phys. Chem.*, 1993, **97**, 8812–8815.

58 F. Cros, L. Malier, J. P. Korb and F. Chaput, *J. Sol-Gel Sci. Technol.*, 1998, **13**, 457–460.

59 R. Kimmich, *Chem. Phys.*, 2002, **284**, 253–285.

60 G. Buntkowsky, H. Breitzke, A. Adamczyk, F. Roelofs, T. Emmler, E. Gedat, B. Gruenberg, Y. Xu, H.-H. Limbach, I. Shenderovich, A. Vyalikh and G. Findenegg, *Phys. Chem. Chem. Phys.*, 2007, **9**, 4843–4853.

61 W. Sangthong, M. Probst and J. Limtrakul, *Chem. Eng. Commun.*, 2008, **195**, 1486–1501.

62 T. Uemura, S. Horike, K. Kitagawa, M. Mizuno, K. Endo, S. Bracco, A. Comotti, P. Sozzani, M. Nagaoka and S. Kitagawa, *J. Am. Chem. Soc.*, 2008, **130**, 6781–6788.

63 R. Kimmich and N. Fatkullin, *Macromolecules*, 2010, **43**, 9821–9827.

64 M. Vogel, *Eur. Phys. J.: Spec. Top.*, 2010, **189**, 47–64.

65 A. M. Nishchenko, D. I. Kolokolov, A. A. Gabrienko and A. G. Stepanov, *J. Phys. Chem. C*, 2012, **116**, 8956–8963.

66 J. Krause, C. Schrage, A. Schuy, T. Woike, E. Kockrick, S. Kaskel and D. Schaniel, *Microporous Mesoporous Mater.*, 2011, **142**, 245–250.

67 A. K. Soper and E. R. Barney, *J. Appl. Crystallogr.*, 2011, **44**, 714–726.

68 A. Khitrin and B. M. Fung, *J. Chem. Phys.*, 2000, **112**, 2392–2398.

69 D. Massiot, F. Fayon, M. Capron, I. King, S. Le Calvé, B. Alonso, J.-O. Durand, B. Bujoli, Z. Gan and G. Hoatson, *Magn. Reson. Chem.*, 2002, **40**, 70–76.

70 V. Zorin, GSim – visualisation and processing tool for NMR experiments and simulations.

71 H. F. Poulsen, J. Neuefeind, H.-B. Neumann, J. R. Schneider and M. D. Zeidler, *J. Non-Cryst. Solids*, 1995, **188**, 63–74.

72 C. J. Benmore and P. J. M. Monteiro, *Cem. Concr. Res.*, 2010, **40**, 892–897.

73 K. W. Chapman, P. J. Chupas and C. J. Kepert, *J. Am. Chem. Soc.*, 2005, **127**, 11232–11233.

74 D. A. Keen, *Phase Transitions*, 1997, **61**, 109–124.

75 T. Proffen and R. B. Neder, *J. Appl. Crystallogr.*, 1999, **32**, 838–839.

76 X. Xue and J. F. Stebbins, *Phys. Chem. Miner.*, 1993, **20**, 297–307.

77 P. Blaha, K. Schwarz, W. Faber and J. Luitz, *Hyperfine Interact.*, 2000, **126**, 389–395.

78 X. Ai, F. Deng, J. Dong, L. Chen and C. Ye, *J. Phys. Chem. B*, 2002, **106**, 9237–9244.

79 E. R. Andrew, A. Bradbury and R. G. Eades, *Nature*, 1958, **182**, 1659–1659.

# Étude multi-échelle des changements structuraux et leur influence sur les propriétés optiques de complexes photoactifs encapsulés dans des matrices mésoporeuses

**Résumé** :

Les matériaux poreux silicatés ont été mis à profit pour encapsuler différents types de molécules, clusters ou nano-objets fonctionnels, donnant lieu à des nanocomposites hybrides organiques-inorganiques à propriétés physiques, chimiques ou biologiques remarquables. Elucider l'organisation structurale à l'échelle moléculaire de tels nanocomposites est indispensable pour l'analyse et la compréhension des propriétés macroscopiques qui en découlent. Ainsi, les techniques de diffusion totale associées à la fois à l'analyse Debye et la Fonction de Distribution de Paires (PDF) sont des méthodes de choix pour la caractérisation des propriétés structurales de matériaux hybrides nano-structurés.

Le principal objectif de ce travail consiste à l'utilisation des approches basées sur la diffusion totale de rayons X pour l'analyse structurale complète de molécules photoactives confinées dans des matrices silicatées amorphes avec différentes tailles de pores, afin d'étudier l'influence de l'organisation structurale sur les propriétés optiques et d'explorer également les limites de ces approches d'analyse. Nous avons étudié deux systèmes photoactifs. L'analyse structurale du premier complexe confiné, $Na_2[Fe(CN)_5NO]\cdot 2H_2O$ (SNP), a été entreprise par une approche multi-échelle combinant la RMN du solide et l'analyse PDF. Cette approche a permis l'identification de la nature des espèces incorporées, l'arrangement des cations et des anions ainsi que la distinction des différentes phases existantes : molécules isolées et nanoparticules. Les analyses Debye et PDF sur le deuxième composé étudié, $[NdCl_2(H_2O)_6]Cl$, montrent que l'organisation structurale du complexe confiné est différente de celle du matériau massif cristallin. De plus, les cations $Nd^{3+}$ changent de coordination de 8 à 9 durant le processus d'imprégnation et adoptent ainsi un arrangement structural très similaire à celui en solution aqueuse. Cette modification structurale est en accord avec le changement des propriétés luminescentes de ce complexe.

**Mots clés** : Diffusion totale, La fonction de distribution des paires (PDF), Nanocristallographie, Analyse Debye, Molécules photoactives, Nanomatériaux hybrides, Luminescence, Terres rares.

---

# Multiscale study of the influence of the structural changes on the optical properties of photoactive complexes confined in mesoporous matrices

**Abstract** :

Silica xerogels are versatile host materials for the inclusion of molecules, clusters, or nano-objects yielding host-guest compounds with unique physical, chemical or biological properties. The knowledge of the structural organization of the guest within the host is crucial for the understanding of its properties. Total scattering methods, based on Debye function analysis (DFA) and Pair Distribution Function (PDF), have become powerful tools for structural characterization of nanostructured hybrid materials.

The aim of this work is to use the X-ray total scattering method to obtain structural information on photoactive molecules embedded into amorphous silica hosts with different pore sizes, to correlate their structure with the optical properties, and to explore the limitations of the chosen method. Two different photoactive complexes have been investigated. In the first example, the combined PDF and NMR study on $Na_2[Fe(CN)_5NO]\cdot 2H_2O$ (SNP) embedded into silica matrices allows to extract the nature of the inserted species: quasi-free isolated molecules can be distinguished from nanoparticles and in the former case a model for the arrangement of cation-anion can be proposed from the PDF analysis. In the second example, a luminescent $Nd^{3+}$ complex, the PDF and DFA analysis reveal that the structural organization of the embedded $Nd^{3+}$ complexes is different from that of the crystalline material. Furthermore, the $Nd^{3+}$ cations change the coordination from 8 to 9 during the wet-impregnation doping and adopt very similar structural arrangement as in aqueous solution, which is in agreement with the observed change in the luminescence properties.

**Keywords**: Total scattering, Pair distribution function (PDF), Debye function, Nanocrystallography, Photoactive molecules, Guest-host nano-materials, Luminescence, Rare-earth.